

AD-762 584

THE EFFECTS OF MESO-SCALE AND SMALL-  
SCALE INTERACTIONS ON GLOBAL CLIMATE

Systems, Science and Software

Prepared for:

Defense Advanced Research Projects Agency

15 June 1973

DISTRIBUTED BY:

**NTIS**

**National Technical Information Service**  
**U. S. DEPARTMENT OF COMMERCE**  
5285 Port Royal Road, Springfield Va. 22151

ARO 9951.5-A

AD 762584



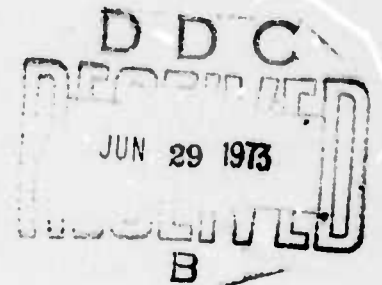
**SYSTEMS, SCIENCE AND SOFTWARE**

Approved for public release; distribution unlimited. The findings in this report are not to be construed as an official Department of the Army position, unless so designated by other authorized documents.

SSS-R-73-1727

**THE EFFECTS OF MESO-SCALE AND SMALL-SCALE  
INTERACTIONS ON GLOBAL CLIMATE**

Semiannual Technical Report  
for Period  
16 October 1972 through 16 April 1973



Sponsored by:

Defense Advanced Research Projects Agency  
DARPA Order No. 1752  
Program Element Code No. 62706E

Reproduced by  
NATIONAL TECHNICAL  
INFORMATION SERVICE  
U S Department of Commerce  
Springfield VA 22151

Contract No.: DAHC04-73-C-0003  
Effective Date of Contract: 16 October 1972  
Contract Expiration Date: 15 October 1973  
Amount of Contract: \$125,000

15 June 1973



**SYSTEMS, SCIENCE AND SOFTWARE**

---

SSS-R-73-1727

THE EFFECTS OF MESO-SCALE AND SMALL-SCALE  
INTERACTIONS ON GLOBAL CLIMATE

Semiannual Technical Report  
for Period  
16 October 1972 through 16 April 1973

Sponsored by:

Defense Advanced Research Projects Agency  
DARPA Order No. 1752  
Program Element Code No. 62706E

Contract No.: DAHC04-73-C-0003  
Effective Date of Contract: 16 October 1972  
Contract Expiration Date: 15 October 1973  
Amount of Contract: \$125,000

15 June 1973

P. O. BOX 1620, LA JOLLA, CALIFORNIA 92037. TELEPHONE (714) 453-0060

ia'

## ABSTRACT

The results reported are part of a continuing study to improve numerical models for meso-scale and small-scale effects which influence global weather and its modification. The two major areas being studied are the effects of mountain ranges on momentum transfer, and the transient interaction of solar radiation with the earth's atmosphere.

The results of the research on the solar radiation include several calculations and comparisons with experimental data of heat fluxes in the atmosphere. Comparative cases were also completed using the radiation parameterization which is presently used in the UCLA global circulation model. In addition to the calculations performed, several numerical techniques used in the code were modified in order to decrease the computer run time associated with the calculations.

The major tasks of the orographic study have been to:

- (1) develop a three-dimensional transient Boussinesq code,
- (2) continue development and check out of the linear steady state codes, and
- (3) continue to test the HAIFA codes and make runs using real topography data.

## TABLE OF CONTENTS

	<u>Page</u>
ABSTRACT . . . . .	ii
1. INTRODUCTION . . . . .	1
1.1 Radiative Transfer . . . . .	1
1.2 Orographic Effects on Global Climate . . . . .	1
2. RADIATION IN THE EARTH'S ATMOSPHERE: ATRAD IMPROVEMENTS . . . . .	3
2.1 Exponential Fitting Improvements . . . . .	4
2.1.1 A Global Minimization Procedure for Polynomials . . . . .	4
2.1.2 Splitting the Polynomial . . . . .	10
2.1.3 Exponential Fits of Representative Transmission Functions . . . . .	16
2.1.4 Tables of Fitting Parameters . . . . .	33
2.2 Mie Scattering . . . . .	34
2.2.1 Mie Scattering for a Single Sphere . . . . .	34
2.2.2 Integration over Size Distribution . . . . .	35
2.2.3 Tables . . . . .	37
2.2.4 Henyey-Greenstein Approximation . . . . .	38
3. RADIATION IN THE EARTH'S ATMOSPHERE - ATRAD PREDICTIONS FOR MODEL ATMOSPHERES AND COMPARISONS WITH SIMPLIFIED MODELS . . . . .	40
3.1 Arctic Stratus Problem . . . . .	40
3.1.1 Comparison of ATRAD with Experiment. . . . .	41
3.1.2 Dependence of Surface Flux on Solar Elevation . . . . .	49
3.1.3 Comparisons of ATRAD with Simpler Models . . . . .	51
3.2 ATRAD Compared with Katayama Models for Clear-Sky Cases . . . . .	65

## TABLE OF CONTENTS, contd.

	<u>Page</u>
3.3 ATRAD Compared with Katayama Model for Arctic Stratus Problems . . . . .	89
3.3.1 Scattering in the IR . . . . .	90
3.3.2 Sensitivity to Surface Temperature . . . . .	92
3.3.3 Cloud Albedo . . . . .	93
3.3.4 Albedo of a Cloudy Atmosphere . . . . .	95
4. HAIFA CODE MODIFICATIONS . . . . .	97
4.1 Triangular Zones . . . . .	97
4.2 The HAIFA Code . . . . .	104
4.2.1 The Dry Equations . . . . .	105
4.2.2 The Moist Equation . . . . .	105
5. SIERRA NEVADA LEE WAVE STUDY . . . . .	113
6. DEVELOPMENT OF THE LINEAR STEADY STATE CODES . . . . .	138
6.1 A Derivation of Reynolds Stress for Linear-Steady State Formulations . . . . .	139
6.1.1 Linear Steady State Equations . . . . .	140
6.1.2 Boundary Condition . . . . .	143
6.2 Code Development . . . . .	153
6.3 Topography Data . . . . .	157
7. A THREE-DIMENSIONAL BOUSSINESQ CODE 'STUFF' . . . . .	159
7.1 Derivation of Equations . . . . .	160
7.2 The Numerical Scheme . . . . .	169
7.3 Boundary Conditions . . . . .	171
7.4 Initial Conditions . . . . .	172
7.5 Buffering . . . . .	173
7.6 Other Features . . . . .	174

## TABLE OF CONTENTS, contd.

	<u>Page</u>
7.7 Sample Calculations . . . . .	174
7.7.1 Treatment of Advection - Viscous Wave Calculations . . . . .	176
REFERENCES . . . . .	187
APPENDIX A - EXPONENTIAL FIT TABLES . . . . .	A-1
A.1 Input . . . . .	A-1
A.2 Output . . . . .	A-6
APPENDIX B - CALCULATION AND TABULATION OF MIE SCATTERING FUNCTIONS FOR A SINGLE SPHERE	B-1
B.1 Computational Scheme . . . . .	B-2
B.2 Tables . . . . .	B-11
References . . . . .	B-15
APPENDIX C - TABULATION OF MIE SCATTERING FUNCTIONS FOR A SPHERICAL POLYDISPERSION . . . . .	C-1
APPENDIX D - ATRAD STRUCTURE AND INPUT . . . . .	D-1

## 1. INTRODUCTION

The results reported herein are the continuation of numerical studies of meso-scale phenomena related to the effects of orography on momentum transfer in the atmosphere and the interaction of solar radiation with the earth's atmosphere.

### 1.1 RADIATIVE TRANSFER

The development of the atmospheric radiation code ATRAD was completed during the past six months. The code was optimized to reduce the computational time for each run. Calculational results were compared with the radiation parameterization presently used in the RAND global circulation model (GCM) and a newer model recently developed by Katayama. Discrepancies between the results are discussed and suggestions for improvements in the parameterizations are made.

The budget for the radiation study has been depleted and these studies will not continue during the remaining contract period. Some related studies with the code will be performed on an NSF study contract.

### 1.2 OROGRAPHIC EFFECTS ON GLOBAL CLIMATE

The scope of the work during the past six month's study has emphasized a continuing effort to develop and use numerical codes to aid in the understanding of the physical processes

which influence momentum transfer in the atmosphere. The major items completed include: (1) the development and initial test runs of a three-dimensional transient Boussinesq code; (2) a check of the formulation of the HAIFA codes which include moisture and triangular zones, and computations of the Sierra Nevada problem previously described using these codes; (3) a continuation of the understanding and development of the 2-D and 3-D linear steady state codes; and (4) obtaining worldwide topography data for use in developing the parameterizations for the GCM.

The major effort of the remainder of the contract will be to: (1) continue computational studies of momentum transfer with the linear steady state models using real topography data to arrive at simplified parameterizations similar to those reported previously,<sup>(3)</sup> and (2) run comparative problems using the linear and nonlinear codes in order to aid in defining the differences in the calculated wave drag.

## 2. RADIATION IN THE EARTH'S ATMOSPHERE: ATRAD IMPROVEMENTS

Efforts under the radiation portion of this contract have been primarily directed toward two objectives: (1) to improve the computational speed of ATRAD, in the main by reading the exponential fits to transmission functions and the Mie scattering functions from pre-computed tables; (2) to perform further comparisons between the radiative heating rates predicted by ATRAD and those predicted by the Katayama radiation model currently used in the Mintz-Arakawa general circulation model. In connection with the code improvement effort, a more sophisticated polynomial minimization procedure has increased the computational speed of the exponential fitting module by almost a factor of three; the Mie scattering module has also been speeded up somewhat by optimizing the coding, but as was pointed out in the previous semi-annual report,<sup>(1)</sup> there is a certain irreducible (and large) amount of computing involved in doing Mie scattering calculations accurately.

In the present section, we shall discuss the major code improvements which have been made since our previous semi-annual report. Section 2.1 deals with improvements in the code module which fits transmission functions with sums of exponentials. Section 2.2 discusses the substantial revisions which have been made in the treatment of Mie scattering.

## 2.1 EXPONENTIAL FITTING IMPROVEMENTS

In the previous semi-annual report,<sup>(1)</sup> a polynomial which we shall refer to as  $P(\theta)$  was defined in Equation (4.38). Finding the absolute minimum of  $P(\theta)$  over  $[0,1]$  was the crucial (and by far the most time-consuming) step in the exponential fitting algorithm discussed there. Timing studies on ATRAD further showed that after the Mie scattering computation, the pacing item in the code was this polynomial minimization. Therefore, considerable theoretical attention was directed to the problem and the result has been the discovery of a new minimization algorithm which is of great importance in its own right and which has decreased the running time of the exponential fitting module by a factor of three while at the same time markedly improving its accuracy. This new method is detailed in Sections 2.1.1 and 2.1.2. Typical results of the fitting process are shown and commented upon in Section 2.1.3. Finally, Section 2.1.4 discusses code modifications by which the exponential fitting calculation is done separately in order to make tables for ATRAD.

### 2.1.1 A Global Minimization Procedure for Polynomials

The problem is to find the absolute minimum of  $P(\theta)$  for  $0 \leq \theta \leq 1$ . The method which we shall give can of course be generalized to an arbitrary interval  $[a,b]$ , and it applies to any function  $P(\theta)$  which can be decomposed,

$$P(\theta) = P^+(\theta) - P^-(\theta) \quad (2.1)$$

into the difference of two functions  $P^+$  and  $P^-$  with monotone non-decreasing second derivatives on  $[a,b]$ . An algorithm for performing this decomposition for a polynomial is given in Section 2.1.2. Such a decomposition is of course not unique, since one can add any function with positive third derivative

to both  $P^+$  and  $P^-$ . Nevertheless, because the efficiency of the procedure depends on the extent to which  $\left| \frac{d^2 P^+}{d\theta^2} + \frac{d^2 P^-}{d\theta^2} \right|$  exceeds  $|P'''(\theta)|$  on  $[0,1]$ , not all decompositions are equally useful. The one that has been selected is quite sophisticated because a simpler one proved inadequate to produce rapid convergence to the minimum.

The algorithm is based on bounding properties of certain quadratic approximants to  $P^+(\theta)$  and  $P^-(\theta)$ . Consider first the quadratic  $Q^+(\theta)$  which matches  $P^+(\theta)$  at  $\theta_1$  and  $\theta_2$  ( $0 \leq \theta_1 < \theta_2 \leq 1$ ) and which matches the derivative of  $P^+(\theta)$  at  $\theta_2$ :

$$Q^+(\theta_1) = P^+(\theta_1) \quad ,$$

$$Q^+(\theta_2) = P^+(\theta_2) \quad ,$$

and

$$\frac{dQ^+}{d\theta}(\theta_2) = \frac{dP^+}{d\theta}(\theta_2) \quad .$$

By construction of  $P^+$  ,

$$\frac{d^3 P^+}{d\theta^3} \geq 0 \quad \text{for } \theta \in [0,1] \quad .$$

The error in the approximation

$$\Delta(\theta) = P^+(\theta) - Q^+(\theta)$$

therefore, has the properties

$$\Delta'''(\theta) \geq 0 \quad , \quad \theta \in [\theta_1, \theta_2] \quad ,$$

$$\Delta(\theta_1) = \Delta(\theta_2) = \Delta'(\theta_2) = 0 \quad .$$

Based on these properties, a proof is now given that  $\Delta \geq 0$  throughout the interval  $[\theta_1, \theta_2]$ . By Rolle's theorem, because  $\Delta(\theta_1) = \Delta(\theta_2) = 0$ , there is a point  $\bar{\theta} \in (\theta_1, \theta_2)$  such that  $\Delta'(\bar{\theta}) = 0$ . By Taylor's theorem, we may expand  $\Delta'(\theta)$  about  $\bar{\theta}$  as follows:

$$\Delta'(\theta) = \Delta''(\bar{\theta})(\theta - \bar{\theta}) + \frac{1}{2}\Delta'''[\xi(\theta)](\theta - \bar{\theta})^2 \quad (2.2)$$

where  $\xi(\theta)$  is a point between  $\theta$  and  $\bar{\theta}$ . Evaluating this at  $\theta = \theta_2$ ,

$$0 = \Delta''(\bar{\theta})(\theta_2 - \bar{\theta}) + \frac{1}{2}\Delta'''[\xi(\theta_2)](\theta_2 - \bar{\theta})^2$$

Since the second term of this expression is non-negative, it follows that

$$\Delta''(\bar{\theta}) \leq 0 .$$

The case  $\Delta''(\bar{\theta}) = 0$  is only possible when  $P^+(\theta)$  is quadratic, for then by Equation (2.2)  $\Delta'(\theta) \geq 0$  which is irreconcilable with  $\Delta(\theta_1) = \Delta(\theta_2) = 0$  unless  $\Delta(\theta) \equiv 0$ . Ignoring the trivial case when  $P^+$  is quadratic, then, we have

$$\Delta''(\bar{\theta}) < 0$$

so that  $\bar{\theta}$  is a local maximum. Hence, there are no local minima in  $(\theta_1, \theta_2)$  and so  $\Delta(\theta)$  must attain its minimum on  $[\theta_1, \theta_2]$  at an endpoint,

$$\Delta(\theta) \geq \min[\Delta(\theta_1), \Delta(\theta_2)] = 0 \quad \text{on } [\theta_1, \theta_2] .$$

Hence it has been proven that  $Q^+(\theta)$  forms a lower bound for  $P^+(\theta)$  on the whole interval  $[\theta_1, \theta_2]$ ,

$$Q^+(\theta) \leq P^+(\theta) , \quad \theta \in [\theta_1, \theta_2] .$$

A similar proof will establish that if the quadratic  $Q^-(\theta)$  is chosen such that

$$Q^-(\theta_1) = P^-(\theta_1) \quad ,$$

$$Q^-(\theta_2) = P^-(\theta_2) \quad ,$$

and

$$\frac{dQ^-}{d\theta}(\theta_1) = \frac{dP^-}{d\theta}(\theta_1) \quad .$$

then  $Q^-(\theta)$  forms an upper bound for  $P^-(\theta)$  ,

$$Q^-(\theta) \geq P^-(\theta) \quad , \quad \theta \in [\theta_1, \theta_2] \quad .$$

Clearly, then,  $Q = Q^+ - Q^-$  forms a lower bound for  $P$ ,

$$Q(\theta) = Q^+(\theta) - Q^-(\theta) \leq P^+(\theta) - P^-(\theta) = P(\theta)$$

on  $[\theta_1, \theta_2]$  . The minimization algorithm rests on this property.

Let us now trace through a single iterative step of the minimization algorithm. Presume that the original interval  $[0,1]$  on which the minimum of  $P(\theta)$  is desired has been divided into subintervals  $[\theta_1, \theta_2], [\theta_3, \theta_4], \dots, [\theta_{2N-1}, \theta_{2N}]$  which are the remaining candidates to contain the minimum. The ordering of these intervals is such that if  $Q_i(\theta)$  is the quadratic approximant of the type defined above for the interval  $[\theta_{2i-1}, \theta_{2i}]$ , and

$$q_i = \min_{\theta \in [\theta_{2i-1}, \theta_{2i}]} Q_i(\theta)$$

then

$$q_1 \leq q_2 \leq q_3 \dots \leq q_N \quad .$$

In other words, the intervals are ordered according to the minima of their quadratic bounds. Since the quadratic bound in the first interval  $[\theta_1, \theta_2]$  dips lowest, this interval is regarded as the most likely candidate to contain the minimum. Let  $y_1$  be the position at which  $Q_1(\theta)$  attains its minimum, that is,

$$Q_1(y_1) = q_1$$

Divide  $[\theta_1, \theta_2]$  into two new intervals  $[\theta_1, y_1]$  and  $[y_1, \theta_2]$ , establish quadratic bounds separately for each of the new intervals, and insert the new intervals into the candidate stack based on their corresponding  $q$ 's. Drop the old interval  $[\theta_1, \theta_2]$ , and drop either of the two new intervals if its quadratic bound: (a) arches upward (has negative curvature) rather than dipping downward, or (b) does not have a local minimum within the interval. Finally, drop any intervals  $k$  for which

$$q_k \geq \min_{1 \leq j \leq 2N} P(\theta_j) \quad (2.3)$$

since in such intervals  $P$  is bounded above an already-known value of the polynomial. (The latter criterion for interval-dropping is particularly simple when the intervals are  $q$ -ordered; for if we begin our search at  $q_1$ , and  $q_k$  is the first  $q$  such that (2.3) is satisfied, then it is also satisfied for  $q_{k+1}, q_{k+2}, \dots$ )

The iteration is initialized by  $N = 1$ ,  $[\theta_1, \theta_2] = [0, 1]$ . It terminates when any one of the following convergence criteria is satisfied:

- (1) after any interval-dropping operation, only one interval remains in the candidate stack;
- (2) more than a pre-set number of iterations has been performed;
- (3) the sum of the number of iterations performed and the number of remaining intervals in the candidate stack exceeds a certain constant;
- (4)  $P(y_1) < 0$  and  $q_1/P(y_1) < \epsilon$  for some  $\epsilon \gtrsim 1$  (we currently use  $\epsilon = 1.01$ ).

The reasons for criteria (1) and (2) are fairly obvious. The third criterion was based on the idea that as the number of iterations increases, fewer and fewer intervals should remain in the candidate stack if the algorithm is functioning properly. The fourth criterion has been specialized to the exponential fitting application because we require the polynomial minimum to be negative, but the idea behind it, that we are close to the minimum when the quadratic bound in the leading interval closely approximates the polynomial, is general. In practice, surprisingly, it is usually criterion (1) which terminates the iteration which means that the interval-dropping feature is very effective.

Another version of this algorithm was also developed which required no derivative evaluations of  $P(\theta)$  except at the endpoints  $\theta = 0$  and  $\theta = 1$ , but it proved to be somewhat less accurate and efficient than the present version and it also necessitated considerably more complex logic (especially with regard to interval-dropping). It was based on the fact that the quadratic  $Q(\theta)$  which matches any function with non-negative third derivative  $f(\theta)$  at three points

$$0 \leq \theta_1 < \theta_2 < \theta_3 \leq 1,$$

$$Q(\theta_i) = f(\theta_i) \quad (i = 1, 2, 3)$$

exhibits the "under-over" property,

$$Q(\theta) \leq f(\theta) \quad \text{in } [\theta_1, \theta_2] \quad ,$$

and

$$Q(\theta) \geq f(\theta) \quad \text{in } [\theta_2, \theta_3] \quad .$$

Hence by fitting  $P^+$  by  $Q^+$  at  $\theta_2 < \theta_3 < \theta_4$  and  $P^-$  by  $Q^-$  at  $\theta_1 < \theta_2 < \theta_3$ , we have:

$$Q^+ - Q^- \leq P^+ - P^- = P \quad \text{in } [\theta_2, \theta_3] \quad .$$

The remainder of the algorithm is then similar to that described above.

Convergence of the algorithm can be proved; however, the proof will not be given here. It will be included in a forthcoming journal article on this method.

### 2.1.2 Splitting the Polynomial

The crucial step in the minimization algorithm of Section 2.1.1 involves splitting  $P(\theta)$  into the difference of two polynomials:

$$P(\theta) = P^+(\theta) - P^-(\theta)$$

with non-negative third derivatives,

$$\frac{d^3 P^+}{d\theta^3} \geq 0 \quad \text{for } \theta \in [0, 1] \quad .$$

The algorithm which we use to accomplish this splitting will be illustrated by actually decomposing several sample polynomials.

Suppose that  $D(\theta) = P''''(\theta)$ . Then we want to decompose  $D(\theta)$  into a difference:

$$D(\theta) = D^+(\theta) - D^-(\theta)$$

such that

$$D^\pm(\theta) \geq 0 \text{ for } \theta \in [0,1] \text{ .}$$

In order to split  $D(\theta)$  into positive ( $D^+$ ) and negative ( $D^-$ ) parts, we shall make use of the elementary observation that:

$$\theta^m \leq \theta^n \text{ when } m > n \text{ and } \theta \in [0,1] \text{ .} \quad (2.4)$$

Then if we have, for example, the pair of terms

$$3\theta^3 - 5\theta^5$$

we can take the part  $-3\theta^5$  of the negative term and include it with the positive term,

$$3\theta^3 - 3\theta^5$$

and still have an expression which is non-negative on  $0 \leq \theta \leq 1$ . For this simple example, then,

$$D^+(\theta) = 3\theta^3 - 3\theta^5 \text{ ,}$$

and

$$D^-(\theta) = 2\theta^5 \text{ .}$$

Proceeding to a more complex example, consider the quadratic:

$$D(\theta) = 1 - \theta - \theta^2 \text{ .}$$

Divide  $D(\theta)$  into blocks in each of which the coefficients are mono-signed:

$$\underbrace{1}_{\text{block 1}} \quad - \underbrace{\theta - \theta^2}_{\text{block 2}}$$

The second block's coefficients are multiplied by a constant such that their sum equals the negative of the coefficient sum for the first block:

$$1 - \frac{1}{2}\theta - \frac{1}{2}\theta^2 \quad . \quad (2.5)$$

This expression is then non-negative by the property (2.4) and furthermore there are no more coefficient blocks to process. Note that the expression (2.5) vanishes at  $\theta = 1$ , a property which we build into it; therefore, it may be factored,

$$(1 - \theta) \left(1 + \frac{1}{2}\theta\right) \quad .$$

Since the second factor is strictly positive, we are finished (in the next example this will not be so). The splitting is:

$$D^+(\theta) = 1 - \frac{1}{2}\theta - \frac{1}{2}\theta^2 \quad ,$$

and

$$D^-(\theta) = \frac{1}{2}\theta + \frac{1}{2}\theta^2 \quad .$$

An example with an odd number of mono-signed blocks introduces the further complications of: (a) keeping track of 'remainders', and (b) performing a second blocking operation on what is left after the first factor of  $(1 - \theta)$  is removed. Consider:

$$D(\theta) = 2 - 7\theta + 6\theta^2 \quad .$$

The mono-signed blocks are merely single terms here. We can take the part  $-2\theta$  of the second term and include it with the first term to yield:

$$2 - 2\theta - 5\theta + 6\theta^2 .$$

The first two terms now form a non-negative expression. By dividing further,

$$2 - 2\theta - 5\theta + 5\theta^2 + \theta^2 ,$$

the second two terms can be made into a non-positive expression. The extra  $\theta^2$  which is left over has no terms to match with it and hence is called a 'remainder.' All remainders are strictly non-negative or non-positive. They are shunted off into a 'remainder table' during the blocking-factorization process, and each repetition of this process creates (in general) a new remainder for the table. After all possible blocking-factorization processes have been done, the remainders are re-assembled into either  $D^+$  or  $D^-$ , depending on their sign. As a shorthand notation, we shall keep the remainders to the right of the polynomial, so for our current example:

$$2 - 2\theta - 5\theta + 5\theta^2 \qquad \theta^2$$

Factoring,

$$(1 - \theta) (2 - 5\theta) \qquad \theta^2$$

Now we block and separate the second factor in the same fashion:

$$(1 - \theta) (2 - 2\theta - 3\theta) \qquad \theta^2$$

Shunting off the remainder,

$$(1 - \theta)(2 - 2\theta) \quad \theta^2, -3\theta(1 - \theta).$$

Now we are finished, since the second factor can be blocked and separated no further. Re-assembling the positive and negative parts,

$$D^+ = (1 - \theta)(2 - 2\theta) + \theta^2 = 2 - 4\theta + 3\theta^2,$$

and

$$D^- = -3\theta(1 - \theta) = -3\theta + 3\theta^2.$$

As a final example, consider:

$$\underbrace{1}_1 - \underbrace{2\theta - \theta^2}_2 + \underbrace{3\theta^3}_3.$$

The polynomial is separated into three mono-signed blocks as indicated. Since the largest negative value of the second block (at  $\theta = 1$ ) is  $-3$ , we can take  $\frac{1}{3}$  of the second block and adjoin it to the first block and still have a non-negative first block:

$$\underbrace{1 - \frac{2}{3}\theta - \frac{1}{3}\theta^2}_1 - \underbrace{\frac{4}{3}\theta - \frac{2}{3}\theta^2}_2 + \underbrace{3\theta^3}_3$$

Since the largest negative value of block 2 is now  $-2$ , we can adjoin  $\frac{2}{3}$  of block 3 to it and still have a non-positive second block:

$$\underbrace{1 - \frac{2}{3}\theta - \frac{1}{3}\theta^2}_1 - \underbrace{\frac{4}{3}\theta - \frac{2}{3}\theta^2 + 2\theta^3}_2 + \underbrace{\theta^3}_3$$

Block 3 now has nothing to match with it, and so is placed in the remainder table.  $(1 - \theta)$  is factored out of blocks 1 and 2:

$$(1 - \theta) \left[ \underbrace{1 + \frac{1}{3}\theta}_1 - \underbrace{\left(\frac{4}{3}\theta + 2\theta^2\right)}_2 \right] \theta^3$$

We now have new blocks 1 and 2, as indicated, and the whole process begins again (note that the  $\frac{1}{3}\theta$  and  $-\frac{4}{3}\theta$  are not combined - this is in order to avoid doing the actual factorization in the computational implementation of this method). The value of blocks 1 and 2 at  $\theta = 1$  are  $\frac{4}{3}$  and  $\frac{10}{3}$ , respectively, so we can adjoin  $\frac{4}{10}$  of block 2 to block 1 and still have a non-negative first block:

$$(1 - \theta) \left[ \underbrace{1 + \frac{1}{3}\theta - \frac{4}{10}\left(\frac{4}{3}\theta + 2\theta^2\right)}_1 - \underbrace{\frac{6}{10}\left(\frac{4}{3}\theta + 2\theta^2\right)}_2 \right] \theta^3$$

Block 2 has nothing to match with it, and so is added to the remainder table. Another  $(1 - \theta)$  is factored out of block 1, to yield:

$$(1 - \theta)^2 \left( 1 + \frac{8}{10}\theta \right) \theta^3, - \frac{6}{10}(1 - \theta) \left( \frac{4}{3}\theta + 2\theta^2 \right)$$

The factor multiplying  $(1 - \theta)^2$  is positive, so we are finished. We may therefore identify:

$$\begin{aligned} D^+ &= (1 - \theta)^2 \left( 1 + \frac{8}{10}\theta \right) + \theta^3 \\ &= 1 - 1.2\theta - 0.6\theta^2 + 1.8\theta^3 \end{aligned} ,$$

and

$$D^- = \frac{6}{10}(1 - \theta) \left( \frac{4}{3}\theta + 2\theta^2 \right) = 0.8\theta + 0.4\theta^2 - 1.2\theta^3 .$$

As noted above, the computational implementation of this algorithm avoids doing the actual factorizations involving  $(1 - \theta)$  by noting that what we really want out of the factor multiplying  $(1 - \theta)^n$  for each  $n$  is the value of each of its blocks at  $\theta = 1$ . This can be simply related to the  $n^{\text{th}}$  derivative of blocks of the 'reduced' polynomial (the polynomial with remainders removed) at  $\theta = 1$ . Therefore, these derivatives are calculated instead of the factorizations. This saves a substantial amount of computer time.

### 2.1.3 Exponential Fits of Representative Transmission Functions

In order to illustrate the type of exponential fits to transmission functions which are generated, sample calculations are shown in Tables 2.1 to 2.3 for the five frequency intervals  $180 - 240 \text{ cm}^{-1}$  (far-infrared water vapor rotation band),  $720 - 740 \text{ cm}^{-1}$  ( $\text{CO}_2$   $15\mu$  band),  $800 - 840 \text{ cm}^{-1}$  (8 -  $12\mu$  "window"),  $5440 - 5760 \text{ cm}^{-1}$  (near-infrared  $\Omega$ -band of water vapor), and  $32000 - 33000 \text{ cm}^{-1}$  (Huggins band of ozone). These intervals are representative of the parts of the spectrum in which they lie, and will serve to point up peculiarities of the fitting process. Table 2.1 contains the values  $T_{\Delta v}(n\Delta u)$ ,  $n = 0, 1, 2, \dots, n_t$ , of the transmission function to which the exponential sum

$$E_{\Delta v}(u) = \sum a_i e^{-k_i u}$$

is to be fitted, the corresponding values  $E_{\Delta v}(n\Delta u)$ , the percent difference between  $E_{\Delta v}$  and  $T_{\Delta v}$ , and the coefficients  $a_i$  and exponents  $k_i$  resulting from the fitting. Tables 2.2 and 2.3 illustrate the effects of changing certain fitting parameters, and contain only coefficients  $a_i$  and exponents  $k_i$ .

The range of transmission values,  $1.0 - T_{\Delta\nu}(n_t \Delta u)$ , used in the tables is not fixed, but depends on the maximum estimated effective amount  $u_{\max}^*$  of each absorber which could possibly be encountered along a slant path making an angle of  $80^\circ$  with the zenith. (Actually, maximum  $H_2O$ ,  $CO_2$ , and  $O_3$  amounts have been taken to be twice the current values in order that our exponential fits might be applicable to changed future or past climatic conditions.) Thus, for example, in the  $800 - 840 \text{ cm}^{-1}$  case of Table 2.1(c), the range of water vapor transmission fitted is 0.775 to 1.0 because  $T_{\Delta\nu}(u_{\max}^*) = 0.775$  for water vapor in this spectral interval. At the other extreme are spectral intervals such as  $180 - 240 \text{ cm}^{-1}$  (see Table 2.1(a)) for which  $T_{\Delta\nu}(u_{\max}^*)$  is orders of magnitude below 0.001, the smallest transmission predictable with McClatchey's scheme<sup>(2)</sup> (which sets any transmission below 0.001 to zero.) Even should we manage to extend the transmission data below 0.001, however, it would not be desirable for two reasons connected with the numerics of fitting. First, because the fitting scheme takes equal steps  $\Delta u$  of absorber amount between the transmission data points, fitting to transmission ranges even as large as 0.001 - 1.0 results in taking many data points below 0.1 and relatively few between 1.0 and 0.1, so that the transmission function is inadequately resolved in 0.1 - 1.0 and the fit is relatively poor there. Secondly, the fitting algorithm becomes unacceptably poor if more than about 125 data points are used, so that increasing the resolution in 0.1 - 1.0 by taking a larger  $n_t$  is also unfeasible. We have temporarily solved this problem by putting a lower bound  $Tr_{\min}$  (usually 0.005 or 0.01) on the transmission data actually fitted. The variation of the fit with  $Tr_{\min}$  will be discussed below.

Evans\* believes that we can relax the equal  $\Delta u$  restriction by taking  $M$  steps of  $\Delta u$  (starting at  $u = 0$ ), then  $M$  steps of  $2\Delta u$ , then  $M$  steps of  $4\Delta u$ , etc., where  $M$  is the maximum number of terms we expect the exponential fit to contain ( $M = 20$  for the band model we use in the far IR,  $M = 8$  for McClatchey's transmission data). This involves some rather extensive code modifications, however, and has not been done because of more pressing problems. Once done, it would eliminate the problem of adequately resolving  $T_{\Delta\nu}(u)$  over its full range of variation.

The number of values  $n_t$  of the transmission which are used for fitting is made a function of the smallest transmission value  $t_{\min} = \max[T_{\Delta\nu}(u_{\max}^*), Tr_{\min}]$ :

$$n_t = t_{\min} n_{\min} + (1 - t_{\min}) n_{\max}$$

where  $n_{\min} = 5$  for Tables 2.1 - 3 and  $n_{\max} = 40$  for Table 2.1 and 80 for Tables 2.2 - 3. This leads to computational savings when  $t_{\min}$  is near unity and assures that a full  $n_{\max}$  points are used when  $t_{\min}$  is near zero. The linear nature of this formula is not optimal, however, for it leads to unnecessarily large values of  $n_t$  when  $t_{\min} \in [0.1, 0.9]$ . Further study is needed.

Tables 2.1 - 2.3 contain information about both the underlying line structure in each spectral interval and about the nature of the fitting process. We begin by comparing the various tables as regards the fitting process. In the far-IR spectral interval  $180 - 240 \text{ cm}^{-1}$ , the transmission data are supplied by a Goody random band model (which is used for  $\nu < 340 \text{ cm}^{-1}$  in ATRAD); for the other spectral intervals, the tabular transmission data of McClatchey are used. Because

---

\* Private communication.

Table 2.1 Results of exponential fitting of transmission functions in five spectral intervals: 180 - 240 cm<sup>-1</sup>; 720 - 740 cm<sup>-1</sup>; 800 - 840 cm<sup>-1</sup>; 5440 - 5760 cm<sup>-1</sup>; 32000 - 33000 cm<sup>-1</sup>. (n<sub>max</sub> = 40, T<sub>min</sub> = 0.01) Exponent units: H<sub>2</sub>O, cm<sup>2</sup>/g; CO<sub>2</sub>, km<sup>-1</sup>; O<sub>3</sub>, (atm-cm)<sup>-1</sup>.

(a) 180 - 240 cm<sup>-1</sup>

TRANSMISSION FCN		EXPONENTIAL APPROX		V A P O R		PERCENT ERROR	
1	1.00000000	9.9999994-C1	-5.9674646-06				
2	4.5531495-01	4.5531474-01	-3.5454414-06				
3	3.3211003-01	3.3211002-01	-4.6737652-06				
4	2.6232530-01	2.6232529-01	-2.3669389-06				
5	2.1562433-01	2.1562432-01	-1.5822357-06				
6	1.8221181-01	1.8221180-01	-2.5556044-06				
7	1.5666045-01	1.5666045-01	-1.0892668-06				
8	1.3654988-01	1.3654988-01	-1.1367306-06				
9	1.2030999-01	1.2030999-01	-1.5482048-06				
10	1.0693280-01	1.0693280-01	-1.3964129-06				
11	9.5737230-02	9.5737230-02	-1.6213173-07				
12	8.6244479-02	8.6244479-02	-7.1990894-07				
13	7.8107098-02	7.8107098-02	-1.6579130-06				
14	7.1066311-02	7.1066310-02	-1.7473307-06				
15	6.4925155-02	6.4925156-02	2.9084493-07				
16	5.9530922-02	5.9530922-02	-6.5184791-08				
17	5.4763307-02	5.4763307-02	-4.7601780-07				
18	5.0526224-02	5.0526223-02	-8.4482107-07				
19	4.6741978-02	4.6741978-02	-4.5660902-07				
20	4.3347076-02	4.3347075-02	-1.2533060-06				
21	4.0289110-02	4.0289111-02	9.6316614-07				
22	3.7524466-02	3.7524465-02	-5.6877050-07				
23	3.5016547-02	3.5016542-02	1.2744226-06				
24	3.2734417-02	3.2734417-02	6.5199904-07				
25	3.0651788-02	3.0651787-02	-9.8114859-07				
26	2.8746149-02	2.8746149-02	7.0870993-07				
27	2.6998141-02	2.6998141-02	5.7493006-07				
28	2.5391020-02	2.5391020-02	9.1698026-07				
29	2.3910242-02	2.3910242-02	6.4917968-07				
30	2.2543110-02	2.2543111-02	2.4959912-06				
31	2.1278507-02	2.1278507-02	-2.6671265-06				
32	2.0106646-02	2.0106646-02	6.5136291-07				
33	1.9018894-02	1.9018894-02	8.9265098-07				
34	1.8007603-02	1.8007603-02	1.2121476-06				
35	1.7065977-02	1.7065978-02	2.7001714-06				
36	1.6187963-02	1.6187963-02	9.2887879-07				
37	1.5368147-02	1.5368147-02	-8.5219929-07				
38	1.4601681-02	1.4601681-02	1.0962509-06				
39	1.3884210-02	1.3884210-02	3.4062957-06				
40	1.3211811-02	1.3211812-02	4.9564451-07				

COEFFICIENTS	EXPONENTS
1	1.9429179-01
2	4.3356751-02
3	5.5865030-02
4	6.3969325-02
5	3.6646696-02
6	6.4763136-02
7	4.4868906-03
8	4.7378590-02
9	4.3472499-02
10	8.7835575-02
11	5.4996306-02
12	8.6400848-02
13	8.3277536-02
14	4.0438320-02
15	4.5279354-02
16	3.2743827-02
17	1.4776124-02
18	3.4911824-05

Table 2.1(b) 720 - 740 cm<sup>-1</sup>

..... F O R W A T E R V A P O R .....

TRANSMISSION FCN	EXPONENTIAL APPROX	PERCENT ERROR	COEFFICIENTS	EXPONENTS
1	1.000000+00	5.3419236-03	1	1.1128345-02
2	9.1323271-01	-4.6963830-02	2	2.0138374-01
3	8.7087587-01	1.3913764-01	3	6.3754135-01
4	8.4503491-01	-1.3733235-01		
5	8.2184497-01	2.7260118-03		
6	8.0117868-01	1.8397416-02		
7	7.8177939-01	7.3097155-02		
8	7.6491233-01	-2.7273047-02		
9	7.4847859-01	-3.4069418-02		
10	7.3310389-01	-3.9550263-02		
11	7.1910941-01	-1.0060257-01		
12	7.0405752-01	1.1406129-01		
13	6.9129725-01	1.2552533-01		
14	6.7993663-01	4.3620983-02		
15	6.6934962-01	-5.1742826-02		
16	6.5940411-01	-1.4941147-01		
17	6.4856128-01	-2.0141394-02		
18	6.3846225-01	8.2515320-02		

..... F O R U Z O N E .....

TRANSMISSION FCN	EXPONENTIAL APPROX	PERCENT ERROR	COEFFICIENTS	EXPONENTS
1	1.000000+00	4.7683704-05	1	4.3554307-05
2	9.8800537-01	-1.3076236-03	2	1.6908757-01
3	9.7663565-01	1.0573753-02	3	8.3086935-01
4	9.6639603-01	-2.4460332-02		
5	9.5606127-01	1.5379072-02		
6	9.4671703-01	1.3386613-02		
7	9.3822055-01	-2.0533241-02		
8	9.29966113-01	6.8784347-03		



Table 2.1(b) - contd.

..... FOR CO2 + OTHER UNIFORMLY MIXED GASES .....

	TRANSMISSION FCN	EXPONENTIAL APPROX	PERCENT ERROR		COEFFICIENTS	EXPONENTS
1	1.000000+00	1.000000+00	1.4901161-06		1	1.1526701-01
2	5.8215742-01	6.8258655-01	6.3225475-02		2	2.2423710-01
3	5.6881523-01	5.6734645-01	-2.5855713-01		3	3.3366329-01
4	4.9134684-01	4.9257342-01	2.4891827-01		4	3.2683263-01
5	4.3787103-01	4.3827150-01	9.1418033-02			
6	3.9532853-01	3.9554662-01	5.5063842-02			
7	3.6178677-01	3.6021745-01	-4.3471201-01			
8	3.2995347-01	3.3014239-01	5.7240366-02			
9	3.0256958-01	3.0409489-01	5.0284969-01			
10	2.8114019-01	2.8128455-01	5.1337064-02			
11	2.6189547-01	2.6114865-01	-2.0556535-01			
12	2.4374848-01	2.4325765-01	-2.0156856-01			
13	2.2743368-01	2.2726938-01	-7.2267031-02			
14	2.1322656-01	2.1290463-01	-1.5109444-01			
15	2.0072765-01	1.9993247-01	-3.9693306-01			
16	1.8781365-01	1.8816048-01	1.8449500-01			
17	1.7655137-01	1.7742755-01	4.9504373-01			
18	1.6748806-01	1.6759835-01	6.5626135-02			
19	1.5887104-01	1.5855871-01	-1.9666363-01			
20	1.5023828-01	1.5021296-01	-1.6856419-02			
21	1.4204444-01	1.4247903-01	3.0266993-01			
22	1.3444578-01	1.3528794-01	2.5323161-01			
23	1.2840746-01	1.2858078-01	1.3488488-01			
24	1.2215984-01	1.2230724-01	1.2050614-01			
25	1.1640502-01	1.1642418-01	1.6454502-02			
26	1.1100813-01	1.1089449-01	-1.0242412-01			
27	1.0582295-01	1.0568612-01	-1.2937827-01			
28	1.0083348-01	1.0077124-01	-6.1735632-02			
29	9.6260253-02	9.6125620-02	-1.6073633-01			
30	9.1938386-02	9.1728019-02	-2.2907525-01			
31	8.7743722-02	8.7559761-02	-2.0987758-01			
32	8.3636624-02	8.3604339-02	-9.8383712-02			
33	7.9779672-02	7.9847042-02	8.4409446-02			
34	7.6308515-02	7.6274763-02	-4.4213977-02			
35	7.2940993-02	7.2875777-02	-8.9449057-02			
36	6.9671091-02	6.9639393-02	-4.5499671-02			
37	6.6473312-02	6.6556009-02	9.4247105-02			
38	6.3402603-02	6.3616856-02	3.3732327-01			

Table 2.1(c) 800 - 840 cm<sup>-1</sup>

..... F O R W A T E R V A P O R .....			
TRANSMISSION FCN	EXPONENTIAL APPROX	EXPONENTIAL APPROX	PERCENT ERROR
1	1.000000+00	1.0000318+00	3.1768771-03
2	9.4042661-01	9.4021364-01	-2.2649581-02
3	9.1020309-01	9.1060375-01	4.4010146-02
4	8.9014296-01	8.8995322-01	-2.1318391-02
5	8.7211727-01	8.7256579-01	5.1415782-02
6	8.5693191-01	8.5667049-01	-7.1675546-03
7	8.4260471-01	8.4239362-01	-2.5054757-02
8	8.3036546-01	8.2875619-01	-1.6986231-01
9	8.1648200-01	8.1646101-01	-2.5706084-03
10	8.0373137-01	8.0483601-01	1.3734478-01
11	7.9335209-01	7.9401901-01	8.4028721-02
12	7.8369474-01	7.8395342-01	3.3002358-02
13	7.7540431-01	7.7456694-01	-1.0546813-01
.....			
..... F O R C O 2 + O T H E R U N I F O R M L Y M I X E D G A S E S .....			
TRANSMISSION FCN	EXPONENTIAL APPROX	EXPONENTIAL APPROX	PERCENT ERROR
1	1.000000+00	1.000000+00	0.000000
2	9.8631965-01	9.8831677-01	2.0227731-01
3	9.7778041-01	9.7677004-01	-1.0338630-01
.....			
COEFFICIENTS	EXPONENTS	COEFFICIENTS	EXPONENTS
1	5.3252484-02	1.000000+00	2.2769510+00
2	2.9769137-01	0.000000	1.2339420-01
3	6.4906793-01	0.000000	0.000000
.....			
TRANSMISSION FCN	EXPONENTIAL APPROX	EXPONENTIAL APPROX	PERCENT ERROR
1	1.000000+00	1.000000+00	0.000000
2	9.8631965-01	9.8831677-01	2.0227731-01
3	9.7778041-01	9.7677004-01	-1.0338630-01
.....			
COEFFICIENTS	EXPONENTS	COEFFICIENTS	EXPONENTS
1	1.000000+00	1.000000+00	2.3504029-03

Table 2.1(d) 5440 - 5760 cm<sup>-1</sup>

..... F O R W A T E R V A P O R ..... .....			
	TRANSMISSION FCU	EXPONENTIAL APPROX	PERCENT ERROR
1	1.000000+00	9.999999-01	-1.4901161-06
2	6.4619749-01	6.4619727-01	-3.4139265-05
3	5.7467587-01	5.7468100-01	8.9208587-04
4	5.3333506-01	5.3332159-01	-2.5254206-03
5	5.0429673-01	5.0427164-01	-4.9749347-03
6	4.8166101-01	4.8175348-01	1.9195429-02
7	4.6322583-01	4.6323560-01	2.9719218-03
8	4.4762514-01	4.4747227-01	-3.4157013-02
9	4.3371792-01	4.3373513-01	3.9692058-03
10	4.2147405-01	4.2156825-01	2.2347500-02
11	4.1064691-01	4.105013-01	-7.8425680-04
12	4.0086194-01	4.0074400-01	-2.9419935-02
13	3.9157828-01	3.9167049-01	2.3545210-02
14	3.8329461-01	3.8329118-01	-8.9477524-04
15	3.7554555-01	3.7549635-01	-1.2570249-02
16	3.6821349-01	3.6820746-01	-1.6393025-03
17	3.6124826-01	3.6155169-01	2.0627046-02
18	3.5479525-01	3.5467707-01	-2.3283033-02
19	3.4868080-01	3.4874335-01	1.7936953-02
20	3.4295805-01	3.4291364-01	-1.2949336-02
21	3.3751711-01	3.3736057-01	-4.6391339-02
22	3.3224897-01	3.3206069-01	-5.6624820-02
23	3.2703148-01	3.2699518-01	-1.1101576-02
24	3.2213384-01	3.2214702-01	4.0937082-03
25	3.1736696-01	3.1750239-01	4.2662836-02
26	3.1292453-01	3.1304910-01	3.9799049-02
27	3.0871639-01	3.0877646-01	1.9461056-02
28	3.0468638-01	3.0467504-01	-3.7223697-03
29	3.0080248-01	3.0073626-01	-2.2017245-02
30	2.96988453-01	2.9695243-01	-1.0810775-02
.....			
	COEFFICIENTS	EXPONENTS	
1	2.2790496-01	1.6704346+01	
2	1.3616368-01	4.1405703+00	
3	1.4114620-01	1.0936147+00	
4	2.9307161-01	1.6067562-01	
5	2.0171355-01	C.00C000C	

Table 2.1(e) 3200 - 3300 cm<sup>-1</sup>

..... F O R U Z O N E .....

	TRANSMISSION FCN	EXPONENTIAL APPROX	PERCENT ERROR	COEFFICIENTS	EXPONENTS
1	1.000000+00	9.9999762-01	-2.3767380-04	1.5133501-01	6.3029917+00
2	9.2162972-01	9.2162821-01	-1.6299750-04	2.7841505-01	5.0168507+00
3	8.5004603-01	8.5004519-01	-9.9026051-05	1.9825387-01	3.5065411+00
4	7.8461202-01	7.8461166-01	-4.4763583-05	1.6963843-01	3.1942169+00
5	7.2475424-01	7.2475424-01	1.8504266-07	1.2282156-01	2.3337323+00
6	6.6995614-01	6.6995639-01	3.7455512-05	7.9533725-02	2.1455175+00
7	6.1975216-01	6.1975258-01	6.6769449-05		
8	5.7372245-01	5.7372295-01	6.7528196-05		
9	5.3148814-01	5.3148869-01	1.0367950-04		
10	4.9270716-01	4.9270774-01	1.1383625-04		
11	4.5707057-01	4.5707111-01	1.2010365-04		
12	4.2429896-01	4.2429948-01	1.2247913-04		
13	3.9413971-01	3.9414018-01	1.1940325-04		
14	3.6636416-01	3.6636458-01	1.1525729-04		
15	3.4076520-01	3.4076557-01	1.0635866-04		
16	3.1715519-01	3.1715550-01	9.7326929-05		
17	2.9533693-01	2.9533648-01	8.4440939-05		
18	2.7523704-01	2.7523724-01	7.3257313-05		
19	2.5663431-01	2.5663446-01	5.9210534-05		
20	2.3942836-01	2.3942846-01	4.3993351-05		
21	2.2350338-01	2.2350344-01	2.9435178-05		
22	2.0875420-01	2.0875403-01	1.2714818-05		
23	1.9508431-01	1.9508430-01	-2.4538099-06		
24	1.8240691-01	1.8240688-01	-1.0687016-05		
25	1.7064215-01	1.7064209-01	-3.3064099-05		
26	1.5971734-01	1.5971727-01	-4.7908060-05		
27	1.4956614-01	1.4956605-01	-6.1595796-05		
28	1.4012795-01	1.4012784-01	-7.5055904-05		
29	1.3134735-01	1.3134723-01	-8.8043174-05		
30	1.2317366-01	1.2317353-01	-1.0023693-04		
31	1.1556048-01	1.1556035-01	-1.1051961-04		
32	1.0846531-01	1.0846518-01	-1.2162591-04		
33	1.0184919-01	1.0184905-01	-1.3210995-04		
34	9.5676377-02	9.5676243-02	-1.3969160-04		
35	8.9914050-02	8.9913727-02	-1.4813130-04		
36	8.4532106-02	8.4531973-02	-1.5679952-04		
37	7.9502907-02	7.9502678-02	-1.6246333-04		
38	7.4800681-02	7.4800558-02	-1.6447107-04		



of the different origins of the data, there are rather striking differences between both the accuracy of the fits and the number of terms in them: the fit in Table 2.1(a) is exact to the accuracy carried by our computer and consists of 18 terms; the fits in Table 2.1(b) - (e) are considerably more approximate and consist at most of 6 terms. As a general principle, the larger the number of continuous derivatives possessed by the transmission function  $T_{\Delta\nu}(u)$  generating the data, the closer will be the exponential fit. This is obvious from an intuitive standpoint because a sum of exponentials is infinitely differentiable, and so can only match exactly with another infinitely differentiable function belonging to the function space of exponential sums. The  $T_{\Delta\nu}(u)$  used in the band model is in fact infinitely differentiable on  $0 \leq u < \infty$ , while the McClatchey data, involving as it does linear interpolation in a table of transmissions, has discontinuous first derivatives. (This suggests one way in which the appropriateness of the McClatchey scheme for exponential fitting might be improved, which is to use instead of linear interpolation, interpolation schemes of higher differentiability such as cubic splines.)

A common feature of every one of the fits in Table 2.1 is the seemingly random variation of the sign of error. This indicates that the exponential fit wanders above and below the transmission data, as it should if it is a least squares fit. Inaccuracies in the fitting process, caused for example by using too many data points (like  $n_{\max} = 150$ ), can often be detected by observing this sign pattern. When all the errors are of one sign, for example, computational problems are definitely indicated.

We have, in previous reports,<sup>(10)</sup> viewed

$$\frac{1}{\Delta\nu} \int_{\Delta\nu} e^{-k_\nu u} d\nu \cong \sum a_i e^{-k_i u}$$

as a Lebesgue quadrature rule with coefficient  $a_i$  representing the fraction of the spectral interval  $\Delta\nu$  over which the absorption coefficient is roughly  $k_i$ . Thus, the exponential fits provide some insight into the underlying distribution of line intensity in  $\Delta\nu$ . In the 180 - 240  $\text{cm}^{-1}$  interval of Table 2.1(a), for example, one could deduce a sizable proportion ( $\sim 0.2$ ) of strong absorption near  $k_1 = 17386.1 \text{ cm}^2/\text{g}$  and a fairly uniform distribution of absorption ranging all the way from 3580  $\text{cm}^2/\text{g}$  to 24  $\text{cm}^2/\text{g}$ . For water vapor in the 720 - 740  $\text{cm}^{-1}$  interval (Table 2.1(b)), we observe a preponderant fraction (0.64) of very weak absorption ( $k \sim 0.015 \text{ cm}^2/\text{g}$ ), half as much ( $\sim 0.28$ ) of 14 times stronger absorption ( $k \sim 0.208 \text{ cm}^2/\text{g}$ ), and a small fraction (0.08) of yet 16 times stronger absorption ( $k \sim 3.28 \text{ cm}^2/\text{g}$ ). For ozone in the 32000 - 33000  $\text{cm}^{-1}$  interval (Table 2.1(e)), the range of  $k$ 's is quite small, only 0.63  $(\text{atm-cm})^{-1}$  to 0.21  $(\text{atm-cm})^{-1}$ , indicating very little line structure. Of course, the  $a$ 's and the  $k$ 's vary as we change the number of data points  $n_t$ , the lower limit  $Tr_{\min}$ , and the spacing  $\Delta u$ , so the  $a$ 's and the  $k$ 's cannot be taken too literally. Nevertheless, qualitative features such as the range of the  $k_i$ 's remain invariant as the details of the fitting process are varied. The only exception to this rule is when the fitting is changed so as to resolve parts of the  $T_{\Delta\nu}(u)$  curve not previously resolved; in this case, much larger and much smaller  $k$ -values may arise than were found using the inadequate resolution.

To show the effects of changing the fitting parameters, Table 2.2 contains the coefficients and exponents generated for all five spectral intervals when  $n_{\max}$  is increased to 80 (from 40) and  $Tr_{\min}$  is increased to 0.04 (from 0.01). Table 2.3 contains similar information for 180 - 240  $\text{cm}^{-1}$ ,  $\text{CO}_2$  in 720 - 740  $\text{cm}^{-1}$ , and ozone in 32000 - 33000  $\text{cm}^{-1}$  when  $n_{\max}$  is left at 80 and  $Tr_{\min}$  is further increased to 0.15 (the other fits are unchanged from Table 2.2).

The transmission data for the 180 - 240  $\text{cm}^{-1}$  interval of Table 2.2(a) contain better but still inadequate resolution in the range 0.1 - 1.0 as compared to Table 2.1 (a). The largest exponent in Table 2.2(a) is a factor of four larger than in Table 2.1(a), in order to account for the initial steep decrease of the transmission which had been even more poorly resolved before. There are many more large exponents in Table 2.2(a) than in Table 2.1(a). A continuation of this trend is observable in Table 2.3(a), in which the largest exponent has increased a further factor of three on account of even better resolution in 0.1 - 1.0. Note that the smallest exponent also increases from Table 2.1(a) to Table 2.2(a) to Table 2.3(a), which is due to the progressive increase in  $Tr_{\min}$  and the consequent loss of resolution in the tail of the transmission, where the small exponents predominate. Granted these quite understandable changes in the exponent range, however, the most important thing to notice about Tables 2.1(a), 2.2(a), and 2.3(a) is their qualitative similarities; the number of exponents and their distribution between the extremes, and the size and general pattern of the coefficients exhibit regularities which are preserved as the range and resolution of the data change.



Table 2.2, contd.

For Water Vapor		For Water Vapor	
COEFFICIENTS	EXPONENTS	COEFFICIENTS	EXPONENTS
1 7.6118593-03	5.5262042+01	1.9154203-01	2.6494272+01
2 4.5755173-02	2.0952084+00	5.3648681-02	7.5389322+00
3 2.9937959-01	1.2204550-01	1.1990704-01	4.0007756+00
4 6.4705335-01	0.0000000	1.4072478-01	1.0944522+00
		2.9305787-01	1.6097549-01
		2.0191963-01	0.0000000
		(d) 5440 - 5760 cm <sup>-1</sup>	
For CO <sub>2</sub>		For Ozone	
COEFFICIENTS	EXPONENTS	COEFFICIENTS	EXPONENTS
1 1.0000000+00	2.3504029-03	1 8.7551614-02	6.4310453+00
		2 1.0109020-01	5.8711309+00
		3 2.1750932-01	5.0109434+00
		4 1.8476970-01	3.7868060+00
		5 1.9318001-01	3.1520071+00
		6 0.5236210-02	2.5067036+00
		7 1.3556731-01	2.1668418+00
		(e) 32000 - 33000 cm <sup>-1</sup>	

Table 2.3

Coefficients and exponents for the exponential fits of transmission functions in the three spectral intervals, 180 - 240 cm<sup>-1</sup>, 720 - 740 cm<sup>-1</sup>, (CO<sub>2</sub> + only), and 32000 - 33000 cm<sup>-1</sup> (u<sub>max</sub> = 80, Tr<sub>min</sub> = 0.15)

For Water Vapor

	COEFFICIENTS	EXPONENTS
1	2.8437159-02	2.1821593+05
2	7.5091862-03	8.4885131+04
3	2.8541729-02	3.3458946+04
4	1.8738582-02	2.0627184+04
5	1.0280145-02	1.8085987+04
6	1.1281167-02	1.3841822+04
7	2.2959148-02	1.1723123+04
8	2.4307048-02	8.2488214+03
9	1.3739203-02	7.1271766+03
10	2.9963100-02	5.4729254+03
11	3.8770854-02	3.9736457+03
12	2.7157997-02	3.0435076+03
13	5.3681642-02	2.2464229+03
14	4.1890734-02	1.5705673+03
15	8.5116676-02	1.1108971+03
16	7.2094296-02	7.2261260+02
17	1.8719054-01	4.1192960+02
18	7.3082718-01	1.4231581+02
19	4.7870888-02	4.8531871+01
20	1.3632708-02	0.0000000

(a) 180 - 240 cm<sup>-1</sup>

For CO<sub>2</sub>

	COEFFICIENTS	EXPONENTS
1	4.8741068-02	2.8454967+02
2	5.6251018-02	2.2082878+01
3	1.9694652-01	3.6680425+00
4	1.7703375-01	1.2121288+00
5	4.5975857-01	3.7030622-01
6	6.1269065-02	0.0000000

(b) 720 - 740 cm<sup>-1</sup>

For Ozone

	COEFFICIENTS	EXPONENTS
1	3.1182365-03	7.8242436+00
2	8.8540089-02	6.2307800+00
3	2.0446707-01	5.8856288+00
4	1.3586891-01	4.4008119+00
5	3.1842369-01	3.5220810+00
6	1.5753501-01	2.4054787+00
7	8.0546988-02	2.1844162+00

(c) 32000 - 33000 cm<sup>-1</sup>

Comparing the water vapor parts of Tables 2.1(b) and 2.2(b) for  $720 - 740 \text{ cm}^{-1}$ , it is apparent that the only change due to the better resolution in Table 2.2(b) is to add a large exponent (84.2) with a small coefficient. The other coefficients and exponents are virtually unchanged. The fit is independent of  $\text{Tr}_{\text{min}}$  since the transmission range is so small.

The  $\text{CO}_2$  fit for  $720 - 740 \text{ cm}^{-1}$  (a region of large  $\text{CO}_2$  absorption) in Table 2.2(b) is very similar to that of Table 2.1(b) except that the largest exponent has decreased by a factor of three due primarily to fitting a single extra transmission datum between 0.682 and 1.0 (at 0.776). The comparison  $\text{CO}_2$  fit of Table 2.3(b), which fits transmission data having even more resolution between 0.7 and 1.0 (namely points 0.71, 0.76, and 0.83) but no points in the tail beyond 0.15, adds a large exponent ten times bigger than the largest exponent of Table 2.2(b), retains similar exponents in the mid-range, then deviates again for small exponents. The addition of the zero exponent with a non-negligible coefficient seems strange, but it is due to the fact that cutting off the data at 0.15 allows the method to insert a constant term (zero-exponent term) into the fit with any coefficient up to 0.15 if it so desires, in an attempt to fit the data. Without any transmission resolution below 0.15, and without some physical basis for putting a lower bound on the exponents (hard to come by because of lack of knowledge of line wings), there is no sound reason for rejecting this zero exponent.

The ozone 32000 - 33000  $\text{cm}^{-1}$  fit of Table 2.3(c) illustrates the danger of making generalizations about the exponential fitting process. Here we have severely reduced the resolution in the transmission tail by taking  $\text{Tr}_{\text{min}} = 0.15$ , and yet we observe practically no impact on the minimum exponent compared to Table 2.2(e). This is quite different from the situations in Table 2.3(a) and (b), where knowledge of the small exponents was reduced in the same circumstances. Ozone in this region is of course anomalous in its relatively small range of absorption coefficient, but it nevertheless serves to illustrate the point that it is not always necessary to consider very small values of the transmission.

There is very little substantive difference between the remainder of the fits in Table 2.2 and their analogues in Table 2.1.

In conclusion, we mention that when the range of transmission values which need to be considered is small enough ( $T_{\Delta\nu}(u_{\text{max}}^*) \geq 0.93$  in the current code), the full exponential fitting routine is bypassed in favor of a one-term least-squares exponential fit to three data points, which can be done analytically. Assuming that the one-term exponential approximation is

$$e^{-ku}$$

in order to give unit transmission for  $u = 0$ , and defining

$$\theta = e^{-ku_{\text{max}}^*/2},$$

the least-squares residual becomes

$$R = [T_{\Delta v}(\frac{u_{\max}^*}{2}) - \theta]^2 + [T_{\Delta v}(u_{\max}^*) - \theta^2]^2 .$$

The condition  $\frac{dR}{d\theta} = 0$  then yields a cubic equation for  $\theta$ ,

$$2\theta^3 + [1 - 2T_{\Delta v}(u_{\max}^*)]\theta - T_{\Delta v}(\frac{u_{\max}^*}{2}) = 0 ,$$

which can be shown to have only one positive real root for  $T_{\Delta v}$ 's of interest. An example of such a one-term fit, for  $\text{CO}_2$  can be seen in Table 2.1(c).

#### 2.1.4 Tables of Fitting Parameters

It is desirable to make ATRAD as computationally efficient as possible, with a view to executing it a large number of times for: (a) heat budget studies involving a large fraction of the globe, (b) diurnal cycle studies, and (c) parameter studies involving the albedo, aerosol density, cloud cover, sun angle, etc. In none of these multiple executions would there be any need to change the ATRAD spectral interval structure - and since the transmission function fitting depends on the spectral intervals, the fitting parameters can be computed once and for all and kept in tables. This is especially important in view of the fact that, in the original version of ATRAD, the pacing items as regards computer time were the Mie calculation and the fitting calculation.

Therefore, the fitting is now done by a separate code module, called EVANS-TABLES, which is described in Appendix A. The table currently used for ATRAD consists of fitting parameters for 120 spectral intervals spanning the spectral range of  $60 - 48500 \text{ cm}^{-1}$ . ATRAD has the capability of using the full fitting tables, or any sub-set thereof. Using

these tables, it is possible to perform a complete ATRAD calculation (without Mie scattering) for 40 levels, and for from 6 to 12 Gaussian angles, at a cost of anywhere between 300 and 400 CPU seconds on the UNIVAC 1108. If edits of each spectral interval are suppressed, this reduces to 200 - 250 CPU seconds. Clearly, the use of fitting tables effects tremendous computational savings over the earlier version of ATRAD, which required 40 - 60 minutes for a complete clear-sky calculation.

## 2.2 MIE SCATTERING

A large amount of effort and thought has been devoted to reducing the complexity and computational burden of the Mie scattering part of ATRAD. The Mie subroutines have all been modified substantially in order to increase their computational speed, their sophistication, and their accuracy. Notable improvements have been made in the calculation of the Mie functions ( $\sigma_{\text{sca}}$ ,  $\sigma_{\text{ext}}$ , and  $i_1 + i_2$ ) for a single sphere (Section 2.2.1) and in the scheme for integrating these functions over size distributions (Section 2.2.2). Tables are now made of the size-integrated Mie functions  $\bar{\sigma}_{\text{sca}}$ ,  $\bar{\sigma}_{\text{ext}}$ , and  $P_{\nu, M}(\theta)$  as well as of the fundamental functions  $\sigma_{\text{sca}}$ ,  $\sigma_{\text{ext}}$ , and  $i_1 + i_2$  (Sections 2.2.1 and 2.2.3). Finally, a new approximate scheme involving the Henyey-Greenstein phase function is presented in Section 2.2.4.

### 2.2.1 Mie Scattering for a Single Sphere

The computation of the Mie scattering functions  $\sigma_{\text{sca}}$  and  $\sigma_{\text{ext}}$  (scattering and extinction cross-sections) and  $i_1 + i_2$  (distribution of scattered intensity) for a homogeneous sphere is well documented in the literature. Our previous semi-annual report<sup>(1)</sup> indicated the many references

on which our treatment is based. Since our treatment is eclectic, however, it seemed useful to gather together the formulas on which it rests, which has been done in Appendix B. The computational aspects of the formulas are stressed there, including questions of single vs double precision.

Often ATRAD must take fine spectral resolution across spectral regions in which the index of refraction of an aerosol substance varies little. An example of this is liquid water in the visible. Appendix B describes a method by which vast amounts of computation can be saved in such circumstances; it involves making tables of  $i_1 + i_2$ ,  $\sigma_{sca}$ , and  $\sigma_{ext}$  for fixed index of refraction. A user's guide is provided for the code module which creates these tables.

### 2.2.2 Integration over Size Distribution

Our Romberg scheme for integration of the fundamental Mie functions  $\sigma_{sca}$ ,  $\sigma_{ext}$ , and  $i_1 + i_2$  over aerosol size distribution  $n(a)$ <sup>(1)</sup> has been abandoned in favor of a trapezoidal scheme with a variable integration increment  $\Delta\alpha$  ( $a$  = particle radius,  $\lambda$  = wavelength,  $\alpha = \frac{2\pi a}{\lambda}$ ). This decision was based in large part on a note of Dave's<sup>(3)</sup> in which he pointed out the computational economies of increasing  $\Delta\alpha$  after the integration covers a certain fraction of the particles. In Dave's examples, the integration increment was kept at  $\Delta\alpha = 0.1$  until the fraction 0.99 of the particles had been processed, then increased to  $\Delta\alpha = 0.5$ . This is, of course, the simplest type of variable -  $\Delta\alpha$  scheme. A somewhat more complicated variant is now used in our code; it will be described below. The former Romberg scheme, while desirable for observing the convergence of the integrals, was not only computationally cumbersome, but required fixed  $\Delta\alpha$ . Hence, while useful as a research tool, it could not be

retained for doing large numbers of more or less routine Mie computations.

Our present size distribution integration scheme errs on the side of caution in order to do the extreme cases ( $\lambda \rightarrow 0$ ) correctly, but in so doing undoubtedly takes too small an integration increment in other cases. Fortunately, when the Mie calculation uses tables of  $\sigma_{\text{sca}}$ ,  $\sigma_{\text{ext}}$ , and  $i_1 + i_2$ , the integration increment is fixed by the tables; it need not, therefore, be a source of concern, for even a greatly over-conservative  $\Delta\alpha$  is of little import to the trivial amount of computation necessary to produce the polydisperse Mie functions from these tables. When tables of  $\sigma_{\text{sca}}$ , etc., are not used, the initial integration increment is taken as:

$$\Delta\alpha = \min \left( 0.1, \frac{\alpha_{\text{max}} - \alpha_{\text{min}}}{200} \right) \quad (2.6)$$

where the interval of integration is  $[\alpha_{\text{min}}, \alpha_{\text{max}}]$ . This choice is based on a conversation with Dave in which he maintained that 0.1 was the largest  $\Delta\alpha$  one can safely use, but that  $\Delta\alpha$  must also be small enough to adequately resolve the interval  $[\alpha_{\text{min}}, \alpha_{\text{max}}]$  (i.e., to resolve  $n(\alpha)$ ). The increment is kept fixed until a fraction  $f$  of the particles have been integrated over, then the increment is allowed to double as many as  $n_d$  times before the integration is finally terminated. The criterion for increment-doubling is that the maximum relative change in any quantity being integrated, due to the previous integration step, be less than  $\delta_0$ . An acceptable set of parameters is

$$f = 0.99 \quad ,$$

$$n_d = 6 \quad ,$$

and

$$\delta_0 = 0.001 \quad .$$

However, these are definitely too conservative for most situations.

The effects of varying  $\Delta\alpha$ ,  $f$ ,  $n_d$ , and  $\delta_o$  were examined in several spectral regions for the Arctic stratus cloud whose size distribution is shown in Figure 3.1. It was found that an increment  $\Delta\alpha = 0.1$  is indeed necessary to accurately integrate  $\sigma_{sca}$ , etc., in the visible and down to  $\lambda \sim 0.3\mu$ , that somewhat larger increments ( $\Delta\alpha = 0.2$  at  $1\mu$ ) are permissible as the wavelength increases into the near IR, but that progressively smaller increments ( $\Delta\alpha = 0.05$  at  $11\mu$ ) must again be used in the IR. The  $\frac{\alpha_{max} - \alpha_{min}}{200}$  estimate of Equation (2.6) takes care of the IR quite well, and the 0.1 estimate takes care of the visible. Nevertheless, Equation (2.6) is shown by these studies to be too conservative through the near IR, a deficiency which will be remedied shortly.

The fraction  $f$  must indeed be 0.99 for extreme cases such as  $\lambda \sim 0.3\mu$  - even values as large as 0.95 lead to error then. However, it has been found possible to decrease  $f$  somewhat for larger wavelengths. The largest value of  $\delta_o$  which leads to acceptable accuracy is 0.01, and generally the number of doublings  $n_d$  should be kept to 5 or 6. Decreasing  $\delta_o$  to 0.001 or less will usually suppress doubling for the longer wavelengths while allowing it to proceed for the shorter ones. This is desirable since Mie computations at longer wavelengths are relatively inexpensive anyway.

### 2.2.3 Tables

The Mie computation is by far and away the most expensive part of ATRAD. For example, for a single wavelength  $\lambda = 0.33\mu$ , for the Arctic stratus cloud of Figure 3.1, 30 - 60 minutes of UNIVAC 1108 time (depending on the angular

resolution in the phase function) is required. The time required is progressively less at longer wavelengths, but the sum of all these times for the 120 spectral intervals currently used by ATRAD amounts to many, many hours. Clearly, ATRAD could never be a satisfactory research tool if every problem with clouds or aerosols took so long to compute. The only answer was to split off the entire Mie computation as a separate code module, which then makes tables of  $\bar{\sigma}_{\text{sca}}$ ,  $\bar{\sigma}_{\text{ext}}$ , and  $P_{\nu, M}(\theta)$  to be read by ATRAD. A description of and user's guide for this code module are given in Appendix C. Using these Mie tables, and the fitting tables of Appendix A, ATRAD can now be run for a typical cloud or aerosol problem in (UNIVAC 1108) times of the order of 5-10 minutes.

#### 2.2.4 Henye-Greenstein Approximation

Since its inception, ATRAD has contained an option to replace the real phase function by a Henye-Greenstein (H-G) phase function,

$$P_{\nu, M}(\theta) = \frac{1 - g^2}{(1 + g^2 - 2g \cos\theta)^{3/2}}$$

in which the single parameter  $g$  is selected to match some property of the real phase function. The H-G parameter was originally chosen so that the values of the H-G and real phase functions at  $\theta = 0^\circ$  were the same. Since this led to a phase function with a substantially altered area under its forward peak, and since this forward peak was often truncated and the scattering coefficient modified accordingly, the net impact of using the H-G option was often to cause a drastically different scattering coefficient to be used. In order to mitigate this circumstance, the parameter  $g$  is now chosen so that the area  $A$  under the real phase function

between  $0^\circ$  and  $D^\circ$  (computed by a modified Simpson's rule) equals the area under the H-G approximation between  $0^\circ$  and  $D^\circ$ :

$$A = \int_{\mu_0}^1 \frac{1 - g^2}{(1 + g^2 - 2g\mu)^{3/2}} d\mu$$

$$\mu_0 = \cos D$$

This turns out to reduce to a cubic equation in  $g$ ,

$$A(2 - A)g^3 - 2(1 - A)[A + \epsilon(1 - A)]g^2 - [2A + A^2 + 4\epsilon(1 - A)]g + 2(A - \epsilon) = 0$$

where

$$\epsilon \equiv 1 - \mu_0$$

Studies of this cubic have shown that for realistic ranges of  $A$  and  $\epsilon$ , it has three real roots, one of which is always negative, one of which always exceeds one, and one of which lies between zero and one. The last root is the desired one.

The current H-G scheme has lost one thing which made the earlier scheme attractive - computational speed. The old scheme only required the value of the real phase function at  $\theta = 0^\circ$ ; the new one requires enough values to resolve the real phase function between  $0^\circ$  and  $D^\circ$ . As a result, the new scheme is only about a factor of 5 faster than a full Mie computation.

### 3. RADIATION IN THE EARTH'S ATMOSPHERE - ATRAD PREDICTIONS FOR MODEL ATMOSPHERES AND COMPARISONS WITH SIMPLIFIED MODELS

ATRAD has now reached a stage in its development where it can be run economically for atmospheres of arbitrary cloud and aerosol content. The first cloudy problem to be run with ATRAD is for a model Arctic atmosphere with a low stratus deck. Some experimental measurements of ground-level solar fluxes are compared with ATRAD's predictions for this problem in Section 3.1, and it is shown how the simple model usually used to predict these fluxes must be altered if it is to be correct. In Section 3.2, the investigation of the two clear-sky problems discussed in the previous semi-annual report<sup>(1)</sup> is continued, with emphasis on: (a) comparisons with the new Katayama radiation model used in the three-level Mintz-Arakawa GCM, and (b) discussion of the sources of error in the Katayama models (two-level and three-level). Section 3.3 returns to the Arctic stratus problem in order to compare some of the cloudy-sky predictions of the Katayama model with ATRAD.

#### 3.1 ARCTIC STRATUS PROBLEM

The choice of an Arctic stratus problem for our first cloudy calculation with ATRAD may at first sight seem somewhat strange, but there are several good reasons for it. First, we are involved in some radiation studies for AIDJEX (Arctic

Ice Dynamics Joint Experiment) upon which this problem bears directly. Second, Arctic problems come very close to satisfying the ATRAD assumption (see Reference 1) of horizontal homogeneity, both with respect to the surface and with respect to the stratus cloud deck. Obviously, this assumption needs to be examined, but not before ATRAD is tested in situations which closely approximate horizontal homogeneity. Third, measurements were made on three different days with widely varying albedos, but similar cloud conditions so that a stringent test of ATRAD's response to albedo variation alone was possible. And localized albedo measurements in the Arctic can, with greater assurance than in lower latitudes, be taken as representative of larger areas because of the lack of substantial variations in the terrain. Finally, cloud size distribution measurements were available, which is unfortunately not always the case when radiation measurements are made.

### 3.1.1 Comparison of ATRAD with Experiment

The measurements to which we will compare ATRAD are reported in Weller, et. al.,<sup>(4)</sup> and were made near Pt. Barrow, Alaska during the month of June, 1971 when the snow was melting. The data consist of ground-level solar down-fluxes (0.3 - 2.6 $\mu$ ), albedos, and solar elevations for three different days, and are shown in Table 3.1. Also shown are the flux measurements "interpolated to 30°" according to Weller, et.al., and the corresponding ATRAD predictions of both sets of fluxes.

Before discussing Table 3.1, let us specify the atmospheric structure used in ATRAD for the Arctic stratus problem. This structure, consisting of altitude, pressure, temperature, water vapor density, ozone density, and aerosol (cloud) number density, as taken from an actual ATRAD run, is shown in Table 3.2. The offset of levels 20 and 21 indicates that the

Table 3.1

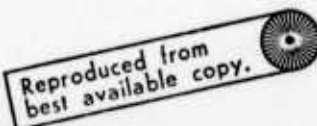
Comparison of flux measurements of Weller, et. al., (4) with flux predictions of ATRAD. (ATRAD fluxes have been rounded to two significant figures since measurements are only quoted to this accuracy). The double-headed arrow indicates the two flux values whose agreement was forced by adjusting the ATRAD cloud droplet number density.

Date (1971)	Pt. Barrow, Alaska		
	June 2	June 10	June 29
Albedo	79%	58%	20%
Solar elevation	31°	24°	21°
Measured surface down-flux*	0.56	0.38	0.26
ATRAD surface down flux*	0.60	0.38	↕ 0.26
Measured surface down-flux,* interpolated to 30° solar elevation	0.54	0.47	0.37
ATRAD surface down-flux,* 30° solar elevation	0.58	0.51	0.43

\*All fluxes in cal/cm<sup>2</sup>/min

Table 3.2  
 Actual ATRAD atmospheric structure used in Arctic stratus problem. Altitude is in km, pressure in mb, temperature in °K, H<sub>2</sub>O vapor density in g/m<sup>3</sup>, O<sub>3</sub> density in atm-cm/km, and aerosol density in particles/cm<sup>3</sup>

I N P U T D A T A									
I	ALT	70N	PRESS	TEMP	H2O DEN	O3 DEN	AER DEN		
1	5.0000+01	0.0000	1.0000+00	2.8000+02	0.0000	2.0000-04	0.0000		
2	3.0000+01	2.0000+01	1.1980+01	2.3905+02	1.4000-03	6.5000-03	0.0000		
3	2.5000+01	2.5000+01	2.4587+01	2.3309+02	8.0400-04	1.7000-02	0.0000		
4	2.3000+01	2.7000+01	3.2950+01	2.3071+02	6.5000-04	1.4000-02	0.0000		
5	2.1000+01	2.9000+01	4.4280+01	2.3015+02	5.1500-04	1.7000-02	0.0000		
6	1.9000+01	3.1000+01	5.9500+01	2.3015+02	4.1000-04	1.9000-02	0.0000		
7	1.7000+01	3.3000+01	7.6990+01	2.3015+02	3.3000-04	1.8000-02	0.0000		
8	1.5000+01	3.5000+01	1.0752+02	2.3015+02	2.4000-04	1.5000-02	0.0000		
9	1.3000+01	3.7000+01	1.6770+02	2.2965+02	6.9000-04	1.2000-02	0.0000		
10	1.0000+01	4.0000+01	2.5251+02	2.2666+02	1.1000-02	6.1000-03	0.0000		
11	9.0000+00	4.1000+01	3.0525+02	2.2935+02	2.5000-02	4.9000-03	0.0000		
12	8.0000+00	4.2000+01	3.5349+02	2.3585+02	5.8000-02	3.7000-03	0.0000		
13	7.0000+00	4.3000+01	4.7777+02	2.4235+02	1.4000-01	3.5000-03	0.0000		
14	6.0000+00	4.4000+01	4.6862+02	2.4885+02	2.4000-01	3.3000-03	0.0000		
15	5.0000+00	4.5000+01	5.3667+02	2.5535+02	6.4000-01	3.0000-03	0.0000		
16	4.0000+00	4.6000+01	6.1249+02	2.6186+02	1.1000+00	2.8000-03	0.0000		
17	3.0000+00	4.7000+01	6.6671+02	2.6837+02	2.5600+00	2.7000-03	0.0000		
18	2.0000+00	4.8000+01	7.9020+02	2.7294+02	3.1200+00	2.6000-03	0.0000		
19	1.5000+00	4.8500+01	8.4067+02	2.7424+02	4.2400+00	2.5500-03	0.0000		
20	1.0000+00	4.9000+01	8.9502+02	2.7555+02	5.7679+00	2.5000-03	2.8350+01		
21	5.0000-01	4.9500+01	9.5195+02	2.7685+02	6.2023+00	2.4000-03	0.0000		
22	5.0000-01	5.0000+01	1.0125+03	2.7815+02	6.8600+00	2.3000-03	0.0000		



cloud layer is between those two levels. The profiles have been taken from various sources, since no radiosonde data was given in Reference 4. The temperature and humidity profiles were taken from the supplemental Standard Atmosphere for 75°N for July,<sup>(5)</sup> except that the relative humidity values within and below the cloud were increased to 100 percent. Humidity values above 10 km were obtained from the stratospheric polar model of Reference 5, which presumes an exponential decrease in mixing ratio by a factor of 10 between 10 km and 12 km, a constant mixing ratio between 12 km and 17 km, and an exponential increase in mixing ratio by a factor of 30 between 17 km and 30 km. The total water vapor amount is 1.65 g/cm<sup>2</sup> of which 0.33 g/cm<sup>2</sup> is between the ground and the cloud base and 0.30 g/cm<sup>2</sup> is within the cloud. The ozone profile used was from the sub-arctic summer atmosphere of McClatchey, et. al.,<sup>(2)</sup> resulting in a total vertical ozone amount of 0.33 atm-cm. The cloud is located between  $\frac{1}{2}$  km and 1 km, which is typical for Arctic summer stratus according to Huschke.<sup>(6)</sup> The cloud size distribution is taken from Weller, et. al., and was measured near Pt. Barrow in September, 1971. We are assured that these measurements are typical for summer stratus, however, so there is no difficulty in applying them to our June situations. The size distribution is reproduced in Figure 3.1; the histogram data, which is more fundamental, was used in preference to the smooth fit.

The ATRAD calculation used 22 levels and 75 spectral intervals. The spectral interval structure was (in cm<sup>-1</sup>): 3600(240)4800(320)8000(500)32000(1000)35000(1500)48500. This structure covers the instrumental response range of 0.2 - 2.6 $\mu$ . Twelve Gaussian angles were used in each spectral interval.

Since the atmospheric structure chosen for ATRAD is, to say the least, somewhat eclectic, some comments need to

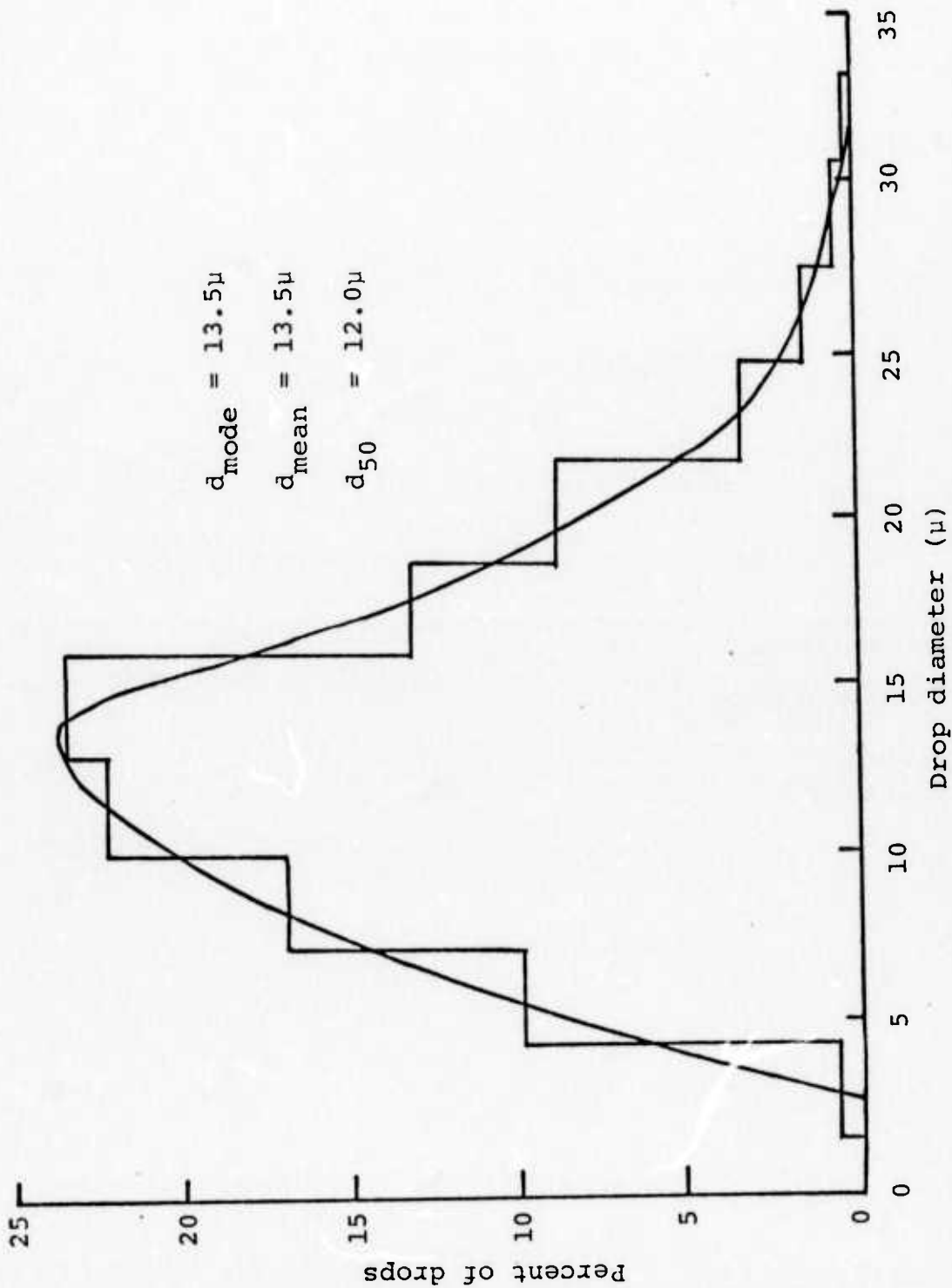


Figure 3.1 Number distribution of Arctic stratus clouds at Barrow.

be made about the sensitivity of the computed fluxes to the input data. The surface fluxes are almost totally insensitive to the cloud height and the ozone profile, within physically realistic limits. (The measurements of Weller, et., al., bear this out from the experimental side, as far as the insensitivity to stratus ceiling height goes). Sensitivity to the size distribution has not been investigated; however, based on the success of calculations which go so far as to approximate Mie scattering by isotropic scattering, and on the success of simple models such as we shall discuss shortly, one gains the impression that it is only a few gross cloud parameters (droplet density, mean droplet radius, etc.) which are really important. It might even reasonably be hypothesized that any size distribution which leads to the same set of gross cloud properties will also lead to the same flux predictions. (ATRAD will be used in the future to try and formulate this hypothesis more rigorously). Since we are dealing only with the solar spectrum  $0.3 - 2.6\mu$  (the instrumental response range), the temperature profile only enters the calculation through the effective absorber amount of water vapor and through the Rayleigh scattering coefficient, and in both cases the derived quantities are insensitive to realistic temperature variations.

The input data to which the calculation is sensitive are the albedo, solar elevation, moisture profile, droplet density, and cloud thickness. The albedo and solar elevation are known (see Table 3.1). The moisture profile, while not known, cannot differ too greatly from the standard one that we use, for Arctic summer conditions are considerably less variable than mid-latitude and tropical regimes, where cumulus convection and frontal systems are important. And furthermore, the absorption of solar radiation by water vapor is decidedly a secondary effect in this problem compared to the reflection of solar radiation at the cloud top and bottom

and at the surface. As for the droplet density and cloud thickness, it is really just their product, which is proportional to the optical thickness of the cloud, that is important. The cloud thickness was fixed at  $\frac{1}{2}$  km; then we varied the (unknown) droplet density until we obtained exact agreement between the ATRAD surface down-flux prediction and the measurement in Table 3.1 for June 29. The droplet density necessary was  $28.35 \text{ cm}^{-3}$ . Based on the observation in Ref. 4, that the cloud was similar on the three days, the same droplet density was used for the other two days.

The ATRAD flux prediction for June 10 agrees exactly with the measurement to the two significant figures given in the measurement. For June 2, the ATRAD flux prediction differs from the measurement by 7%. Considering the difficulty of the problem, this sort of agreement is remarkable and constitutes an excellent experimental verification of ATRAD.

The source of the 7 percent disagreement on June 2 could be any combination of several factors. One factor of course is errors in ATRAD itself. However, the disagreement could also be eliminated by: (a) changing the solar elevation from  $31^\circ$  to  $29^\circ$ , (b) decreasing the albedo from 79 percent to 65 percent, or (c) increasing the droplet density from  $28.35 \text{ cm}^{-3}$  to  $43.5 \text{ cm}^{-3}$ . It seems highly unlikely that the albedo measurement could have been in error by anything like the 14 percent necessary to completely account for the discrepancy; neither does it seem very likely that the droplet concentration was some 53 percent higher on June 2 than on the other two days. Therefore, if we are to ascribe the disagreement to measurement errors (other than errors in the pyranometer itself), it is clear that (a) is the most likely candidate. The computed surface fluxes are particularly sensitive to the solar elevation (and surprisingly insensitive to the albedo and the droplet concentration). The measured values of solar elevation in Reference 4 are referred to as

'mean solar angles', implying that the solar elevation varied during the course of the measurement and that subsequently some sort of average was taken. If the weighting function used in this average was improper and the correct average was, say,  $30^\circ$ , already half of the discrepancy would have been accounted for. The rest of the discrepancy could then more easily be accounted for, perhaps by a combination of a too-high measured albedo and a higher cloud optical thickness on June 2 than on June 10 and June 29 (note that the droplet concentration could have been nearly the same, but with a geometrically thicker cloud on June 2).

The ATRAD sensitivity studies of the last paragraph have an important bearing on any radiation measurements which are conducted under Arctic summer stratus. They indicate that great accuracy is not required in either the albedo or the cloud droplet concentration when one wishes to predict the downward radiation flux at the surface. In the above examples, an 18 percent decrease in the albedo or, alternatively, a 53 percent increase in the cloud droplet concentration, were necessary in order to produce a mere 7 percent drop in the down-flux. On the other hand, accurate knowledge of the solar elevation  $\theta_s$  is very important. This is because the down-flux above the cloud varies closely as  $\sin \theta_s$ , while, according to ATRAD computations, the down-flux at the surface has the even stronger dependence  $(\sin \theta_s)^{3/2}$ . The enhanced  $\theta_s$ -dependence of the surface flux is due partly to the diffusion of the radiation within the cloud and partly to the strong dependence of cloud-top albedo on  $\theta_s$ . At any rate, because of this sensitivity to  $\theta_s$ , care must be exercised in the taking and processing of experimental data involving even small ( $1^\circ - 2^\circ$ ) variations in sun angle.

### 3.1.2 Dependence of Surface Flux on Solar Elevation

The last two lines of Table 3.1 indicate the pitfalls of extrapolating data taken at one sun angle to other sun angles. The first of these lines contains the original measurements 'interpolated to 30° solar elevation',<sup>(4)</sup> and the second contains the ATRAD predictions for  $\theta_s \rightarrow 30^\circ$ , all other parameters remaining the same. While we cannot be absolutely certain, it appears that the 'interpolated' values were actually extrapolated according to an assumed  $\sin \theta_s$  dependence, as witness the following comparisons:

$$\frac{0.56}{0.54} = 1.04$$

$$\frac{\sin 31^\circ}{\sin 30^\circ} = 1.03$$

$$\frac{0.38}{0.47} = 0.81$$

$$\frac{\sin 24^\circ}{\sin 30^\circ} = 0.81$$

$$\frac{0.26}{0.37} = 0.70$$

$$\frac{\sin 21^\circ}{\sin 30^\circ} = 0.72$$

The left-hand ratios are of measured to 'interpolated' fluxes, and the right-hand ratios are of the sines of the corresponding measured  $\theta_s$ 's to the sine of 30°. It is obvious from Table 3.1 that ATRAD does not predict a  $\sin \theta_s$  variation of surface down-flux, nor should such a variation really be expected except for a clear sky. Therefore, an extensive series of ATRAD calculations were made for varying albedo and sun angle in order to investigate the actual functional form of the extrapolation to other sun angles.

The results of this parameter study are shown in Table 3.3. Both the full down-flux  $F_g^\downarrow$  and the purely scattered part  $^s F_g^\downarrow$  at the ground are included. The droplet concentration is  $28.35 \text{ cm}^{-3}$ . Suppose that  $F_g^\downarrow$  varies as some power  $\alpha$  of  $\sin \theta_s$ ,

Table 3.3

ATRAD predicted down-fluxes at the ground ( $F_{\downarrow}$ ) for the full instrumental range 3600 - 48500  $\text{cm}^{-1}$  and for<sup>g</sup> the purely-scattering spectral range 11000 - 48500  $\text{cm}^{-1}$ , as a function of albedo and solar elevation ( $\theta_s$ )

albedo	$\theta_s$	$F_{\downarrow}^g$	$^s F_{\downarrow}^g$
		3600 - 48500 $\text{cm}^{-1}$ (watts/m <sup>2</sup> )	11000 - 48500 $\text{cm}^{-1}$ (watts/m <sup>2</sup> )
0	40°	410.5	299.6
	30°	277.3	203.3
	20°	156.6	115.5
0.20	40°	443.1	324.1
	30°	299.4	220.0
	20°	169.9	125.5
0.58	40°	529.3	389.5
	30°	357.8	264.3
	20°	202.6	150.5
0.79	40°	593.6	438.6
	30°	401.3	297.7
	20°	226.9	169.1

$$F_g^\downarrow = F_o (\sin \theta_s)^\alpha \quad (3.1)$$

Then for fixed albedo, each pair of values of  $F_g^\downarrow$  can be used to eliminate  $F_o$  and solve for  $\alpha$ . It is found that  $\alpha$  varies in the narrow range 1.50 - 1.58, with a tendency to decrease slightly from  $\sim 1.56$  for  $\theta_s \in (30^\circ, 40^\circ)$  to  $\sim 1.51$  for  $\theta_s \in (20^\circ, 30^\circ)$ . The best over-all value of  $\alpha$  for  $\theta_s \in (20^\circ, 40^\circ)$  is 1.53.  $\alpha$  is furthermore entirely independent of albedo. Thus the entire albedo variation resides in  $F_o$ ; however, we do not have sufficient data to empirically fit this variation. Neither do we know the dependence of either  $F_o$  or  $\alpha$  on cloud droplet concentration. Both of these dependencies shall be investigated in the future.

If a relation similar to Equation (3.1) is postulated for just the purely scattered component  $^s F_g^\downarrow$  of Table 3.3 exactly similar results are obtained. The exponent  $\alpha$  varies between 1.49 and 1.56, with a best over-all value of 1.51. It decreases slightly from 1.54 in the  $30^\circ - 40^\circ$  range of  $\theta_s$  to 1.49 in the  $20^\circ - 30^\circ$  range. And it is independent of albedo. The fact that the exponent is almost the same as for the full solar spectrum is surprising, and must indicate that the scattering is the relatively dominant influence upon the  $\theta_s$ -variation, with absorption playing only a minor role.

### 3.1.3 Comparisons of ATRAD with Simpler Models

Weller, et. al., propose a multiple cloud-ground reflection model with which to predict their experimental results. This model is practically identical to that used for cloudy cases in the Mintz-Arakawa GCM, <sup>(7)</sup> and for that reason the discussion below takes on added interest.

The model of Weller, et. al., is illustrated in Figure 3.2. The cloud albedo, as seen

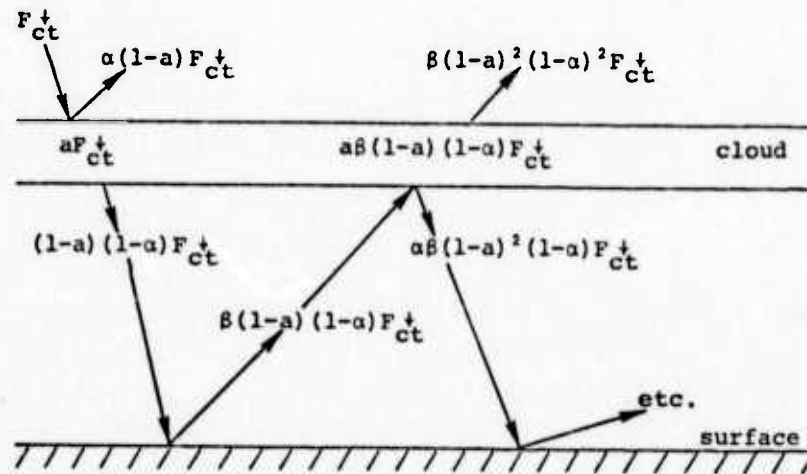


Figure 3.2 Multiple cloud-ground reflection model of Weller, et. al. (4)  $F_{ct}^{\downarrow}$  is the down-flux at the cloud top,  $a$  and  $\alpha$  are related to the cloud absorption and albedo, respectively, and  $\beta$  is the surface albedo.

from either the top or the bottom, is equal to  $\alpha(1-a)$ . The cloud absorbs a fraction  $a$  of the down-flux  $F_{ct}^{\downarrow}$  incident on the cloud top.  $\beta$  is the surface albedo. No absorption between the cloud and the surface is assumed and therefore the down-flux  $F_g^{\downarrow}$  at the surface resulting from the multiple reflection is:

$$\begin{aligned}
 F_g^{\downarrow} &= F_{ct}^{\downarrow} (1-a) (1-\alpha) \sum_{n=0}^{\infty} [\alpha\beta(1-a)]^n \\
 &= F_{ct}^{\downarrow} \frac{(1-a)(1-\alpha)}{1 - \alpha\beta(1-a)} \quad (3.2)
 \end{aligned}$$

Unfortunately, Reference 4 attempts to fit this model to the fluxes which were incorrectly extrapolated to  $30^\circ$ , arriving thereby at parameter values  $\alpha = 0.55$  and  $a = 0.07$ . For completeness, however, the predictions with these parameter values are included in Table 3.4.

In order to ascertain the predictive capabilities of Equation (3.2) as a function of  $\beta$ , for fixed sun angle, the parameters  $a$  and  $\alpha$  were chosen to give the ATRAD values of cloud top albedo and cloud absorption when  $\beta = 0$ ,  $\theta_s = 30^\circ$ . Referring to Figure 3.2, it may be seen that:

$$\alpha(1-a) = \frac{F_{ct}^\uparrow(\beta = 0)}{F_{ct}^\downarrow(\beta = 0)} \quad (3.3)$$

$$(1-\alpha)(1-a) = \frac{F_g^\downarrow(\beta = 0)}{F_{ct}^\downarrow(\beta = 0)} \quad (3.4)$$

The ratios on the right-hand sides were taken from an ATRAD calculation with  $\beta = 0$ ,  $\theta_s = 30^\circ$ , yielding for  $a$  and  $\alpha$ ,

$$\alpha = 0.4541 \quad ,$$

and

$$a = 0.0274 \quad .$$

Using these values of  $a$  and  $\alpha$ , the predictions of Equation (3.2) and the predictions of ATRAD for the ratio  $F_g^\downarrow/F_{ct}^\downarrow$  are compared in Table 3.4 for various values of  $\beta$ . (The other columns in Table 3.4 shall be discussed later).

The parameters  $\alpha = 0.55$ ,  $a = 0.07$ , clearly lead to poor predictions vis á vis ATRAD. The parameters  $\alpha = 0.4541$ ,  $a = 0.0274$  of course lead to agreement with ATRAD for  $\beta = 0$ , since this has been rigged, but as  $\beta$  increases, the predictions of Equation (3.2) increasingly exceed those of ATRAD. Some physical effect is apparently being ignored in the simple model, Equation (3.2).

Table 3.4

Ratio of the down-flux at the ground to the down-flux at the Arctic stratus cloud top, as predicted by various models for solar elevation,  $30^\circ$ , for several values of surface albedo,  $\beta$

$\beta$	$F_g^+ / F_{ct}^+$				
	Eq. (3.2) $\alpha=0.4541,$ $a=0.0274$	Eq. (3.2) $\alpha=0.55,$ $a=0.07$	ATRAD	Eq. (3.12) parameters from Eq. (3.10)	Eq. (3.17) parameters from Eq. (3.21)
0	0.5310	0.4185	0.5310	0.5310	0.5310
0.20	0.5824	0.4662	0.5731	0.5817	0.5731
0.58	0.7138	0.5950	0.6748	0.7106	0.6749
0.79	0.8155	0.7023	0.7484	0.8098	0.7484

There are two physical effects which an examination of the ATRAD fluxes show to be marginally important. One is the absorption of solar radiation within the cloud-to-ground (c→g) layer (by the near IR bands of water vapor) and the other is the Rayleigh back-scattering from the c→g layer. Therefore, a more complex multiple reflection model accounting for c→g absorption and back-scatter has been derived. (Note that the  $a$  and  $\alpha$  derived from Equations (3.3) and (3.4) contain these effects in some crude fashion, since the ATRAD fluxes do; however, until the effects are made explicit, the extent to which they are accounted for can only be conjectured). In the process, the notation of Figure 3.2 has been rejected in favor of the following:

$\alpha_c$  = cloud albedo,

$a_c$  = cloud fractional absorption,

$\alpha_R$  = albedo of c→g layer,

and

$a_w$  = fractional absorption in c→g layer.

These quantities are related to those of Figure 3.2 by:

$$\alpha_c = \alpha(1-a),$$

and

$$a_c = \frac{a}{1-\alpha_c}.$$

We also define:

$$\begin{aligned} T_c &= \text{transmission of cloud} \\ &= (1-\alpha_c)(1-a_c), \end{aligned}$$

and

$$\begin{aligned} T_a &= \text{transmission of c+g layer} \\ &= (1-\alpha_R)(1-a_w). \end{aligned}$$

Consider now the case  $\beta = 0$ , illustrated in Figure 3.3. The upward-directed fluxes at the cloud bottom are then entirely ascribable to Rayleigh back-scattering, since the surface contributes nothing. If we sum the infinite geometric series implied by the "etc." in Figure 3.3, we arrive at the equations:

$$\gamma_1 \equiv \frac{F_g^\downarrow(\beta=0)}{F_{ct}^\downarrow(\beta=0)} = \Gamma_c T_a T_c, \quad (3.5)$$

$$\gamma_2 \equiv \frac{F_{ct}^\uparrow(\beta=0)}{F_{ct}^\downarrow(\beta=0)} = \alpha_c + \Gamma_c \alpha_R T_c^2, \quad (3.6)$$

$$\gamma_3 \equiv \frac{F_{cb}^\downarrow(\beta=0)}{F_{ct}^\downarrow(\beta=0)} = \Gamma_c T_c, \quad (3.7)$$

and

$$\gamma_4 \equiv \frac{F_{cb}^\uparrow(\beta=0)}{F_{ct}^\downarrow(\beta=0)} = \Gamma_c \alpha_R T_c \quad (3.8)$$

where

$$\Gamma_c \equiv \frac{1}{1 - \alpha_R \alpha_c} \quad (3.9)$$

and "cb" refers to the cloud base.

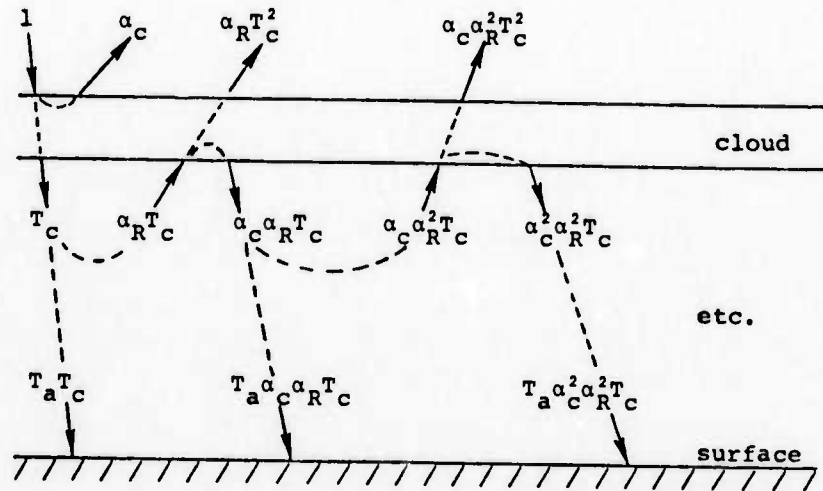


Figure 3.3 Multiple cloud-ground reflection model including the effects of absorption and back-scattering from the cloud-to-ground layer for the case of zero surface albedo,  $\beta = 0$ . The incident flux at the cloud top is taken to be unity.

If the ratios  $\gamma_1, \gamma_2, \gamma_3, \gamma_4$  are regarded as known from an ATRAD calculation with  $\beta = 0$ , then Equations (3.5) to (3.8) uniquely determine the four parameters  $\alpha_c, a_c, \alpha_R,$  and  $a_w$ . For the  $\theta_s = 30^\circ, \beta = 0$  ATRAD calculation of the Arctic stratus problem, the parameters are found to be:

$$\alpha_R = \frac{\gamma_4}{\gamma_3} = 0.005687 \quad ,$$

$$a_w = 1 - \frac{\gamma_1/\gamma_3}{1 - \alpha_R} = 0.006850 \quad ,$$

(3.10)

$$\alpha_c = \frac{\gamma_2 - (\gamma_4^2/\alpha_R)}{1 - \gamma_4^2} = 0.43998 \quad ,$$

and

$$a_c = 1 - \left( \frac{1 - \alpha_c \alpha_R}{1 - \alpha_c} \right) \gamma_3 = 0.04229 \quad .$$

Both the Rayleigh back-scatter  $\alpha_R$  and the absorption  $a_w$  are small; they could only be important when the surface albedo is high and the radiation bounces between cloud and ground many times.

Now we extend the model to  $\beta > 0$ . In order to avoid confusion, all the multiple reflections between the cloud and the c→g layer are summed up by use of the factor  $\Gamma_c$  of Equation (3.9). All the multiple reflections between the ground and the c→g layer are summed up by use of the factor

$$\Gamma_g = \frac{1}{1 - \alpha_R \beta} \quad (3.11)$$

With these simplifications, the model is presented in Figure 3.4. The algorithm used in its construction is as follows:

- (a) a down-flux at the cloud base coming from the cloud top is enhanced by the factor  $\Gamma_c$ , then a fraction  $\alpha_R$  of this is reflected upward and proceeds without further reflection (but attenuated by the factor  $T_c$ ) to the cloud top;

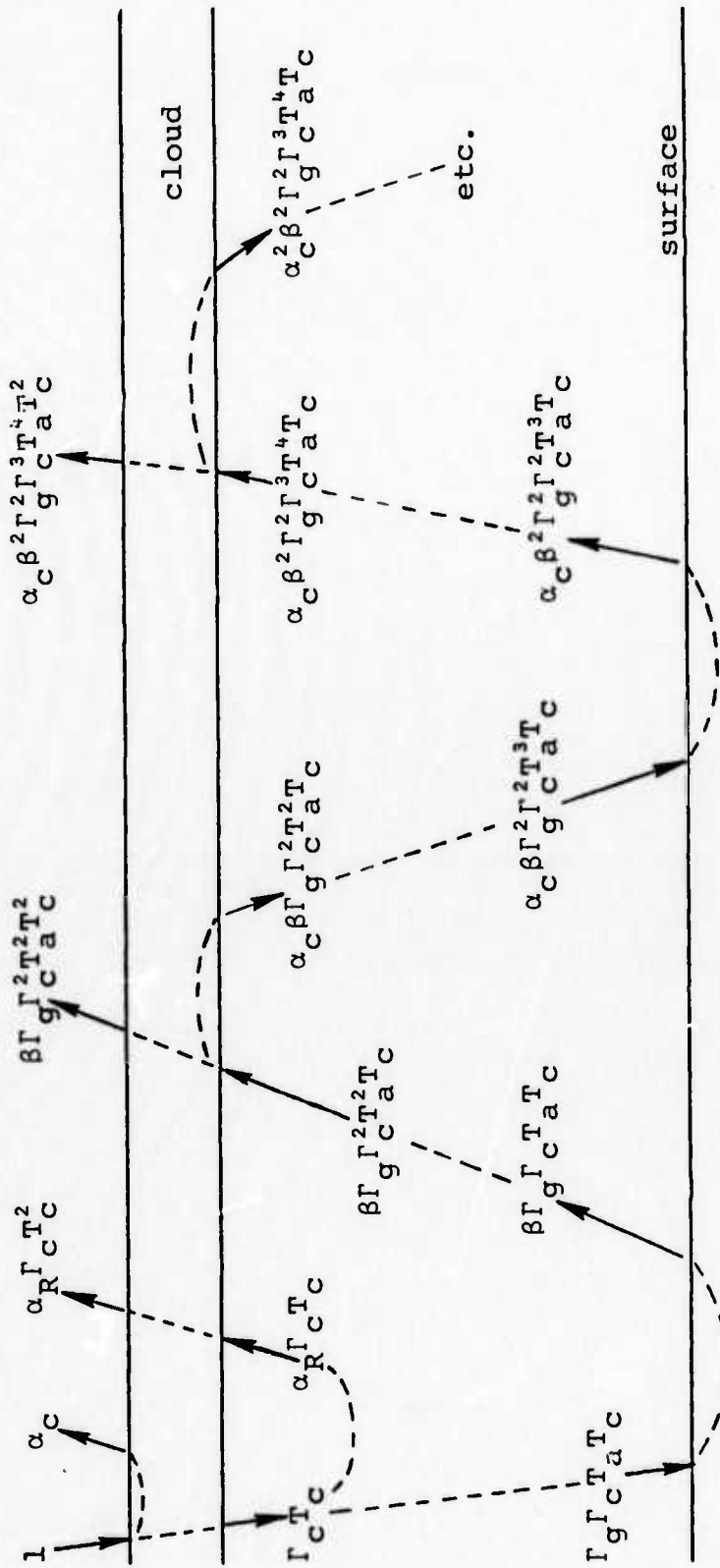


Figure 3.4 Multiple reflection model which includes the effects of absorption and back-scattering in the cloud-to-ground layer, for arbitrary surface albedo,  $\beta$ .

- (b) a down-flux at the ground is enhanced by the factor  $\Gamma_g$ , then a fraction  $\beta$  of this is reflected upward and proceeds without further reflection (but attenuated by the factor  $T_a$ ) to the cloud base;
- (c) an up-flux at the cloud base coming from the ground is enhanced by the factor  $\Gamma_c$ , then a fraction  $\alpha_c$  of this is reflected downward and proceeds without further reflection (but attenuated by the factor  $T_a$ ) to the ground.

Note that part (a) of the algorithm is only exercised once, since we are neglecting Rayleigh back-scattering of the up-fluxes at the cloud top. This neglect is justifiable because, first, the effect is small, and second, the error is partially compensated by looking only at the ratios of fluxes to the down-flux at the cloud top ( $F_{ct}^\downarrow$ ).

Summing the infinite geometric series implied in Figure 3.4, we arrive at the model:

$$\frac{F_g^\downarrow}{F_{ct}^\downarrow} = \frac{\Gamma_g \Gamma_c T_a T_c}{1 - \alpha_c \beta \Gamma_g \Gamma_c T_a^2} \quad , \quad (3.12)$$

$$\frac{F_{ct}^\uparrow}{F_{ct}^\downarrow} = \alpha_c + \alpha_R \Gamma_c T_c^2 + \frac{\beta \Gamma_g \Gamma_c^2 T_a^2 T_c^2}{1 - \alpha_c \beta \Gamma_g \Gamma_c T_a^2} \quad , \quad (3.13)$$

$$\frac{F_{cb}^\downarrow}{F_{ct}^\downarrow} = \frac{\Gamma_c T_c}{1 - \alpha_c \beta \Gamma_g \Gamma_c T_a^2} \quad , \quad (3.14)$$

and

$$\frac{F_{cb}^\uparrow}{F_{ct}^\downarrow} = \alpha_R \Gamma_c T_c + \frac{\beta \Gamma_g \Gamma_c^2 T_a^2 T_c}{1 - \alpha_c \beta \Gamma_g \Gamma_c T_a^2} \quad (3.15)$$

That Equations (3.12) to (3.15) reduce properly in various limiting cases may be verified. Obviously for  $\beta = 0$ , they reduce to Equations (3.5) to (3.8). For  $\alpha_R = 0$ , Equation (3.12) reduces to:

$$\frac{F_g^\downarrow}{F_{ct}^\downarrow} = \frac{(1-a_w)(1-\alpha_c)(1-a_c)}{1 - (1-a_w)^2 \alpha_c \beta} .$$

which is similar to the simple model, Equation (3.2), except that the transmission of the c→g layer is  $(1-a_w)$  rather than unity.

Using Eq. (3.12) with parameter values from Eq. (3.10) leads to the column which is so labeled in Table 3.4. The flux ratios predicted by Eq. (3.12) are slightly lower for  $\beta > 0$  than those predicted by the simpler model of Eq. (3.2), and the adjustments are in the right direction to bring the ratios into agreement with ATRAD. However, the adjustments are much too small. Hence we must look further for the physical effect which has been ignored.

A fact which is often overlooked vis á vis the parameter which we call 'albedo' is that this quantity is not an intrinsic property, but depends on the angular distribution of the incident radiation.<sup>(1)</sup> This is true whether we are speaking of surfaces or of clouds, but for clouds the angular dependence is particularly strong. For example, for the Arctic stratus cloud, ATRAD predicts a cloud-top albedo of ~52 percent when  $\theta_s = 20^\circ$  and of ~44 percent when  $\theta_s = 30^\circ$ . Hence it is unreasonable to expect the top and bottom of a cloud to have the same albedo, for they experience quite different fields of radiant intensity. The intensity at the cloud top is primarily collimated, while that at the cloud bottom is thoroughly diffuse. In order to account for this effect, we

shall define:

$\alpha_d$  = diffuse albedo of cloud

and use  $\alpha_d$  for the albedo of the cloud bottom. Defining the new symbols:

$t_c$  = transmission of cloud from bottom to top

$$= (1 - \alpha_d)(1 - a_c)$$

$$\Gamma_d = \frac{1}{1 - \alpha_R \alpha_d} \quad , \quad (3.16)$$

the revised model becomes:

$$\frac{F_g \downarrow}{F_{ct} \downarrow} = \frac{\Gamma_g \Gamma_d T_a T_c}{1 - \alpha_d \beta \Gamma_g \Gamma_d T_a^2} \quad , \quad (3.17)$$

$$\frac{F_{ct} \uparrow}{F_{ct} \downarrow} = \alpha_c + \alpha_R \Gamma_d T_c t_c + \frac{\beta \Gamma_g \Gamma_d^2 T_a^2 T_c t_c}{1 - \alpha_d \beta \Gamma_g \Gamma_d T_a^2} \quad , \quad (3.18)$$

$$\frac{F_{cb} \downarrow}{F_{ct} \downarrow} = \frac{\Gamma_d T_c}{1 - \alpha_d \beta \Gamma_g \Gamma_d T_a^2} \quad , \quad (3.19)$$

$$\frac{F_{cb} \uparrow}{F_{ct} \downarrow} = \alpha_R \Gamma_d T_c + \frac{\beta \Gamma_g \Gamma_d^2 T_a^2 T_c}{1 - \alpha_d \beta \Gamma_g \Gamma_d T_a^2} \quad . \quad (3.20)$$

With the addition of  $\alpha_d$ , Equations (3.17) to (3.20) are now a five-parameter model. Therefore the four values of the above ratios at  $\beta = 0$  ( $\gamma_1, \gamma_2, \gamma_3, \gamma_4$ ; see Equations (3.5) to (3.8)) are insufficient to determine all five parameters.

One finds, however, that  $\alpha_R$  and  $a_w$  are given by the same expressions as in Equation (3.10) and therefore they have the same numerical values as given there (for  $\theta_s = 30^\circ$ ). This is as it should be since the model alteration concerns the cloud and not the air beneath it. To solve for  $\alpha_c$ ,  $\alpha_d$ , and  $a_c$ , we shall take, as an additional datum, the value of  $F_g^\downarrow/F_{ct}^\downarrow$  from an ATRAD calculation for  $\theta_s = 30^\circ$ ,  $\beta = 0.20$ ,

$$\gamma_5 = \frac{F_g^\downarrow(\beta=0.20)}{F_{ct}^\downarrow(\beta=0.20)} .$$

It is then possible to deduce that:

$$\alpha_R = 0.005687 ,$$

$$a_w = 0.006850 ,$$

$$\alpha_d = 0.3706 ,$$

(3.21)

$$\alpha_c = 0.4398 ,$$

and

$$a_c = 0.04226 .$$

Using this parameter set in Equation (3.17), the last column of Table 3.4 is generated. The agreement with ATRAD is exact for the two albedos 0.58 and 0.79 for which the result is not rigged. Thus, the model seems very promising.

In order to test the model further, ATRAD calculations were made at solar elevations  $\theta_s$  of  $20^\circ$  and  $40^\circ$ . Clearly, we expect  $\alpha_c$  to vary with  $\theta_s$ . If the model is correct, however, we should expect  $\alpha_d$  to remain practically unchanged. Therefore, we hold  $\alpha_d$  fixed at 0.3706 and recalculate only the other four parameters, forcing them to agree with the  $\beta = 0$  ATRAD calculation as before. For  $\theta_s = 20^\circ$ , the parameters are:

Table 3.4

Comparisons of ATRAD and Eq. (3.17) predictions of flux ratio  $F_g^\downarrow/F_{ct}^\downarrow$  (down-flux at the surface to down-flux at the cloud top) for solar elevations  $20^\circ$  and  $40^\circ$ , for various albedos.

Albedo	$F_g^\downarrow/F_{ct}^\downarrow$			
	$\theta_s = 20^\circ$		$\theta_s = 40^\circ$	
	Equation (3.17) and Equation (3.22)	ATRAD	Equation (3.17) and Equation (3.23)	ATRAD
0	0.4578	0.4578	0.5984	0.5984
0.20	0.4942	0.4945	0.6459	0.6454
0.58	0.5824	0.5835	0.7603	0.7586
0.79	0.6460	0.6482	0.8429	0.8402

$$\alpha_c = 0.5165$$

$$a_c = 0.04443 \quad (3.22)$$

$$\alpha_R = 0.005705$$

$$a_w = 0.005562$$

and for  $\theta_s = 40^\circ$  they are:

$$\alpha_c = 0.3702$$

$$a_c = 0.03888 \quad (3.23)$$

$$\alpha_R = 0.005587$$

$$a_w = 0.007819$$

Using these parameter sets, the multiple-reflection model (Eq. 3.17) predictions of the ratio of surface down-flux to cloud-top down-flux are compared with the corresponding ATRAD predictions in Table 3.4. The agreement is excellent. The differences are considerably less than 1%. Thus, the multiple-reflection model (Eq. 3.17) incorporates all the major physical effects and can be relied upon to extrapolate the surface flux to any albedo, if its parameters are adjusted to predict the correct fluxes for  $\beta = 0$ .

It is of interest to study the variations of the parameters  $\alpha_c$ ,  $a_c$ ,  $\alpha_R$ ,  $a_w$  with solar elevation, since ultimately it is desirable to parameterize these variations and free the multiple-reflection model entirely from its dependence on ATRAD. Insufficient calculational data prevents our making any definitive conclusions as yet, however, the following trends are evident for typical Arctic solar elevations:

- (a)  $\alpha_R$  is practically independent of  $\theta_s$ ;
- (b)  $a_w$  increases slowly with  $\theta_s$ , approximately as  $(\sin\theta_s)^{0.54}$ ;
- (c)  $\alpha_c$  decreases markedly as  $\theta_s$  increases, and its variation is not even close to a power of  $\sin\theta_s$  or  $\cos\theta_s$ ;
- (d)  $a_c$  decreases slowly as  $\theta_s$  increases, very approximately as  $(\cos\theta_s)^{0.65}$ .

The behavior (c) of the cloud-top albedo is very similar to the behavior of the albedo of natural surfaces, including snow, ice, and water. Therefore, empirical formulas which have been found useful for fitting the albedo of natural surfaces should be applicable to  $\alpha_c$  also. The behavior of  $a_w$ , which should be strictly constant if the under-cloud radiation

field is strictly diffuse, indicates that some deviation from diffuseness exists under the cloud. And, finally, the decrease of cloud absorption as the sun rises higher is understandable in terms of the relatively shorter average path traversed by a photon impinging on the cloud top at a large angle.

### 3.2 ATRAD COMPARED WITH KATAYAMA MODELS FOR CLEAR-SKY CASES

In our previous semiannual report,<sup>(1)</sup> we presented comparisons between the predictions of ATRAD and those of the older Katayama radiation model as used in the 2-level Mintz-Arakawa GCM at RAND. Two clear-sky problems, a wet one and a dry one, were discussed. Further analysis has subsequently been performed on those problems, and, in addition, comparisons have been made with the newer Katayama radiation model used in the 3-level Mintz-Arakawa GCM at UCLA. The latter model has been found to give dramatically better results in the IR as compared to the older version. Problems remain, however, in the parameterization of near IR solar absorption, and in the choice of a pressure scaling factor.

The atmospheric structures for the two clear-sky problems are shown in tabular form in Tables 3.6 and 3.7, which were taken from actual ATRAD runs. (It would facilitate inter-comparison of models if all authors would present their model's atmospheric profiles in tabular as well as graphical form.) The temperature and humidity profiles from actual M/A (Mintz-Arakawa) 2-level grid locations in Chad (North Africa) and Bolivia were interpolated to the 39 ATRAD levels according to formulas given by Gates, et.al.,<sup>(7)</sup> as discussed at some length in Ref. (1). The Chad and Bolivia problems are opposite extremes in terms of water vapor content; the total vertical water vapor amount for Chad is  $0.204 \text{ g/cm}^2$ , while for Bolivia it is  $2.530 \text{ g/cm}^2$ , or 12.4 times as much. The ozone profile is the same for both problems.

Table 3.6

Atmospheric profiles of altitude (km), pressure (mb), temperature ( $^{\circ}$ K), water vapor ( $\text{g}/\text{m}^3$ ), ozone density ( $\text{atm-cm}/\text{km}$ ), and aerosol density ( $= 0$ ) for Chad problem.

I N P U T    R A T A							
i	ALT	ZDN	PRESS	TEMP	H2ODEN	O3DEN	AER DEN
1	4.4373+01	0.0000	2.0000+00	2.6011+02	2.7642-04	4.3524-04	0.0000
2	2.6584+01	1.7789+01	2.1800+01	2.4276+02	2.9618-04	1.0590-02	0.0000
3	2.2051+01	2.2323+01	4.1600+01	2.3629+02	3.0429-04	1.1699-02	0.0000
4	1.9383+01	2.4990+01	6.1400+01	2.3198+02	3.0994-04	1.0124-02	0.0000
5	1.7499+01	2.6874+01	8.1200+01	2.2868+02	3.1441-04	8.2558-03	0.0000
6	1.6048+01	2.8325+01	1.0100+02	2.2599+02	3.1815-04	6.7687-03	0.0000
7	1.4870+01	2.9503+01	1.2080+02	2.2371+02	3.3427-04	5.6377-03	0.0000
8	1.3881+01	3.0492+01	1.4060+02	2.2171+02	6.2082-04	4.7755-03	0.0000
9	1.3030+01	3.1343+01	1.6040+02	2.1994+02	1.0628-03	4.1081-03	0.0000
10	1.2284+01	3.2089+01	1.8020+02	2.1834+02	1.7093-03	3.5820-03	0.0000
11	1.1628+01	3.2745+01	2.0000+02	2.1169+02	2.6807-03	3.1649-03	0.0000
12	1.0731+01	3.3642+01	2.3060+02	2.1944+02	4.5834-03	2.6599-03	0.0000
13	9.9187+00	3.4455+01	2.6121+02	2.2642+02	7.3306-03	2.2639-03	0.0000
14	9.1748+00	3.5198+01	2.9181+02	2.3278+02	1.1131-02	1.9481-03	0.0000
15	8.4874+00	3.5886+01	3.2242+02	2.3862+02	1.6213-02	1.6922-03	0.0000
16	7.8474+00	3.6526+01	3.5302+02	2.4404+02	2.2826-02	1.4820-03	0.0000
17	7.2479+00	3.7125+01	3.8362+02	2.4909+02	3.1237-02	1.3075-03	0.0000
18	6.6834+00	3.7690+01	4.1423+02	2.5382+02	4.1733-02	1.1609-03	0.0000
19	6.1496+00	3.8224+01	4.4483+02	2.5828+02	5.4620-02	1.0367-03	0.0000
20	5.6429+00	3.8730+01	4.7543+02	2.6250+02	7.0222-02	9.3067-04	0.0000
21	5.1603+00	3.9213+01	5.0604+02	2.6650+02	8.8881-02	8.3937-04	0.0000
22	4.6993+00	3.9674+01	5.3664+02	2.7031+02	1.1096-01	7.6025-04	0.0000
23	4.2579+00	4.0115+01	5.6725+02	2.7394+02	1.3683-01	6.9127-04	0.0000
24	3.9385+00	4.0435+01	5.9020+02	2.7656+02	1.5896-01	6.4520-04	0.0000
25	3.6285+00	4.0745+01	6.1315+02	2.7910+02	1.8362-01	6.0332-04	0.0000
26	3.3272+00	4.1046+01	6.3610+02	2.8156+02	2.1100-01	5.6517-04	0.0000
27	3.0340+00	4.1339+01	6.5906+02	2.8395+02	2.4126-01	5.3031-04	0.0000
28	2.7485+00	4.1625+01	6.8201+02	2.8627+02	2.7461-01	4.9837-04	0.0000
29	2.4703+00	4.1903+01	7.0496+02	2.8853+02	3.1124-01	4.6909-04	0.0000
30	2.1988+00	4.2174+01	7.2791+02	2.9072+02	3.5135-01	4.4214-04	0.0000
31	1.9339+00	4.2439+01	7.5087+02	2.9286+02	3.9514-01	4.1730-04	0.0000
32	1.6748+00	4.2698+01	7.7382+02	2.9539+02	4.4216-01	3.9434-04	0.0000
33	1.4212+00	4.2952+01	7.9677+02	2.9767+02	4.9315-01	3.7306-04	0.0000
34	1.1728+00	4.3201+01	8.1973+02	3.0030+02	5.4831-01	3.5332-04	0.0000
35	9.2925-01	4.3444+01	8.4268+02	3.0268+02	6.0786-01	3.3497-04	0.0000
36	6.9041-01	4.3683+01	8.6563+02	3.0502+02	6.7202-01	3.1788-04	0.0000
37	4.5605-01	4.3917+01	8.8858+02	3.0731+02	7.4100-01	3.0195-04	0.0000
38	2.2598-01	4.4147+01	9.1154+02	3.0956+02	8.1503-01	2.8708-04	0.0000
39	0.0000	4.4373+01	9.3449+02	3.1177+02	8.9433-01	2.7318-04	0.0000

Table 3.7

Atmospheric profiles of altitude (km), pressure (mb), temperature ( $^{\circ}$ K), water vapor ( $\text{g}/\text{m}^3$ ), ozone density ( $\text{atm-cm}/\text{km}$ ), and aerosol density ( $= 0$ ) for Bolivia problem.

I N P U T   D A T A									
I	ALT	ZDN	PRESS	TEMP	H2ODEN	O3DEN	AER	OEN	
1	4.5875+01	0.0000	2.0000+00	2.7765+02	2.5896-04	3.1335-04	0.0000		
2	2.6886+01	1.8989+01	2.1800+01	2.5913+02	2.7747+04	1.0331-02	0.0000		
3	2.2047+01	2.3828+01	4.1600+01	2.5223+02	2.8506-04	1.1897-02	0.0000		
4	1.9199+01	2.6676+01	6.1400+01	2.4762+02	2.9036-04	9.9547-03	0.0000		
5	1.7189+01	2.8686+01	8.1200+01	2.4411+02	2.9454-04	7.9341-03	0.0000		
6	1.5639+01	3.0236+01	1.0100+02	2.4123+02	2.9805-04	6.3654-03	0.0000		
7	1.4382+01	3.1493+01	1.2080+02	2.3879+02	3.1661-04	5.2012-03	0.0000		
8	1.3327+01	3.2548+01	1.4060+02	2.3667+02	7.5566-04	4.3325-03	0.0000		
9	1.2418+01	3.3457+01	1.6040+02	2.3477+02	1.6083-03	3.6726-03	0.0000		
10	1.1622+01	3.4253+01	1.8020+02	2.3307+02	3.1353-03	3.1610-03	0.0000		
11	1.0922+01	3.4953+01	2.0000+02	2.2601+02	5.8406-03	2.7611-03	0.0000		
12	1.0070+01	3.5805+01	2.2717+02	2.2316+02	1.1734-02	2.3333-03	0.0000		
13	9.2960+00	3.6579+01	2.5433+02	2.3669+02	2.1797-02	1.9967-03	0.0000		
14	8.5868+00	3.7288+01	2.8150+02	2.4120+02	3.8037-02	1.7272-03	0.0000		
15	7.9314+00	3.7944+01	3.0866+02	2.4528+02	6.3077-02	1.5082-03	0.0000		
16	7.3217+00	3.8553+01	3.3583+02	2.4900+02	1.0026-01	1.3279-03	0.0000		
17	6.7514+00	3.9124+01	3.6299+02	2.5241+02	1.5376-01	1.1777-03	0.0000		
18	6.2153+00	3.9660+01	3.9016+02	2.5555+02	2.2869-01	1.0513-03	0.0000		
19	5.7093+00	4.0166+01	4.1732+02	2.5847+02	3.3124-01	9.4396-04	0.0000		
20	5.2301+00	4.0645+01	4.4449+02	2.6117+02	4.6879-01	8.5201-04	0.0000		
21	4.7747+00	4.1100+01	4.7165+02	2.6370+02	6.5003-01	7.7268-04	0.0000		
22	4.3404+00	4.1534+01	4.9882+02	2.6606+02	8.8514-01	7.0376-04	0.0000		
23	3.9265+00	4.1949+01	5.2599+02	2.6827+02	1.1859+00	6.4352-04	0.0000		
24	3.6274+00	4.2248+01	5.4636+02	2.6984+02	1.4626+00	6.0319-04	0.0000		
25	3.3377+00	4.2537+01	5.6673+02	2.7134+02	1.7902+00	5.6646-04	0.0000		
26	3.0566+00	4.2818+01	5.8711+02	2.7278+02	2.1758+00	5.3292-04	0.0000		
27	2.7837+00	4.3091+01	6.0748+02	2.7416+02	2.6271+00	5.0323-04	0.0000		
28	2.5186+00	4.3356+01	6.2786+02	2.7548+02	3.1525+00	4.7405-04	0.0000		
29	2.2607+00	4.3614+01	6.4823+02	2.7674+02	3.7612+00	4.4814-04	0.0000		
30	2.0096+00	4.3865+01	6.6860+02	2.7796+02	4.4633+00	4.2426-04	0.0000		
31	1.7650+00	4.4110+01	6.8898+02	2.7913+02	5.2697+00	4.0219-04	0.0000		
32	1.5265+00	4.4349+01	7.0935+02	2.8053+02	6.1860+00	3.8176-04	0.0000		
33	1.2936+00	4.4581+01	7.2973+02	2.8188+02	7.2290+00	3.6279-04	0.0000		
34	1.0660+00	4.4809+01	7.5010+02	2.8319+02	8.4121+00	3.4516-04	0.0000		
35	8.4355-01	4.5031+01	7.7047+02	2.8446+02	9.7494+00	3.2873-04	0.0000		
36	6.2592-01	4.5249+01	7.9085+02	2.8569+02	1.1256+01	3.1342-04	0.0000		
37	4.1291-01	4.5462+01	8.1122+02	2.8689+02	1.2949+01	2.9911-04	0.0000		
38	2.0434-01	4.5671+01	8.3160+02	2.8806+02	1.4845+01	2.8572-04	0.0000		
39	0.0000	4.5875+01	8.5197+02	2.8919+02	1.6963+01	2.7318-04	0.0000		

$$\frac{We^{(z-z_0)/h}}{h \left[ 1 + e^{(z-z_0)/h} \right]^2} \quad \text{atm-cm/km}$$

with  $W = 0.218$  atm-cm,  $z_0 = 23.25$  km, and  $h = 4.5$  km. Due to insufficient resolution in the ozone layer, ATRAD actually computes a total ozone amount of 0.200 atm-cm rather than 0.218 atm-cm. The remaining model parameters for Chad and Bolivia, consisting of sun angle, albedo, and surface temperature, are given in Table 3.8. Note the discontinuities in temperature at the surface in both problems. The  $\sigma$ -levels 0, 1/2, and 1 correspond to levels 11, 23, and 39 in the ATRAD atmosphere.

The spectral intervals used by ATRAD for the Chad and Bolivia problems are 60(60)600(20)800(40)1200(80)1600(160)2400(240)4800(320)8000(500)11000(120)11120(380)11500(500)32000(1000)35000(1500)48500  $\text{cm}^{-1}$ . Anywhere from 6 to 12 Gaussian angles are used, depending on the degree of isotropy of the intensity in each hemisphere (upward and downward).

A point which was not noted in the previous comparisons<sup>(1)</sup> between ATRAD and the older Katayama ('OK') model was that the two models use different solar constants. ATRAD uses the more current value of 1.94 ly/min<sup>(8)</sup> while the

Table 3.8

Solar elevation ( $\theta_s$ ), albedo ( $\beta$ ), and surface temperature ( $T_g$ ) for Chad and Bolivia problems. ( $\beta=0$  for  $\lambda \geq 3\mu$ ).

	$\theta_s$	$\beta$	$T_g$ ( $^{\circ}\text{K}$ )
Chad	57.824	0.20	343.26
Bolivia	27.055	0.09	304.19

older Katayama model uses 2.00 ly/min. This has obvious consequences for the fluxes, and in fact correcting the 'OK' solar fluxes to the more modern solar constant produces much better flux agreement between the two models in the solar spectrum. The revised flux tables are presented in Table 3.9. In spite of better agreement in the solar spectrum (differences no larger than 2.6% at any level), the poor agreement in the IR still causes the net fluxes to differ by as much as 20%. The average net flux disagreement between the two models, for all three levels and for both problems, is 8-1/2%. At their face value, errors of even as much as 20% may not seem disturbing. However, it is well to remember that we have been discussing fluxes and not flux differences. The picture as regards flux differences is much more bleak, as we shall see below.

Some comments on Table 3.9 are needed here, in light of the fact that these fluxes, and others like them, are used to construct the flux difference tables to follow. The first fact to note is the accuracy to which the fluxes are quoted. It has been found possible, in varying the spectral interval structure used in ATRAD for the Chad and Bolivia problems, to produce changes in the fluxes in the first place after the decimal point. Such changes are ascribed primarily to the exponential fitting algorithm, and to the way the intervals are arranged relative to the absorption bands. Perhaps when some of the problems are ironed out of the fitting algorithm (cf. Section 2.1) this limitation on the accuracy of ATRAD flux predictions will become less important. In the meantime, the ATRAD fluxes quoted in Table 3.9 are estimated to have an uncertainty of  $\pm 0.5$  watts/m<sup>2</sup> due essentially to the lack of infinitely fine spectral resolution. The impact of other errors (such as in the McClatchey transmission data<sup>(2)</sup> used by ATRAD) upon the fluxes has not been estimated as yet.

Table 3.9  
 Comparison between ATRAD (unparenthesized) and older Katayama model (parenthesized) flux predictions, in watts/m<sup>2</sup>, for Chad and Bolivia problems.

	$\sigma = 0$ (200 mb)	$\sigma = 1/2$ (567 mb)	$\sigma = 1$ (934 mb)
(1) IR (60 - 2640 cm <sup>-1</sup> )	-447.0 (-471.6)	-412.3 (-422.1)	-481.5 (-437.9)
(2) Near-IR (2640 - 11,120 cm <sup>-1</sup> )	345.6 ( 333.4)	316.2 ( 308.8)	270.5 ( 272.9)
(3) Visible (11,120 - 48,500 cm <sup>-1</sup> )	541.8 ( 554.9)	539.1 ( 554.9)	536.4 ( 554.9)
Solar [(2)+(3)]	887.4 ( 888.3)	855.3 ( 863.7)	806.9 ( 827.8)
Net [(1)+(2)+(3)]	440.4 ( 446.7)	436.0 ( 441.6)	325.4 ( 389.9)

BOLIVIA (18°S, 65°W)

	$\sigma = 0$ (200 mb)	$\sigma = 1/2$ (526 mb)	$\sigma = 1$ (852 mb)
(1) IR (60 - 2640 cm <sup>-1</sup> )	-260.5 (-271.7)	-190.3 (-208.1)	-156.8 (-181.5)
(2) Near-IR (2640 - 11,120 cm <sup>-1</sup> )	207.0 ( 203.0)	170.7 ( 173.1)	128.2 ( 115.1)
(3) Visible (11,120 - 48,500 cm <sup>-1</sup> )	310.8 ( 308.4)	308.7 ( 308.4)	303.5 ( 308.4)
Solar [(2)+(3)]	517.8 ( 511.4)	479.4 ( 481.5)	431.7 ( 423.5)
Net [(1)+(2)+(3)]	257.3 ( 239.7)	289.1 ( 273.4)	274.9 ( 242.0)

The dividing point between the IR and solar spectra is not specified in the Katayama models, and so the value  $2640 \text{ cm}^{-1}$  ( $3.79\mu$ ) was selected based on the observation that in the interval  $2400\text{--}2640 \text{ cm}^{-1}$  the ATRAD net fluxes were primarily upward while in  $2640\text{--}2880 \text{ cm}^{-1}$  they were all downward. Moving the IR dividing point to  $2880 \text{ cm}^{-1}$  ( $3.47\mu$ ) would cause a uniform decrease in the magnitude of the IR fluxes of about  $1.7 \text{ w/m}^2$  for Chad and between  $1.1$  and  $1.6 \text{ w/m}^2$  for Bolivia. Moving it to  $2400 \text{ cm}^{-1}$  ( $4.17\mu$ ) would cause an increase in the magnitude of the IR fluxes of less than  $0.95 \text{ w/m}^2$  for both Chad and Bolivia. Of course, there would be compensatory changes in the solar-flux in both cases. The other dividing point, at  $11,120 \text{ cm}^{-1}$  ( $0.8993\mu$ ), is not exactly equal to the Katayama separation point of  $0.9\mu$ . Again, the change in visible vs. near IR flux resulting from this discrepancy is less than  $0.5 \text{ w/m}^2$ . These figures are quoted to show that the flux breakdown is not sensitive to the choice of either dividing point.

Not only the 'OK' value for the solar constant ( $2.00 \text{ ly/min}$ ), but also the fractional breakdown of the solar flux between  $\lambda > 0.9\mu$  and  $\lambda < 0.9\mu$ , can be called into question. Since either fraction determines the other, consider only the  $\lambda < 0.9\mu$  fraction,  $f_o$ . For the older and the newer Katayama models,  $f_o = 0.651$ . From the detailed spectral data of Thekaekara, <sup>(8)</sup>  $f_o = 0.634$ . But since the Katayama models neglect ozone, and since the stratospheric ozone layer will absorb all solar flux in the wavelength region  $\lambda < 0.3\mu$ , which amounts to  $1.2\%$  of the solar constant, <sup>(8)</sup> it should be reasonable to take  $f_o = 0.634 - 0.012 = 0.622$  (while leaving the  $\lambda > 0.9\mu$  fraction at  $1 - 0.634 = 0.366$ ). Or, if ozone were to be included in the same way that stratospheric water vapor is, the  $\lambda < 0.9\mu$  part of the solar flux could be appropriately attenuated between the top of the atmosphere and  $\sigma = 0$  ( $200 \text{ mb}$ ),

in which case  $f_0 = 0.634$  would be appropriate. However, because of the way in which absorption of solar flux is parameterized in the Katayama models, the atmospheric heating rates in the solar spectrum are independent of both  $f_0$  and the solar constant. Hence, the only impact of changing  $f_0$  and/or the solar constant is that the flux into the surface is changed. Let us derive the appropriate formulas for this surface flux from the treatment in Gates, et.al.,<sup>(7)</sup> for clear-sky situations.

We begin by defining the effective water vapor amount  $u^*$  between the surface and any level  $n$ :<sup>(7)</sup>

$$u_n^* = \frac{1}{g} \int_{p_n}^{p_s} q(p) \left( \frac{p}{p_0} \right)^\alpha dp \quad (3.24)$$

$q$  is the water vapor mixing ratio,  $\alpha$  is the pressure scaling factor,  $g$  is the acceleration due to gravity,  $p_s$  is the surface pressure, and  $u_n^*$  must be in units of  $g/cm^2$ . For the 'OK' model,  $\alpha = 1$ .  $n = \infty$  will refer to the top of the atmosphere. Also define

$$S_\infty^{sca} = f_0 S_0 \mu_0 \quad (3.25)$$

$$S_\infty^{abs} = (1 - f_0) S_0 \mu_0$$

which are the 'scattered' and 'absorbed' parts of the solar flux in terms of the fraction  $f_0$  discussed in the last paragraph, the solar constant  $S_0$ , and the cosine of the solar zenith angle  $\mu_0$ . The fractional absorption of the 'absorbed' part due to an amount  $u^*$  of water vapor is parameterized by

$$A(u^*, \mu_o) = \frac{0.189}{(1 - f_o) \bar{S}_o} (u^*/\mu_o)^{0.303} \quad (3.26)$$

where  $\bar{S}_o$  is the mean solar constant in ly/min. The 'absorbed' flux at any level  $n$  is therefore

$$S_n^{abs} = S_\infty^{abs} \left[ 1 - A(u_\infty^* - u_n^*, \mu_o) \right] \quad (3.27)$$

The flux differences between  $\sigma = 0$  and  $\sigma = 1/2$  and between  $\sigma = 1/2$  and  $\sigma = 1$  are then, respectively,

$$\begin{aligned} \Delta_1 &= S_0^{abs} - S_2^{abs} \\ &= 0.189 \mu_o (S_o/\bar{S}_o) \left[ \left( \frac{u_\infty^* - u_2^*}{\mu_o} \right)^{0.303} - \left( \frac{u_\infty^* - u_0^*}{\mu_o} \right)^{0.303} \right] \end{aligned} \quad (3.28)$$

$$\begin{aligned} \Delta_3 &= S_2^{abs} - S_4^{abs} \\ &= 0.189 \mu_o (S_o/\bar{S}_o) \left[ \left( \frac{u_\infty^*}{\mu_o} \right)^{0.303} - \left( \frac{u_\infty^* - u_2^*}{\mu_o} \right)^{0.303} \right] \end{aligned} \quad (3.29)$$

The ratio  $(S_o/\bar{S}_o)$  depends only on the Earth-sun distance. Therefore,  $\Delta_1$  and  $\Delta_3$  are independent of  $f_o$  and  $S_o$ . The scattered flux at all levels is

$$S_4^{sca} = S_{\infty}^{sca} \frac{(1-\beta)(1-\alpha_0)}{1-\beta\alpha_0} \quad (3.30)$$

where

$$\alpha_0 = 0.085 - 0.247 \log_{10} \left( \frac{P_s \text{ (mb)}}{1000} \mu_0 \right) \quad (3.31)$$

and where  $\beta$  is the surface albedo. The net solar flux into the surface is, therefore,

$$\begin{aligned} S_4 &= S_4^{abs} + S_4^{sca} \\ &= S_0 \mu_0 \left\{ (1-f_0) [1-A(u_{\infty}^*, \mu_0)] + f_0 \frac{(1-\beta)(1-\alpha_0)}{1-\beta\alpha_0} \right\} \end{aligned} \quad (3.32)$$

The surface flux is proportional to  $S_0$ . (Lest the importance of using the best possible value of  $S_0$  to calculate  $S_4$  be underestimated, suffice it to say that the SMIC Report<sup>(94)</sup> associates a 1% decrease in  $S_0$  with a decrease in global average surface temperature of 1.5°C.) The dependence of  $S_4$  on  $f_0$  is slightly more complicated. The rate of change of  $S_4$  with  $f_0$  is

$$\frac{dS_4}{df_0} = S_0 \mu_0 \left\{ \frac{(1-\beta)(1-\alpha_0)}{1-\beta\alpha_0} - 1 \right\}$$

For  $\beta \in (0,1)$  and  $\alpha_0 \in (0,1)$ , it can be shown that

$$\frac{dS_4}{df_0} < 0 .$$

Therefore, if we decreased  $f_o$ , as proposed in the last paragraph, the surface flux  $S_4$  would increase. For both the Chad and Bolivia problems,  $S_4$  was calculated from Eq. (3.32) for  $i_o = 0.625$  and  $f_o = 0.651$  in order to determine the quantitative change in  $S_4$  produced. The results for Chad were

$$S_4 = \begin{cases} 827.1 \text{ w/m}^2 & f_o = 0.651 \\ 829.3 \text{ w/m}^2 & f_o = 0.625 \end{cases}$$

and for Bolivia,

$$S_4 = \begin{cases} 423.1 \text{ w/m}^2 & f_o = 0.651 \\ 425.6 \text{ w/m}^2 & f_o = 0.625 \end{cases}$$

The change in  $S_4$  in both cases is about 2 watts/m<sup>2</sup>, or 0.3% for Chad and 0.6% for Bolivia. This change is produced by a 4% change in  $f_o$ . Hence, it must be concluded that the results of the Katayama models are insensitive to  $f_o$ , except perhaps for extreme values of albedo, sun angle, etc.

While flux values have an intrinsic interest, it is really only flux differences between atmospheric levels which are used in a general circulation model (the only exception being that the net flux at the surface is used to compute surface heating). In our experience, the taking of such differences almost always leads to the loss of one (and sometimes two) significant digits, even when the levels are as widely separated as in the M/A 2-level GCM. Thus a flux-prediction model which is accurate to, say, 1% will have uncertainties in its flux difference predictions of the order of 10%. Even though the 'OK' model produces reasonable flux predictions, therefore, one cannot for that reason alone expect good flux difference predictions.

In Tables 3.10 and 3.11, the flux differences and surface fluxes as computed by ATRAD and by the newer and older Katayama models are presented. ATRAD computations were made with and without the ozone profile included, in order to assess the influence of ozone on heating rates. Before discussing these tables, however, some remarks need to be made on the newer Katayama ('NK') model.

The 'NK' model is described in an as yet unpublished manuscript written by Katayama at UCLA. Parts of this manuscript as well as a FORTRAN listing for the model were kindly furnished to us by Mr. Hans Giroux. The FORTRAN version of the model is used in UCLA's 3-level version of the M/A GCM. Rather than re-coding the 'NK' model for 2 levels, which is non-trivial, we ran it 'as-is' by putting one level between  $\sigma = 0$  and  $\sigma = 1/2$  and two levels ( $\sigma = 1/2$  to  $\sigma = 3/4$ ,  $\sigma = 3/4$  to  $\sigma = 1$ ) between  $\sigma = 1/2$  and  $\sigma = 1$ . This puts the increased resolution where most of the water vapor resides. The extra temperature values required (as compared to the 2-level model) were obtained using the temperature interpolation formulas of the 'OK' model. (1,7)

Two options were included for the 'NK' humidity profile. The first was to obtain the three mixing ratio values (Q1, Q3, Q5) required by the 'NK' model from the interpolation formula used in the 'OK' model. (1,7) The second was to insert the effective water vapor amounts ( $u^*$ ) into the 'NK' model directly, using the 'OK' values of  $q$  and  $\alpha$  ( $\alpha = 1$ ) in Eq. (3.24). The first option will be called the 'q-option,' the second the 'u\*-option.' Results from both options are given in Tables 3.10 and 3.11. Since both options use Eq. (3.24) to compute  $u^*$ , there are only two reasons for their absorber amounts to differ: (1) they use different  $q$ -profiles; or (2) they use different pressure scaling factors  $\alpha$ . In fact, the differences in absorber amount between the options are almost

Table 3.10

Flux differences and surface fluxes (watts/m<sup>2</sup>) for Chad as predicted by ATRAD with and without an ozone profile, and by the newer and older Katayama models ('NK' and 'OK' respectively). The unparenthesized 'NK' values are for the q-option, while the parenthesized ones are for the u\*-option. The upper level is  $\sigma = 0$  to  $\sigma = 1/2$ , the lower level is  $\sigma = 1/2$  to  $\sigma = 1$ .

	UPPER LEVEL				LOWER LEVEL			
	ATRAD	ATRAD (no O <sub>3</sub> )	'NK'	'OK'	ATRAD	ATRAD (no O <sub>3</sub> )	'NK'	'OK'
IR	-27.7	-33.1	-28.2 (-30.5)	-49.5	62.2	61.4	59.5 (53.5)	15.8
Solar	32.1	31.2	25.2 (24.6)	24.6	48.4	48.3	35.0 (35.9)	35.9
Net	4.4	-1.9	-2.9 (-6.0)	-24.9	110.6	109.7	94.5 (89.4)	51.7
Flux into Surface	325.4	335.4	329.7 (327.6)	389.9				

Table 3.11

Flux differences and surface fluxes (watts/m<sup>2</sup>) for Bolivia as predicted by ATRAD with and without an ozone profile, and by the newer ('NK') and older ('OK') Kata-yama models, with the same conventions applying as for Table 3.10.

	UPPER LEVEL				LOWER LEVEL			
	ATRAD	ATRAD (no O <sub>3</sub> )	'NK'	'OK'	ATRAD	ATRAD (no O <sub>3</sub> )	'NK'	'OK'
IR	-70.2	-72.2	-71.6 (-73.2)	-63.6	-33.5	-35.8	-25.5 (-31.2)	-26.6
Solar	38.4	38.0	31.3 (29.9)	29.9	47.7	47.6	58.4 (58.0)	58.0
Net	-31.7	-34.1	-40.3 (-43.4)	-33.7	14.1	11.8	32.9 (26.8)	31.4
Flux into Surface	274.9	282.1	240.7 (240.1)	242.0				

entirely due to different  $\alpha$ 's. (For 'OK',  $\alpha = 1$ ; for 'NK',  $\alpha = 0.6$ ; and for ATRAD, the McClatchey scheme<sup>(2)</sup> uses  $\alpha = 0.9$ , but with  $p/p_0$  replaced by  $p/p_0(T_0/T)^{1/2}$  to account for the temperature variation of line half-width.) The mixing ratio profiles used in the 'OK' and 'NK' calculations were identical up to pressure level  $p_1$  ( $\sigma = 3/4$ ) in both models, and almost all the effective water vapor amount lies below this level.

The 'NK' model contains no improvements in the parameterization of the solar spectrum when clouds are absent. Hence the 'OK' solar flux differences agree with the 'NK'  $u^*$ -option flux differences. The 'NK' model, however, contains a considerably more sophisticated treatment of the IR, and its predictions of IR flux differences agree much more closely with ATRAD than do the 'OK' predictions. In the Chad problem, the net (solar + IR) flux differences and net surface flux predicted by 'NK' agree well with ATRAD and are a vast improvement over 'OK'. In the Bolivia problem, the 'NK' and 'OK' net flux difference predictions are close to each other in the lower level ( $\sigma = 1/2$  to  $\sigma = 1$ ) and both differ by roughly a factor of 2 from ATRAD. In the upper Bolivia layer, a fortuitous cancellation of errors in the solar and IR flux differences causes the net 'OK' flux difference to be very close to the ATRAD value(s); the 'NK' net flux difference is too large by roughly a factor of 4/3. Both the 'NK' and 'OK' surface flux predictions are off by about 14% for Bolivia. Thus, the following general conclusions emerge from the comparisons in Tables 3.10 and 3.11:

- (1) for a dry or a wet atmosphere, the IR treatment in the newer Katayama model is far superior to that in the older model;

- (2) there is no clear-cut advantage in the IR of the q-option over the u\*-option, that is, of a pressure scaling factor of 0.6 over one of 1.0; in the (dry) lower level of Chad, 0.6 is clearly preferable, while in the (wet) lower level of Bolivia, 1.0 is clearly preferable; in the (dry) upper levels of both problems, neither 0.6 nor 1.0 has a clear advantage;
- (3) the solar absorption treatment common to both Katayama models causes too little flux to be absorbed in dry levels (upper and lower Chad, upper Bolivia) and too much in wet levels (lower Bolivia);
- (4) for a dry atmosphere, the newer Katayama model is vastly superior to the older one in predicting net heating rates and surface fluxes; for a wet atmosphere, the newer Katayama model may actually be slightly worse than the older one in predicting those same quantities;
- (5) ozone has a substantial impact on the heating rates of the upper levels, and even affects the heating rate of the Bolivian lower level non-negligibly; the effect is concentrated almost entirely in the IR and thus is due to the  $O_3$  9.6 $\mu$  band.

In order to quantify the statements above referring to 'dry' and 'wet,' let us note that the effective water vapor amounts for Chad and Bolivia are as given in Table 3.12. Thus, 'dry' means having effective water vapor content less than  $\sim 0.2$  g/cm<sup>2</sup> and 'wet' means having effective water vapor content larger than  $\sim 1.7$  g/cm<sup>2</sup>.

Table 3.12

Effective water vapor amounts in g/cm<sup>2</sup> in upper ( $\sigma = 0$  to  $\sigma = 1/2$ ) and lower ( $\sigma = 1/2$  to  $\sigma = 1$ ) levels for Chad and Bolivia, for pressure scaling factors ( $\alpha$ ) of 0.6 to 1.0 and for ATRAD.

	CHAD		BOLIVIA	
	Upper	Lower	Upper	Lower
'NK' $\sigma = 0.6$	0.01715	0.15294	0.10267	2.00645
'OK' $\sigma = 1.0$	0.01217	0.13775	0.07249	1.73746
ATRAD $\alpha = 0.9$	0.01341	0.13538	0.07983	1.76058

In view of the fact that the IR seems to be in fairly good shape for clear-sky situations, if the newer Katayama treatment is used, the main difficulty in predicting clear-sky heating rates centers around the absorption of solar radiation in the atmosphere. In order to localize the source of the error, we first checked the Katayama model assumption that Rayleigh scattering could be ignored for  $\lambda > 0.9\mu$ . For the spectral interval  $3360 - 11,000$  cm<sup>-1</sup> for the Chad problem, we found that ignoring Rayleigh scattering increased all the net fluxes by 0.5 watts/m<sup>2</sup> and did not affect the heating rates

at all. This is truly a negligible effect, although a more thorough study might show a marginally non-negligible effect, perhaps at high albedos and/or low sun angles. Similarly, an examination of ATRAD runs with and without ozone (Tables 3.10 and 3.11) showed that the largest solar flux difference change as a result of neglecting ozone was  $0.9 \text{ watts/m}^2$ , which cannot begin to account for the errors in solar heating rate. The only other important absorbers in the solar spectrum beside ozone are water vapor and  $\text{CO}_2$ . Thus, the Katayama model errors must be due to some combination of the following causes:

- (1) the parameterization of the absorption of solar down-flux by water vapor [Eq. (3.26)];
- (2) the neglect of the absorption of the surface-reflected solar up-flux;
- (3) the neglect of  $\text{CO}_2$  absorption.

A comparison of the solar up- and down-flux differences for Chad and Bolivia is presented in Table 3.13. We have broken these results down further into  $\lambda < 0.9\mu$  and  $\lambda > 0.9\mu$  values, but this breakdown is rather artificial since as we have shown in Eqs. (3.28) and (3.29) the Katayama parameterization is independent of any partitioning of the solar spectrum. The breakdown is shown primarily to illustrate the error incurred if one were to lump all absorption into  $\lambda > 0.9\mu$ .

The salient facts which emerge from Table 3.13 are:

- (1) there is a fundamental disagreement between ATRAD and the Katayama parameterization of absorbed solar flux [Eqs. (3.28) and (3.29)] whether or not we include the absorbed near IR ( $\lambda > 0.9\mu$ ) up-flux and absorbed 'visible' ( $\lambda < 0.9\mu$ ) flux; (2) the absorbed near-IR up-flux is at most an 8%

Table 3.13

Flux differences (watts/m<sup>2</sup>) in the near-IR (2640 - 11,120 cm<sup>-1</sup>) and 'visible' (11,120 - 48,500 cm<sup>-1</sup>) for the Chad and Bolivia problems. Near-IR values are broken down into contributions from up-flux and down-flux. ATRAD with no ozone (unparenthesized) predictions are compared with Katayama model (parenthesized) predictions.

		CHAD	
		$\sigma=0$ to 1/2	$\sigma=1/2$ to 1
(1)	2640 - 11,120 cm <sup>-1</sup> , down	29.2 (24.6)	41.6 (35.9)
(2)	2640 - 11,120 cm <sup>-1</sup> , up	0.1 (0)	4.1 (0)
(3)	11,120 - 48,500 cm <sup>-1</sup>	1.8 (0)	2.6 (0)
	Solar [(1)+(2)+(3)]	31.2 (24.6)	48.3 (35.9)

		BOLIVIA	
		$\sigma=0$ to 1/2	$\sigma=1/2$ to 1
(1)	2640 - 11,120 cm <sup>-1</sup> , down	36.4 (29.9)	41.7 (58.0)
(2)	2640 - 11,120 cm <sup>-1</sup> , up	-0.1 (0)	0.9 (0)
(3)	11,120 - 48,500 cm <sup>-1</sup>	1.7 (0)	5.1 (0)
	Solar [(1)+(2)+(3)]	38.0 (29.9)	47.6 (58.0)

effect (in the Chad lower level) but may be decidedly non-negligible for dry problems with albedos substantially larger than the 0.20 of Chad; and (3) the absorbed 'visible' flux is at most an 11% effect (in the Bolivian lower level) and is thus marginally negligible. Clearly there are fundamental difficulties with the function  $A(u^*, \mu_0)$  of Eq. (3.26); it simply causes too much absorption in wet levels and not enough in dry ones. The simplified model which we shall present below offers an attractive alternative in the search for a replacement for  $A$ . Also, we shall comment on the possibility of simply improving on  $A$  itself, by changing its parameters.

The simple model to which we refer ignores Rayleigh scattering and thermal emission in the spectral region  $2640 - 11,120 \text{ cm}^{-1}$ . ATRAD calculations have demonstrated that including Rayleigh scattering in this region produces a very small net flux decrease at all levels. The Planck function effect is even smaller, even for the high temperatures of Chad. Hence, the radiative transfer equation<sup>(1)</sup> reduces to

$$\mu \frac{\partial I_\nu}{\partial z} = - \alpha'_\nu(z) I_\nu \quad , \quad \nu \in [2640 - 11,120] \quad .$$

where  $\alpha'_\nu$  is the absorption coefficient. If the boundary condition at the top of the atmosphere is

$$I_\nu \Big|_{z=0} = S_\nu \delta(\vec{\Omega} - \vec{\Omega}_0)$$

(for solar flux  $S_\nu$ ) then the down-flux is simply

$$F_\nu^\downarrow = \mu_0 S_\nu \exp \left[ - \frac{1}{\mu_0} \int_0^z \alpha'_\nu(z) dz \right] \quad (3.33)$$

If an albedo  $\beta_v$  and diffuse reflection at the surface  $z = z_g$  are assumed, the up-flux is

$$F_v^\uparrow = 2\beta_v F_v^\downarrow(z_g) E_3 \left[ \int_z^{z_g} \alpha_v'(z) dz \right] \quad (3.34)$$

where  $E_3$  is the exponential integral of third degree. Equations (3.33) and (3.34) constitute a simple model for the near-IR when the atmosphere is aerosol-free. Calculations have so far been performed only with Eq. (3.33) in order to compare both with ATRAD and with the Katayama model.

The calculations for Eq. (3.33) were actually performed with the frequency-averaged form

$$F_{\Delta v}^\downarrow(z) = \mu_0 S_{\Delta v} T_{\Delta v}^{H_2O} \left[ u^*(0 \rightarrow z) / \mu_0 \right] T_{\Delta v}^{CO_2} \left[ w^*(0 \rightarrow z) / \mu_0 \right] \quad (3.35)$$

where

$$S_{\Delta v} = \frac{1}{\Delta v} \int_v^{v+\Delta v} S_v dv$$

(as estimated by cubic interpolation in Thekaekara's tables<sup>(8)</sup>) and where  $T_{\Delta v}$  is the transmission function for either water vapor, for vertical  $H_2O$  amount  $u^*(0 \rightarrow z)$  between 0 and  $z$ , or for vertical  $CO_2$  amount  $w(0 \rightarrow z)$ , taken from McClatchey, et al.<sup>(2)</sup> Using an interval  $\Delta v = 20 \text{ cm}^{-1}$ , the fluxes from Eq. (3.35) were summed across the entire spectral region 2640 - 11,120  $\text{cm}^{-1}$  to yield the results of Table 3.14. Calculations were made with and without  $CO_2$ . Comparison values of down-flux and down-flux difference are presented as predicted by ATRAD and by Katayama (Eqs. (3.26) and (3.29)). The ATRAD spectral

Table 3.14

2640 - 11,120 cm<sup>-1</sup> down-fluxes in watts/m<sup>2</sup> at the top of the atmosphere ( $F_{top}^{\downarrow}$ ) and at  $\sigma = 0, 1/2, \text{ and } 1$  ( $F_0^{\downarrow}, F_{1/2}^{\downarrow}, F_1^{\downarrow}$ ), and down-flux differences across the upper and lower levels ( $\Delta F_0^{\downarrow} - 1/2$  and  $\Delta F_{1/2}^{\downarrow} - 1$  respectively) for the Chad and Bolivia problems, as predicted by three different models [Eq. (3.35) with  $\Delta v = 20 \text{ cm}^{-1}$ , ATRAD and Katayama].

CHAD

	$F_{top}^{\downarrow}$	$F_0^{\downarrow}$	$F_{1/2}^{\downarrow}$	$F_1^{\downarrow}$	$\Delta F_0^{\downarrow} - 1/2$	$\Delta F_{1/2}^{\downarrow} - 1$
Equation (3.35), no CO <sub>2</sub>	416.3	414.1	386.4	344.8	27.7	41.6
Equation (3.35)	416.3	409.4	381.3	340.0	28.1	41.3
ATRAD	416.3	410.4	381.2	339.6	29.2	41.6
Katayama	408.7	401.6	377.0	341.1	24.6	35.9

BOLIVIA

	$F_{top}^{\downarrow}$	$F_0^{\downarrow}$	$F_{1/2}^{\downarrow}$	$F_1^{\downarrow}$	$\Delta F_0^{\downarrow} - 1/2$	$\Delta F_{1/2}^{\downarrow} - 1$
Equation (3.35), no CO <sub>2</sub>	223.7	221.4	185.3	143.2	36.1	42.1
Equation (3.35)	223.7	218.5	183.1	141.3	35.3	41.8
ATRAD	223.7	219.4	183.0	141.3	36.4	41.7
Katayama	219.6	214.4	184.5	126.5	29.9	58.0

interval structure for these calculations was 2640(240) 4800(320) 8000(500) 11,000(120) 11,120  $\text{cm}^{-1}$ , so that the ATRAD frequency resolution was considerably coarser than that of Eq. (3.35). The predictions of Eq. (3.35) confirm the ATRAD predictions remarkably well, and in fact Table 3.14 furnishes an excellent validation of the exponential fitting idea upon which ATRAD is based. The residual differences between ATRAD and Eq. (3.35) must be partly due to Rayleigh scattering, partly due to the approximation of  $T_{\Delta v}$  by an exponential sum in ATRAD, and partly due to ATRAD's coarser spectral resolution. Removing  $\text{CO}_2$  from the atmosphere causes the near-IR down-flux to change by at most  $1 - 1 - \frac{1}{2}\%$ , and the largest tropospheric change in down-flux difference is 0.8 watt/m<sup>2</sup>. The primary impact of  $\text{CO}_2$  in the near-IR is to change the stratospheric heating, which is grossly mis-estimated if only water vapor is considered. Note that the inclusion of  $\text{CO}_2$  in the model of Eq. (3.35) actually decreases the heating rate due to near-IR down-flux in the upper and lower Bolivian and lower Chad levels. This points up the unreliability of simple intuition in complex radiative transfer problems. The only reliable intuitive deduction is that the fluxes must decrease when the effects of  $\text{CO}_2$  are added, and Table 3.14 of course bears this out. In the discussion of the solar absorption function A which follows, the Eq. (3.35) predictions without  $\text{CO}_2$  shall be used as benchmark values.

None of the results of Table 3.14 contradict the observation, made in connection with Table 3.13, that the function A [Eq. (3.26)] is deficient in both wet and dry situations. An obvious direction one might take in order to improve the parameterization would be to study the predictions of the simple model Eq. (3.35) and derive a new empirical function to replace A. In the long run, this will be the only satisfactory way to proceed. Undoubtedly, this new function should be of a tabular nature in order to eliminate

the computing costs associated with analytic functions like Eq. (3.26).

In the shorter term, however, it would be desirable to re-parameterize  $A$  in order to make it more accurate. There are three possible ways to do this: (1) change the definition of  $u^*$ ; (2) change the coefficient (0.187); and (3) change the exponent (0.303). As far as changing  $u^*$  goes, although there are infinitude of exotic formulas one might consider, we shall restrict ourselves to observing what change in the pressure scaling factor  $\alpha$  (see Eq. (3.24)) would improve matters. But we already have sufficient information at hand in Table 3.10 and 3.11 to observe how changing  $\alpha$  from 1.0 (parenthesized 'NK' values) to 0.6 (unparenthesized 'NK' values) affects the absorbed solar flux. The conclusion one is forced to draw is that there is no net gain with  $\alpha = 0.6$  - the results in both the Chad and Bolivia upper levels are slightly improved, in both lower levels slightly worse. Furthermore, the changes in Katayama's model solar absorption resulting from varying  $\alpha$  are much too small to offer any hope that agreement with ATRAD can be obtained in this fashion.

Next we consider if  $A$  can be improved by changing its exponent. To this end, we present in Table 3.15 calculations of the upper and lower level flux differences ( $\Delta_1$  and  $\Delta_3$ ) from Eqs. (3.28) and (3.29) with varying exponent. The values of  $u^*$  used are those of the 'OK' model in Table 3.12. For Chad, a value of the exponent between 0.25 and 0.303 would lead to agreement of  $\Delta_1$  with Eq. (3.35), but the value of  $\Delta_3$  would be made worse thereby. On the other hand, there is no exponent which would lead to agreement of  $\Delta_3$  with Eq. (3.35); the maximum  $\Delta_3$  attainable by varying the exponent (36.3 watts/m<sup>2</sup>) is still 12% below the Eq. (3.35) value. As for Bolivia, there is no exponent which will bring  $\Delta_1$  into agreement with Eq. (3.35); no

Table 3.15

Predictions of Eqs. (3.28) and (3.29) for solar flux differences (watts/m<sup>2</sup>) across upper ( $\Delta_1$ ) and lower ( $\Delta_3$ ) layers as we vary the exponent from the Katayama value of 0.303, for Chad and Bolivia problems. The predictions of Eq. (3.35) are included for comparison.

CHAD			BOLIVIA		
Exponent	$\Delta_1$	$\Delta_3$	Exponent	$\Delta_1$	$\Delta_3$
0.10	29.2	21.3	0.10	23.8	19.4
0.15	31.7	27.6	0.15	28.4	28.9
0.20	30.8	31.8	0.20	30.4	38.3
0.25	28.1	34.4	0.215	30.6	41.2
0.303	24.6	35.9	0.25	30.7	47.9
0.325	23.1	36.2	0.303	29.9	58.0
0.35	21.4	36.3	0.325	29.4	62.3
0.375	19.7	36.3	0.35	28.7	67.2
0.40	18.1	36.1	0.40	27.0	77.1
0.45	15.1	35.4	0.50	23.4	97.8
0.50	12.6	34.3	0.60	19.9	120.0
0.60	8.5	31.4			
Equation (3.35)	27.7	41.6	Equation (3.35)	36.1	42.1

matter how we vary the exponent,  $\Delta_1$  remains at least 15% too small. However, an exponent of about 0.215 will force  $\Delta_3$  into agreement with Eq. (3.35), and this exponent also leads to a slightly better value of  $\Delta_1$ . But an exponent of 0.215 leads to definitely worse values of  $\Delta_1$  and  $\Delta_3$  for Chad. Hence, there seems to be no exponent which is consistently better than 0.303.

Next, we ask if any value of the coefficient of  $A$  would be better than 0.189. But the error we are dealing with is not monosigned. A larger coefficient is needed for levels with a small amount of water vapor, and vice versa.

Finally, there remains the possibility that some judicious variation of both the coefficient and exponent might improve  $A$ . The exponent first must be changed so that all the errors are monosigned, then the coefficient changed to bring  $A$  into agreement with Eq. (3.35). An examination of Table 3.15 reveals that  $\Delta_3$  for Chad can never be larger than 36.3 watts/m<sup>2</sup> (and needs to be 41.6 watts/m<sup>2</sup>) and that  $\Delta_1$  for Bolivia can never exceed 30.7 watts/m<sup>2</sup> (and needs to be 36.1 watts/m<sup>2</sup>) no matter how we vary the exponent. Thus, the exponent can be varied so that all values of  $\Delta_1$  and  $\Delta_3$  are less than Eq. (3.35) predictions, but not vice versa. In order to make  $\Delta_3$  for Bolivia less than 42.1 watts/m<sup>2</sup>, the exponent must be less than  $\sim 0.215$ . But for exponents  $< 0.215$ , we find  $\Delta_1 \geq \Delta_3$  (roughly) for Chad so that no coefficient adjustment could ever produce agreement with Eq. (3.35).

Thus, the resolution of the difficulty really awaits the creation of the new tabular function of which we spoke earlier.

### 3.3 ATRAD COMPARED WITH KATAYAMA MODEL FOR ARCTIC STRATUS PROBLEM

The Arctic stratus problem was discussed in detail in Section 3.1. We continue that discussion here by briefly

comparing some of the Katayama model cloudy-sky approximations against ATRAD.

### 3.3.1 Scattering in the IR

It is assumed in the Katayama model, and indeed by practically all extant radiation models, that scattering in the IR can be neglected. However, until the advent of ATRAD, no model was capable of actually checking this assumption, for the combined line absorption-scattering problem was viewed as insuperable. As a start towards examining this assumption quantitatively, therefore, two ATRAD calculations were made for the IR ( $60 - 1920 \text{ cm}^{-1}$ ) spectral region for the Arctic stratus problem. The first included Mie scattering in the normal fashion, the second was identical to the first in all respects save that the Mie scattering coefficient (but not the Mie absorption coefficient) was set to zero. Selected results from these calculations for down-flux, up-flux, net flux, and heating rate (flux difference) are presented in Table 3.16. The impact of ignoring scattering may be summarized as follows:

- (a) the down-flux below the cloud is decreased by  $1.5 \text{ watts/m}^2$ , or 0.5%; above the cloud, it is unchanged;
- (b) the up-flux above the cloud is increased by  $1-2 \text{ watts/m}^2$ , or 0.5%; below the cloud, it is unchanged;
- (c) the net flux becomes more negative by  $1.1-2.2 \text{ watts/m}^2$ ;
- (d) heating rates are unaffected except in the cloud (0.7%) and immediately above the cloud (3.3%).

Table 3.16

Comparison between ATRAD predictions for down-flux  $F\downarrow$ , up-flux  $F\uparrow$ , net flux  $F$ , and net flux differences  $\Delta F$  (all in  $\text{watts/m}^2$ ) as a function of altitude  $z$  (km) and pressure  $p$  (mb) for  $60 - 1920 \text{ cm}^{-1}$  for the Arctic stratus problem. Unparenthesized values are for full Mie treatment and parenthesized values are for Mie scattering zeroed out. (The cloud is located between 0.5 and 1.0 km,  $T_g = 273^\circ\text{K}$  except where noted.)

$z$	$p$	$F\downarrow$	$F\uparrow$	$F$
0.0	1012.5	327.5 (326.0)	311.7 (311.7)	15.8 ( 14.2)
0.5	951.9	323.9 (322.3)	322.4 (322.4)	1.5 ( -0.1)
1.0	895.0	236.7 (236.5)	322.0 (324.0)	-85.3 ( -87.5)
2.0	790.2	210.1 (210.1)	316.4 (318.0)	-106.4 (-107.9)
5.0	536.7	127.5 (127.5)	244.8 (246.0)	-153.7 (-155.0)
10.0	262.6	43.7 ( 43.7)	244.8 (246.0)	-201.1 (-202.3)
50.0	1.0	1.2 ( 1.2)	245.5 (246.6)	-244.3 (-245.4)

$\Delta z$	$\Delta F$	$\Delta F (T_g = 300^\circ\text{K})$
0.0 - 0.5	-14.3 (-14.3)	65.2
0.5 - 1.0	-86.8 (-87.4)	-31.3
1.0 - 2.0	-21.1 (-20.4)	-20.7
2.0 - 5.0	-47.3 (-47.1)	-47.1
5.0 - 10.0	-47.4 (-47.3)	-47.2
10.0 - 50.0	-43.2 (-43.1)	-43.0

Thus, the neglect of Mie scattering is borne out extremely well for water clouds at least as optically thick as the Arctic stratus cloud. The strong absorption due to liquid water in the IR is, of course, responsible for the suppression of scattering in the cloud, and thus this result might not apply to an aerosol material with transmission windows in the IR. It may also be inapplicable to optically thin clouds, particularly cirrus.

### 3.3.2 Sensitivity to Surface Temperature

Because of the large inaccuracies involved in the computation of the Mintz-Arakawa surface temperature  $T_g$ ,<sup>(7)</sup> it is of interest to assess the sensitivity of radiative heating and cooling rates in the atmosphere to this parameter. A normal ATRAD calculation of the Arctic stratus problem for  $60 - 1920 \text{ cm}^{-1}$ , with  $T_g = 273^\circ\text{K}$  was, therefore, compared with a similar calculation with  $T_g = 300^\circ\text{K}$ . In the first case, the surface is  $\sim 5^\circ\text{K}$  colder than the cloud-to-ground layer and  $\sim 3^\circ\text{K}$  colder than the cloud; in the second case, the surface is  $\sim 22^\circ\text{K}$  warmer than the cloud-to-ground layer and  $\sim 24^\circ$  warmer than the cloud. The changes in heating rate between the two cases may be observed in Table 3.16. The cloud-to-ground layer, which was cooling for  $T_g = 273^\circ$ , is heating for  $T_g = 300^\circ$ , and at almost five times the rate at which it was formerly cooling. The cloud is cooling in both cases, but only one-third as rapidly for  $T_g = 300^\circ$  as for  $T_g = 273^\circ$ . The cooling of all levels above the cloud is practically unchanged, so that the cloud effectively shields these upper levels from the effects of a surface temperature change. In spite of this shielding, however,  $\Delta F$  for 0 to 5 Km is  $-169.5 \text{ watts/m}^2$  for  $T_g = 273^\circ\text{K}$  and  $-33.9 \text{ watts/m}^2$  for  $T_g = 300^\circ\text{K}$ , so that the cooling of the

whole lower half of the atmosphere is dramatically reduced (by a factor of 5) as a result of a 10% increase in surface temperature.

These results establish the sensitivity of IR heating and cooling to surface temperature. There is very little point in having a reasonably sophisticated IR treatment in the Mintz-Arakawa GCM if it is only to be coupled with an inadequate predictive scheme for  $T_g$ .

### 3.3.3 Cloud Albedo

A quantity which is required in all the Katayama parameterizations relating to clouds is the cloud albedo,  $\alpha_c$ . In the 'OK' model  $\alpha_c$  is always either 0.6 or 0.7. In the 'NK' model  $\alpha_c$  assumes different values for  $\lambda > 0.9\mu$  and  $\lambda < 0.9\mu$ , and ranges all the way from 0.19 (for high cloud) to 0.76 (for cumulonimbus cloud). For low cloud, into which class the Arctic stratus cloud must fall, the 'NK' model assumes  $\alpha_c = 0.66$  for  $\lambda < 0.9\mu$  and  $\alpha_c = 0.50$  for  $\lambda > 0.9\mu$ .

Section 3.1 contained an extensive discussion of cloud albedo, particularly as it related to surface fluxes. A model was developed for cloud 'albedo' ( $F_{ct}^\uparrow/F_{ct}^\downarrow$ ) as it would actually be observed, as a function of surface albedo  $\beta$ . Only for  $\beta = 0$  do we recover the actual cloud albedo  $\alpha_c$ , which is an intrinsic property of the cloud, from a measurement of  $F_{ct}^\uparrow/F_{ct}^\downarrow$  (ct = cloud top). The Katayama model does not include this dependence on  $\beta$ , nor indeed does it include any dependence on droplet concentration, cloud thickness, and solar elevation  $\theta_s$ . ATRAD is an ideal vehicle for studying these various dependencies with a view to parameterizing them. As an example, consider the results

of Table 3.17, in which the variation of  $F_{ct}^{\uparrow}/F_{ct}^{\downarrow}$  over a limited range of sun angles and albedos is shown. It is important to remember that all of these albedo values are for exactly the same cloud. The hopelessness of approximating cloud 'albedo' as a single number, rather than a function of several parameters, is brought home with particular force here. We feel that the lack of a parameterization for cloud albedo in the Katayama model is its most serious deficiency for cloudy-sky situations. Until such a parameterization is obtained, the other formulas in the Katayama model which use cloud 'albedo' can only be believed insofar as they have a certain climatological correctness built into them.

Table 3.17

The ATRAD-predicted ratio of up-flux at the cloud-top ( $F_{ct}^{\uparrow}$ ) to down-flux at the cloud top ( $F_{ct}^{\downarrow}$ ) for the Arctic stratus problem, for various values of solar elevation  $\theta_s$  and surface albedo  $\beta$ . Unparenthesized values are for the full spectral interval  $3600 - 48,500 \text{ cm}^{-1}$ . The first parenthesized value refers to  $3600 - 11,000 \text{ cm}^{-1}$  only, the second parenthesized value refers to  $11,000 - 48,500 \text{ cm}^{-1}$  only.

$F_{ct}^{\uparrow}/F_{ct}^{\downarrow}$			
$\beta \backslash \theta_s$	20°	30°	40°
0.	0.52 (0.52,0.52)	0.44 (0.44,0.44)	0.37 (0.36,0.38)
0.20	0.58 (0.57,0.58)	0.51 (0.49,0.52)	0.45 (0.43,0.46)
0.58	0.72 (0.69,0.74)	0.68 (0.64,0.70)	0.64 (0.59,0.66)
0.79	0.83 (0.78,0.85)	0.80 (0.74,0.83)	0.78 (0.71,0.81)

### 3.3.4 Albedo of a Cloudy Atmosphere

Presume that we know the cloud albedo

$$R' = \frac{F_{ct}^{\uparrow}}{F_{ct}^{\downarrow}}$$

for  $\lambda < 0.9\mu$ . Then let us enquire into the accuracy of the Katayama approximation

$$\alpha_{atm} = 1 - (1-R')(1-\alpha_0) \quad (3.36)$$

for the albedo  $\alpha_{atm}$  of the whole atmosphere in the presence of a single cloud layer.  $\alpha_0$  is the albedo of the corresponding clear atmosphere due to Rayleigh scattering, and is approximated as in Eq. (3.31) by the Katayama model. In Table 3.18 are assembled values of  $\alpha_{atm}$  for the Arctic stratus problem as predicted by ATRAD and by Eq. (3.36) for the spectral region 11,000 - 48,500  $\text{cm}^{-1}$ . The large error in the formula (3.36) is clearly apparent. In these examples, Eq. (3.36) seriously overestimates the cloudy atmospheric albedo, whether one compares it with the ATRAD value at the top of the atmosphere (1 mb) or at 167 mb (the difference in the ATRAD values at 1 mb and 167 mb is due to Rayleigh scattering and ozone absorption between the two levels). Our parameter studies have not been extensive enough, however, to say with certainty whether Eq. (3.36) always overestimates the cloudy atmospheric albedo. One interesting observation, however, is that the error cannot be laid on the approximation (3.31) for  $\alpha_0$ . According to the unpublished Katayama manuscript describing the new model, the correct  $\alpha_0$  should be even larger than Eq. (3.31) predicts for  $\theta_s = 33.6^\circ$ .

Table 3.18

Comparisons of cloudy atmospheric albedo  $\alpha_{\text{atm}}$  as calculated by Eq. (3.36) (using the  $R'$  values shown) and by ATRAD at 1 mb and 167 mb, for 11,000 - 48,500  $\text{cm}^{-1}$  for the Arctic stratus problem with surface albedo  $\beta = 0$  and various values of solar elevation  $\theta_s$ .

$\theta_s$	$R'$ (ATRAD)	$\alpha_{\text{atm}}$ (Eq. 3.36)	$\alpha_{\text{atm}}$ (1 mb) (ATRAD)	$\alpha_{\text{atm}}$ (167 mb) (ATRAD)
20°	0.5162	0.612	0.497	0.534
30°	0.4438	0.531	0.430	0.459
40°	0.3758	0.457	0.369	0.391

Thus, at least for the  $\theta_s = 30^\circ$  case in Table 3.18, the prediction of  $\alpha_{\text{atm}}$  in Eq. (3.36) would be even worse if the correct  $\alpha_o$  were used.

It need hardly be emphasized that significant errors in  $\alpha_{\text{atm}}$  have serious consequences for the prediction of climate. Even simple global climatic models, such as that of Buđyko,<sup>(9)</sup> point up the sensitivity of the Earth's surface temperature to fluctuations in the atmospheric albedo.

## 4. HAIFA CODE MODIFICATIONS

While no new physical phenomena were added to the HAIFA codes, two previously described models were further tested and reworked to both improve and correct prior prescriptions. These modifications, which had been previously included in the codes but had not been thoroughly checked out, were used in the calculations of flow over the Sierra Nevada range in the area of the Owens Valley. The results of these calculations are shown in Section 5 of this report. The modifications are described below.

### 4.1 TRIANGULAR ZONES

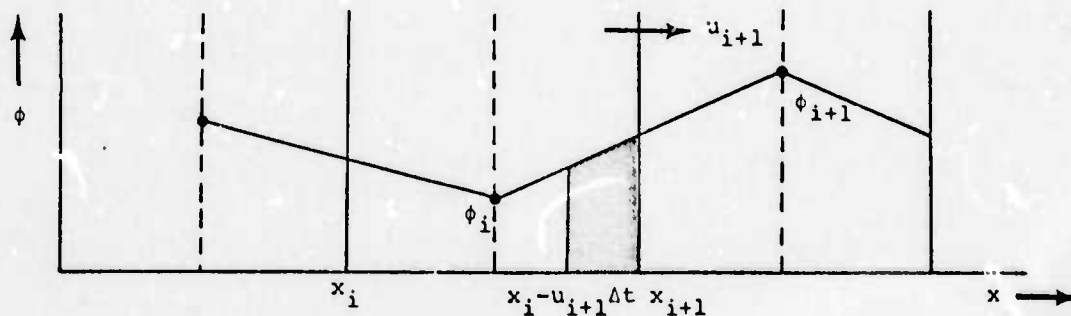
In order that sloping boundaries, such as mountain slopes, be more accurately characterized in the HAIFA code, triangular zones were previously introduced.<sup>(10)</sup> During testing of this scheme, errors were found in the formulation and corrected. The new formulation follows.

The addition of non-rectangular zones to the grid requires alteration of the code in three major areas. The Crowley advection scheme must be modified to include flow between rectangular and triangular zones. The Poisson solver must consider calculation of node-centered vorticities in the presence of triangular zones. Finally, needed space derivatives must be appropriately approximated in regions near triangular zones.

The practice of using triangular zones requires assumptions concerning the nature of the flow through the zone boundaries. We have assumed in this case that the flux is uniform along the unobstructed boundaries with all cell centered quantities located at the centroids of the cells. Clearly, there are other assumptions concerning the location for the cell centered quantities which could be made. These two assumptions, however, allow a simple adaptation of the flux scheme which seems to give qualitatively reasonable results. This scheme needs further testing, however, and further modifications may be required.

For completeness, the Crowley advection scheme<sup>(11)</sup> is described below for the case of rectangular zones. The case of triangular zoning follows immediately with results for left facing and right facing slopes presented. Since the Crowley scheme utilizes the splitting technique in which spatial dimensions are calculated sequentially, the scheme is derived for the one-dimensional case, it being a trivial matter to extend to two dimensions.

Assuming that the dynamic variable  $\phi$  varies linearly between cells we obtain the following pictorial representation:



where the ordinate represents the variable  $\phi$ , whose distribution is given by the piecewise continuous diagonal line. This assumption results in Crowley's second-order scheme. If  $\phi$  were fitted to a cubic between cells, the fourth-order scheme would be realized. The vertical bars represent cell boundaries in  $x$ , while the dashed lines indicate cell midpoints. The shaded area represents the material advected out of face  $x = x_{i+1}$  in a time  $\Delta t$ . The flux through this boundary is given by:

$$\begin{aligned}
 F_{i+1} &= \frac{1}{\Delta t} \int_{x_{i+1} - u_{i+1} \Delta t}^{x_{i+1}} \phi(x) dx = \frac{1}{\Delta t} \int_{x_{i+1} - u_{i+1} \Delta t}^{x_{i+1}} (a + bx) dx, \\
 &= \frac{1}{\Delta t} \left( ax + \frac{b}{2} x^2 \right) \Big|_{x_{i+1} - u_{i+1} \Delta t}^{x_{i+1}}, \\
 &= a u_{i+1} + b x_{i+1} u_{i+1} - \frac{b}{2} u_{i+1}^2 \Delta t. \quad (4.1)
 \end{aligned}$$

Under the assumption of linearity:

$$\begin{aligned}
 \phi_i &= a + b x_{i+1/2} & b &= \frac{\phi_{i+1} - \phi_i}{x_{i+3/2} - x_{i+1/2}} \\
 & & \text{or} & \\
 \phi_{i+1} &= a + b x_{i+3/2} & a &= \phi_i - b x_{i+1/2}
 \end{aligned} \quad (4.2)$$

For a constant  $\Delta x$ :

$$x_{i+1/2} = x_i + \Delta x/2,$$

$$x_{i+3/2} = x_{i+1} + \Delta x/2 \quad , \quad (4.2)$$

and

$$x_{i+3/2} - x_{i+1/2} = \Delta x \quad .$$

Plugging in for  $a$  and  $b$  the flux becomes:

$$F_{i+1} = \frac{1}{2}(\phi_i + \phi_{i+1}) u_{i+1} - \frac{1}{2}(\phi_{i+1} - \phi_i) u_{i+1}^2 \frac{\Delta t}{\Delta x} \quad (4.4)$$

defining

$$\alpha = u_{i+1} \frac{\Delta t}{\Delta x} \quad ,$$

we have

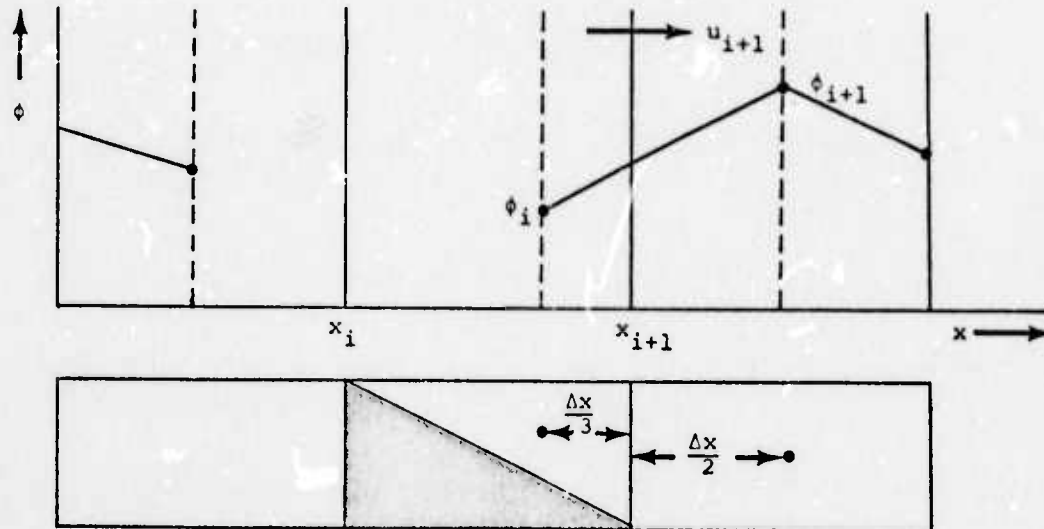
$$F_{i+1} \frac{\Delta t}{\Delta x} = \frac{\alpha}{2}(\phi_{i+1} + \phi_i) - \frac{\alpha^2}{2}(\phi_{i+1} - \phi_i) \quad . \quad (4.5)$$

Finally:

$$(\phi_i^{n+1} - \phi_i^n) = - \frac{\Delta t}{\Delta x} (F_{i+1} - F_i) \quad (4.6)$$

which is Crowley's result.

Upon introduction of triangular zones, the assumption of constant  $\Delta x$  is no longer valid. The scheme is altered as follows for a right facing zone:



The scheme is identical to the above case up to the assumption of linearity. We now have:

$$\phi_i = a + b x_{i+2/3} \quad b = \frac{\phi_{i+1} - \phi_i}{x_{i+3/2} - x_{i+2/3}}$$

or

$$\phi_{i+1} = a + b x_{i+3/2}$$

and

$$x_{i+3/2} - x_{i+2/3} = \frac{5}{6} \Delta x \quad (4.7)$$

Upon substitution for a and b we have:

$$F_{i+1} = \left( \frac{3}{5} \phi_i + \frac{2}{5} \phi_{i+1} \right) u_{i+1} - \frac{3}{5} (\phi_{i+1} - \phi_i) u_{i+1}^2 \frac{\Delta t}{\Delta x} \quad (4.8)$$

defining

$$\alpha = u_{i+1} \frac{\Delta t}{\Delta x}$$

then

$$F_{i+1} \frac{\Delta t}{\Delta x} = \frac{2\alpha}{5} (\phi_{i+1} + 1.5\phi_i) - \frac{3\alpha^2}{5} (\phi_{i+1} - \phi_i) \quad (4.9)$$

Finally:

$$(\phi_i^{n+1} - \phi_i^n) = - \frac{\Delta t}{\Delta x} (F_{i+1} - F_i) \quad (4.10)$$

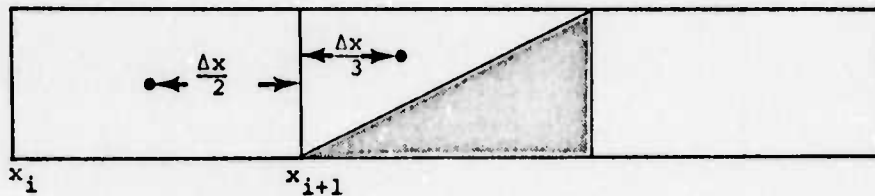
For the case of the left facing zone a similar derivation results in

$$F_{i+1} \frac{\Delta t}{\Delta x} = \frac{2\alpha}{5} (1.5\phi_{i+1} + \phi_i) - \frac{3\alpha^2}{5} (\phi_{i+1} - \phi_i) \quad (4.11)$$

and

$$(\phi_i^{n+1} - \phi_i^n) = - \frac{\Delta t}{\Delta x} (F_{i+1} - F_i) \quad (4.12)$$

where the reference grid is



The fact that adjacent cells in this derivation have centered values which are spatially non-aligned in the complementary dimension was ignored. The effect of this neglect is not negligible (on the order of 10 percent), but the law of diminishing returns applies.

Another necessary modification to the HAIFA code occurs in the Poisson solver routine. Specifically, the Poisson solver requires node-centered vortices in its solution for the stream function. Normally, the vorticity is carried as a cell-centered quantity so that it may be easily handled in the vorticity transport equation, and converted via an

averaging process when the Poisson solver is called. With the introduction of triangular zones, this averaging process must be altered. Utilizing Figure 4.1 we define the following:

$$D = (\Delta x^2 + \Delta z^2)^{1/2} / 2 ,$$

and

$$B = \frac{2}{3} D .$$

Using these quantities, one performs a weighted averaging process on the four cell centered vorticities surrounding the point  $i,j$ .

We have

$$\begin{aligned} \eta_{i,j} &= \left( \frac{\eta_1}{D} + \frac{\eta_2}{D} + \frac{\eta_3}{D} + \frac{\eta_4}{B} \right) / \left( \frac{3}{D} + \frac{1}{B} \right) \\ &= 0.222(\eta_1 + \eta_2 + \eta_3) + 0.333 \eta_4 \end{aligned} \quad (4.13)$$

No further alteration of the Poisson solver is needed.

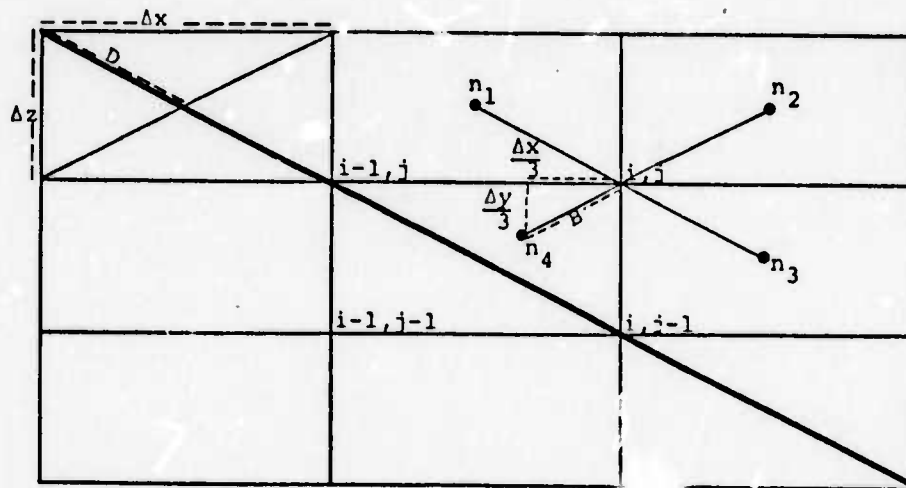
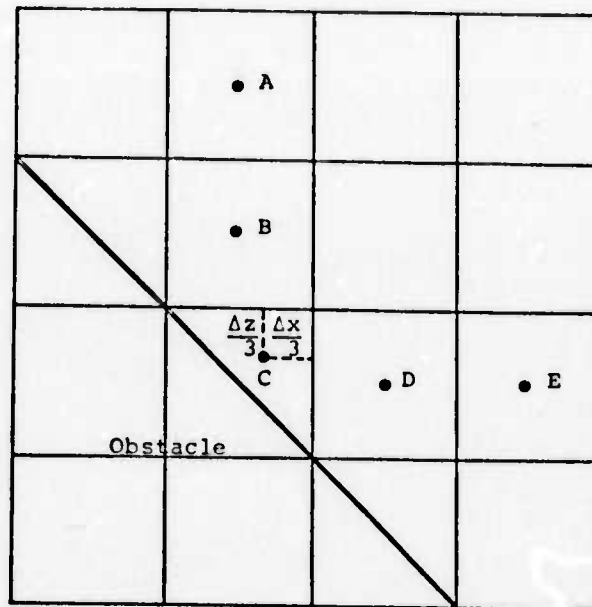


Figure 4.1 Determination of node centered vorticity.

The final code alteration needed to effect incorporation of triangular zones is in the method of calculating the needed space derivatives. In the figure below, space derivatives calculated for cells B, C and D will be affected by the presence of triangular zone C.



The approximations used by HAIFA are summarized below, where  $\phi$  is any dynamic variable:

$$\frac{\partial \phi_C}{\partial x} = (\phi_D - \phi_C) / \frac{5}{6} \Delta x \quad , \quad \frac{\partial \phi_C}{\partial y} = (\phi_B - \phi_C) / \frac{5}{6} \Delta z$$

$$\frac{\partial \phi_D}{\partial x} = (\phi_E - \phi_C) / \frac{11}{6} \Delta x \quad , \quad \frac{\partial \phi_B}{\partial y} = (\phi_A - \phi_C) / \frac{11}{6} \Delta z. \quad (4.14)$$

Again, the spatial misalignment of the cell-centered quantities has been neglected in order to facilitate the calculation. Results have shown that this neglect does not noticeably affect the solution.

#### 4.2 THE HAIFA CODE

In recent months, the hydrodynamic equations of the dry and moist versions of HAIFA have been changed; the dry equations being rendered in a form yielding a more numerically accurate solution, and the moist equations being corrected.

The changes in the equations to their present form are presented below. The nomenclature is the same as that used in the referenced reports.

#### 4.2.1 The Dry Equations

The vorticity and streamline equations are essentially unchanged since previously reported.<sup>(10)</sup> The energy equation, however, is rendered in a more elegant form. The definition of  $T$  has been modified to include the work term.

$$T' = T + \Gamma z \quad (4.15)$$

places the energy equation in the form

$$\frac{DT'}{Dt} = K_T \nabla^2 (T' - \Gamma z) \quad (4.16)$$

where

$$\frac{D}{Dt} = \frac{\partial}{\partial t} + u \frac{\partial}{\partial x} + w \frac{\partial}{\partial z} .$$

This has advantages in the numerical treatment in that the term is calculated in the second-order Crowley advection scheme, resulting in greater accuracy of the solution. For ease of data interpretation, the temperature,  $T$ , is also normalized to a base value  $T_0$  in the HAIFA calculation.

#### 4.2.2 The Moist Equation

The derivation of the hydrodynamic equation set for HAIFA, including the effects of moisture, has been previously reported.<sup>(10,12)</sup> Significant evolutionary changes have occurred in the past few months, however, resulting in a more rigorous treatment and a markedly different equation set.

The terms which have been modified are: (1) the effects of moisture on the buoyancy term in the momentum equation; (2) the correction in the perfect gas equation of state due to moisture; (3) the energetic effects of condensation and evaporation of water vapor, specifically the release and absorption of the latent heat of vaporization to the surrounding air. The above areas carry an implicit assumption regarding the distribution of the moisture; hence equations describing the conservation of the moisture variables must be included in the set. Several authors have developed moisture equation sets. (13,14,15) The one that has been used in HAIFA most closely matches that of Liu and Orville. (15)

The momentum equations and the equation of state for a system with moisture as previously reported are:

$$\frac{Du}{Dt} = - \frac{1}{\rho_0} \frac{\partial P}{\partial x} + F_x ,$$

$$\frac{Dw}{Dt} = - \frac{1}{\rho_0} \frac{\partial P}{\partial z} - g(1 + \ell) + F_z ,$$

and

$$P = \rho RT(1 + Er) ,$$

where

$$\ell = \ell_c + \ell_r \text{ total liquid water content} \\ \text{(kg H}_2\text{O/kg air),}$$

$$\ell_c = \text{cloud water content (kg H}_2\text{O/kg air),}$$

$$\ell_r = \text{rain water content (kg H}_2\text{O/kg air),}$$

$$r = \text{specific humidity (kg H}_2\text{O/kg air),}$$

$$\rho = \text{density of humid air,}$$

$$T = \text{air temperature,}$$

$$F_x, F_y = \text{friction terms,}$$

and

$$E = \frac{\text{(molecular weight of air/molecular weight of H}_2\text{O)} - 1}{1}$$

These equations can be combined to yield a vorticity equation of the form:

$$\frac{D\eta}{Dt} = - \frac{g}{T_0} \frac{\partial T}{\partial x} + g \frac{\partial \ell}{\partial x} + k_m \nabla^2 \eta \quad (4.17)$$

where the Boussinesq approximation and the further restriction that  $T_0/T \approx 1$  have been utilized.

The energy equation for the moist system has been rewritten to include the  $\omega \Gamma$  term in the definition of  $T''$ :

$$T'' = T - T_0 + \frac{Lr}{C_p} + \Gamma z \quad (4.18)$$

This allows the energy equation to be written as

$$\frac{D}{Dt} T'' = k_T \nabla^2 (T'' - \Gamma z) \quad (4.19)$$

In addition to the vorticity and energy equations, the conservation of total water or moisture must be expressed. The atmosphere moisture can be divided into three distinct categories - moisture existing as water vapor, moisture existing as cloud water, and moisture existing as rain water. With this decomposition one may write the equation for total moisture conservation as follows:

$$\begin{aligned} \frac{\partial}{\partial t} (\rho Q) = & - \nabla \cdot (\rho r \vec{V}) - \nabla \cdot (\rho \ell_c \vec{V}) \\ & - \nabla \cdot \left[ \rho \int_D (\vec{V} - \vec{V}_D) \ell_r^D dD \right] + k_Q \nabla^2 \rho (r + \ell_c) \end{aligned} \quad (4.20)$$

where

$Q$  = total moisture content,

$\rho$  = density of dry air,

$\vec{V}_D$  = terminal velocity of rain drops of diameter  $D$ ,

$\vec{V}$  = wind velocity,

and

$k_Q$  = diffusivity for cloud water and water vapor.

The terms on the right express water vapor convergence, cloud water convergence, rain water convergence, and diffusion of vapor and cloud water.

Again, from conservation considerations, one may obtain another equation expressing rain water content.

$$\frac{\partial}{\partial t} (\rho l_r) = -\nabla \cdot [\rho \int_D (\vec{V} - \vec{V}_D) l_r^D dD] + \rho P_r \quad , \quad (4.21)$$

where  $P_r$  is a rain water production term described in a previous semi-annual report.<sup>(10)</sup> These two conservation equations may be subtracted to yield yet another, describing cloud water plus water vapor conservation.

$$\frac{D}{Dt} q = k_Q \nabla^2 q - P_r \quad , \quad \text{where } g = r + l_c \quad . \quad (4.22)$$

Equations (4.21) and (4.22) comprise the moisture set solved in HAIFA. At this point, however, (4.21) is in rather awkward form.

The rain water convergence term may be decomposed as follows:

$$\begin{aligned}
 -\nabla \cdot \rho \int_D (\vec{V} - \vec{V}_D) \ell_r^D dD &= -\nabla \cdot \rho \int_D \vec{V} \ell_r^D dD \\
 &\quad - \nabla \cdot \rho \int_D \vec{V}_D \ell_r^D dD
 \end{aligned} \tag{4.23}$$

but

$$\int_D \ell_r^D dD = \ell_r \tag{4.24}$$

Defining an average terminal velocity of the rain drops by

$$\vec{V}_T = \int_D \vec{V}_D \ell_r^D dD / \int_D \ell_r^D dD \tag{4.25}$$

Equation (4.23) becomes:

$$-\nabla \cdot \rho \int_D (\vec{V} - \vec{V}_D) \ell_r^D dD = -\nabla \cdot (\rho \ell_r \vec{V}) - \nabla \cdot (\rho \ell_r \vec{V}_T) \tag{4.26}$$

Substituting this result into the conservation Equation (4.21) we have:

$$\frac{\partial}{\partial t} (\rho \ell_r) = -\nabla \cdot (\rho \ell_r \vec{V}) - \nabla \cdot (\rho \ell_r \vec{V}_T) + \rho P_r \tag{4.27}$$

Expanding the right side with the realization that  $\vec{V}_T$  only operates in the vertical, we obtain the expression:

$$\frac{D}{Dt} \ell_r = V_T \frac{\partial \ell_r}{\partial z} + V_T \frac{\ell_r}{\rho} \frac{\partial \rho}{\partial z} + \ell_r \frac{\partial V_T}{\partial z} + P_r \tag{4.28}$$

where use of the continuity condition  $\frac{D}{Dt} \rho = 0$  has been made.

With this result, the equation set solved in the moisture version of HAIFA is complete. It is summarized below:

$$\frac{D}{Dt}\eta = + g \left( \frac{\partial \ell_r}{\partial x} + \frac{\partial \ell_c}{\partial x} \right) - \frac{g}{T_0} \frac{\partial T}{\partial x} + k_m \nabla^2 \eta, \quad (4.29)$$

$$\nabla^2 \psi = \eta, \quad (4.30)$$

$$\frac{D}{Dt}T'' = k_T \nabla^2 (T'' - \Gamma z), \quad (4.31)$$

$$\frac{D}{Dt}\ell_r = V_T \frac{\partial \ell_r}{\partial z} + V_T \frac{\ell_r}{\rho} \frac{\partial \rho}{\partial z} + \ell_r \frac{\partial V_T}{\partial z} + P_r', \quad (4.32)$$

and

$$\frac{D}{Dt}q = k_Q \nabla^2 q - P_r. \quad (4.33)$$

The functional form of  $V_T$  has remained unchanged since previously reported. (10)

It should be noticed that once one has progressed beyond  $t = 0$ , there is no explicit method of extracting the air temperature from the energy equation. The magnitude of the air temperature increase experienced by a parcel upon condensation of water vapor is related to the local saturation mixing ratio in that all moisture above this value condenses. The value of  $r_s$  is no longer known, however, since it is a function of the air temperature and the air temperature itself has changed an unknown amount. As a result of this elliptic relation, an iterative procedure is required to obtain  $T$ . This is accomplished in HAIFA via the addition of a new subroutine NEWTON which utilizes a Newton-Raphson iterative scheme to achieve rapid convergence to a self-consistent value of  $T$  in the relations below:

$$T = T'' - \frac{L}{C_p} r_s - \Gamma z + T_0, \quad (4.34)$$

$$r_s = \frac{3.8}{p} \exp \left\{ 17.27 \left( \frac{(T-273.16)}{(T-35.86)} \right) \right\}.$$

For the case where the moisture content of the parcel is less than the saturated value, there is no latent heat change and the temperature changes as in the dry equations.

The flowchart presented in Figure 4.2 depicts the logic used in the routine UPDATE to solve the vorticity, energy, moisture, and rain water equations.

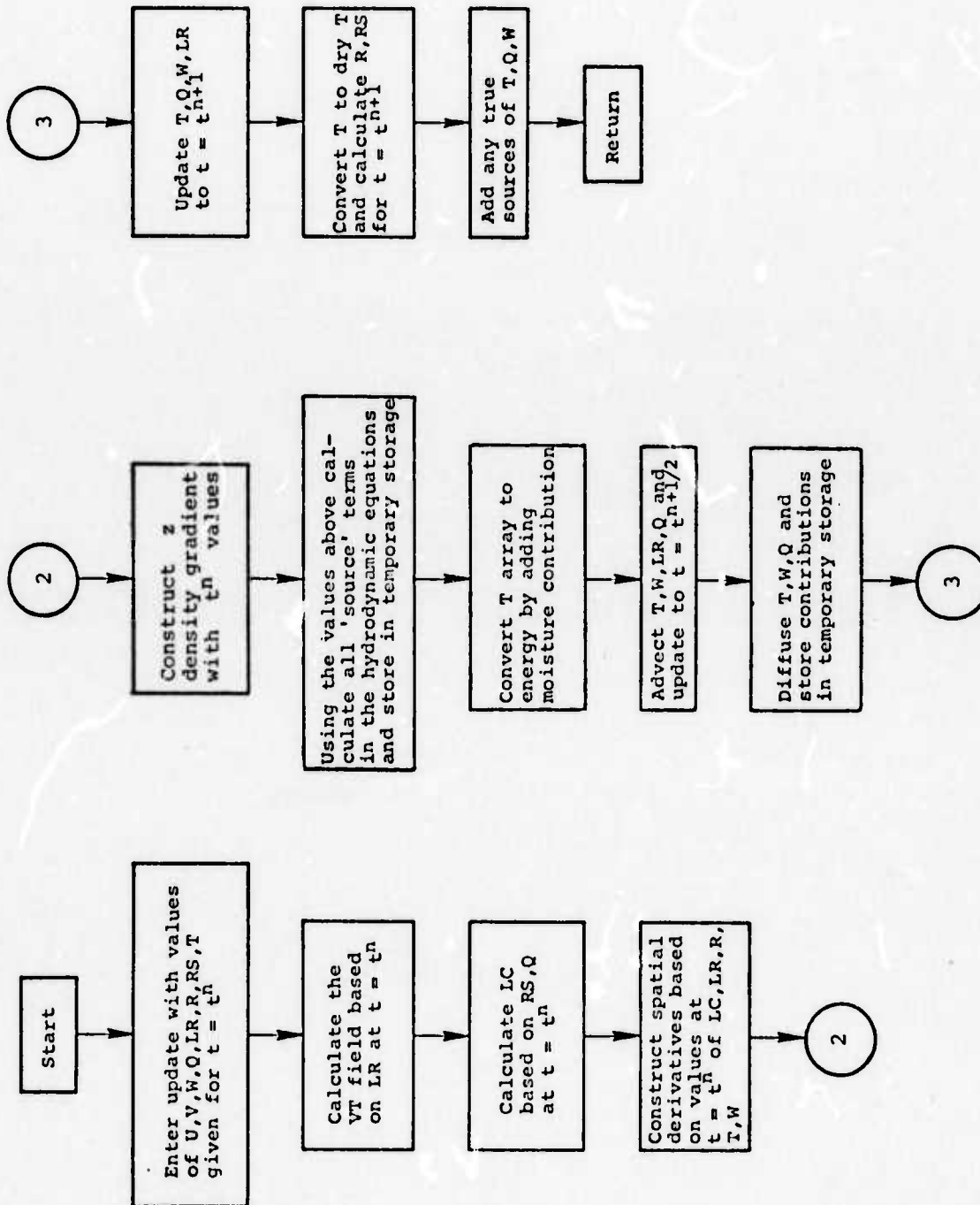


Figure 4.2 Flowchart for routine UPDATE.

## 5. SIERRA NEVADA LEE WAVE STUDY

Upon incorporation of the modifications to HAIFA noted in the previous sections, a second study of the Sierra Nevada lee wave problem was undertaken.<sup>(10)</sup> Experimental data was obtained from a study conducted by the University of California on lee wave phenomena occurring over the Owens Valley.<sup>(16)</sup> This study progressed over many months using sailplanes to record meteorological data over the valley. Rather complete temperature profiles were constructed for each day's work, with an accompanying description of the nature of any lee waves. Wind velocities were also measured, but no profiles could be constructed from the spotty data. Ambient conditions taken at two established weather stations were usually included in each day's report. The data set of February 16, 1952 (Figure 5.1) was chosen for the input conditions in the HAIFA runs. A strong lee wave was present on this day as shown by the streamline plots on Figure 5.2. The wavelength appears to be approximately 18 km at 2 km elevation, but increases to a 20 km wavelength at 6 km elevation.

HAIFA requires the specification of initial profiles of temperature, wind velocity, and in the case of the moist version of HAIFA, a moisture profile and specification of rain water production parameters. Since wind and moisture data were only available at the Merced weather station on the test day (west of the Sierra Nevada Range), the profiles of this station were used as input to HAIFA. A discussion

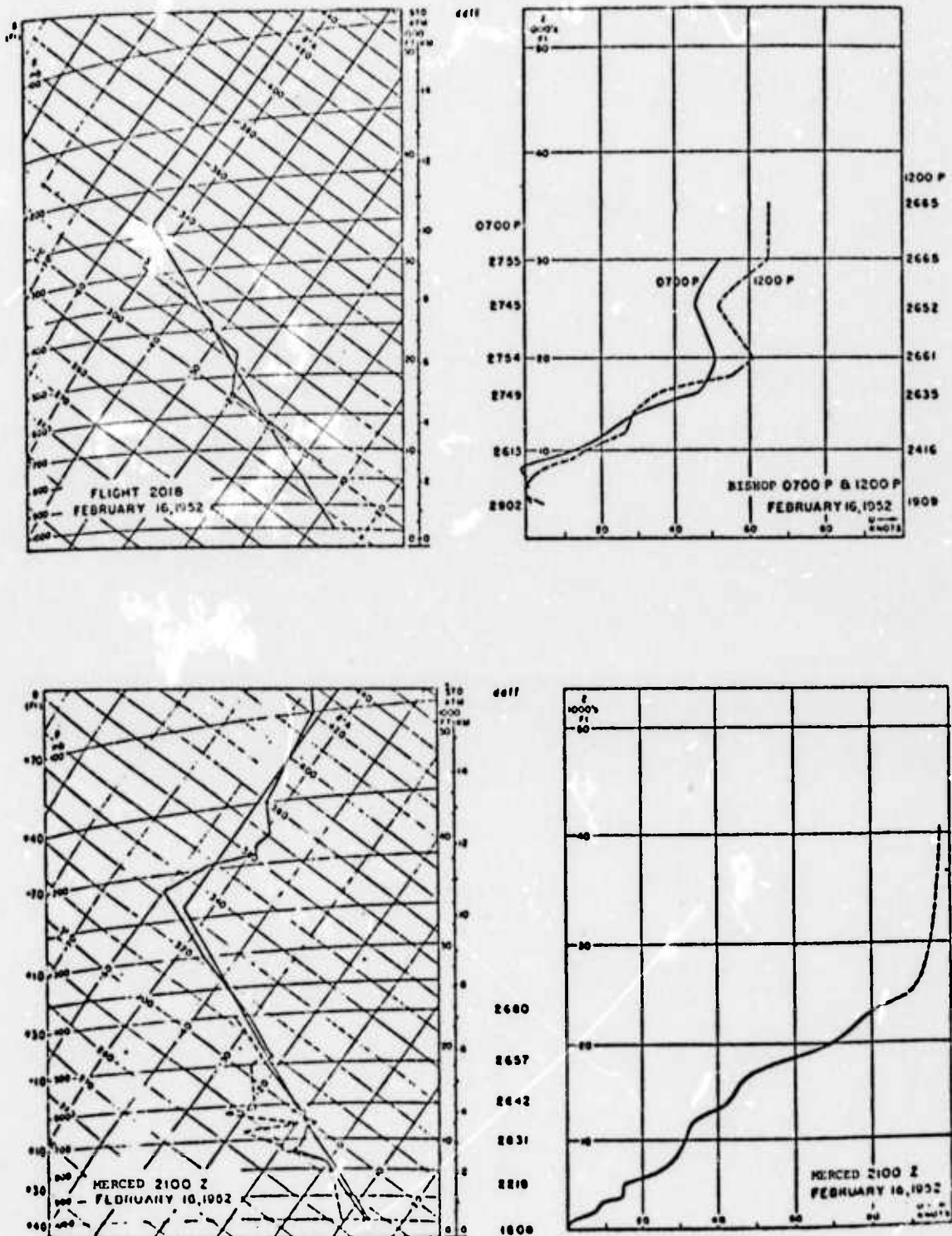


Figure 5.1 Meteorological conditions for February 16, 1952 in the Owens Valley area.

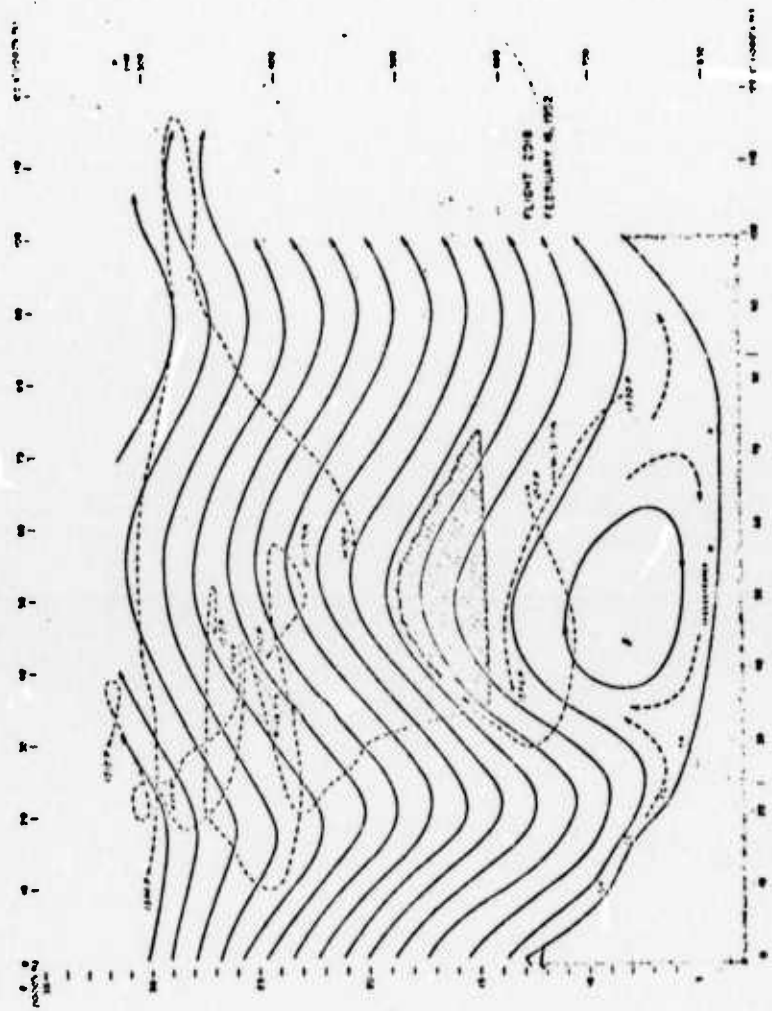


Figure 5.2 Observed flow for February 16, 1952 over Owen's Valley.

of the appropriateness of this choice follows the presentation of results. The production term parameters describing auto-conversion, accretion, and evaporative processes were manipulated such that cloud water converted to rain water at the rate of 0.1 percent/second, rain water evaporation rates were zero and accretion assumed a negligible role compared to autoconversion. This arrangement is only one of many possibilities. It is, however, fairly representative of choices made by Liu and Orville in their cloud modeling work and is thought to be a good first choice. <sup>(15)</sup>

The previous HAIFA study conducted on the Sierra problem utilized a right triangular mountain of 2 km height. Upon examination of the typical cross section of the Sierra Nevada's Owens Valley (see Figure 5.3), it is thought that a more appropriate choice of topography would be a symmetric triangular mountain of height 2 km with a base extending 16 km. The superposition of this choice on that of the real topography is seen in Figure 5.4. The HAIFA grid used in the study was composed of 35 cells in the vertical with a  $\Delta z$  of 500 m, yielding a total extent of 17.5 km. There were 64 cells in the horizontal, with a  $\Delta x$  of 2000 m, yielding an extent of 128 km. The top of the mountain model was located 30 km from the left edge of the grid.

The above HAIFA grid structure was used to simulate mountains at various elevations. This is accomplished by situating the base of the HAIFA grid at various elevations and allowing the HAIFA obstacle to represent only that part of the mountain which extends above the base elevation. The input profiles are picked up from the elevation at which the grid begins. Utilizing this procedure two sets of runs were completed in the Sierra study. Each set consisted of two runs; the first run modeling a dry atmosphere, while the

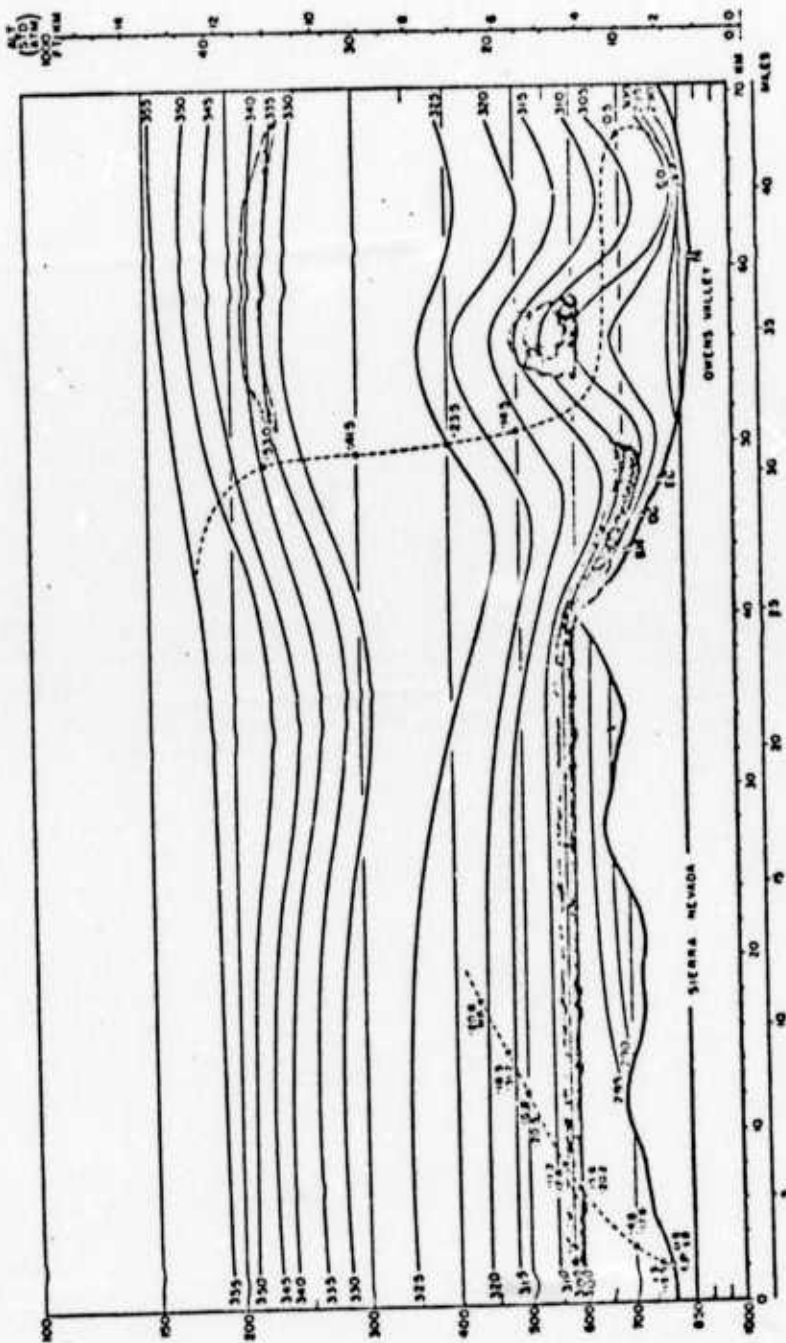


Figure 5.3 Typical cross-section of Sierra Nevada at Owen's Valley.

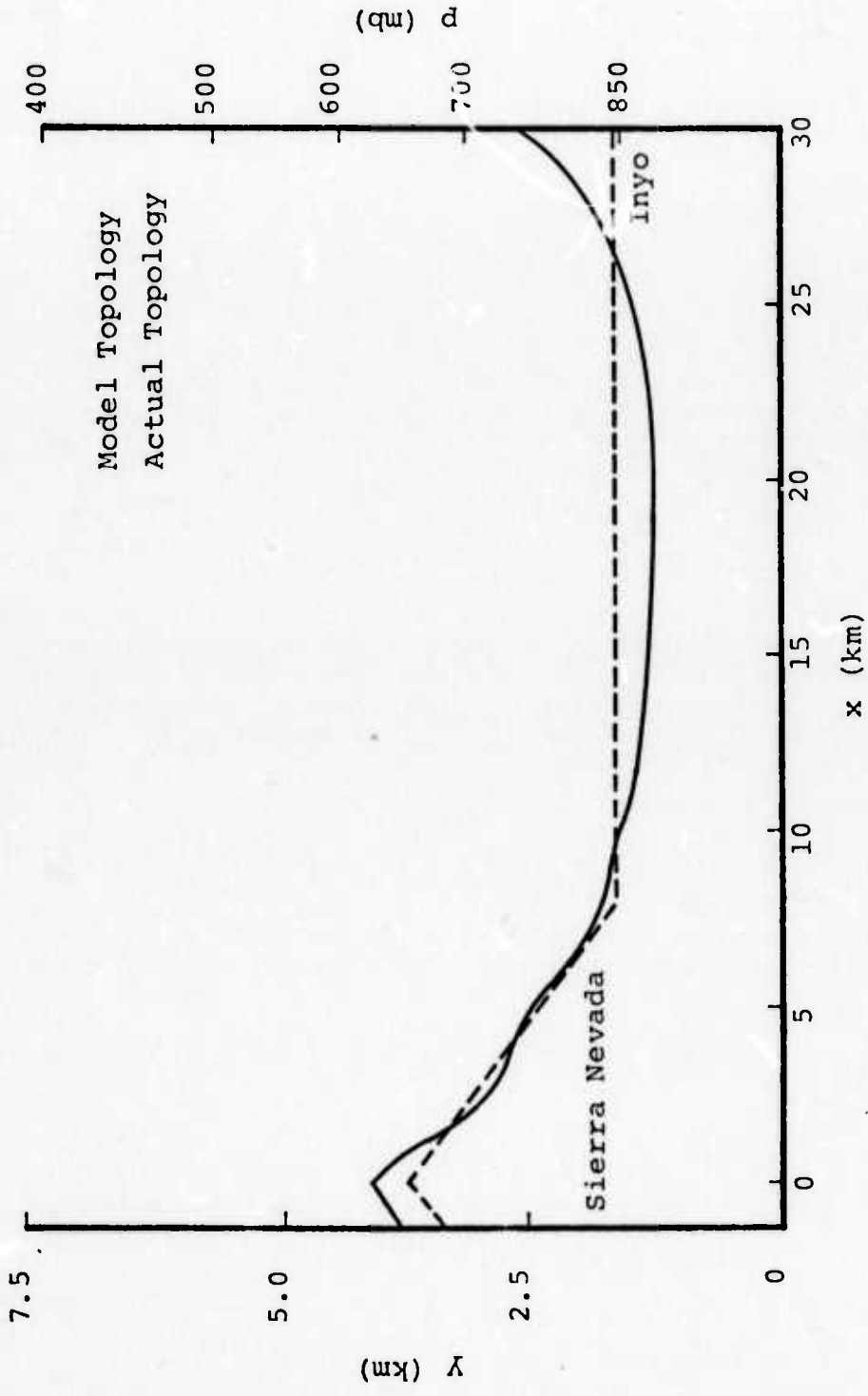


Figure 5.4 Sierra Nevada cross-section with HAIFA approximation.

second run included moisture effects. The sets differed only in their grid base elevations. The first set located the grid base at sea level, thereby modeling a mountain of 2 km height. The second set positioned the grid base at 1.5 km elevation yielding a total mountain peak elevation of 3.5 km. Figure 5.1 depicts the actual weather data obtained at Merced. Wind data from Bishop and the temperature profile obtained from the flights over the valley are also presented. Figures 5.5a, b, and c represent the HAIFA input approximations to the Merced profiles. The approximations are tabulated in Table 5.1.

The results of set one indicate the basic validity of the HAIFA approach. The results of the dry run after a 2000 secs integration are presented in the streamline plots presented in Figure 5.6. A single well developed lee wave is present with a wavelength of approximately 10 km at an elevation of 2 km increasing to 15 km at 4 km. Three rotors are seen. The windward rotor is the result of blocking and is growing in time, as would be expected. Backflow extends almost 15 km. The two leeward rotors were formed from the splitting of a single larger rotor as time progressed. This is an expected result due to the traveling lee wave. Since there are no damping processes occurring in these HAIFA runs (other than truncation error diffusion), one would expect a series of rotors to form as any trapped waves progress downwind; the number and size of rotors produced being dependent on the strength of the flow field.

The flow field in a moist atmosphere at 2000 secs is presented in Figure 5.7. In this case, we find two distinct lee waves - one at 2 km elevation has a wavelength of 8 km. The other, found at 4 km, displays a wavelength of approximately 20 km. This wavelength is in excellent agreement with that observed over the Owens Valley. As in the dry case, three

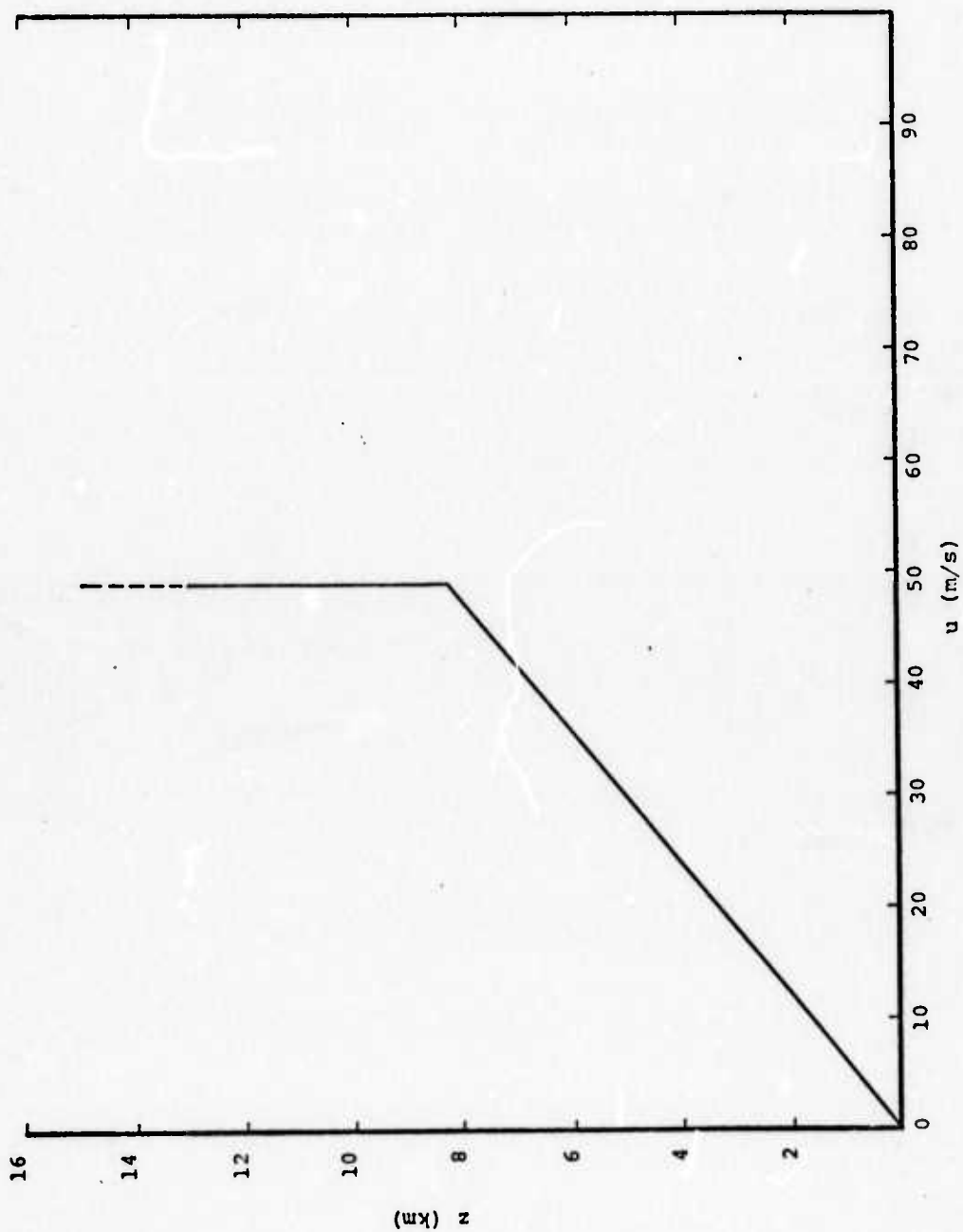


Figure 5.5a Velocity profile, set 1.

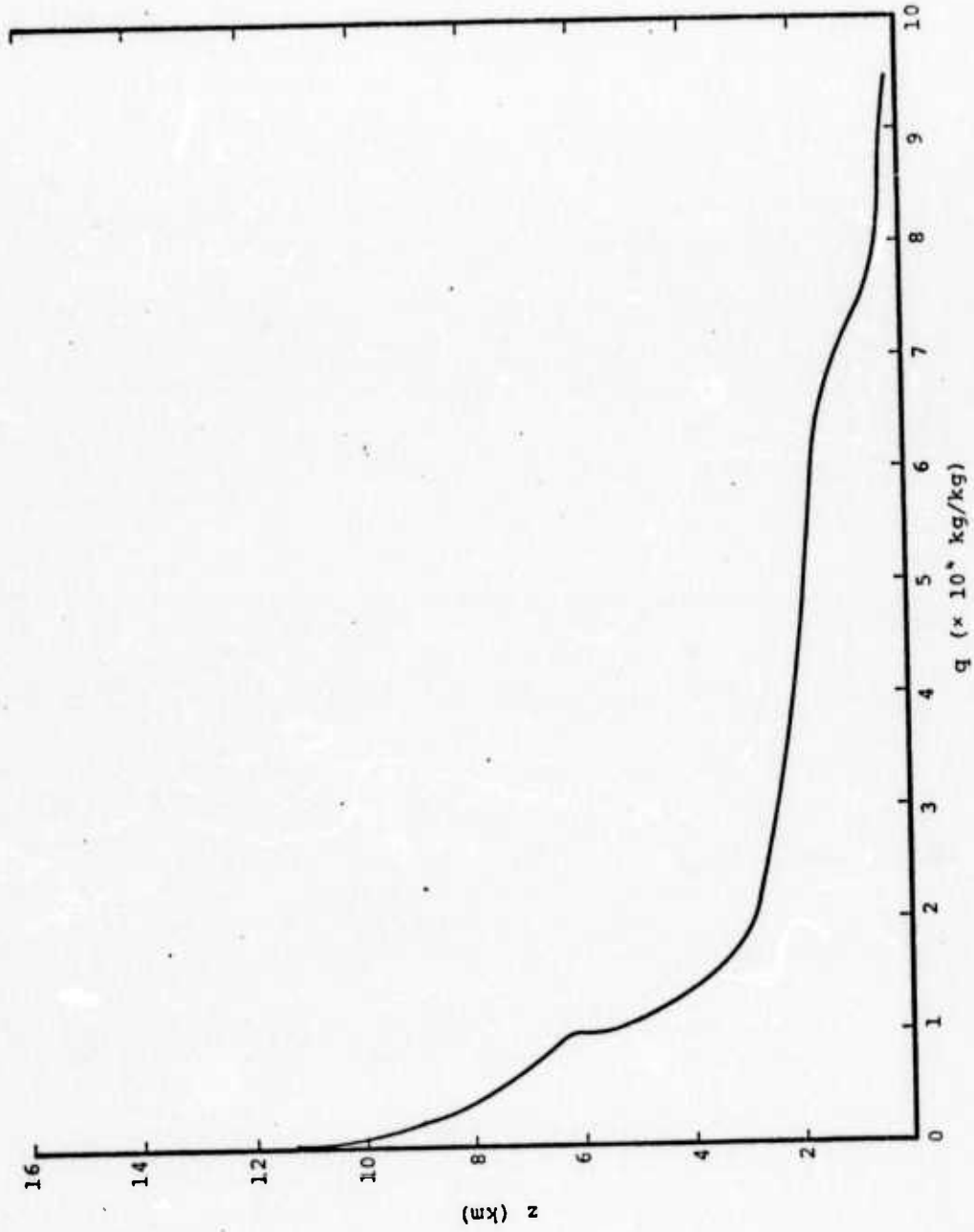


Figure 5.5b Moisture profile, set 1.

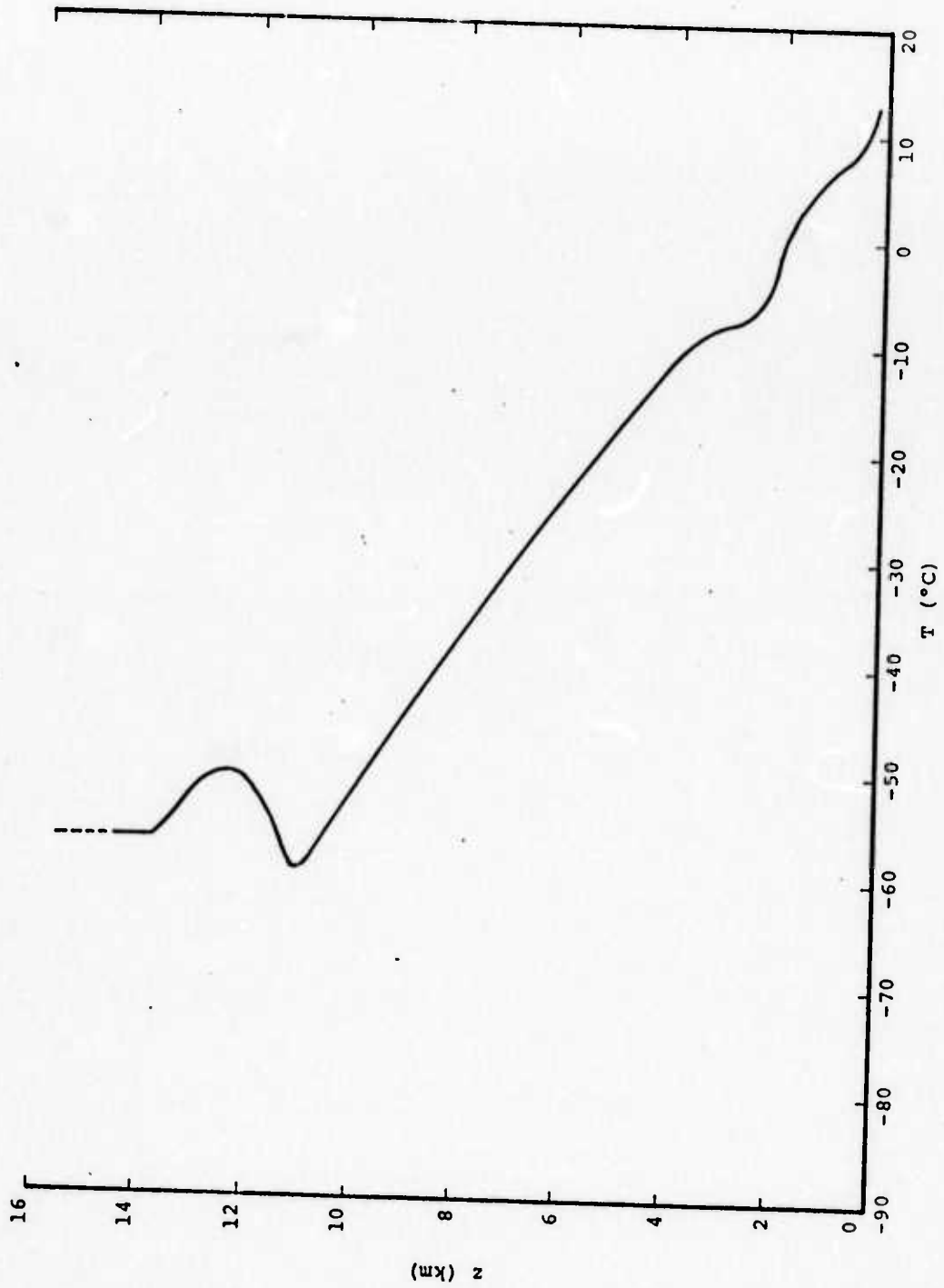


Figure 5.5c Temperature profile, set 1.

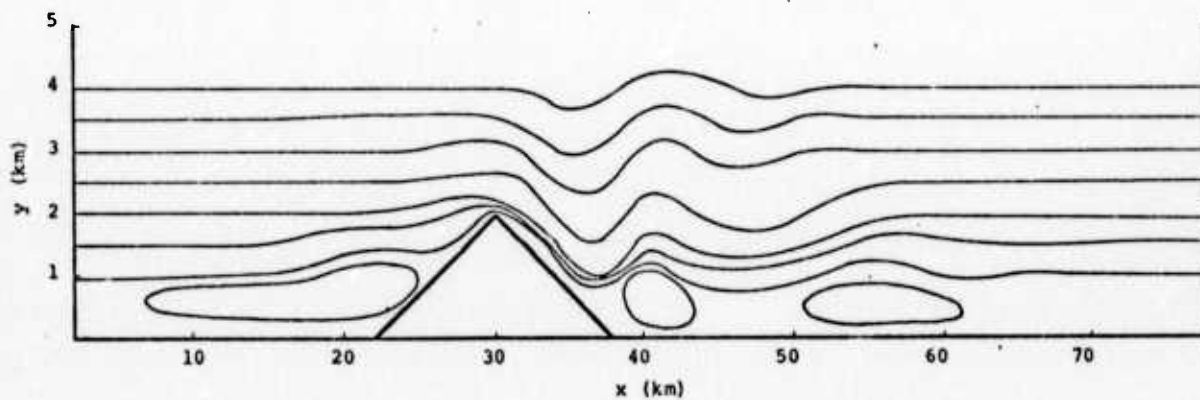


Figure 5.6 Streamlines set 1, dry run, grid base at sea level,  $t = 2000$  sec.

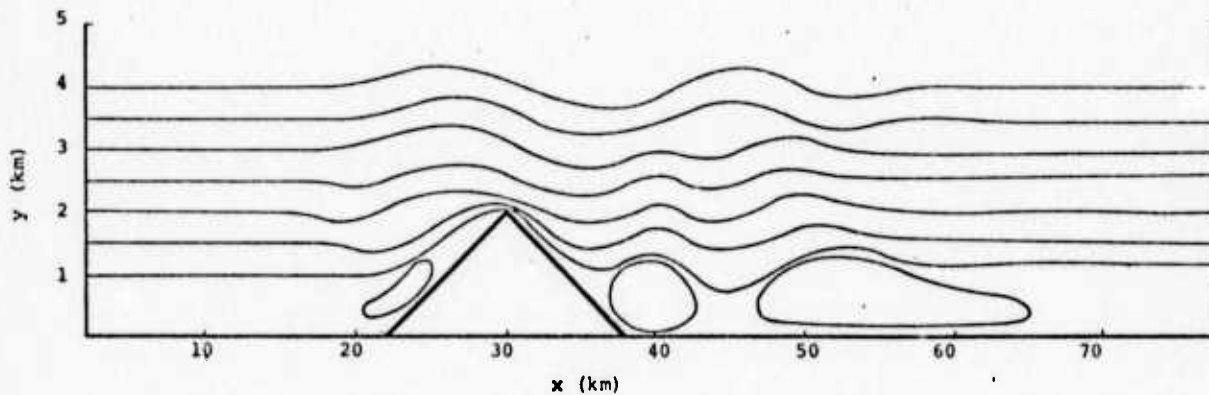


Figure 5.7 Streamlines set 1, wet run, grid base at sea level,  $t = 2000$  sec.

Table 5.1  
 HAIFA Input Profiles for Set 1

z (km)	q ( $\times 10^3$ kg/kg)	T ( $^{\circ}$ C)	u (m/s)
.25	9.50	13.0	1.48
.75	7.47	7.5	4.45
1.25	6.92	5.5	7.42
1.75	5.75	2.0	10.40
2.25	3.70	- 3.5	13.40
2.75	2.30	- 8.0	16.30
3.25	1.70	- 8.0	19.30
3.75	1.50	- 9.5	22.20
4.25	1.30	-12.7	25.20
4.75	1.20	-15.5	28.20
5.25	1.10	-19.0	31.10
5.75	1.00	-22.2	34.10
6.25	1.00	-25.7	37.10
6.75	0.79	-29.0	40.00
7.25	0.62	-32.2	43.00
7.75	0.46	-36.0	46.00
8.25	0.34	-39.5	49.00
8.75	0.25	-43.0	49.00
9.25	0.17	-47.0	49.00
9.75	0.13	-50.0	49.00
10.25	0.08	-54.5	49.00
10.75	0.06	-58.0	49.00
11.25	0.06	-58.0	49.00
11.75	0.12	-53.0	49.00
12.25	0.19	-50.0	49.00
12.75	0.18	-51.0	49.00
13.25	0.14	-54.0	49.00
13.75	0.11	-56.5	49.00
14.25	0.12	-56.5	49.00
14.75	0.13	-56.5	49.00
15.25	0.14	-56.5	49.00
15.75	0.15	-56.5	49.00
16.25	0.16	-56.5	49.00
16.75	0.18	-56.5	49.00
17.25	0.18	-56.5	49.00

rotors are observed. However, their structure is considerably different. The windward rotor is almost absent, while the leeward rotors have become much larger. In addition, the upper wave crest has advanced farther downwind than seen in the dry case.

Maximum cloud water concentrations are shown in Figure 5.8. These occur over the windward slope of the mountain and in the wave crests. This would be expected since the air at lower elevations is rather moist and warm. As this air is lifted by the flow, adiabatic cooling takes place and excess water vapor condenses out.

The second set of runs also utilized the Merced profiles. In this case, however, the grid base was situated at the floor of the Owens Valley. This yields a total mountain height of 3.5 km, a more realistic estimate of the true extent of the Sierra's. This set also consisted of two runs, one wet, one dry. The HAIFA approximated profiles are shown in Figures 5.9a, b, and c and tabulated in Table 5.2. These profiles are approximately the same as those used in set one except they are picked up at a 1.5 km elevation (elevation of Owens Valley). Also, the linear profiles, established in the intermediate atmospheric levels for wind and temperature, are continued to the top of the grid. This approximation eliminates calculational problems in the upper grid regions due to uniform flow. It is felt that this will not alter the solution in the region of interest, however.

The results of the dry run of set two at 2000 secs are presented in Figure 5.10. Only one lee wave appears with a wavelength of approximately 24 km agreeing qualitatively with observed data. Since the flow velocities are considerably higher than in set one, the longer wavelength is not surprising. Two small rotors are seen on the windward side. These would

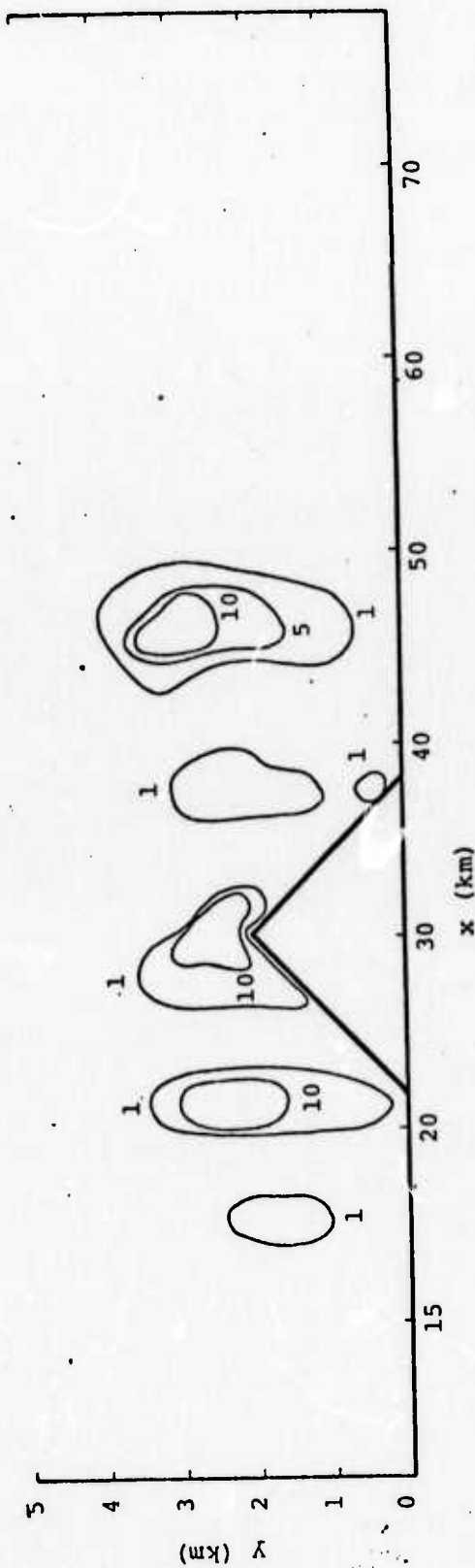


Figure 5.8 Cloud water distribution, set 1, grid base at sea level, contours 1, 5, 10 ( $\times 10^4$  Kg/Kg),  $t = 2000$  sec.

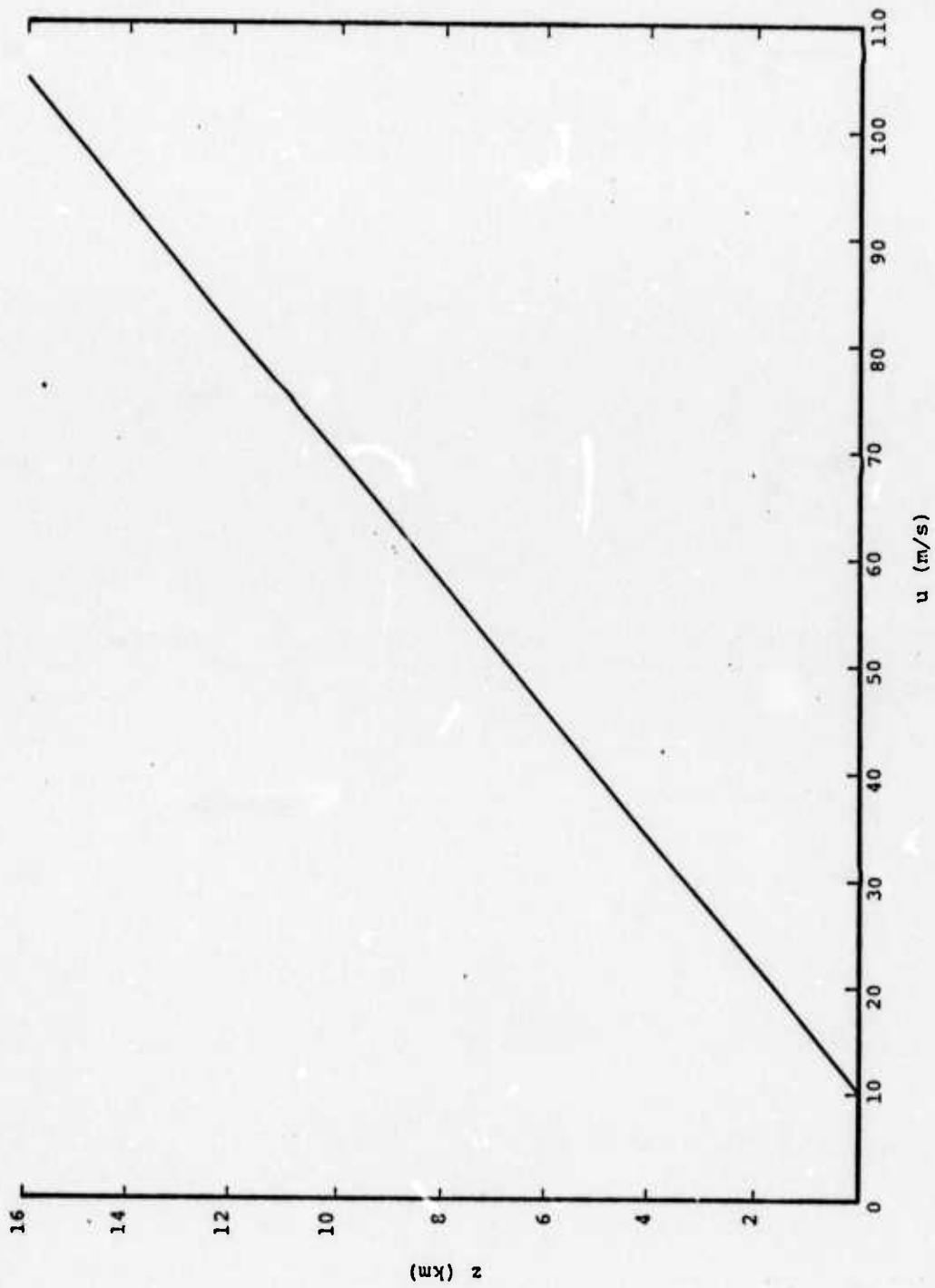


Figure 5.9a Velocity profile, set 2.

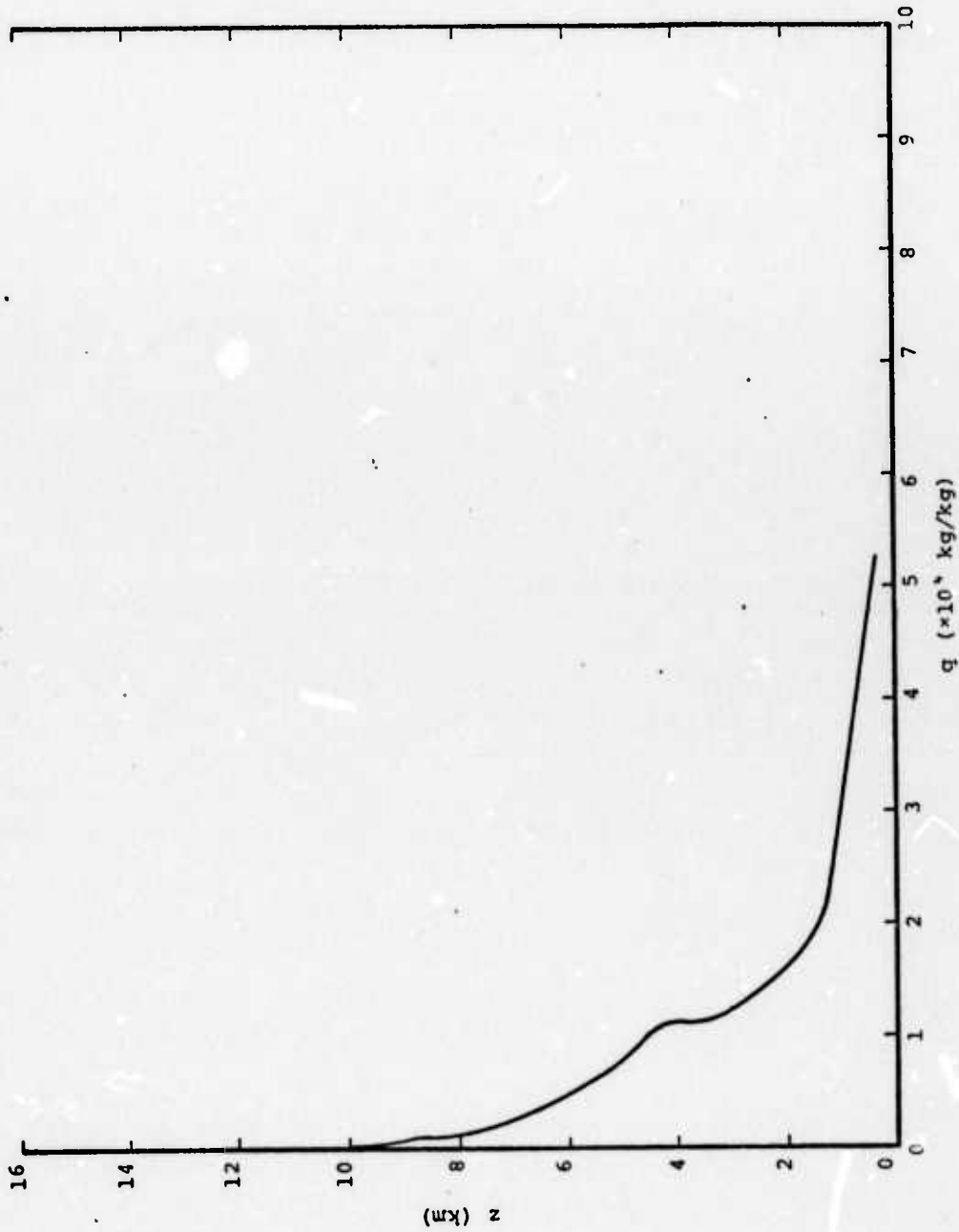


Figure 5.9b Moisture profile, set 2.

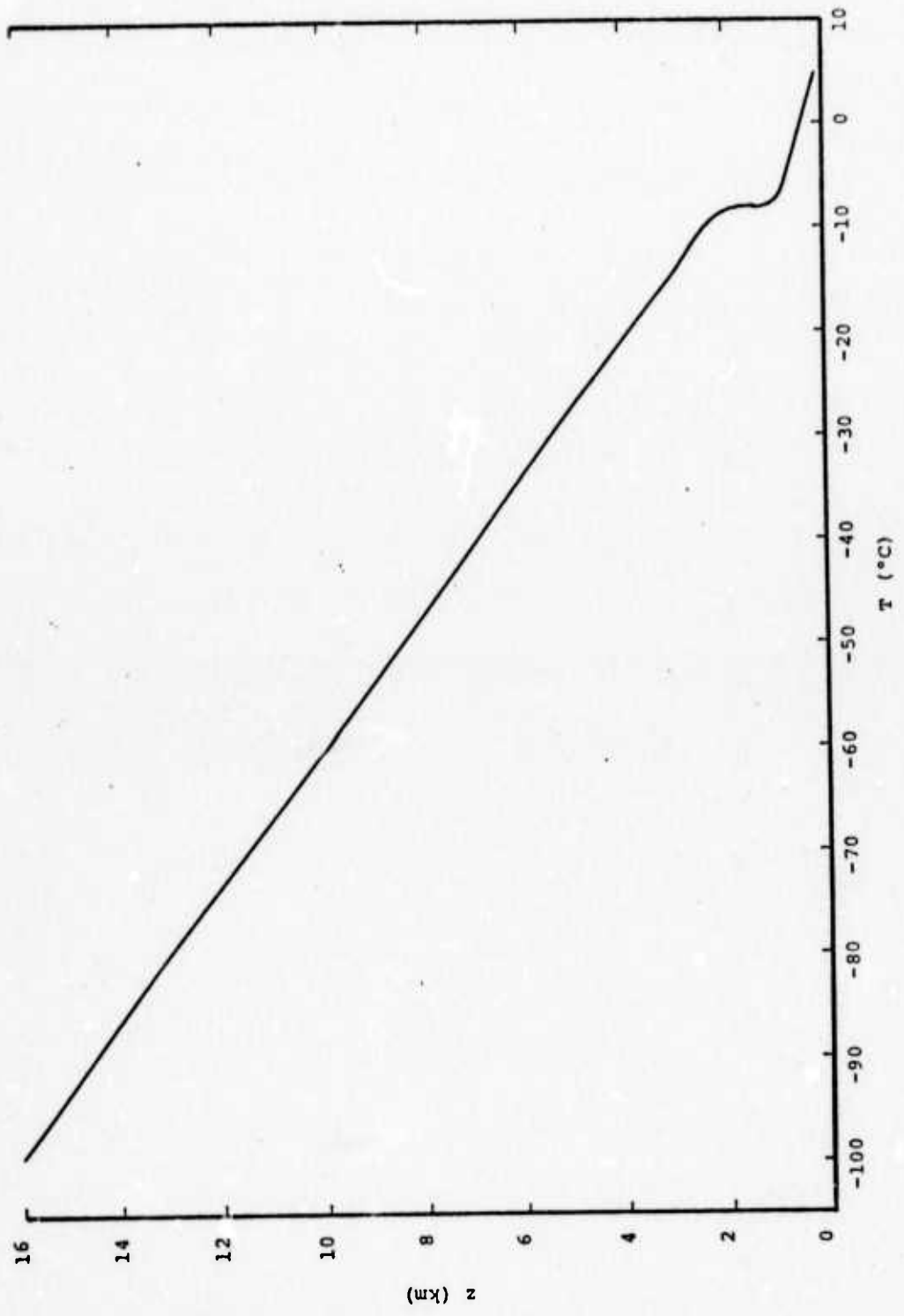


Figure 5.9c Temperature profile, set 2.

Table 5.2  
 HAIFA Input Profiles for Set 2

z (km)	q ( $\times 10^3$ kg/kg)	T ( $^{\circ}$ C)	u (m/s)
.25	5.28	3.4	11.5
.75	3.90	4.0	14.5
1.25	2.30	- 8.0	17.4
1.75	1.70	- 8.0	20.4
2.25	1.50	- 9.6	23.4
2.75	1.30	- 12.9	26.3
3.25	1.20	- 16.1	29.3
3.75	1.10	- 19.4	32.3
4.25	1.10	- 22.6	35.2
4.75	0.90	- 25.9	38.2
5.25	0.71	- 29.1	41.2
5.75	0.56	- 32.4	44.2
6.25	0.43	- 35.6	47.1
6.75	0.33	- 38.9	50.0
7.25	0.25	- 42.1	53.0
7.75	0.19	- 45.4	56.0
8.25	0.14	- 48.6	59.0
8.75	0.10	- 51.9	62.0
9.25	0.07	- 55.1	65.0
9.75	0.05	- 58.4	67.9
10.25	0.04	- 61.6	70.9
10.75	0.03	- 64.9	73.9
11.25	0.02	- 68.1	76.8
11.75	0.01	- 71.4	79.8
12.25	0.01	- 74.6	82.8
12.75	0.01	- 77.9	85.7
13.25	0.00	- 81.1	88.7
13.75	0.00	- 84.4	91.7
14.25	0.00	- 87.6	94.7
14.75	0.00	- 90.9	97.6
15.25	0.00	- 94.1	100.6
15.75	0.00	- 97.4	103.6
16.25	0.00	-100.6	106.5
16.75	0.00	-103.9	109.5
17.25	0.00	-107.1	112.5

be expected to grow and merge at later times. A small rotor may be present under the leeward crest of the wave, but grid resolution prevents its detection.

The streamlines of the wet run at 2000 secs are presented in Figure 5.11. It appears as if the moisture has done little to affect the wave. Only one is present with a wavelength of around 24 km. Since there is considerably less moisture in this set (the moist lower atmosphere has been ignored in the profiles), it is not surprising. The rotors on the windward side have not appeared, although flow is very sluggish there, as seen from examination of wind field edits.

The cloud water (Figure 5.12) again congregates in regions of upward flow, predominantly on the windward slope and in the crest of the lee wave. Maximum values approach  $10^{-3}$  kg/kg. The much larger wave amplitudes present in this run serve to yield cloud water concentrations as large as that of the first run even though less moisture is available.

Momentum flux edits were performed on this set of runs. These are presented in Figures 5.13 and 5.14. As can be seen, neither edit exhibits the same transient structure as found in the previous Sierra drag results (Figure 5.15). The period of oscillation appears to have increased considerably.

The two new edits exhibit a similar period with the moist run showing a consistently lower drag when plotted as a function of time. This appears to be the result of latent heat effects. The energetic processes which are introduced by the inclusion of moisture make interpretation difficult. It appears buoyant effects make the troughs in the streamlines shallower, thereby reducing the flux. More investigation is needed in this area.

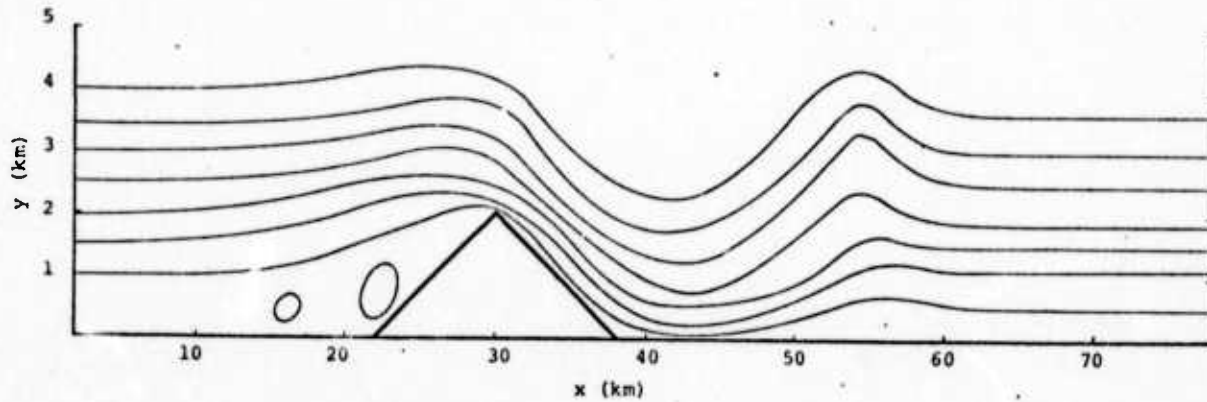


Figure 5.10 Streamlines set 2, dry run, grid base at 1.5 km,  $t = 2000$  sec.

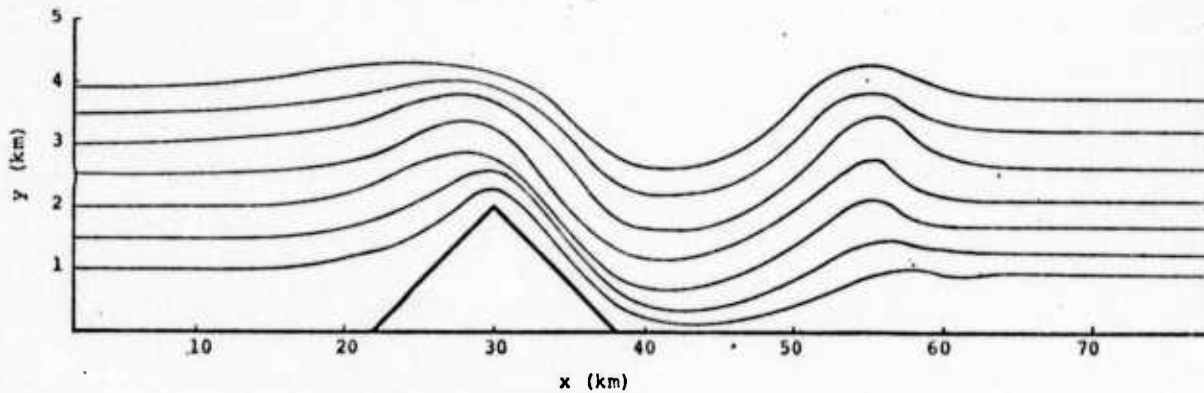


Figure 5.11 Streamlines set 2, wet run, grid base at 1.5 km,  $t = 2000$  sec.

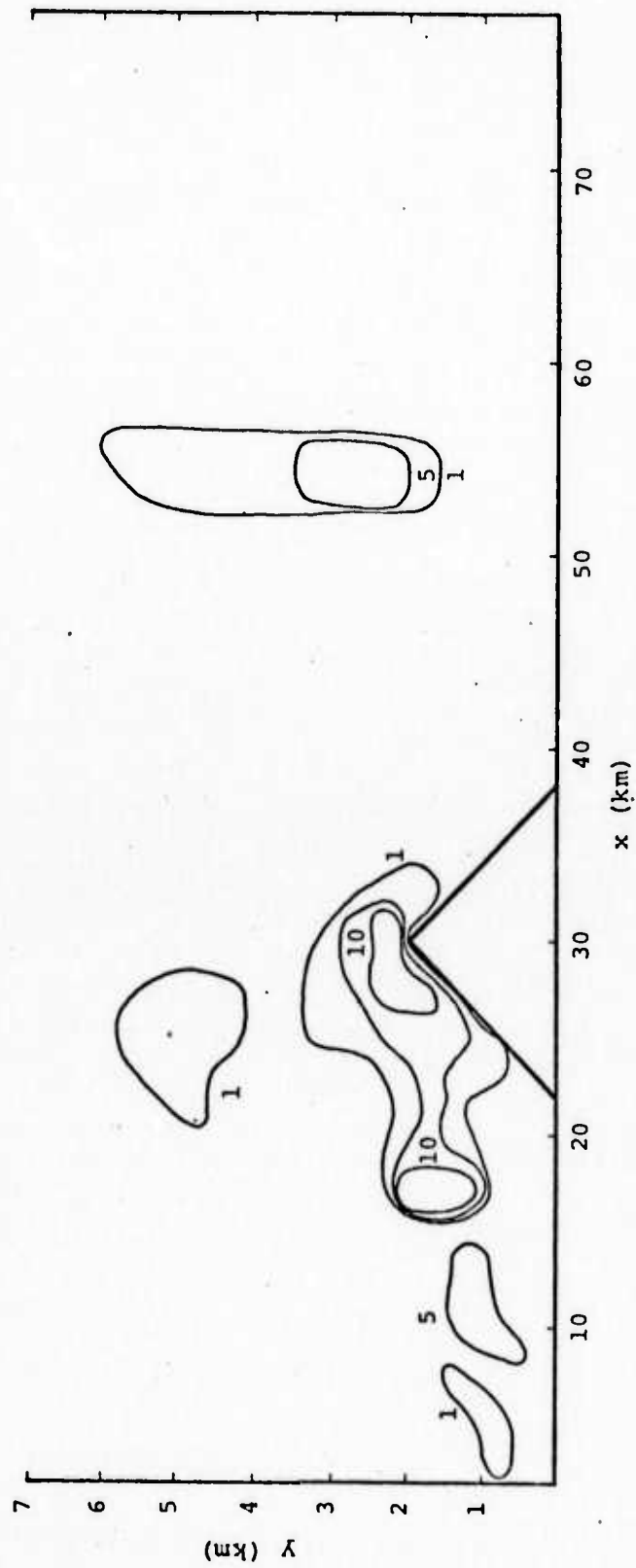


Figure 5.12 Cloud water distribution, set 2, grid base at 1.5 km, contours 1, 5, 10 ( $\times 10^4$  Kg/Kg),  $t = 2000$  sec.

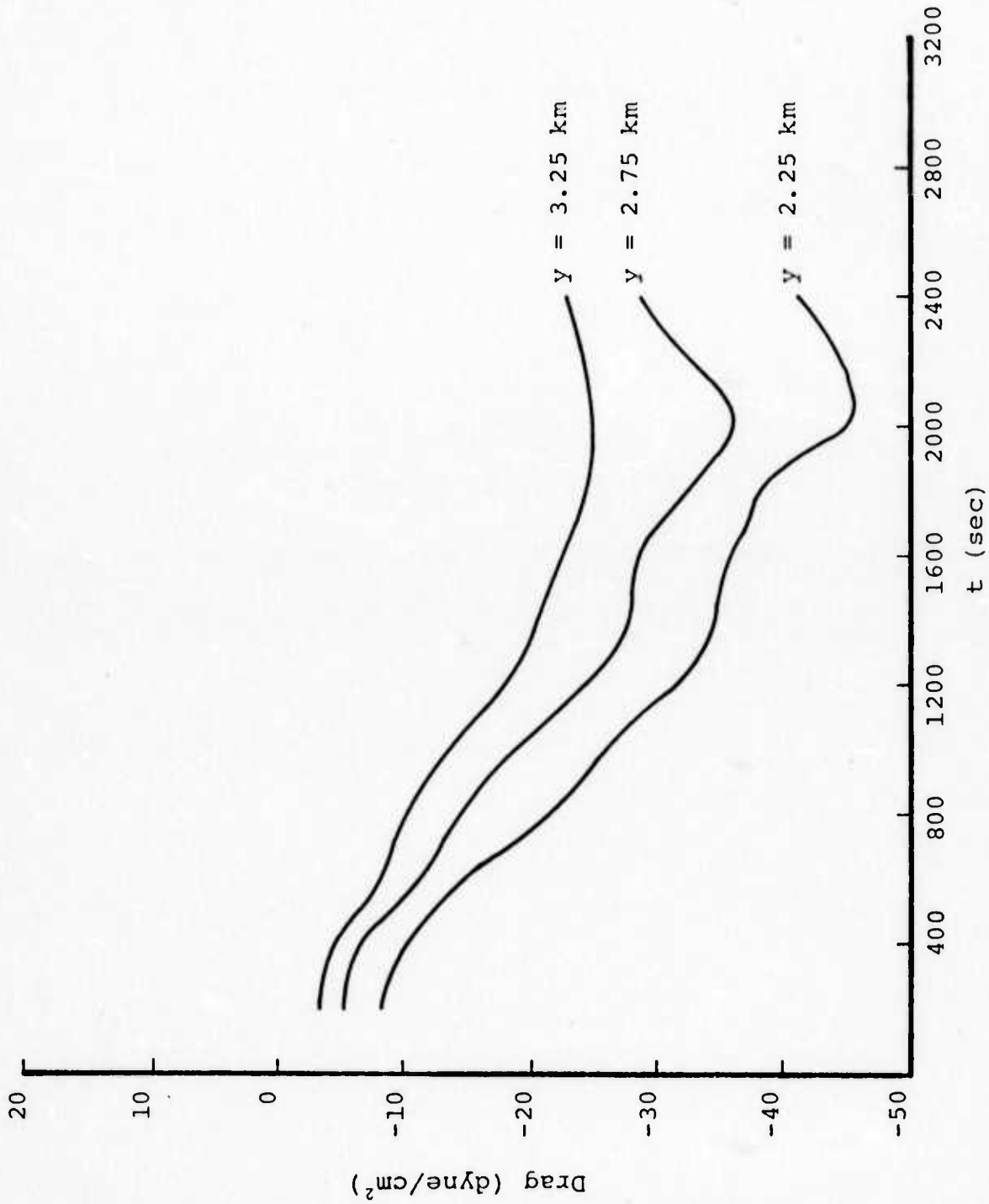


Figure 5.13 Horizontal momentum flux dry run of set 2, grid base at 1.5 km.

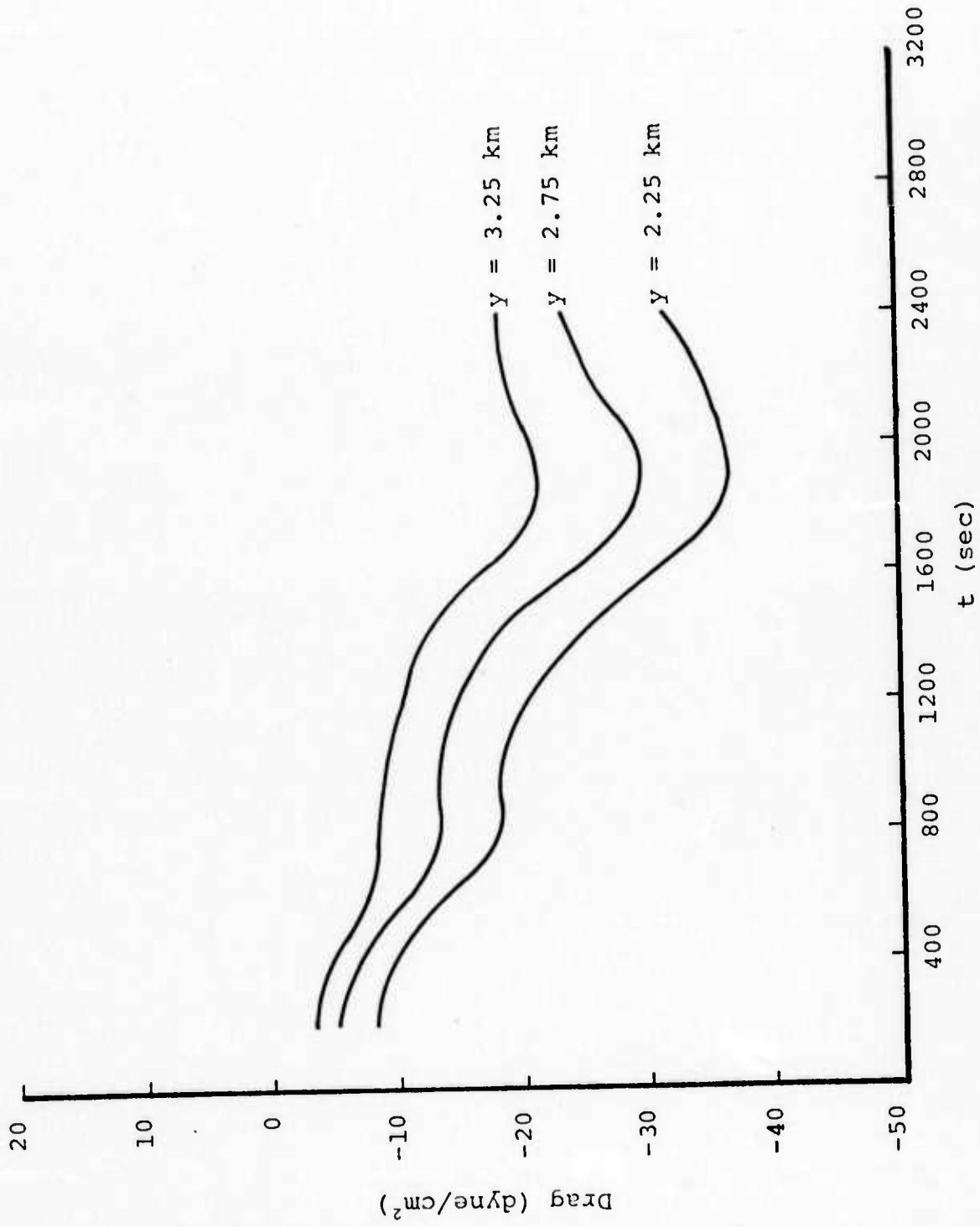


Figure 5.14 Horizontal momentum flux wet run of set 2, grid base at 1.5 km.

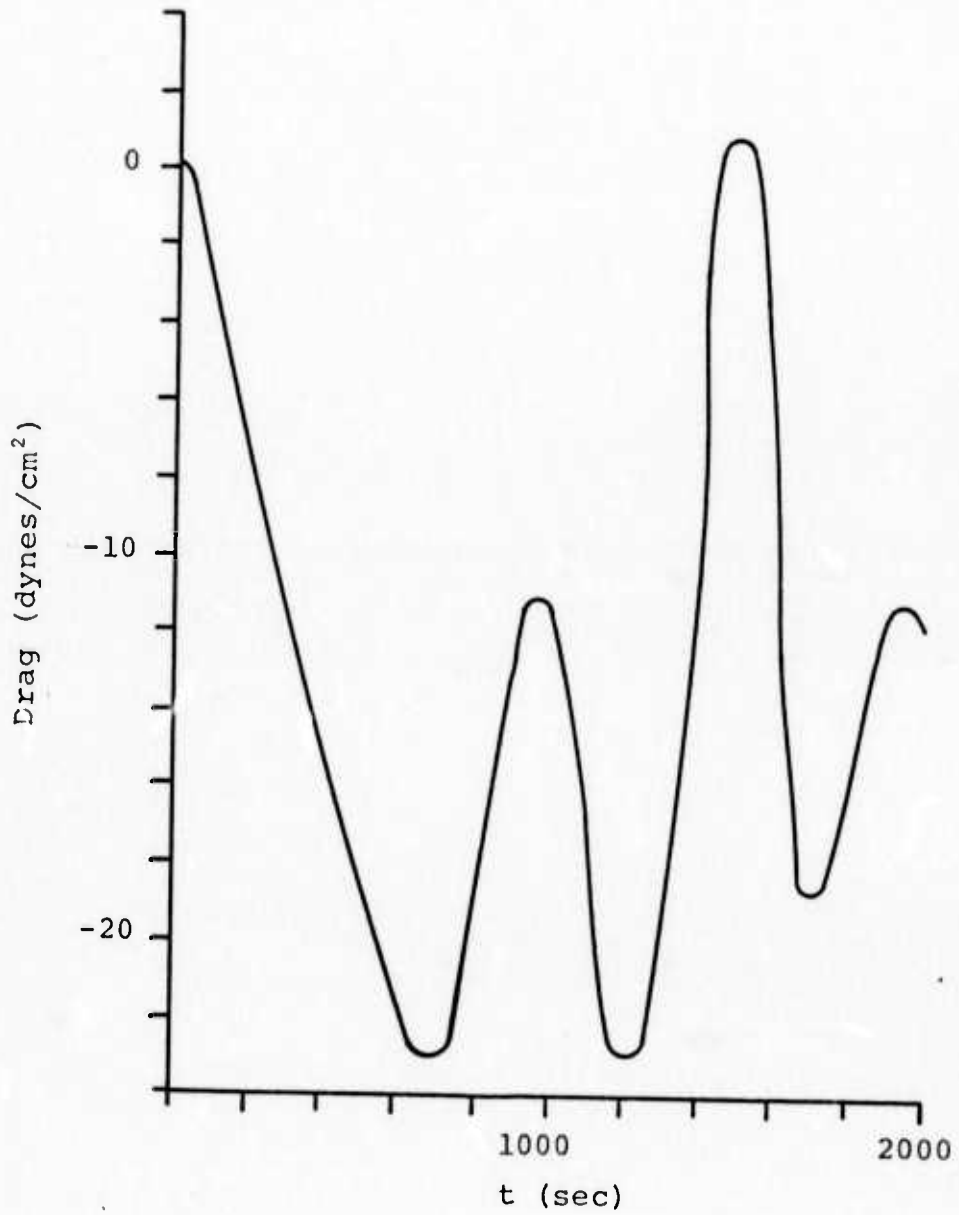


Figure 5.15 Horizontal momentum flux, first Sierra study.

The choice of the Merced profiles was dictated by their availability and not by their obvious applicability. Since Merced is located approximately 50 - 100 miles from the Owens Valley, the prevailing ambient conditions most probably do not reflect the true ambient conditions of the flow as it reaches the Sierra Nevada. In particular, the prevailing winds reported at Bishop on the same day (shown in Figure 5.1) show a marked deviation from those reported at Merced. Unfortunately, no temperature or moisture data was available that day for Bishop. The runs do indicate that the code is very sensitive to the input flow profile. The truncation of the Merced profiles at an elevation of 1.5 km for use in the set two runs is most probably an invalid procedure, resulting in much higher "ground" velocities than is found at 1.5 km on the Sierra Nevada. This artificially high flow may inhibit the formation of a large lee rotor at late integration times. A profile similar to that of Bishop's is probably more accurate.

## 6. DEVELOPMENT OF THE LINEAR STEADY STATE CODES

A two-dimensional linear steady-state numerical model to calculate the vertical flux of horizontal momentum (wave drag), when both the motion of the flow field and the obstacle placed in the field are small, was described previously.<sup>(10)</sup> Results of sample calculations were reported. In addition, a derivation of the linearized fluid flow equation for the vertical velocity field under a variety of assumptions has been reported.<sup>(1)</sup> During the past six months, the three-dimensional model published by Bretherton<sup>(17)</sup> has been checked and the equations coded. Several changes have been made in the two-dimensional code to both speed the computation and to investigate the accuracy and stability of the methods used in the numerical schemes. This chapter will: (1) give a detailed derivation of the Bretherton equations including a discussion of the important assumptions, (2) outline some changes which will make the equations applicable to a more general set of problems, (3) discuss the computations which have been completed using the two-dimensional code and some of the sensitive areas encountered in the calculational techniques, and (4) briefly describe sets of worldwide topography data which have been obtained for use in the wave drag parameterization scheme for the RAND global circulation model.

### 6.1 A DERIVATION OF REYNOLDS STRESS FOR LINEAR-STEADY STATE FORMULATIONS

Bretherton gives without derivation the equations for the components of Reynolds stress corresponding to steady-state flow over three-dimensional (3D) topography in the linear approximation. In this section, the derivations of his result will be presented. We also generalize the equation for the vertical velocity and display correction terms to the Scorer parameter. The resulting equations (when sound waves are neglected) can then be incorporated into Bretherton's computational framework with little modification.

As a point of departure, the linearized steady state Navier Stokes equations for air without diabatic, Coriolis, or dissipative terms are adopted. We consider the perturbation to an unperturbed atmospheric state in which the atmosphere is stably stratified and the wind is steady and horizontal. The unperturbed wind may vary in strength and direction with altitude as given by the east-west and north-south components  $U(z)$  and  $V(z)$ . The formulation and notation of the previous semi-annual report<sup>(1)</sup> is followed.

The inviscid 3D equations of motion before we make the linear and steady-state approximations are:

$$\frac{d\rho}{dt} + \rho \left( \frac{\partial u}{\partial x} + \frac{\partial v}{\partial y} + \frac{\partial w}{\partial z} \right) = 0 \quad ,$$

$$\frac{du}{dt} + \frac{1}{\rho} \frac{\partial p}{\partial x} = 0 \quad ,$$

$$\frac{dv}{dt} + \frac{1}{\rho} \frac{\partial p}{\partial y} = 0 \quad ,$$

$$\frac{dw}{dt} + \frac{1}{\rho} \frac{\partial p}{\partial z} = -g \quad ,$$

$$\frac{dT}{dt} = \frac{1}{\rho C_p} \frac{dp}{dt} ,$$

$$p = \rho RT ,$$

where

$$\frac{d}{dt} = \frac{\partial}{\partial t} + u \frac{\partial}{\partial x} + v \frac{\partial}{\partial y} + w \frac{\partial}{\partial z} .$$

### 6.1.1 Linear Steady State Equations

The linear steady state equations for a small perturbation are obtained by separating the variables into a mean part which is a function of  $z$  only and a perturbation, and substituting these expressions into the above equations. The expressions for the variables are:

$$\rho = \bar{\rho}(z) + \rho_1 ,$$

$$u = U(z) + u_1 ,$$

$$v = V(z) + v_1 ,$$

$$w = w_1 ,$$

$$p = \bar{p}(z) + p_1 ,$$

and

$$T = \bar{T}(z) + T_1 .$$

The derived steady state equations are:

$$U\rho_x + V\rho_y + w\bar{\rho}_z + \bar{\rho} (u_x + v_y + w_z) = 0 , \quad (6.1)$$

$$Uu_x + Vu_y + wU_z + \frac{1}{\bar{\rho}} P_x = 0 , \quad (6.2)$$

$$Uv_x + Vv_y + wv_z + \frac{1}{\rho} P_y = 0 \quad , \quad (6.3)$$

$$Uw_x + Vw_y + \frac{\rho g}{\rho} + \frac{1}{\rho} P_z = 0 \quad , \quad (6.4)$$

$$UT_x + VT_y + w(\bar{T}_z + \Gamma) = \frac{1}{\rho C_p} (Up_x + Vp_y) \quad , \quad (6.5)$$

and

$$\frac{P}{\bar{P}} = \frac{\rho}{\bar{\rho}} + \frac{T}{\bar{T}} \quad . \quad (6.6)$$

The subscript "1" has been dropped in the above equations and the subscripts  $x$ ,  $y$ , and  $z$  are used to denote differentiation. The adiabatic lapse rate  $\Gamma = \frac{g}{C_p}$  has been introduced. In anticipation of the discussion of obliquely propagating plane waves, a transformation to a new coordinate system  $(x', y')$  rotated by an angle  $\phi$  with respect to the  $x, y$  system is completed, i.e.,

$$x = x' \cos \phi - y' \sin \phi$$

$$y = x' \sin \phi + y' \cos \phi$$

and

$$\frac{\partial \phi}{\partial x'} = \frac{\partial \phi}{\partial x} \cos \phi + \frac{\partial \phi}{\partial y} \sin \phi \quad ,$$

$$\frac{\partial \phi}{\partial y'} = - \frac{\partial \phi}{\partial x} \sin \phi + \frac{\partial \phi}{\partial y} \cos \phi \quad .$$

We also introduce the definitions:

$$U_n = U \cos \phi + V \sin \phi \quad ,$$

$$U_p = - V \sin \phi + U \cos \phi \quad ,$$

$$\text{and } u_n = u \cos\phi + v \sin\phi ,$$

$$u_p = -u \sin\phi + v \cos\phi .$$

The following identities are required in the derivation:

$$U_n \phi_{x'} + U_p \phi_{y'} = U \phi_x + V \phi_y ,$$

$$\frac{\partial u_n}{\partial x'} + \frac{\partial u_p}{\partial y'} = \frac{\partial u}{\partial x} + \frac{\partial v}{\partial y} .$$

Using these relations, the conservation equations become:

Continuity

$$U_n \rho_{x'} + U_p \rho_{y'} + w \bar{\rho}_z + \bar{\rho} [(u_n)_{x'} + (u_p)_{y'} + w_z] = 0 ; \quad (6.7)$$

Vertical Momentum

$$U_n w_{x'} + U_p w_{y'} + \frac{\rho g}{\rho} + \frac{1}{\rho} P_z = 0 ; \quad (6.8)$$

Energy

$$U_n T_{x'} + U_p T_{y'} + w(\bar{T}_z + \Gamma) = \frac{1}{\bar{\rho} C_p} (U_n P_{x'} + U_p P_{y'}) ; \quad (6.9)$$

Equation of State

$$P/\bar{p} = \rho/\bar{\rho} + T/\bar{T} . \quad (6.10)$$

The x and y momentum equations:

$$U_n u_{x'} + U_p u_{y'} + w U_z + \frac{1}{\rho} P_x = 0 \quad (6.11)$$

and

$$U_n v_{x'} + U_p v_{y'} + w V_z + \frac{1}{\rho} P_y = 0 , \quad (6.12)$$

respectively, are then combined in two ways:

$$\begin{aligned}
& U_n(u_x \cos\phi + v_x \sin\phi) + U_p(u_y \cos\phi + v_y \sin\phi) \\
& \quad + w(U_z \cos\phi + V_z \sin\phi) + \frac{1}{\rho} P_{x'} \\
& = U_n(u_n)_{x'} + U_p(u_n)_{y'} + w(U_n)_z + \frac{1}{\rho} P_{x'} = 0 ; \quad (6.13)
\end{aligned}$$

and

$$\begin{aligned}
& U_n(-u_x \sin\phi + v_x \cos\phi) + U_p(-u_y \sin\phi + v_y \cos\phi) \\
& \quad + \frac{1}{\rho} P_{y'} + w(-U_z \sin\phi + V_z \cos\phi) \\
& = U_n(u_p)_{x'} + U_p(u_p)_{y'} + w(U_p)_z + \frac{1}{\rho} P_{y'} = 0 \quad . \quad (6.14)
\end{aligned}$$

The above equations are to be expected; they are the result of transforming the equations by rotation to the  $x'$  and  $y'$  directions. They are obtained by the substitutions:

$$\begin{aligned}
U_n &\rightarrow U , & U_p &\rightarrow V , \\
u_n &\rightarrow u , & u_p &\rightarrow v , \\
x' &\rightarrow x \quad \text{and} \quad y' &\rightarrow y
\end{aligned}$$

into the original equations.

### 6.1.2 Boundary Condition

The bottom boundary condition for the mountain flow problem results from linearization of the statement that the wind is parallel to the surface at all points,

$$w(0) = U \frac{\partial h}{\partial x} + V \frac{\partial h}{\partial y} = U_n \frac{\partial h}{\partial x'} + U_p \frac{\partial h}{\partial y'} \quad (6.15)$$

where  $h(x,y)$  = height of the ground surface.

We now introduce Fourier components of the topography such that:

$$\hat{h}(k,\ell) = \frac{1}{2\pi} \int_0^X \int_0^Y h(x,y) e^{-i(kx + \ell y)} dx dy$$

and

$$h(x,y) = \frac{1}{2\pi} \iint \hat{h}(k,\ell) e^{i(kx + \ell y)} dk d\ell .$$

Since both the equations and the boundary conditions are linear, we may consider a single wave component, corresponding to particular values of  $k$  and  $\ell$ ,

$$\hat{h}(k,\ell) e^{i(kx + \ell y)}$$

and superpose the resulting calculated wave drag.

$$\text{Introducing } \tan\phi = \frac{\ell}{k} , \quad x = x' \cos\phi - y' \sin\phi ,$$

$$y = x' \sin\phi + y' \cos\phi ,$$

$$\kappa = \sqrt{k^2 + \ell^2} \quad \text{and} \quad \cos\phi = \frac{k}{\kappa} ,$$

one arrives at the result that

$$kx + \ell y = \kappa x' .$$

Consequently, the disturbance is

$$\hat{h}(\kappa, \phi) e^{i\kappa x'} ,$$

corresponding to corrugations in the  $x'$  direction and having no  $y'$  dependence. All of the perturbation quantities are also independent of  $y'$  for this mode and the linearized

conservation equations become:

$$U_n \rho_{x'} + w \bar{\rho}_z + \bar{\rho} [(u_n)_{x'} + w_z] = 0 \quad ,$$

$$U_n (u_n)_{x'} + w (U_n)_z + \frac{1}{\rho} P_{x'} = 0 \quad ,$$

$$U_n w_{x'} + \frac{\rho g}{\rho} + \frac{1}{\rho} P_z = 0 \quad ,$$

and

$$U_n T_{x'} + w (\bar{T}_z + \Gamma) = \frac{1}{\rho C_p} U_n P_{x'} \quad ,$$

with the boundary condition

$$w(0) = U_n h_{x'} \quad .$$

These equations do not contain  $U_p$  or  $u_p$ . (However,  $u_p$  apparently is not zero or constant with  $x'$  or  $z$  if  $U_p' \neq 0$  since  $U_n (u_p)_{x'} + w (U_p)_z = 0$ .) They are in exactly the form of the 2D equations. Consequently, we can make use of the previously derived 2D analyses<sup>(10)</sup> in substantial degree.

Substituting the spatial dependence  $e^{ikx'}$  into the above equations, we obtain:

$$ik U_n \hat{\rho} + \hat{w} \bar{\rho}_z + \bar{\rho} (ik \hat{u}_n + \hat{w}_z) = 0 \quad ,$$

$$ik U_n \hat{u}_n + \hat{w} (U_n)_z + \frac{ik}{\rho} \hat{p} = 0 \quad ,$$

$$ik U_n \hat{w} + \frac{\hat{\rho} g}{\rho} + \frac{\hat{p}_z}{\rho} = 0 \quad ,$$

$$ik U_n \hat{T} + \hat{w} (\bar{T}_z + \Gamma) = \frac{ik}{\rho C_p} \hat{p} \quad ,$$

$$w(0) = i\kappa\hat{h} \quad ,$$

and

$$\frac{\hat{p}}{\bar{p}} - \frac{\hat{T}}{\bar{T}} - \frac{\hat{\rho}}{\bar{\rho}} = 0$$

where the quantity  $\hat{\phi}$  denotes the coefficient of the Fourier component of  $\phi$  with wavenumbers  $k$  and  $l$ .

These equations are precisely the same as the 2D equations presented in Reference 10 as Equations (5.4a) - (5.4e), except for the replacements:

$$\kappa \rightarrow k$$

$$U_n \rightarrow U$$

and

$$\hat{u}_n \rightarrow \hat{u} \quad .$$

Therefore, we can incorporate the results of Equation (5.8) to obtain the equation for the vertical velocity  $\hat{w}$  :

$$\begin{aligned} \hat{w}_{zz} - \left(s + \frac{\mu_z}{\mu}\right)\hat{w}_z + \left[-\mu\kappa^2 + \frac{g}{U_n^2} \left(s + \frac{\mu_z}{\mu}\right) \right. \\ \left. + \frac{(U_n)_z}{U_n} \left(s + \frac{\mu_z}{\mu}\right) - \frac{(U_n)_{zz}}{U_n}\right]\hat{w} = 0 \end{aligned} \quad (6.16)$$

where

$$\mu = 1 - \left(\frac{U_n}{C_s}\right)^2, \quad s = -\frac{\bar{\rho}_z}{\bar{\rho}} \quad \text{and} \quad S = \frac{\bar{T}_z + \Gamma}{\bar{T}},$$

and  $C_s$  is the sound speed.

The  $\hat{w}_z$  term can be eliminated by the transformation:

$$x = \left(\frac{\bar{\rho}}{\mu}\right)^{\frac{1}{2}} \hat{w} \quad (6.17)$$

to give

$$x_{zz} + \left\{ -\mu\kappa^2 + \frac{g}{U_n^2} \left( s + \frac{\mu_z}{\mu} \right) + \frac{(U_n)_z}{U_n} \left( s + \frac{\mu_z}{\mu} \right) - \frac{(U_n)_{zz}}{U_n} + \frac{1}{4} \left( s + \frac{\mu_z}{\mu} \right)^2 + \frac{1}{2} \left( s + \frac{\mu_z}{\mu} \right)_z \right\} x = 0. \quad (6.18)$$

This equation can be compared with the corresponding 3D equations of Bretherton (Equation 49) and Sawyer<sup>(18)</sup> (Equation 10). The leading terms are seen to agree with the exception of terms which are normally very small. In particular, the approximation  $\mu \approx 1$  is justified, since the atmospheric motions are strongly subsonic. Consequently, the equations become:

$$\hat{w} = \left( \frac{\bar{\rho}}{\rho_0} \right)^{-\frac{1}{2}} \omega,$$

and

$$\omega_{zz} + \left\{ -\kappa^2 + \frac{gS}{U_n^2} + s \frac{(U_n)_z}{U_n} - \frac{(U_n)_{zz}}{U_n} + \left( \frac{s}{2} \right)^2 + \frac{s_z}{2} \right\} \omega = 0 \quad (6.19)$$

where  $\rho_0$  is the unperturbed atmospheric density at the surface.

We now consider the drag force on the lower boundary resulting from a particular Fourier component of the topography  $k, \ell$ . For this component  $\frac{\partial h}{\partial y'} = 0$  and

$$F_{x'} = -\frac{1}{XY} \iint p \frac{\partial h}{\partial x'} dx' dy' = \frac{1}{XY} \iint h \frac{\partial p}{\partial x'} dx' dy'$$

where  $X, Y$  are the horizontal grid limits. Substituting

from the momentum equations we obtain:

$$F_{x'} = - \frac{1}{XY} \iint \bar{\rho} h \left( U_n \frac{\partial u_n}{\partial x'} + w \frac{\partial U_n}{\partial z} \right) dx' dy' ,$$

where all quantities are evaluated at  $z = 0$ . Using the bottom boundary condition  $w(0) = U_n h_{x'}$ , and integrating by parts,

$$F_{x'} = \frac{1}{XY} \iint \bar{\rho} U_n h_{x'} u_n dx' dy' = \frac{1}{XY} \iint \bar{\rho} w u_n dx' dy' .$$

Consequently, the drag is equal to the Reynold's stress evaluated at the surface. In the direction parallel to the wavefront ( $y'$ ),  $F_{y'} = 0$ .

For the same Fourier component we now calculate the vertical dependence of the Reynold's stress and energy flux. The equations are simplified by eliminating the temperature and the density perturbations in favor of the vertical displacement,  $\xi$ . Following Eliassen and Palm,<sup>(19)</sup> the equations become:

$$\bar{\rho} \left( U_n \frac{\partial u_n}{\partial x'} + w U_n' \right) + \frac{\partial p}{\partial x'} = 0 , \quad (6.20)$$

$$\bar{\rho} \left( U_n \frac{\partial w}{\partial x'} + v_0^2 \xi \right) + \frac{\partial p}{\partial z} + \gamma g p = 0 , \quad (6.21)$$

$$\frac{\partial u_n}{\partial x'} + \frac{\partial w}{\partial z} - \gamma g w + \frac{\gamma U_n}{\bar{\rho}} \frac{\partial p}{\partial x'} = 0 , \quad (6.22)$$

and

$$w = U_n \frac{\partial \xi}{\partial z'} , \quad (6.23)$$

where  $\gamma$  characterizes the compressibility of the air  $\gamma = \frac{D\rho}{Dp}$  and  $\gamma^{-\frac{1}{2}}$  is the sound speed, and  $\Gamma = \frac{d\bar{\rho}}{d\bar{p}}$  is the density gradient of the unperturbed atmosphere. The static stability of the atmosphere is described by the Brunt-Vaisala frequency,  $v_o$ , given by  $v_o^2 = (\Gamma - \gamma)g^2$ . These quantities are considered to be constants characteristic of the atmosphere. In terms of them, the density perturbation  $\rho$  is given by:

$$\rho = \frac{v_o^2}{g} \bar{\rho} \xi + \gamma p \quad .$$

We obtain the wave energy equation by forming the sum of the products, Equation (6.20) times  $u_n$ , Equation (6.21) times  $w$ , and Equation (6.22) times  $p$ . The result is:

$$\frac{\partial}{\partial x'} (E u_n + p u_n) + \frac{\partial}{\partial z} (p w) = - \bar{\rho} (U_n)_z u_n w \quad ,$$

where

$$E = \frac{1}{2} \bar{\rho} (u_n^2 + w^2 + v_o^2 \xi^2 + \frac{\gamma p^2}{\rho^2})$$

is the wave energy. Integrating over the domain we obtain:

$$\frac{\partial}{\partial z} \iint p w \, dx' dy' = - (U_n)_z \bar{\rho} \iint u_n w \, dx' dy' \quad . \quad (6.24)$$

We can obtain another relation between these two quantities by multiplying Equation (6.20) by  $(\bar{\rho} U_n u_n + p)$ :

$$\begin{aligned} \frac{\partial}{\partial x'} \left( \frac{\bar{\rho}^2 U_n^2}{2} u_n^2 + \bar{\rho} U_n u_n p + \frac{p^2}{2} \right) \\ + \bar{\rho} (U_n)_z \left( \bar{\rho} U_n u_n w + p w \right) = 0 \quad . \end{aligned}$$

Integrating over the domain we obtain:

$$\iint p w \, dx' dy' = - \bar{\rho} U_n \iint u_n w \, dx' dy' \quad . \quad (6.25)$$

Comparing Equations (6.24) and (6.25) we conclude that:

$$\frac{\partial \left( \bar{\rho} \iint u_n w \, dx' dy' \right)}{\partial z} = 0 \quad ,$$

so that the Reynold's stress is independent of altitude if  $U_n \neq 0$ . Consequently, the momentum flux is constant with  $z$  and equal to the surface drag force in the absence of a critical layer where  $U_n = 0$ .

Since the quantity most readily available describing the perturbed motion is the vertical velocity from Equation (6.19), it is desirable to express the Reynold's stress in terms of the quantity  $w$ . We again follow Eliassen and Palm, using the continuity equation for a Fourier component in the  $\phi$ -direction. Multiplying Equation (6.22) by  $\frac{\partial w}{\partial x'}$ , we obtain:

$$\frac{\partial w}{\partial x'} \frac{\partial w}{\partial z} = - \frac{\partial u_n}{\partial x'} \frac{\partial w}{\partial x'} + \frac{\gamma g}{2} \frac{\partial w^2}{\partial x'} - \frac{\gamma U_n}{\rho} \frac{\partial P}{\partial x'} \frac{\partial w}{\partial x'} \quad .$$

Taking into account the dependence of each of the perturbed quantities on  $x'$  as  $e^{ikx'}$ , plus the result in Equation (6.14), this becomes after integration:

$$\kappa^2 \iint u_n w \, dx' dy' (1 - \gamma U_n^2) = - \iint \frac{\partial w}{\partial x'} \frac{\partial w}{\partial z} \, dx' dy' \quad .$$

Neglecting the small quantity  $\gamma U_n^2$  compared to 1, the average value of the Reynold's stress is expressed in terms of  $w$  as:

$$\frac{\bar{\rho}}{XY} \iint u_n w \, dx' dy' = - \frac{\bar{\rho}}{\kappa^2 XY} \iint \frac{\partial w}{\partial x'} \frac{\partial w}{\partial z} \, dx' dy' .$$

This quantity, the Reynold's stress in the  $x'$  direction due to the  $k, l$  component, can now be expressed in terms of  $\omega$  from the definition  $w = \text{Re} \left\{ \omega \left( \frac{\bar{\rho}}{\rho_0} \right)^{-\frac{1}{2}} e^{ikx'} \right\}$  :

$$F_{x'} = \frac{\bar{\rho}}{XY} \iint u_n w \, dx' dy' = - \frac{\rho_0}{2\kappa} \text{Im} \left\{ \omega^* \omega_z \right\} , \quad (6.26)$$

where  $\omega^*$  is the complex conjugate of  $\omega$  and  $\text{Im}$  denotes the imaginary part. It can readily be shown, from Equation (6.19) for  $\omega$ , that this quantity is strictly constant as a function of  $z$ .

The value of  $w$  in Equation (6.26) depends on the topography through the boundary condition at the surface,

$$w(0) = U_n \frac{\partial h}{\partial x'} .$$

Due to the linearity of the formulation, it is convenient to arrange Equation (6.26) into a topography-independent factor,

$$F = \frac{1}{2} \text{Im} \left\{ \omega^* \omega_z \right\} / \omega^*(0) \omega(0) \quad (6.27)$$

and a factor that depends on topography

$$\omega^*(0) \omega(0) = U_n^2 \kappa^2(0) \hat{n}^* \hat{n} = \frac{U_n^2(0) \kappa^2}{4\pi^2} A X Y \quad (6.28)$$

$$F_{x'} = - \frac{\rho_0 U_n^2(0)}{4\pi^2} F A X Y . \quad (6.29)$$

We now integrate over all wave numbers  $k, \ell$  to obtain the drag components:

$$F_x = \int_{-\infty}^{\infty} \int_{-\infty}^{\infty} \rho u w dx dy = 4\pi^2 \rho_0 \int_{-\infty}^{\infty} \int_{-\infty}^{\infty} \frac{1}{2k} \text{Im}(\omega^* \omega_z) dk d\ell ,$$

and

$$F_y = \int_{-\infty}^{\infty} \int_{-\infty}^{\infty} \rho v w dx dy = 4\pi^2 \rho_0 \int_{-\infty}^{\infty} \int_{-\infty}^{\infty} \frac{1}{2\ell} \text{Im}(\omega^* \omega_z) dk d\ell .$$

These are obtained by taking components of the Reynold's stress in the  $x'$  direction. In terms of  $\kappa$  and  $\phi$  the drag components are:

$$F_x = 4\pi^2 \int_{-\pi}^{\pi} \int_0^{\infty} F_{x'} \cos\phi d\phi \kappa d\kappa ,$$

and

$$F_y = 4\pi^2 \int_{-\pi}^{\pi} \int_0^{\infty} F_{x'} \sin\phi d\phi \kappa d\kappa .$$

Substituting and taking account that contributions from  $-k$  and  $k$  are the same,

$$F_x = -2\rho_0 \int_{-\pi/2}^{\pi/2} \int_0^{\infty} U_n^2(0) \cos\phi \kappa^2 F A d\phi d\kappa$$

and

$$F_y = -2\rho_0 \int_{-\pi/2}^{\pi/2} \int_0^{\infty} U_n^2(0) \sin\phi \kappa^2 F A d\phi d\kappa . \quad (6.30)$$

Equation (6.30) corresponds to Equation (54) of Bretherton and forms the basis for the linear steady-state calculations. The derivation shows that, even though the surface air density enters the equation, the density change with altitude is taken into account. Additional correction terms have been derived in Equation (6.19) which, under most circumstances, are small compared with the terms originally taken into account by Bretherton.

## 6.2 CODE DEVELOPMENT

In Section 6.1, the linear steady-state equations originally derived by Bretherton are generalized to include effects of density stratification. In this section the calculational procedure used in the two- and three-dimensional codes is briefly outlined, and areas which need further investigation are discussed.

A two-dimensional linear steady-state numerical model to calculate the vertical flux of horizontal momentum (wave drag), when both the motion of the flow field and the obstacle placed in the field are small, was described previously<sup>(1)</sup> and sample calculations were performed. This initial linear steady-state model has been extended to three-dimensions and work is in progress to enable both the 2D and 3D models to provide an initial parameterization of real topography in mountainous terrain range for use in the UCLA global circulation model (GCM).

The calculational sequence (valid for both codes) is shown in Figure 6.1. Some modifications from the flowchart presented in the previous progress report may be noted. However, the basic scheme has not been altered significantly.

Prior to running the large number of calculations required for a parameterization based on real topography,

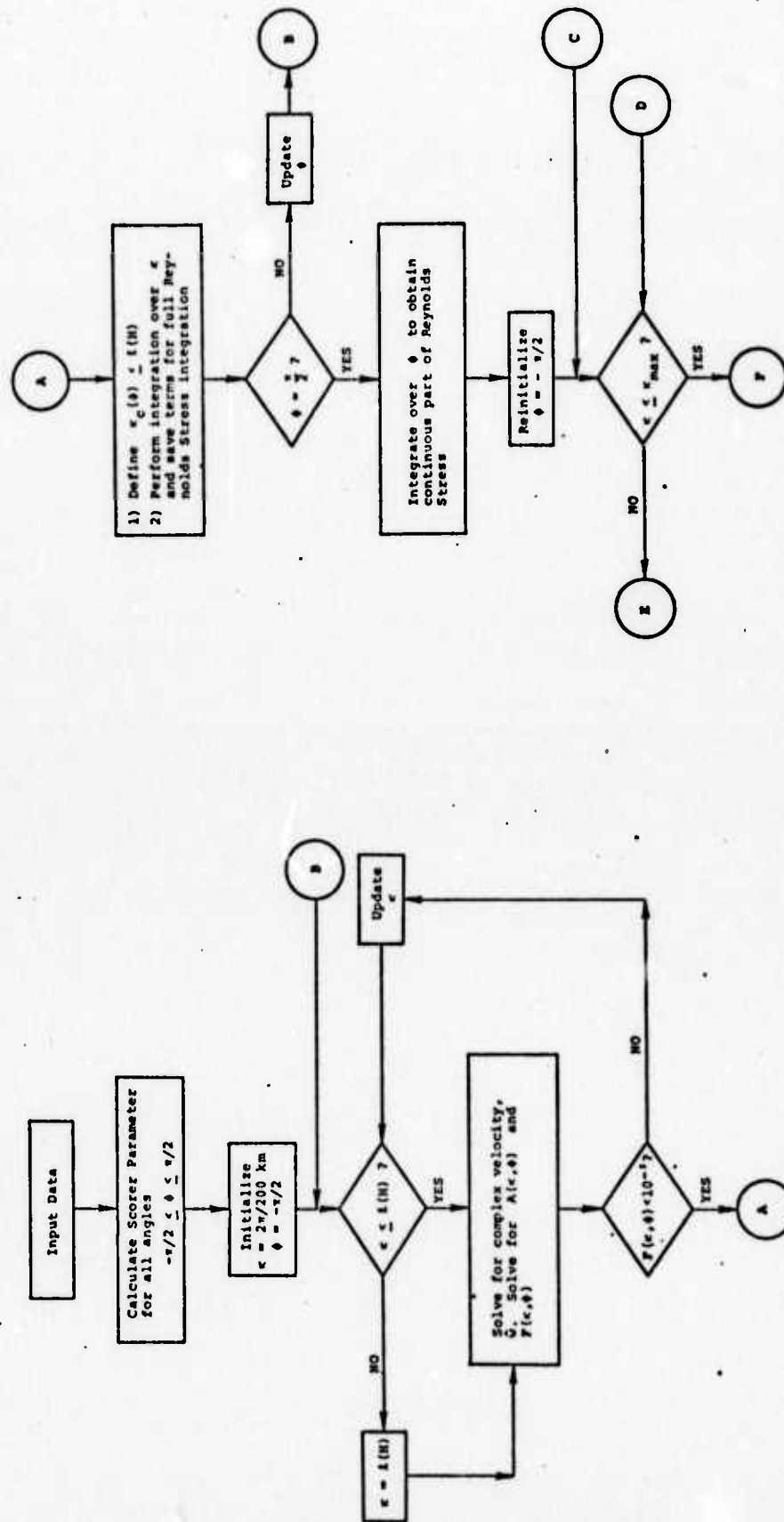


Figure 6.1 Flow chart of 3-D Bretherton code.

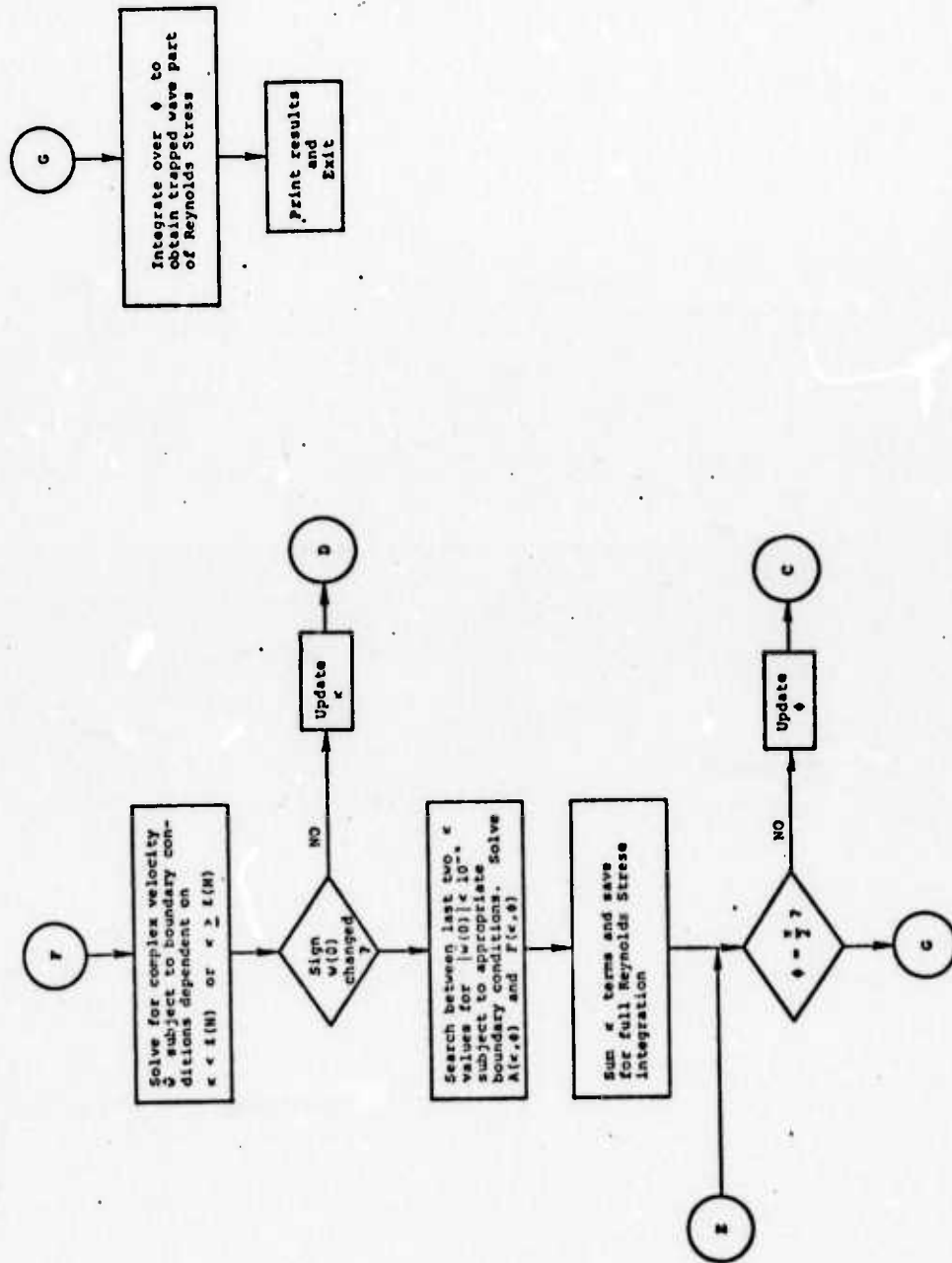


Figure 6.1 cont'd.

several calculations have been made using the two-dimensional code and a topographic description of the Sierra Nevada range obtained from the data tapes discussed in the next section. These calculations have led to several problem areas which are not completely resolved at this time. These principal problem areas, which are presently being explored, are: (1) the strong  $\kappa$  dependence of the spectrum function  $A$ , (2) finding methods to determine the optimum value of  $H$ ,  $\Delta\kappa$  and  $\Delta\phi$  and to explore the sensitivity of the codes to minor changes in their values; and (3) the effect of  $\kappa_c$  being nearly (but not quite) equal to  $l(H)$ .

For mountainous terrain like that of the Sierra Nevada and employing a reasonable  $\Delta x$  and  $\Delta y$  the spectrum function,  $A$ , can vary by several orders of magnitude and is acutely sensitive to the values of  $\kappa$ . A slight difference in  $\Delta\kappa$  has resulted in differences in the wave drag attributable to the continuous spectrum by a factor of two or more. The solution presently being explored is to compute  $A$  values for each point of a very fine grid of  $\kappa$  values and then integrate  $A$  over  $\Delta\kappa$  to obtain an average  $A$  value for each interval.

Suitable values of  $H$ ,  $\Delta\kappa$  and  $\Delta\phi$  are being determined by trial and comparison. Sensitivity cannot be fully explored until the  $A$  function is sufficiently smoothed and techniques are fully developed to utilize a coarse  $\Delta\kappa$  value without missing a trapped wave. This numerical problem is being solved by using smaller values of  $\Delta\kappa$  and different values of  $H$ .

These modifications are in the process of being implemented and tested.

### 6.3 TOPOGRAPHY DATA

In order to aid in the parameterization studies, S<sup>3</sup> has obtained computerized topographic data for the earth's surface. The tapes have been modified in order that the data for any location and grid size may be read and input into the linear steady-state codes. Three separate data collections are available. The first two, provided by the Defense Mapping Agency, include: (1) a worldwide description of 1° by 1° averaged elevations, and (2) 5' by 5' averaged elevation data including most of North America, Europe and Japan. The third data set, obtained from the U.S. Geological Survey gives 1' by 1' and 3' by 3' averaged elevations for the state of California. In addition to the surface elevations, the tapes include information on ocean depths and ice covering.

Figure 6.2 shows contours of elevations for the Owens Valley area in California taken from the 5' by 5' data. The total grid, a 1° by 1° square, represents only a portion of the data presently being used with the Bretherton calculations.

OWENS VALLEY GRID  
SECTOR 10

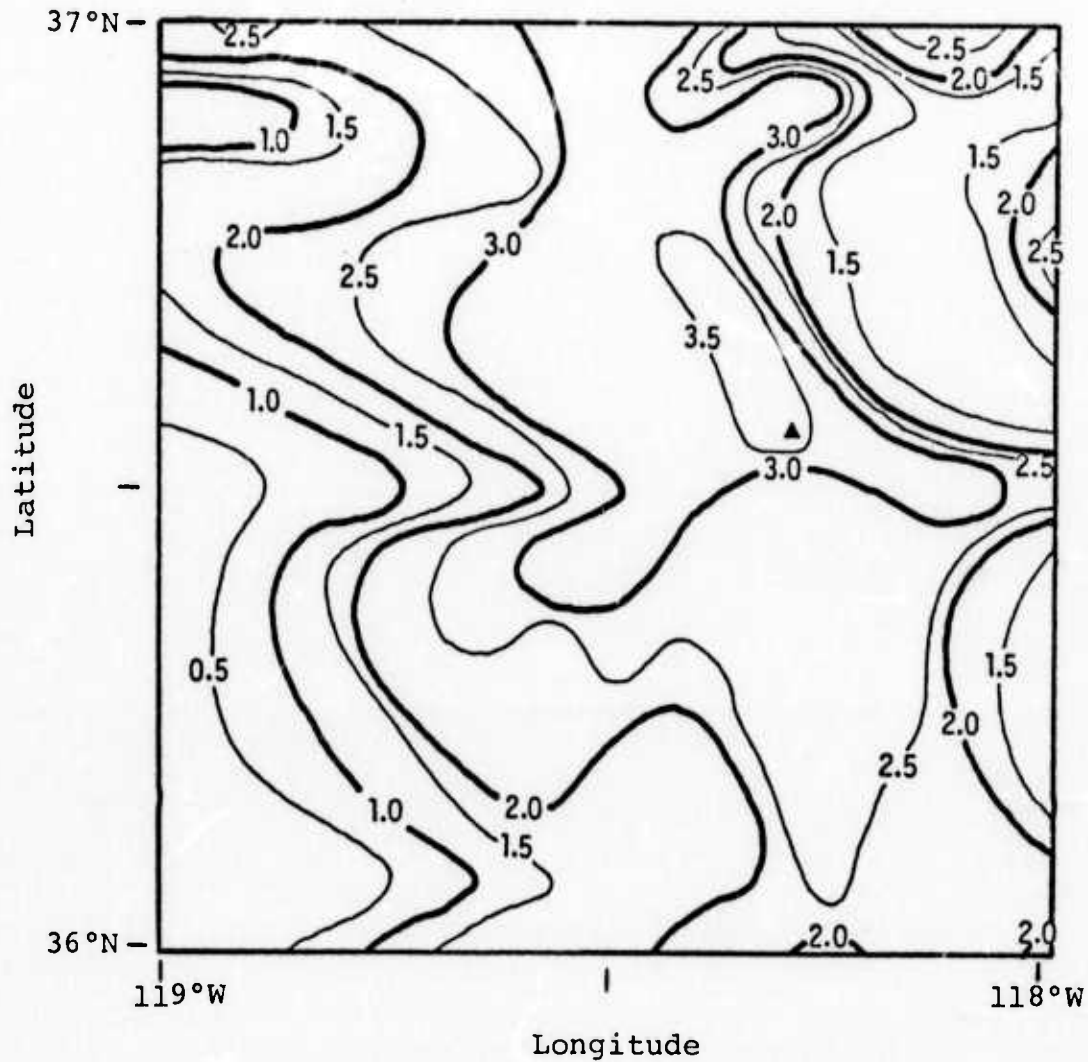


Figure 6.2 Elevation contours of the Owens Valley area of California.

▲ Mt. Whitney  
grid elevations  
in kilometers

## 7. A THREE-DIMENSIONAL BOUSSINESQ CODE 'STUFF'

During the past six months, a three-dimensional Boussinesq code to treat the low-speed laminar and turbulent motion of stratified fluids has been developed. The numerical technique used is unique and was developed using funds from this contract as well as independent research and development funds provided by S<sup>3</sup>. The code was initially written in two dimensions since several new concepts were involved and has since been extended to three dimensions. The code's name, STUFF, is an acronym for Stratifed Turbulent Unsteady Fluid Flow.

The principal difficulty involved in treating flows of this sort in the past has been that purely Eulerian finite difference procedures are diffusive in character. That is, diffusion-like errors in the finite-difference representation of the advection terms of the fundamental field equations will artificially "smear" the distribution of the field variables (i.e., density). Lagrangian procedures, on the other hand, avoid this difficulty but cannot treat flows in which high-amplitude waves or vortices occur such as those present in mountain lee wave phenomena since a Lagrangian grid will become so distorted that the finite difference approximations referred to such a grid will become meaningless.

The S<sup>3</sup> procedure avoids these difficulties by using both a Eulerian grid and an array of Lagrangian particles superimposed upon that grid which moves along with the fluid

as the calculation proceeds. All scalar field variables (density, turbulent energy, thermal energy) are carried by the Lagrangian marker particles as well as by the Eulerian grid. At late times, the Lagrangian net will become distorted just as in the purely Lagrangian case. Such distortion does not adversely affect the calculation, however, since all space derivatives of scalar field variables are determined using the Eulerian grid; the Eulerian values are determined by a "census" procedure which essentially sets the value of each scalar field variable within a Eulerian zone to the average of the values carried by the Lagrangian particles within the zone. On the other hand, the "artificial diffusion" which is characteristic of pure Eulerian schemes is absent, since advection effects are treated by moving the particles in a Lagrangian fashion.

In this chapter, the STUFF computer model, as presently developed at  $S^3$ , is outlined in detail. The equations, boundary and initial conditions, and results of sample calculations are presented.

Also included are two calculations of a viscous internal wave decay problem which demonstrates the numerical diffusion associated with one Eulerian treatment of scalar advection transport (relative to the Eulerian/Lagrangian method in STUFF).

## 7.1 DERIVATION OF EQUATIONS

The equations in the Boussinesq approximation which express the conservation of mass, momentum and energy within the fluid system in the STUFF code are:

Mass

$$\frac{\partial}{\partial x_j} (U'_j) = 0 \quad (7.1)$$

Momentum

$$\begin{aligned} \frac{\partial}{\partial t} (U'_i) + \frac{\partial}{\partial x_j} (U'_i U'_j) &= \frac{\partial}{\partial x_j} \left[ v \frac{\partial}{\partial x_j} (U'_i) \right] - \frac{\partial \phi'}{\partial x_i} \\ &+ Qg_i + S \end{aligned} \quad (7.2)$$

Energy

$$\frac{\partial Q}{\partial t} + \frac{\partial}{\partial x_j} (U'_j Q) = \frac{\partial}{\partial x_j} \left[ D \frac{\partial}{\partial x_j} (Q) \right] + \pi_Q \quad (7.3)$$

where

$U'_1, U'_2, U'_3$  = components of velocity in  $x_1, x_2, x_3$  directions,

$S$  = momentum source ,

$Q$  = Boussinesq parameter =  $(\rho/\rho_0 - 1) = -\beta(T - T_0)$  ,

$\beta$  = volumetric expansion coefficient ,

$\rho$  = density ,

$g_i$  = gravity acceleration component in  $x_i$  direction

$\pi_Q$  = energy source term ,

$v$  = molecular kinematical viscosity ,

$D$  = molecular diffusion coefficient ,

and

$\phi'$  = the departure of the atmospheric pressure from the hydrostatic pressure divided by the reference density.

The turbulence scheme of Gawain and Pritchett<sup>(20)</sup> used previously in the HAIFA code, is an integral part of the computer model and will be reiterated here in some detail for completeness. However, it should be noted that alternative schemes based on a mixing length theory could be used. Additionally, the present model allows a prescribed set of diffusion coefficients at any space points in the numerical grid.

The derivation of the equations including the turbulence scheme is shown below. Only the momentum and mass equations are discussed in detail; the energy equation follows directly with  $D$  being redefined to include both the molecular and turbulent diffusion coefficient. As previously noted,<sup>(1)</sup> the development of the turbulent energy equation as described by Gawain and Pritchett neglects the temperature stratification term  $-\overline{\rho' u_i'} \frac{g}{\rho_0}$  which can have a significant effect on the results of the problems associated with our studies. The investigation of a heuristic model for this term has not yet been carried out at  $S^3$  and a formulation must be developed to describe its relation to the mean flow and temperature fields. This term has been included in the final equations, however, by assuming that the thermal eddy diffusivity  $E'$  can be used to relate this buoyancy term to the mean temperature field and that  $\epsilon'$  is equal to  $\epsilon$ , the momentum eddy diffusivity.

Using a standard procedure, we define the  $U'$ ,  $\phi'$ , and  $\rho'$  fields as the sums of mean and fluctuating components

$$U_i' = U_i + u_i \quad ,$$

$$\phi' = \phi + \phi$$

and

$$\rho' = \rho_0 + \rho \quad .$$

Now performing ensemble averaging, we obtain the conservation equations for the mean flow:

Mean Flow Continuity

$$\frac{\partial}{\partial x_j} (U_j) = 0$$

and

Mean Flow Momentum

$$\frac{\partial}{\partial t} (U_i) + \frac{\partial}{\partial x_j} (U_i U_j) = \frac{\partial}{\partial x_j} \left\{ \nu \left( \frac{\partial U_i}{\partial x_j} + \frac{U_j}{x_i} \right) - \overline{u_i u_j} \right\} - \frac{\partial \phi}{\partial x_i} + Qg_i + S \quad .$$

If it were not for the Reynolds stress term appearing in the momentum equation, the solution would be straightforward. The stress term can, however, be related heuristically to the strain rates of the mean flow through an eddy viscosity  $\epsilon$  via the relation:

$$-\overline{u_i u_j} = -\frac{1}{3} \overline{u_k u_k} \delta_{ij} + \epsilon \left( \frac{\partial U_i}{\partial x_j} + \frac{\partial U_j}{\partial x_i} \right) \quad (7.4)$$

or more simply

$$-\overline{u_i u_j} = -\frac{1}{3} \overline{u_k u_k} \delta_{ij} + \epsilon \Gamma_{ij} \quad (7.5)$$

where

$$\Gamma_{ij} = \frac{\partial U_i}{\partial x_j} + \frac{\partial U_j}{\partial x_i}$$

is the strain rate tensor. With this relation we may now rewrite the mean flow momentum equation as:

$$\begin{aligned} \frac{\partial}{\partial t} (U_i) + \frac{\partial}{\partial x_j} (U_i U_j) = \frac{\partial}{\partial x_j} \left[ (\nu + \epsilon) \Gamma_{ij} \right] - \frac{\partial P}{\partial x_i} \\ + Qg_i + S \end{aligned} \quad (7.6)$$

where

$$P = \phi + \frac{2}{3} \overline{\frac{u_j u_j}{2}} .$$

It now remains to determine the functional form of  $\epsilon$ . Since we are about to postulate a functional dependence of  $\epsilon$  on the local turbulent kinetic energy, we will now include the turbulent energy equation in our equation set.

We return to the conservation equations and obtain an expression of the following form:

$$\begin{aligned}
\frac{\partial}{\partial t} (E) + \frac{\partial}{\partial x_k} (U_k E) &= - \frac{\overline{u_j u_k}}{2} \left( \frac{\partial U_j}{\partial x_k} + \frac{\partial U_k}{\partial x_j} \right) \\
&\quad - \frac{\nu}{2} \left( \frac{\partial u_j}{\partial x_k} + \frac{\partial u_k}{\partial x_j} \right) \left( \frac{\partial u_j}{\partial x_k} + \frac{\partial u_k}{\partial x_j} \right) \\
&\quad - \frac{\partial}{\partial x_k} \left[ \overline{u_k (E + \phi)} \right] + \overline{\rho u_j} \frac{g_i}{\rho_0} \\
&\quad + \nu \frac{\partial}{\partial x_k} \left[ \frac{\partial}{\partial x_k} (E) + \frac{\partial}{\partial x_j} (\overline{u_j u_k}) \right] \quad (7.7)
\end{aligned}$$

where

$$E = \frac{\overline{u_j u_j}}{2} .$$

The terms on the right represent work done by the mean flow against the Reynold's stresses, dissipation as heat,  $(\dot{E}_H)$ , the effects of fluid stratification on turbulent energy dissipation, turbulent diffusion  $(\dot{E}_D)$ , and molecular diffusion. Henceforth, the molecular diffusion term will be assumed negligible as compared to the other terms. Using the relation coupling strain rates to stress we have:

$$\begin{aligned}
\frac{\partial}{\partial t} (E) + \frac{\partial}{\partial x_k} (U_k E) &= \frac{\epsilon}{2} \Gamma_{jk} \Gamma_{jk} \\
&\quad - \frac{\nu}{2} \left( \frac{\partial u_j}{\partial x_k} + \frac{\partial u_k}{\partial x_j} \right) \left( \frac{\partial u_j}{\partial x_k} + \frac{\partial u_k}{\partial x_j} \right) + \overline{\rho u_j} \frac{g_i}{\rho_0} \\
&\quad - \frac{\partial}{\partial x_k} \left[ \overline{u_k (E + \phi)} \right] . \quad (7.8)
\end{aligned}$$

At this point in time it is appropriate to examine the approach to be taken in solving the equation set. The attempt will be made to derive empirical expressions for the dissipative and remaining diffusive term in the turbulent energy equation. Once this has been accomplished, the local eddy viscosity will then be postulated as functionally dependent at the least on the local turbulent energy.

The diffusive term is relatively simple to approximate with a heuristic substitute. Gawain and Pritchett, basing their arguments on dimensional and physical grounds, derive the following expression:

$$u_k \frac{\overline{u_j u_j}}{2} + \phi = -\gamma \epsilon \frac{\partial E}{\partial x_k} \quad (7.9)$$

so that the diffusion term in the turbulent energy equation becomes

$$\dot{E}_D = \frac{\partial}{\partial x_k} \left( \gamma E \frac{\partial E}{\partial x_k} \right)$$

where  $\gamma$  in this case is a slowly varying function whose form is empirically derived from past experiments. An explicit expression of  $\gamma$  will be given later. In a similar manner, the buoyancy term  $\overline{\rho u_j} \frac{g_i}{\rho_0}$  is set equal to  $-\gamma E' \frac{\partial Q}{\partial x_j}$ .

In order to develop expressions for turbulent Reynolds stresses, eddy viscosities, and dissipation rates, it is necessary to establish a "macro-scale" associated with the motion. Utilizing the fact that the flow characteristics at a point are influenced principally by the field immediately surrounding the point, Gawain and Pritchett have derived a heuristic formulation for the macro-scale of the following form:

$$\lambda^2(\vec{x}) = I^2(\vec{x}) / J^2(\vec{x})$$

$$I^2(\vec{x}) = \int_{\text{All Space}} w(\vec{x}, \vec{x}') \Omega^4(\vec{x}') dv'$$

$$J^2(\vec{x}) = \int_{\text{All Space}} w(\vec{x}, \vec{x}') \left[ \Omega \Omega'(\vec{x}') \right]^2 dv'$$

$$w(\vec{x}, \vec{x}') = \frac{\exp \left[ - \frac{(\vec{x} - \vec{x}') \cdot (\vec{x} - \vec{x}')}{\lambda^2(\vec{x})} \right]}{\int_{\text{All Space}} \exp \left[ - \frac{(\vec{x} - \vec{x}') \cdot (\vec{x} - \vec{x}')}{\lambda^2(\vec{x})} \right] dv'}$$

$$\Omega^2 = \frac{1}{2} \Gamma_{ij} \Gamma_{ij}$$

$$(\Omega')^2 = (\partial \Omega / \partial x_i) (\partial \Omega / \partial x_i) \quad . \quad (7.10)$$

Note that  $\lambda$  must be solved for in an iterative fashion, since it appears on both sides of the equation. The Gawain Pritchett scheme models turbulent energy dissipation to heat by:

$$\dot{E}_H = \beta (2E)^{7/6} J^{1/3} \quad ; \quad (7.11)$$

$\beta$  is similar to  $\gamma$ , and will be defined later.

We now need only to obtain an expression for  $\epsilon$  and we will achieve a practical closure. One would expect that the eddy viscosity at a space time point would be somehow related to the local turbulent energy density. Also, it should depend on the macroscale at that point. An appropriate dimensional combination of these quantities is

$$\epsilon = \alpha \lambda (2E)^{1/2} \quad . \quad (7.12)$$

This is the final relation needed to effect closure.  $\alpha$ ,  $\beta$ , and  $\gamma$  are now defined as slowly varying functions which have been determined from experiments and are expressed as follows:

$$\begin{aligned} \alpha &= 0.065 \left\{ 1 + \exp \left[ - \left( \frac{y}{\lambda} - 1 \right)^2 \right] \right\} \\ \frac{1}{\beta} &= 3.7 \left\{ 1 + \exp \left[ - \left( \frac{y}{\lambda} - 1 \right)^2 \right] \right\} \\ \gamma &= 1.4 - 0.4 \exp \left[ - \left( \frac{y}{\lambda} - 1 \right)^2 \right] \end{aligned} \quad (7.13)$$

where  $y$  is the distance to the nearest physical boundary from the space grid point and where  $y/\lambda$  is never permitted to exceed unity.

The final hydrodynamic equations including the assumption that the thermal eddy diffusivities are equal to the momentum eddy diffusivities are:

$$\frac{\partial}{\partial x_i} (U_i) = 0 \quad (7.14)$$

$$\begin{aligned} \frac{\partial}{\partial t} (U_i) + \frac{\partial}{\partial x_j} (U_i U_j) &= \frac{\partial}{\partial x_j} \left[ (v + \alpha \lambda \sqrt{2E}) \left( \frac{\partial U_i}{\partial x_j} + \frac{\partial U_j}{\partial x_i} \right) \right] - \frac{\partial P}{\partial x_i} \\ &+ Qg_i + S \end{aligned} \quad (7.15)$$

$$\frac{\partial}{\partial t} (Q) + \frac{\partial}{\partial x_j} (U_j Q) = \frac{\partial}{\partial x_j} \left[ (\alpha \lambda \gamma \sqrt{2E} + D) \frac{\partial Q}{\partial x_j} \right] + \pi_Q \quad (7.16)$$

$$\begin{aligned} \frac{\partial}{\partial t} (E) + \frac{\partial}{\partial x_j} (U_j E) &= \alpha \lambda \sqrt{2E} \Omega^2 - \beta (2E)^{7/6} J^{1/3} \\ &+ \frac{\partial}{\partial x_j} \left( \alpha \gamma \lambda \sqrt{2E} \frac{\partial E}{\partial x_j} \right) \\ &- \alpha \gamma \lambda \sqrt{2E} g_j \frac{\partial Q}{\partial x_j} \end{aligned} \quad (7.17)$$

In effect, Gawain and Pritchett's equations have been modified to include a buoyancy term in the momentum equation in the vertical direction, and the effects of fluid stratification on turbulent energy dissipation.

Note that the total energy equation carried through the derivation results in a final equation which is identical to Equation (4.3) with  $D$  being redefined to include both the molecular and turbulent diffusion coefficient.

The source/sink terms in the equations may be used to include the effects of radiation losses, and surface friction losses. In each case, the terms would be included using a prescription obtained from the literature.

## 7.2 THE NUMERICAL SCHEME

In this section, the 2-D procedure used will be discussed; the 3-D extension is straightforward. The treatment of the momentum Equation (7.2) is explicit and second-order in space. Time derivatives may be specified as either first or second order by the user. The direct calculation of the pressure is avoided by the method of Chorin.<sup>(21)</sup> In this

method, "tentative" new velocities  $(\tilde{u}^{n+1}, \tilde{w}^{n+1})$  after a short time interval  $(\tau)$  are computed based upon the "old" velocities  $(u^n, w^n)$  using finite-difference versions of the momentum equations, but neglecting the pressure gradient terms. Next, since a pressure field alone cannot impart rotation to the fluid, the true new velocities cannot differ from the "tentative" values by more than a vector field which is the gradient of a scalar "velocity corrector potential"  $\psi$  :

$$u^{n+1} = \tilde{u}^{n+1} + \frac{\partial \psi}{\partial x} \quad , \quad w^{n+1} = \tilde{w}^{n+1} + \frac{\partial \psi}{\partial z} \quad . \quad (7.18)$$

Furthermore, the final new velocities must satisfy the continuity condition:

$$\frac{\partial u^{n+1}}{\partial x} + \frac{\partial w^{n+1}}{\partial z} = 0 \quad (7.19)$$

which, when combined with Equations (7.17) and (7.18), provides a Poissons equation for the  $\psi$  field:

$$\frac{\partial^2 \psi}{\partial x^2} + \frac{\partial^2 \psi}{\partial z^2} = - \frac{\partial \tilde{u}^{n+1}}{\partial x} - \frac{\partial \tilde{w}^{n+1}}{\partial z}$$

This equation is solved by an over-relaxed Gauss Seidel iteration procedure for  $\psi$  , and then the final new velocities are determined using Equation (7.18). The above procedure is first-order in time. The code also allows a second-order time approximation by iterating twice on the above procedure. Upon completion of the solution for the new (updated) velocities, the solution of the turbulent energy equation and thus the eddy diffusion coefficient may be obtained. The energy is then updated based upon the new velocities.

An important property of this code is the treatment of the scalar fields. An array of tracer particles is introduced which move with the mean flow, each particle has associated with it values of each field  $Q$ . To find values for these variables for a given computational cell, a "census" is taken of those particles within the cell at the time and the mean particle-based value is used for the cell as a whole. Given the cell-centered values for  $Q$ , a time rate of change of  $Q$  due to diffusion and source terms (the right-hand side of Equation (7.16) may be computed for each cell. Next, the particle-based values of  $Q$  for those particles within the cell are changed at that rate for a short time interval  $\Delta t$ . Then, new velocities ( $u$  and  $w$ ) are calculated using the momentum equations, and finally the particles are moved to their new positions.

The advantage of this procedure over more conventional techniques is that no "numerical diffusion" of the scalar fields can occur. In ordinary Eulerian finite-difference schemes, it may be shown that high-order truncation errors in the finite-difference treatment of the advection terms of the scalar transport equation will inevitably produce fictitious diffusion-like effects.<sup>(22)</sup> In some procedures, this diffusion is always positive and smears the  $Q$  distribution; in others, it may be negative and cause computational instability. The present procedure circumvents these difficulties by simply not calculating the advection terms explicitly, but instead treating advection implicitly (that is, by moving the marker particles).

### 7.3 BOUNDARY CONDITIONS

Both STUFF2 (2-D) and STUFF3 (3-D) allow several possible boundary structures. Any or all of the outer walls of

the grid may be set to simulate rigid, impermeable "free slip" walls, or one may choose to make the x-direction periodic. The latter case will allow comparison with HAIFA calculations. Internal boundaries are managed by the introduction of obstacle cells with impenetrable walls. The obstacle cells may be placed in any number and arrangement throughout the grid. One sees then that topography is easily handled through judicious arrangement of these cells. The last major feature presently incorporated is the provision for specifying any physically meaningful combination of outer walls as "planes of symmetry." Many problems encountered express some symmetry properties. Taking advantage of this feature of the code will allow considerable saving in computer cost since only a fraction of the physical problem need be modeled.

#### 7.4 INITIAL CONDITIONS

The initial flow field and scalar fields must be specified in STUFF. All scalar fields may be initialized in the following ways: (1) one may construct a field by specifying a series of rectangular cell blocks at a given temperature or density, (2) one may construct the field via specification of a vertical profile of essentially arbitrary functional form, and (3) one may initialize via a series of Gaussian distributions throughout the grid. With the attendant "flags" in the code, one may choose any possible combination of the above techniques to achieve the desired scalar field structure.

The initial flow field also can be specified in several ways. The prime requirement, however, is that no matter how pathological one wishes to be, the resulting field must be non-divergent. The simplest method of flow specification is that of a uniform flow in the x-direction. If this is specified,

then the field will be derived from potential flow and the given boundary flow. One may, as in the case of scalar fields, specify cell blocks as having given flow characteristics. The option is available for combinations of these blocks with the flow derived from the potential function to obtain a resultant field.

In addition to the above options in specifying flow, STUFF contains an elaborate intake/exhaust system. This system consists of groups of intake and/or exhaust cells which may be arbitrarily positioned throughout the grid. They are true sources/sinks of mass, momentum, and energy; hence, one must be careful in constructing the system to insure conservation of these quantities. Through judicious positioning of an intake system at the right edge of the grid and an exhaust system at the left edge of the grid, an upstream flow profile of essentially arbitrary structure may be maintained. This feature is extremely useful in constructing velocity profiles which are  $z$  dependent.

#### 7.5 BUFFERING

Perhaps one of the most advantageous features of STUFF is a technique of buffering the Lagrangian particles to mass storage devices. The particles are buffered in groups of approximately 500 and are retrieved in sequence as the need arises and then once again buffered. The result is that only 500 particles are in core at one time. This feature allows one to effectively specify an unlimited number of particles, if it is desired. Except for pathological cases, program run times are not significantly altered by the buffering scheme since efficient techniques are employed in the information transfer between core and the device. So far, this feature is implemented only in the 3-D code (STUFF3).

## 7.6 OTHER FEATURES

STUFF presently features a "restart" capability. This technique is accomplished via a dump to tape of all current values of interest at the time of the break. Restart simply implies the reading of the tape to initialize the code variables. In addition, one currently has the option of producing printer plots and dumps of the field arrays of interest at user-specified cycle intervals. The contour plots consist of successive vertical cuts of the grid in the x-y plane (where y is the vertical direction) through the midpoints of each cell in the z-direction. The plotted quantities are the cell centered values of the field array in question. The above description of code logic is best summarized in a macro-logic flow diagram for STUFF shown in Figure 7.1

## 7.7 SAMPLE CALCULATIONS

Test problems have been completed using the STUFF code in both a two-dimensional and three-dimensional configuration. The problems give an indication of the code's capabilities to treat flows over mountains. Two-dimensional problems were calculated for flow over a rectangular obstacle, and the results were compared with HAIFA. The agreement was good with no significant differences showing up in the results.

A typical three-dimensional test problem was constructed for the STUFF code. The problem was also configured so as to simulate flow over a rectangular obstacle in a vertically stratified atmosphere. The stratification was represented via a Boussinesq parameter distribution corresponding to a temperature lapse rate of one-half the dry adiabatic lapse rate. An input flow profile corresponding to

$$U(y) = (10 + 0.02y) \text{ m/s}$$

was included. No cross-winds were specified in this problem

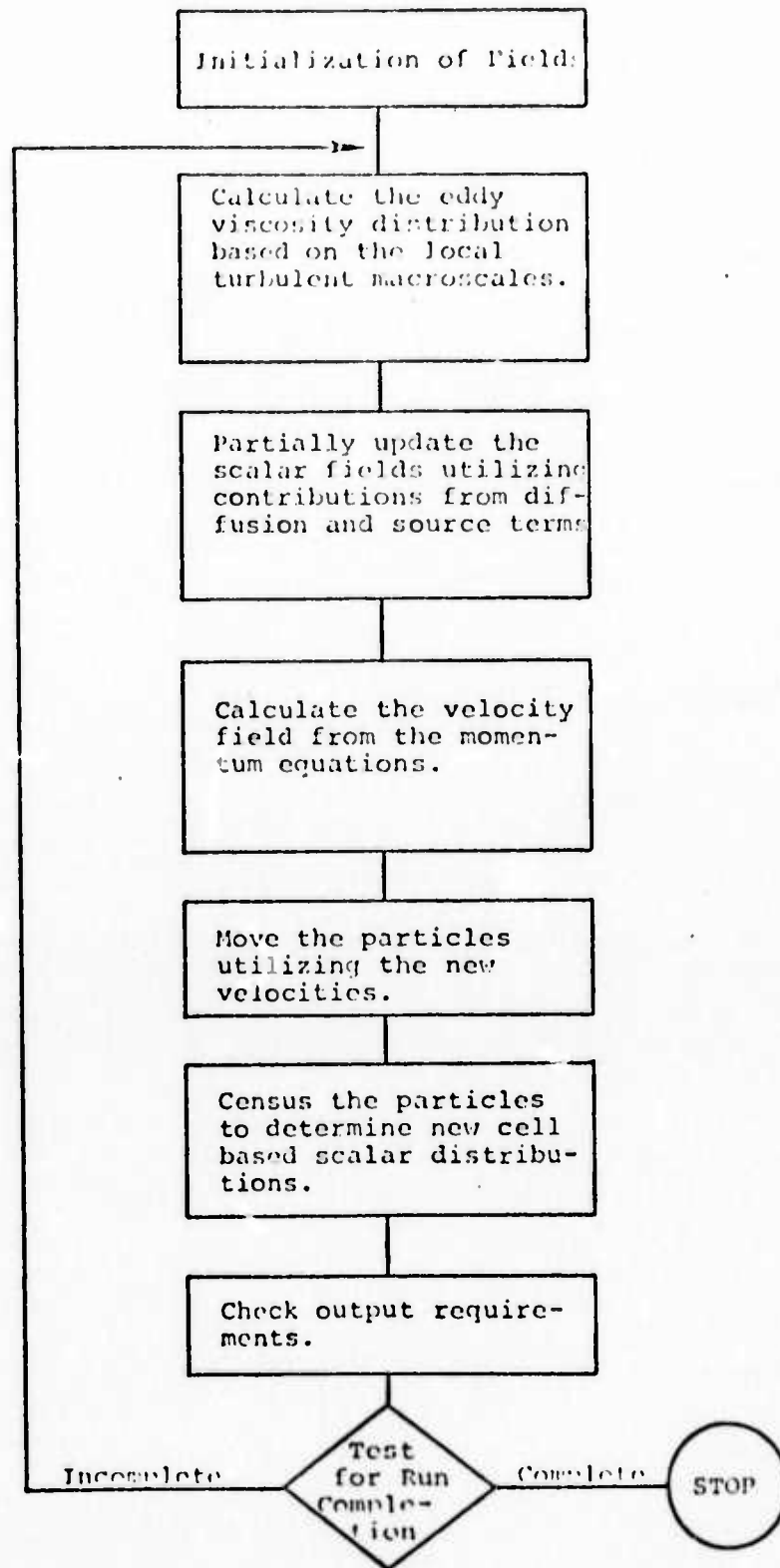


Figure 7.1 General flow diagram for STUFF.

but the option has been checked out in a separate calculation. The obstacle consisted of a rectangular block one cell high, two cells wide and one cell long, where each cell in the grid represents a cubical volume 1 km on a side. The grid extends eight cells in the horizontal direction and five in the vertical. Since the input flow is uni-directional, problem symmetry exists about a plane which bisects the obstacle in the direction of flow. For this reason, the symmetry handling capabilities of STUFF were utilized. The obstacle was placed against the near side of the grid in the bottom cell layer close to the left edge. The obstacle reduces to one cell in the symmetric case. The results of this problem, after 50 iterative cycles, are given in Figures 7.2 through 7.4. These results present the velocity flow field over and around the obstacle. As noted in the figures, acceleration of the flow around the obstacle is much more evident than the acceleration over it. It is necessary to point out that these results are only a summarization of the flow field lifted from the computer printout after 50 calculational cycles. Some further calculations are planned but the major emphasis of the work on this code since this calculation has been to optimize the core storage to allow larger grids to be used in the calculation. Presently, we feel that a three-dimensional grid of 10 x 10 x 20 cells is possible using the 64 K storage in the Univac 1108 machine.

#### 7.7.1 Treatment of Advection - Viscous Wave Calculations

Numerical diffusion errors can have profound effects upon the solutions obtained using hydrodynamic codes. As an illustration, a laminar internal wave problem was solved twice; once using the STUFF 2-D code and once using a conventional Eulerian finite-difference scheme. The case considered was that of the oscillation of a viscous-damped internal wave in a channel of unit height acted upon by a unit downward

20	21	23	25	27	29	28	24
20	21	24	26	28	29	29	24
20	21	24	27	28	29	28	23
20	20	22	24	25	24	24	22
18	13	4	0	4	11	17	19

x-direction

y-direction

Figure 7.2 Lateral (x-direction) velocities (cell centered in m/s) for lowest horizontal layer of cells ( $K > 5$  not represented).

100	100	99	98	97	96	96	96	98
80	81	81	81	80	79	79	79	80
60	60	60	60	60	59	59	59	60
39	38	39	40	39	37	37	36	38
19	13	5	0	4	11	11	17	19

y-direction

x-direction

Figure 7.3 Lateral (x-direction) velocities (cell centered in m/s) in a vertical slice taken through the obstacle centerline.

0	0	0	0	0	0	0	0	0	0
0	0	0	0	0	0	0	0	0	0
0	1	1	1	1	1	1	0	0	-2
1	1	1	1	0	0	0	0	-1	-2
1	2	4	0	-3	-2	-2	-3	-2	-3

x-direction

Figure 7.4 Axial (y-direction) velocities (cell centered in m/s) in a vertical slice taken through the obstacle centerline.

y-direction

gravity acceleration (see Figure 7.5). The wavelength was equal to two, and the fluid's molecular kinematic viscosity ( $\nu$ ) was  $5 \times 10^{-4}$ , yielding a Reynolds number of about 50 ( $N_R = A^2/T\nu$ , where  $A$  = amplitude,  $T$  = period,  $\nu$  = kinematic viscosity). In the upper portion of the fluid, the density was 0.95 and in the lower portion 1.05, as shown; initially, the fluid was motionless. To isolate the effects of numerical diffusion, the thermal diffusivity (i.e., "density diffusivity") of the fluid was set to zero. Thus, in principle, the density of a particular fluid element should never change through the calculation, and the interface between the two regions should remain sharply defined. For both calculations, a 20x20 computational mesh was used, and the time step was fixed at 0.05. The same finite-difference procedure was used for both calculations, except that the density transport equation in one case was treated using the STUFF Eulerian-Lagrangian particle technique. In the other calculation, a conventional pure Eulerian "donor-cell" first order scheme was applied. This latter procedure is in common use in many operational codes (see, for example, Hirt and Cook<sup>(23)</sup>).

Figure 7.6 shows the evolution with time of the density field. As can be seen, in the STUFF calculation the density interface remains sharp (i.e., one computational cell thick) whereas in the purely Eulerian calculation the interface diffuses more and more widely as time goes on. Figure 7.7 shows the density distribution along the left-hand edge of the grid ( $x = 0$ ) at  $t = 25$  for both cases; by this time, the Eulerian procedure has "smeared" the interface over a vertical region comparable to the wave height itself. This "smearing" of the density field, in turn, affects the overall fluid flow pattern.

Figure 7.8 shows, as a function of time, the height of the interface along the left-hand edge of the grid. In the Eulerian case, the interface height was taken as the height where  $\rho = 1.0$ . Agreement is fairly good out to  $t = 7$  or so,

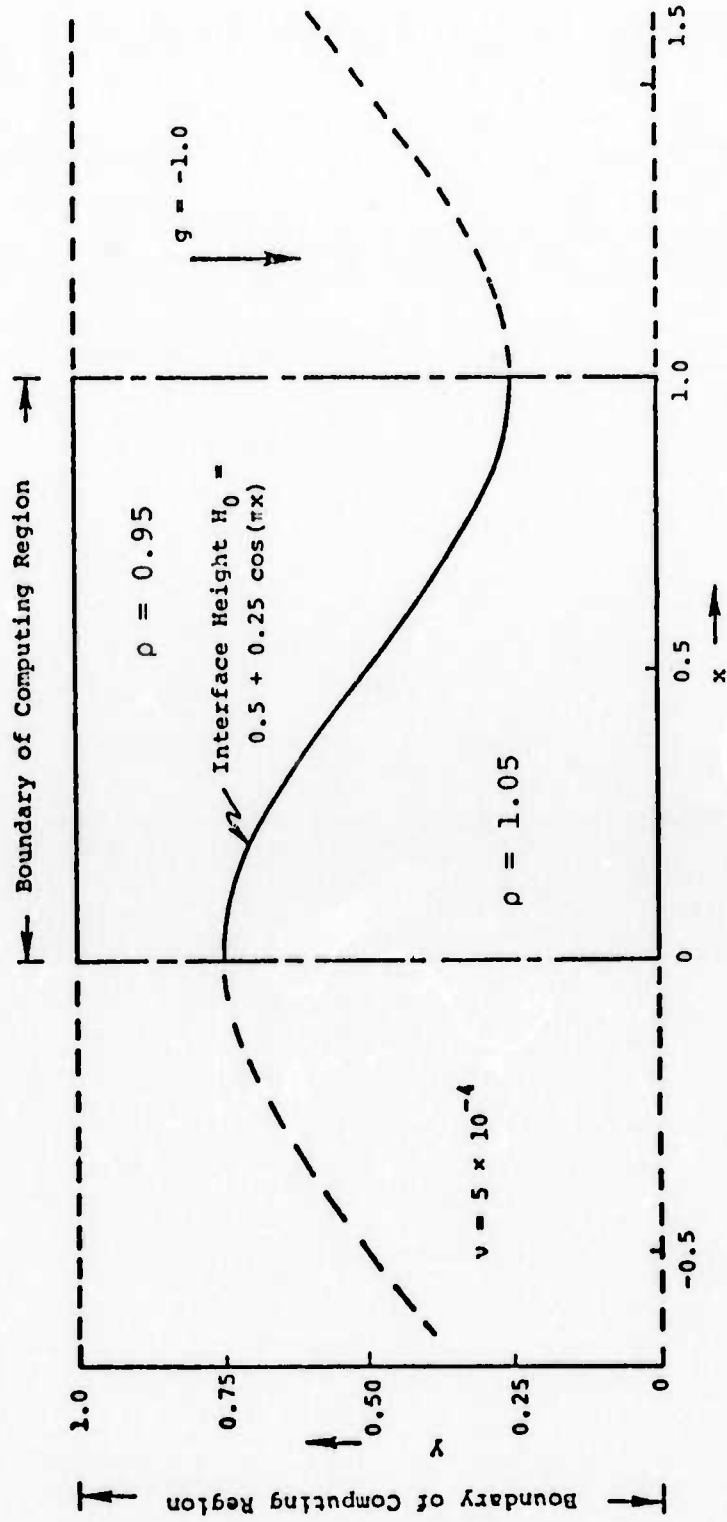
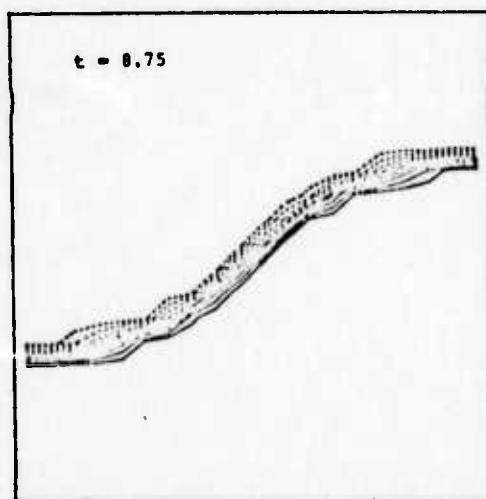
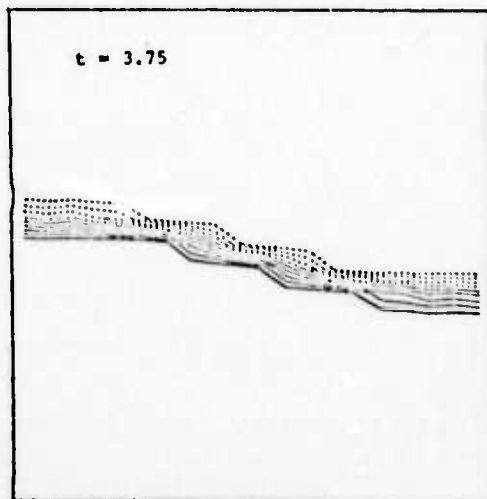
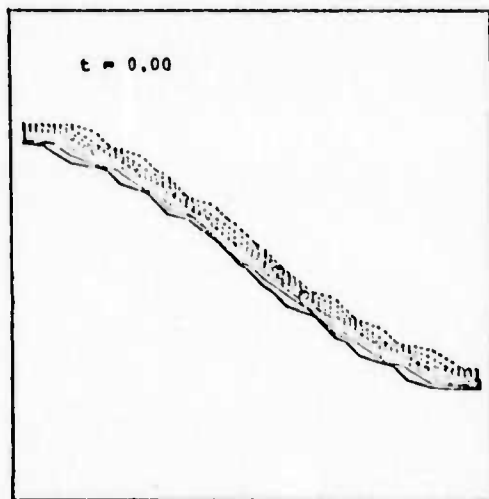


Figure 7.5 Initial conditions for laminar internal wave test problem.

## EULERIAN/LAGRANGIAN



## PURE EULERIAN

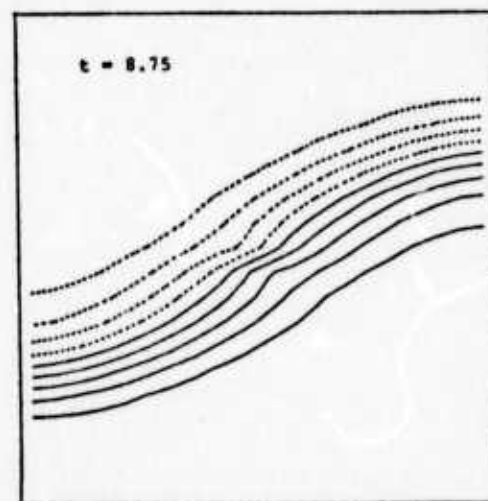
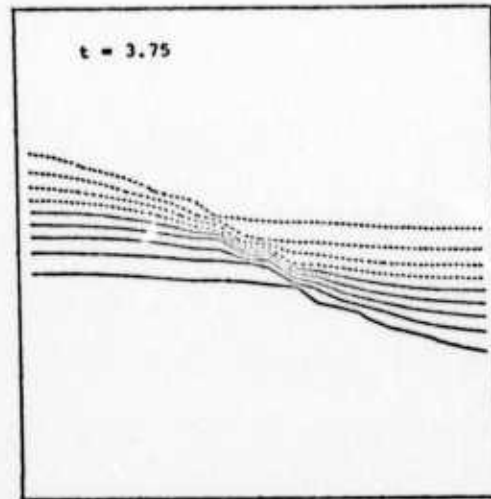
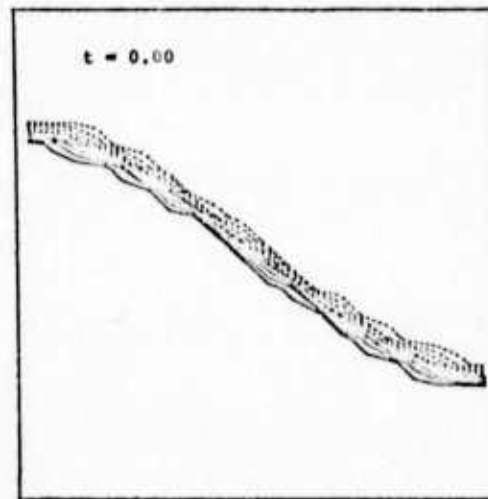
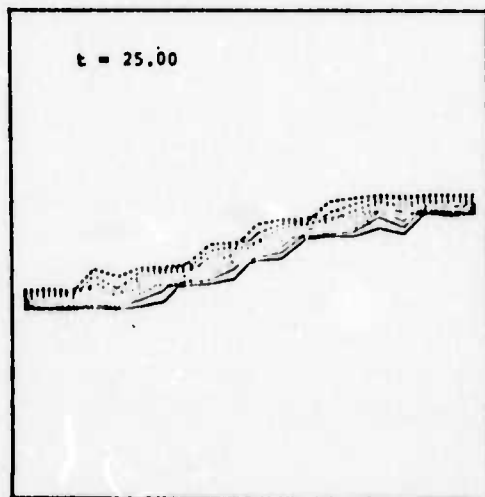
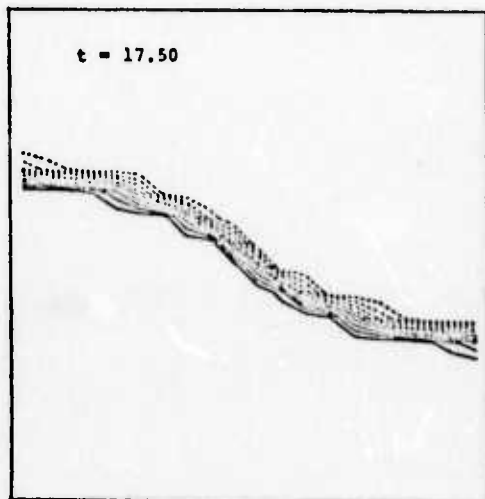
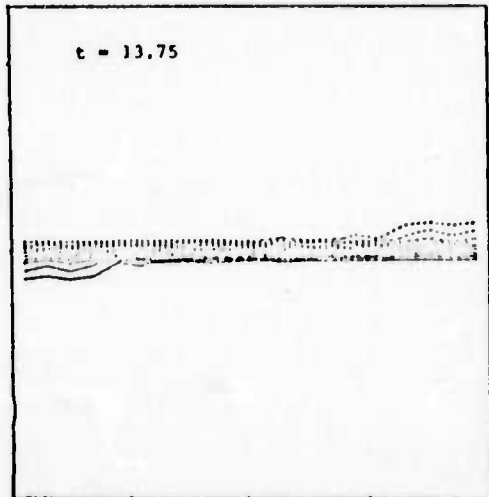


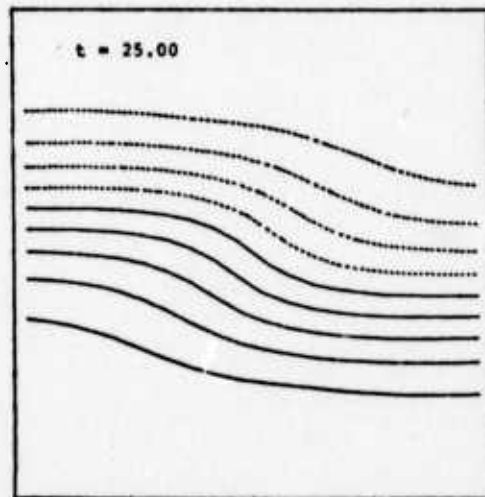
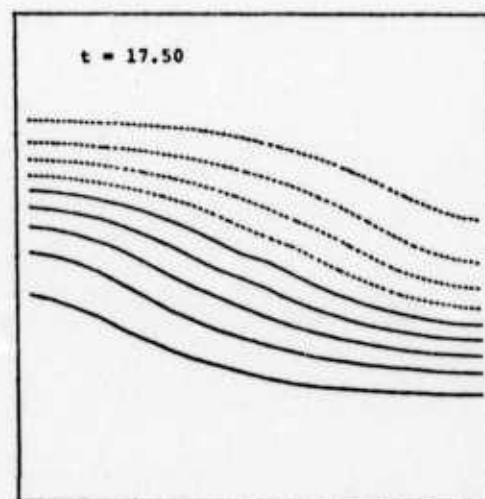
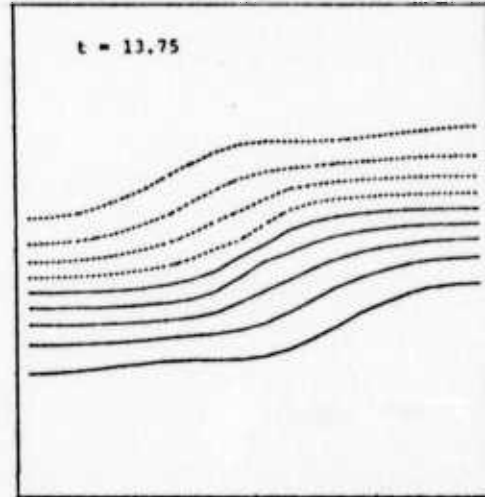
Figure 7.6 Evolution of the density field with time - laminar internal wave test problem (contour levels:  $\rho = 0.96, 0.97, 0.98, 0.99, 1.00, 1.01, 1.02, 1.03, 1.04$ ).

Figure 7.6 - Contd.

EULERIAN/LAGRANGIAN



PURE EULERIAN



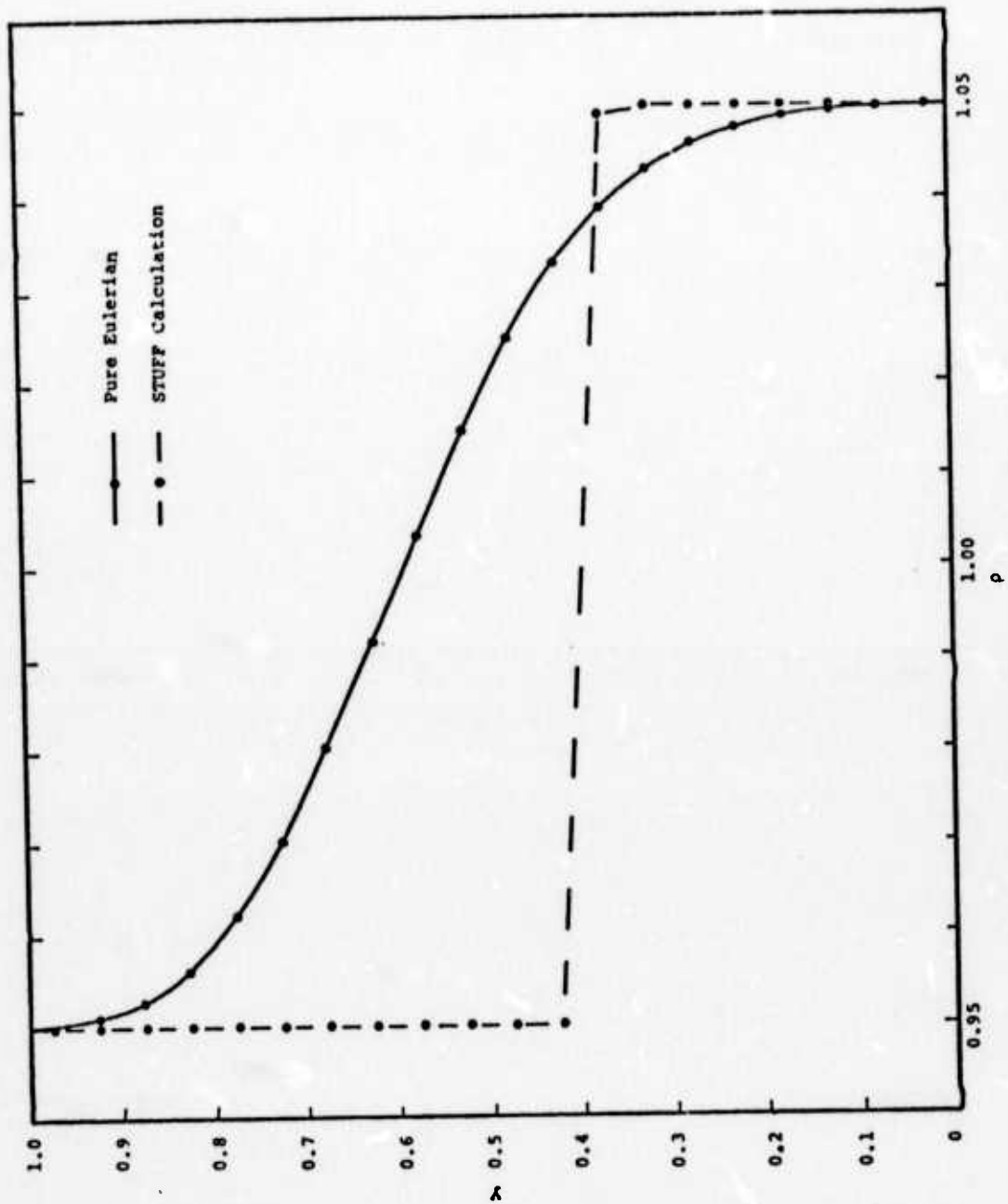


Figure 7.7 Vertical distribution of density at  $t=25$ ,  $x=0$  for internal wave problem.

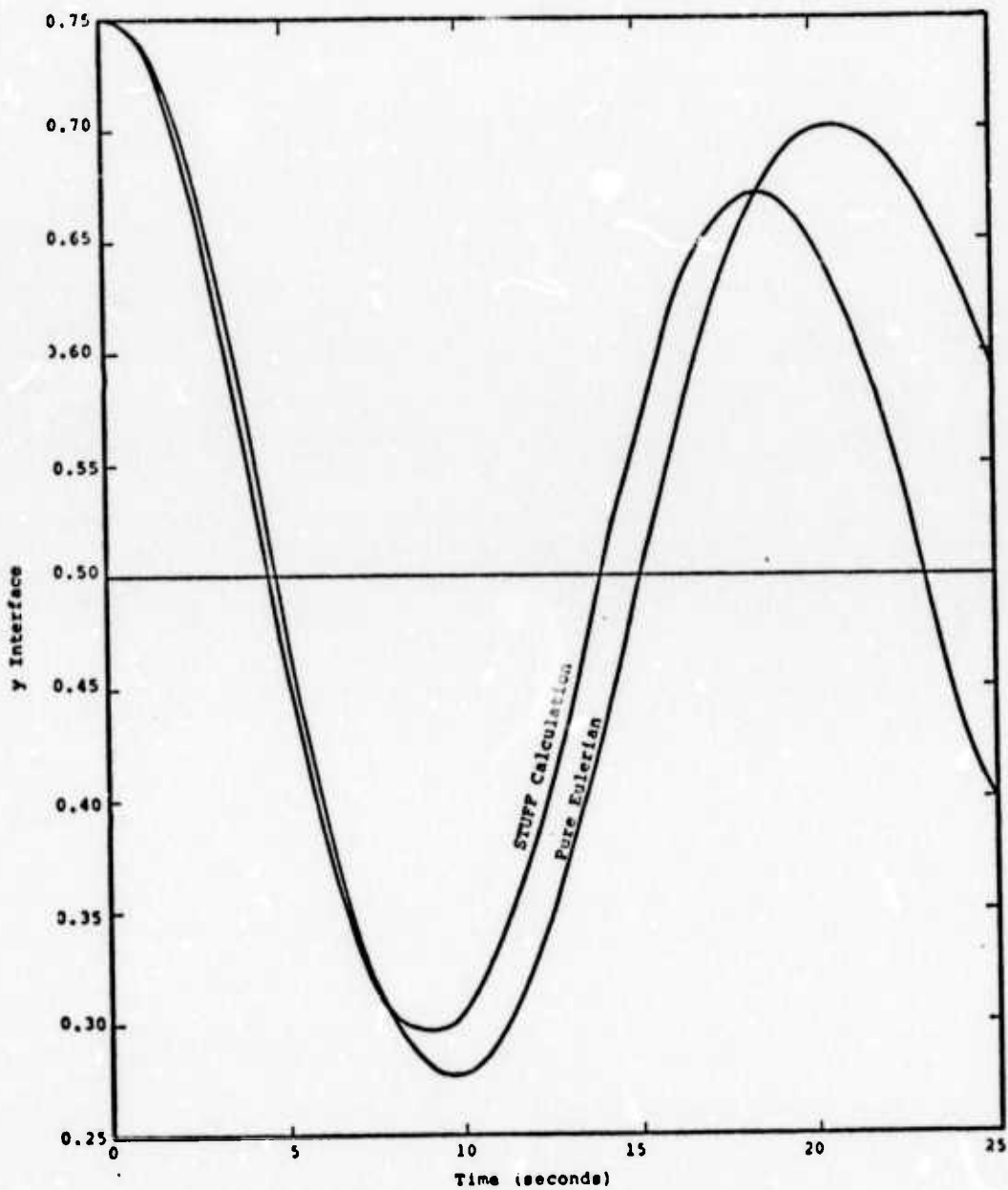


Figure 7.8 Internal wave problem - height vs time of interface at  $x=0$ .

but, thereafter, the "natural period" of the oscillation in the pure Eulerian calculation begins to increase with time. If the Eulerian calculation were carried further, the "numerical diffusion" effect would eventually homogenize the density field completely; thus the buoyant restoring force would be lost and the natural oscillation period would become infinite. In the STUFF calculation, the period remains essentially constant since the numerical procedure automatically precludes "numerical diffusion."

## REFERENCES

1. "The Effects of Meso-Scale and Small-Scale Interactions on Global Climate," Report No. SSS-R-72-1255, Contract No. DAHC 04-71-0018 (15 September 1972), Systems, Science and Software, La Jolla, California.
2. McClatchey, R., et.al., "Optical Properties of the Atmosphere," AFCRL-70-0527 (1970), Air Force Cambridge Research Labs., Cambridge, Mass.
3. Dave, J., "Effect of Varying Integration Increment on the Computed Polarization Characteristics of the Radiation Scattered by Polydispersed Aerosols," Appl. Opt. (1969), 8, 2153.
4. Weller, G., S. Bowling, K. Jayaweera, T. Ohtaki, S. Parker, G. Shaw, and G. Wendler, "Studies of the Solar and Terrestrial Radiation Fluxes Over Arctic Pack Ice," (1972), Geophysical Institute, University of Alaska, Fairbanks, Alaska.
5. Valley, S., Ed., Handbook of Geophysics and Space Environments, McGraw-Hill, New York (1965):
6. Huschke, R., "Arctic Cloud Statistics from 'Air-Calibrated' Surface Weather Observations," RAND Memorandum RM-6173-PR (1969), The RAND Corporation, Santa Monica, California.
7. Gates, W., E. Batten, A. Kahle, and A. Nelson, "A Documentation of the Mintz-Arakawa Two-Level General Circulation Model," RAND Report No. R-877-ARPA (December, 1971), The RAND Corporation, Santa Monica, California.
8. Thekaekara, M., et.al., "The Solar Constant and the Solar Spectrum Measured from a Research Aircraft," Technical Report TR-R-351 (1970) NASA.
9. "Inadvertent Climate Modification: Report of the Study of Man's Impact on Climate (SMIC)," (1971), MIT Press, Cambridge, Mass.
10. "The Effects of Meso-Scale and Small-Scale Interactions on Global Climate," Report No. 3SR-1034, Contract No. DAHC 04-71-0018 (31 March 1972), Systems, Science and Software, La Jolla, California.

11. Crowley, W.P., "Numerical Advection Experiment," Monthly Weather Review (January, 1968), 1, pp. 1-11.
12. "The Effects of Meso-Scale and Small-Scale Interactions on Global Climate," Report No. 3SR-795, Contract No DAHC 04-71-0018 (30 September 1971), Systems, Science and Software, La Jolla, California.
13. Orville, H.D., "Ambient Wind Effects on the Initiation and Development of Cumulus Clouds over Mountains," J. Atmos. Sci. (May, 1968), pp. 385-402.
14. Kessler, E., "On the Distribution and Continuity of Water Substance in Atmospheric Circulation," Meteor. Monographs (November, 1969), No. 32.
15. Liu, J.Y. and H.D. Orville, "Numerical Modeling of Precipitation and Cloud Shadow Effects on Mountain Induced Cumuli," J. Atmos. Sci. (November, 1969), 6, pp. 1283-1298.
16. "Investigations of Mountain Lee Waves and the Air Flow over the Sierra Nevada," (March, 1957), Dept. of Meteorology, University of California at Los Angeles.
17. Bretherton, F.P., "Momentum Transport by Gravity Waves," Qtrly. J. R. Met. Soc. (April, 1969), Volume 95.
18. Sawyer, J.S., "The Introduction of the Effects of Topography into Methods of Numerical Forecasting," Qtrly. J. R. Met. Soc. (1959).
19. Eliassen, A. and E. Palm, "On the Transfer of Energy in Stationary Mountain Waves," Geofysiske Publikasjoner Geophysica Norvegica (1960), Vol. 22, No. 3, pp. 1-23.
20. Gawain, T.H. and J.W. Pritchett, "A Unified Heuristic Model of Fluid Turbulence," J. Computational Physics (June, 1970), Vol. 5.
21. Chorin, A.J. "Numerical Solution of the Navier-Stokes Equations," Mathematics of Computation (October, 1968).
22. Richtmeyer, R.D. and K.W. Morton, Difference Methods for Initial-Value Problems, Interscience Publications, New York (1967).
23. Hirt, C.W. and J.L. Cook, "Calculating 3-D Flows Around Structures and Over Rough Terrain," J. Comp. Physics (October, 1972), Vol. 10. No. 2, pp. 324-340.

## APPENDIX A

### EXPONENTIAL FIT TABLES

ATRAD has been divided into several modules in order to effect computational savings. The module to be described here performs exponential fits of transmission functions for an arbitrary user-supplied set of spectral intervals, and outputs the results to tables. The tables can then be accessed by an ATRAD run which uses any sub-set of this set of intervals (ATRAD will cycle through the tables to obtain data for the intervals it needs). Input to the fitting module is through a Fortran Namelist called EVTABL and, depending on a variable in EVTABL, through another Namelist called FREQS. The variables required by EVTABL and FREQS are listed below. If a variable is not specified in EVTABL input, it may assume a default value, which is given in parentheses at the end of the description of the variable. The output of the module is described in Section A.2.

#### A.1 INPUT

##### Namelist EVTABL

<u>Variable</u>	<u>Type</u>	<u>Description</u>
FITPRT	Logical	If TRUE, edits for each frequency group and for each molecular species (H <sub>2</sub> O, CO <sub>2</sub> +, O <sub>3</sub> ) the transmission function, its exponential-sum approximant, and the percent error. Also

<u>Variable</u>	<u>Type</u>	<u>Description</u>
		edits the coefficients $a_i$ and exponents $k_i$ of the approximant. (TRUE)
FITPR2	Logical	If TRUE, edits the exponential-sum fitting algorithm in detail, including the coefficients $a_i$ and exponential factors $\theta_i$ , the residual, and the polynomial $P(\theta)$ at its minimum for each iteration. Also edits information about pairs of exponential factors which are combined. (FALSE)
PRSETF	Logical	If TRUE, user intends to input spectral intervals through "FREQS" Namelist. If FALSE, user intends to set NWA, WAV, DWAV or NGRPS, IWV (see below) and let the code calculate the spectral interval structure. (FALSE)
NWA	Integer	Number of spectral "regions" defined by WAV's.
WAV(1-15)	Integer	Wavenumber boundaries in $\text{cm}^{-1}$ in increasing order for each spectral "region." E.g., $\text{WAV}(1) < \text{WAV}(2)$ are the wavenumbers bounding spectral region 1. Must be integer multiples of $20 \text{ cm}^{-1}$ in order to agree with the McClatchey transmission data.
DWAV(1-14)	Integer	Width in $\text{cm}^{-1}$ for each of the spectral intervals within a spectral "region." Must be integer multiples of $20 \text{ cm}^{-1}$ . E.g., between $\text{WAV}(1)$ and $\text{WAV}(2)$ all spectral intervals are of size $\text{DWAV}(1)$ .

<u>Variable</u>	<u>Type</u>	<u>Description</u>
NGRPS	Integer	If $15 \geq \text{NGRPS} > 0$ , it overrides the WAV, DWAV option. The NGRPS option allows one to do NGRPS possibly disjoint spectral intervals with boundaries IWV (see below); it can be used to sample the spectrum.
IWV(1-30)	Integer	Used when $\text{NGRPS} > 0$ . Successive pairs of IWV values define the wavenumber boundaries ( $\text{cm}^{-1}$ ) of the spectral intervals being sampled. E.g., if $\text{NGRPS} = 2$ , the first interval is [IWV(1), IWV(2)] and the second is [IWV(3), IWV(4)].
NOPT2	Integer	If $> 0$ , stop calculation just before entering frequency loop. This allows user to check that his problem set-up is correct before doing a full run of the code. (1)
NOPT5	Integer	Logical unit number on which tables are to be written. If $\leq 0$ , output is suppressed. If = 1, output to cards. If = 6, output to printer. (1)
NPTS	Integer	The maximum number of transmission function data points to be used in the exponential fitting procedure. (100)
MINPTS	Integer	The minimum number of transmission function data points to be used in the exponential fitting procedure. (5)

<u>Variable</u>	<u>Type</u>	<u>Description</u>
THMN, THMX	Double Precision	The lower and upper limits, $\theta_{\min}$ and $\theta_{\max}$ , on the search interval used to find a new exponential factor $\theta$ in the exponential-sum fitting iteration. These limits are imposed because $\theta = 0$ and $\theta = 1$ correspond to unphysical values of the exponent $k$ ( $\infty$ and $0$ , respectively). (1.D-8, 1.D0)
TRMIN	Real	The smallest value of the transmission function to be used as a data point for exponential fitting. (.005)
TRMAX	Real	If the slant path transmission (see SLANT) through a vertical amount UMAX of the absorber in question exceeds TRMAX, then the transmission for that species is taken to be unity and no fitting is done. (.99)
TRONE	Real	If the slant path transmission (see SLANT) through a vertical amount UMAX of the absorber in question exceeds TRONE, then a one-term exponential fit of the transmission data is performed. (.93)
COALES	Double Precision	The criterion for whether or not to coalesce a close pair of exponential factors $\theta_i, \theta_{i+1}$ . If $2 \left  \frac{\ln \theta_{i+1} - \ln \theta_i}{\ln \theta_{i+1} + \ln \theta_i} \right  \leq \text{COALES}$ then $\theta_i, \theta_{i+1}$ are replaced by a single exponential factor. (.05)

<u>Variable</u>	<u>Type</u>	<u>Description</u>									
RTEST	Double Precision	The exponential fitting iteration is stopped when $\left  \frac{R_{\text{new}} - R_{\text{old}}}{R_{\text{new}}} \right  < \text{RTEST}$ where R is the least-squares residual and 'old' and 'new' refer to the previous and current iterations. (1.D-16)									
ITMAX	Integer	The maximum allowed number of exponential fitting iterations. (150)									
ISEC1	Integer	Maximum number of iterations of secant method used in pair-coalescence procedure in FITTRN (see COALES). (20)									
SLANT	Real	If $u_v$ is the vertical absorber amount of a given molecular species (input through UMAX), then the smallest value of the transmission function $T_{\Delta v}(u)$ used in fitting is $T_{\Delta v}(\text{SLANT} * u_v)$ provided this value is $> \text{TRMIN}$ . (6)									
UMAX(1-4)	Real	The largest vertical absorber amount of a given species which will be encountered in any ATRAD run using these tables <table border="1" style="margin-left: auto; margin-right: auto;"> <thead> <tr> <th></th> <th><u>Species</u></th> <th><u>Units</u></th> </tr> </thead> <tbody> <tr> <td>UMAX(1)</td> <td>H<sub>2</sub>O vapor</td> <td>g/cm<sup>2</sup></td> </tr> <tr> <td>UMAX(2)</td> <td>CO<sub>2</sub> + other uniformly mixed gases</td> <td>km</td> </tr> </tbody> </table>		<u>Species</u>	<u>Units</u>	UMAX(1)	H <sub>2</sub> O vapor	g/cm <sup>2</sup>	UMAX(2)	CO <sub>2</sub> + other uniformly mixed gases	km
	<u>Species</u>	<u>Units</u>									
UMAX(1)	H <sub>2</sub> O vapor	g/cm <sup>2</sup>									
UMAX(2)	CO <sub>2</sub> + other uniformly mixed gases	km									

<u>Variable</u>	<u>Type</u>	<u>Description</u>	<u>Units</u>
		<u>Species</u>	
UMAX(3)		O <sub>3</sub> in the IR	atm-cm
UMAX(4)		O <sub>3</sub> in the UV	atm-cm

Namelist FREQS

WAVNUM(NU)	Integer	The frequencies in cm <sup>-1</sup> bounding the spectral intervals, in increasing order (WAVNUM(1) is the smallest).
NNU	Integer	The number of non-zero WAVNUM's (or one plus the number of spectral intervals).

## A.2 OUTPUT

Typical printer output is shown in Table 2.1 of the text. The particular type of edit shown there is produced by the FITPRT flag in the input Namelist EVTABL. The FITPR2 flag produces large amounts of printing which normally is of little interest unless one wishes to follow the details of the algorithm.

The tables are generated separately from the printer output and are sent to logical unit NOPT5 (see EVTABL). Presuming that this refers to cards (NOPT5 = 1), the table pattern for a particular spectral interval  $\nu_1 \rightarrow \nu_2$  is as follows:

- (1) the first card contains  $\nu_1$  and  $\nu_2$ ;
- (2) the second card contains, in succession,
  - (a) NAB = number of absorbers active in this spectral interval;
  - (b)  $\{NTERMS(I), I=1(1)3\}$  = number of terms in the exponential fit for the  $I^{\text{th}}$  absorber;

(c)  $\{\text{SKIP}(I), I=1(1)3\}$  = logical flag determining whether or not  $I^{\text{th}}$  absorber is active in this spectral interval;

- (3) the third and following cards contain the coefficients  $a_i$  and exponents  $k_i$  for each of the active absorbers in turn (if  $\text{NAB}=0$ , this set is vacuous).

The indexing convention employed is that  $I=1$  refers to water vapor,  $I=2$  refers to  $\text{CO}_2$ + other uniformly mixed gases, and  $I=3$  refers to ozone.

APPENDIX B  
CALCULATION AND TABULATION OF MIE SCATTERING  
FUNCTIONS FOR A SINGLE SPHERE

The Mie scattering functions for a single homogeneous sphere of radius  $a$ , index of refraction  $m = n_1 - in_2$ , at wavelength  $\lambda$ , were given in our previous semi-annual report. (B1) We repeat the formulas here for ease of reference:

$$\sigma_{\text{ext}} = \frac{\lambda^2}{2\pi} \sum_{n=1}^{\infty} (2n+1) \operatorname{Re}(a_n + b_n) \quad (\text{B.1})$$

$$\sigma_{\text{sca}} = \frac{\lambda^2}{2\pi} \sum_{n=1}^{\infty} (2n+1) (|a_n|^2 + |b_n|^2) \quad (\text{B.2})$$

$$i_1 = \left| \sum_{n=1}^{\infty} \frac{2n+1}{n(n+1)} \left[ a_n(\alpha, m) \pi_n(\mu) + b_n(\alpha, m) \tau_n(\mu) \right] \right|^2 \quad (\text{B.3})$$

$$i_2 = \left| \sum_{n=1}^{\infty} \frac{2n+1}{n(n+1)} \left[ a_n(\alpha, m) \tau_n(\mu) + b_n(\alpha, m) \pi_n(\mu) \right] \right|^2 \quad (\text{B.4})$$

Nothing was said in the previous report about the actual computation of the  $a_n$ 's,  $b_n$ 's,  $\pi_n$ 's, and  $\tau_n$ 's, however. This is far from a trivial task, since various, possibly unstable, recurrences are involved. Therefore, an exposition of our computational scheme has been included as Section B.1 of this appendix. Section B.2 discusses a code module which makes tables of  $\sigma_{\text{sca}}$ ,  $\sigma_{\text{ext}}$ , and  $i_1 + i_2$  for use in the Mie tables module of Appendix C.

### B.1 COMPUTATIONAL SCHEME

An extensive literature search, coupled with our own independent investigations, has led to the computational scheme which is given below. The various formulas have been chosen to minimize the number of arithmetic operations needed, and yet have been carefully checked against less efficient forms to be sure that accuracy is not being sacrificed. In cases where optimization reduces accuracy significantly, optimization has been suppressed.

Optimization has also been performed vis a vis single-precision (36-bit words,  $\sim 8$  significant digits) versus double-precision (72-bit words,  $\sim 18$  significant digits) operations. Basically, the only operations which we found needed to be performed in double precision were the recursions on the functions  $A_n$ ,  $\psi_n$ , and  $\chi_n$  (see Equations (B.7-B.9)) used in forming the coefficients  $a_n$  and  $b_n$ . The remainder of the computations, particularly the recursions on  $\pi_n$  and  $\tau_n$  and the series summation to form  $i_1$  and  $i_2$ , were sufficiently accurate in single-precision (i.e., good to 5-6 significant figures) for any realistic atmospheric aerosol or cloud particle (size parameter  $\alpha \leq 1000$ ). Formulas which are executed in double-precision will be indicated by a (d.p.) to their left.

Before beginning the Mie calculations, the following quantities are formed and stored:

$$\left. \begin{aligned} c_n &= 2n - 1 \\ \gamma_n &= \frac{2n + 1}{n(n+1)} \\ \delta_n &= n + 1 \\ \omega_n &= \frac{n + 1}{n} \end{aligned} \right\} n = 1, n_{\max}$$

$$|n| = \sqrt{n_1^2 + n_2^2}$$

$$(d.p.) z_r = \frac{n_1}{\alpha |n|^2}$$

$$(d.p.) z_i = \frac{n_2}{\alpha |n|^2}$$

$$\mu_i = \cos \theta_i$$

$n_{\max}$  is chosen as the largest number of terms the Mie series will ever contain. In practice, we have found that for size parameter  $\alpha$ , the number of terms  $n_\alpha$  that must be carried in the series for  $\sigma_{\text{sca}}$ ,  $\sigma_{\text{ext}}$ ,  $i_1$ , and  $i_2$  satisfies

$$n_\alpha \lesssim 1.06 \alpha + 13$$

for all  $\alpha > 0$ . ( $n_\alpha$  does not depend on the indices of refraction  $n_1$  and  $n_2$  because the convergence of the series depends on  $\psi_n(\alpha)$ , which is independent of  $n_1$  and  $n_2$ ).  $z_r$  and  $z_i$  are computed in double-precision because they are used in the  $A_n$  recursion.  $\{\theta_i\}$  is the set of angles at which it is desired to compute  $i_1$  and  $i_2$ .

The formulas for the coefficients  $a_n$  and  $b_n$  in Equations (B.1-B.4) may be put in the following form:

$$a_n = \frac{\left[ \frac{1}{m} A_n(\beta) + \frac{n}{\alpha} \right] \psi_n(\alpha) - \psi_{n-1}(\alpha)}{\left[ \frac{1}{m} A_n(\beta) + \frac{n}{\alpha} \right] \left[ \psi_n(\alpha) + i\chi_n(\alpha) \right] - \left[ \psi_{n-1}(\alpha) + i\chi_{n-1}(\alpha) \right]} \quad (B.5)$$

$$b_n = \frac{\left[ m A_n(\beta) + \frac{n}{\alpha} \right] \psi_n(\alpha) - \psi_{n-1}(\alpha)}{\left[ m A_n(\beta) + \frac{n}{\alpha} \right] \left[ \psi_n(\alpha) + i\chi_n(\alpha) \right] - \left[ \psi_{n-1}(\alpha) + i\chi_{n-1}(\alpha) \right]} \quad (B.6)$$

$$|n| = \sqrt{n_1^2 + n_2^2}$$

$$\text{(d.p.) } z_r = \frac{n_1}{\alpha |n|^2}$$

$$\text{(d.p.) } z_i = \frac{n_2}{\alpha |n|^2}$$

$$\mu_i = \cos \theta_i$$

$n_{\max}$  is chosen as the largest number of terms the Mie series will ever contain. In practice, we have found that for size parameter  $\alpha$ , the number of terms  $n_\alpha$  that must be carried in the series for  $\sigma_{\text{sca}}$ ,  $\sigma_{\text{ext}}$ ,  $i_1$ , and  $i_2$  satisfies

$$n_\alpha \lesssim 1.06 \alpha + 13$$

for all  $\alpha > 0$ . ( $n_\alpha$  does not depend on the indices of refraction  $n_1$  and  $n_2$  because the convergence of the series depends on  $\psi_n(\alpha)$ , which is independent of  $n_1$  and  $n_2$ .)  $z_r$  and  $z_i$  are computed in double-precision because they are used in the  $A_n$  recursion.  $\{\theta_i\}$  is the set of angles at which it is desired to compute  $i_1$  and  $i_2$ .

The formulas for the coefficients  $a_n$  and  $b_n$  in Equations (B.1-B.4) may be put in the following form:

$$a_n = \frac{\left[ \frac{1}{m} A_n(\beta) + \frac{n}{\alpha} \right] \psi_n(\alpha) - \psi_{n-1}(\alpha)}{\left[ \frac{1}{m} A_n(\beta) + \frac{n}{\alpha} \right] [\psi_n(\alpha) + i\chi_n(\alpha)] - [\psi_{n-1}(\alpha) + i\chi_{n-1}(\alpha)]} \quad (\text{B.5})$$

$$b_n = \frac{\left[ m A_n(\beta) + \frac{n}{\alpha} \right] \psi_n(\alpha) - \psi_{n-1}(\alpha)}{\left[ m A_n(\beta) + \frac{n}{\alpha} \right] [\psi_n(\alpha) + i\chi_n(\alpha)] - [\psi_{n-1}(\alpha) + i\chi_{n-1}(\alpha)]} \quad (\text{B.6})$$

where  $\beta = m\alpha$  and

$$A_n(\beta) \equiv \frac{\psi_n'(\beta)}{\psi_n(\beta)}$$

Both  $\psi_n$  and  $\chi_n$  satisfy the recurrence relation

$$(d.p.) f_n(\alpha) = \frac{c_n}{\alpha} f_{n-1}(\alpha) - f_{n-2}(\alpha) \quad (B.7)$$

( $c_n = 2n-1$ , is tabulated) which is initialized in the case of  $\psi_n$  by

$$(d.p.) \psi_{-1}(\alpha) = \cos \alpha \quad \psi_0(\alpha) = \sin \alpha$$

and in the case of  $\chi_n$  by

$$(d.p.) \chi_{-1}(\alpha) = -\sin \alpha \quad \chi_0(\alpha) = \cos \alpha$$

$A_n$  satisfies the upward recurrence relation

$$(d.p.) A_n(\beta) = -\frac{n}{\beta} + \frac{1}{\frac{n}{\beta} - A_{n-1}(\beta)} \quad (B.8)$$

or, alternatively, the downward recurrence relation

$$(d.p.) A_{n-1}(\beta) = \frac{n}{\beta} - \frac{1}{\frac{n}{\beta} + A_n(\beta)} \quad (B.9)$$

If the upward recurrence (B.8) is used, the starting value is

$$(d.p.) A_0(\beta) = \frac{\cos \beta}{\sin \beta} = \frac{\sin 2n_1\alpha + i \sinh 2n_2\alpha}{\cosh 2n_2\alpha - \cos 2n_1\alpha}$$

If the downward recurrence is used, the starting value is

$$A_N(\beta) = 0$$

where

$$N = 1.1 |\beta| + 25 \quad (\text{B.10})$$

The advantage of using upward recursion wherever possible is that the coefficients  $a_n$  and  $b_n$  are calculated and stored in an upward fashion, until the criterion

$$|a_n|^2 + |b_n|^2 \leq 10^{-14} \quad (\text{B.11})$$

is satisfied, at which point ( $n = n_\alpha$ ) the Mie series is regarded to have converged. When downward recursion is used, it is impossible to know the exact value of  $n_\alpha$ , so computations are wasted in working downward from some conservative estimate of  $n_\alpha$  to the point where (B.11) is actually satisfied. For example, when downward recursion must be used on  $A_n$ , the starting point  $N$  of Equation (B.10) always considerably exceeds  $n_\alpha$ .

The upward recursion (B.7) is unstable for  $\psi_n$  and stable for  $\chi_n$ .<sup>(B2)</sup> However, the instability for  $\psi_n$  does not result in a serious deterioration of accuracy until  $n$  exceeds  $\alpha$ , and by that point the Mie series has already begun to converge rapidly. Extensive numerical experimentation with this recursion has shown that in every case the Mie series converges before the accuracy of  $\psi_n$  has fallen to four significant digits, if double-precision is used. In single-precision, the deterioration of accuracy in  $\psi_n$  for  $n > \alpha$  is much too catastrophic. (Note: in all cases, upward recursion on  $\psi_n$  was compared against 'exact' results generated by Gautschi's method.<sup>(B2)</sup>)

Kattawar and Plass,<sup>(B3)</sup> among others, have demonstrated that the upward recursion (B.8) for  $A_n$  is unstable when

$n \gg |\beta|$ . They proved that, if  $\epsilon_n$  = the error in  $A_n$ , then  $|\epsilon_n| \gg |\epsilon_{n-1}|$  if  $n \gg |\beta|$ . By the same token, the downward recursion (B.9) for  $A_n$  is stable for  $n \gg |\beta|$ , so that the error diminishes rapidly at each step and all memory of the starting value is soon lost. This is the rationale for initializing (B.9) with  $A_N = 0$ . The value of  $N$  in Equation (B.10) is found by numerical experimentation to be satisfactory; surprisingly, it does not need to satisfy  $N \gg |\beta|$ . The Kattawar-Plass result is, of course, not strictly applicable to the Mie series, which converges well before  $n \gg |\beta| = |n|\alpha$ . Therefore, we made extensive comparisons of upward and downward recursion on  $A_n$ , in both single- and double-precision, for a range of  $n_1$  and  $n_2$ . We found single-precision to be quite inadequate for both upward and downward recursion (the downward deteriorated as  $n \rightarrow 1$ ). In double-precision upward recursion, we defined the onset of instability for  $n_1$  and  $n_2$  fixed and  $\alpha$  increasing, as the value of  $\alpha$  for which accuracy at  $n = n_\alpha$  had deteriorated to four significant digits. For physically realistic  $n_1$  and  $n_2$ , we were able to show that this point could be well approximated by the analytic formula

$$n_2\alpha = 80(n_1 - 0.9)$$

Thus, in our code, we use upward recursion on  $A_n$  when

$$\alpha < \frac{80(n_1 - 0.9)}{n_2}$$

(in particular, for  $n_2 = 0$ ), and downward recursion otherwise.

Since  $A_n$  is in general complex, the recursion of Equation (B.8) is actually structured as follows:

$$t_1 = nz_r$$

$$t_2 = nz_i$$

$$t_3 = t_1 - \operatorname{Re} A_{n-1}$$

$$t_4 = t_2 - \operatorname{Im} A_{n-1}$$

$$t_5 = t_3^2 + t_4^2$$

$$\operatorname{Re} A_n = -t_1 + \frac{t_3}{t_5}$$

$$\operatorname{Im} A_n = -t_2 - \frac{t_4}{t_5}$$

The recursion of Equation (B.9) is computed similarly.

$a_n$  and  $b_n$  are also complex, so that they, too, are not actually computed by formulas (B.5) and (B.6), but by an optimized algorithm which finds their real and imaginary parts separately. Advantage is taken of the fact that the only difference between Equation (B.5) and (B.6) is in the factor ( $m$  or  $\frac{1}{m}$ ) which multiplies  $A_n(\beta)$ . It was originally thought that the complex number features of FORTRAN would be useful in calculating  $a_n$  and  $b_n$  and subsequently  $i_1$  and  $i_2$ , but it was discovered that our compiler (UNIVAC 1108) does not recognize the simplifications in complex multiplication and division which arise when one of the numbers involved is purely real; the use of complex multiplies and divides was accordingly curtailed.

Special simplified branches are provided in the recursions (B.7), (B.8), and (B.9) and in the computations of  $a_n$  and  $b_n$  for the case  $n_2 = 0$  (non-absorbing spheres), in view of the importance of this case in practice. We have

found the Mie results for  $n_2 \leq 10^{-6}$  to be almost indistinguishable from those for  $n_2 = 0$ , so whenever  $n_2 \leq 10^{-6}$  it is reset to zero in order that these coding simplifications may be triggered.

We now consider the functions  $\pi_n(\mu)$  and  $\tau_n(\mu)$  involved in the sums in Equations (B.3) and (B.4). These functions are defined as

$$\pi_n(\mu) = P'_n(\mu)$$

$$\tau_n(\mu) = \mu\pi_n(\mu) - (1-\mu^2)\pi'_n(\mu) \quad .$$

when  $P_n$  is a Legendre polynomial. They may be generated from upward recursions derived from various Legendre polynomial identities [of Reference B4]. The most computationally efficient forms of those recursions we have been able to find are

$$\pi_{n+1}(\mu) = \mu\pi_n(\mu) + \omega_n [\mu\pi_n(\mu) - \pi_{n-1}(\mu)] \quad (B.12)$$

$$\tau_{n+1}(\mu) = \delta_n [\mu\pi_{n+1}(\mu) - \pi_n(\mu)] - \pi_n(\mu) \quad (B.13)$$

where  $\omega_n$  and  $\delta_n$ , defined earlier as

$$\omega_n = \frac{n+1}{n} \quad \delta_n = n+1$$

are kept in tables. A total of three multiplications are required, which we would hazard is the best one can hope for. The recursion is initialized by  $\pi_0(\mu) = 0$ ,  $\pi_1(\mu) = 1$ ,  $\tau_1(\mu) = \mu$ . The results of (B.12) and (B.13) have been checked against other forms of the same recursions and no substantial differences were found. Questions of stability do not enter here, since (B.12) is stable in either the upward or downward

direction. (B4) The only source of error is round-off, and comparisons of single versus double-precision executions of (B.12) and (B.13) indicate that at  $n = 800$  the single-precision results still have four to six significant digits.

The  $\pi_n$ 's and  $\tau_n$ 's have useful reflection properties,

$$\pi_n(-\mu) = (-1)^{n+1} \pi_n(\mu) \quad (\text{B.14})$$

$$\tau_n(-\mu) = (-1)^n \tau_n(\mu)$$

which means that, provided we choose angles in  $[90^\circ, 180^\circ]$  which are the supplements of those in  $[0^\circ, 90^\circ]$ , then the recursions (B.12) and (B.13) need only be performed for angles in  $[0^\circ, 90^\circ]$ . The  $\pi_n$ 's and  $\tau_n$ 's for the angles in  $[90^\circ, 180^\circ]$  then follow automatically from Equation (B.14). A drawback to this scheme is that it usually provides more resolution in the region of the glory than one needs for flux calculations, because of the high angular resolution required in the forward peak, near  $0^\circ$ . One could, of course, use a subset of the supplementary angles, but this entails the use of indexing and branching in the most expensive part of the calculation -- the formation of the sums in Equations (B.3) and (B.4). At this time, we use the entire set of supplementary angles.

The special cases  $\theta = 0^\circ$  ( $\mu = 1$ ) and  $\theta = 180^\circ$  ( $\mu = -1$ ) of Equations (B.3) and (B.4) are actually computed along with the coefficients  $a_n$  and  $b_n$ , in view of the fact that

$$\pi_n(1) = \tau_n(1) = \frac{n(n+1)}{2}$$

$$\pi_n(-1) = -\tau_n(-1) = (-1)^{n+1} \pi_n(1)$$

The code forms the sums

$$\sigma_0 = \sum_1^{n_\alpha} (2n+1) (a_n + b_n)$$

$$\sigma_{180} = \sum_1^{n_\alpha} (-1)^{n+1} (2n+1) (a_n - b_n)$$

from which it derives

$$\sigma_{\text{ext}} = \text{Re } \sigma_0$$

$$i_1 + i_2 \Big|_{0^\circ} = \frac{1}{2} \left[ (\text{Re } \sigma_0)^2 + (\text{Im } \sigma_0)^2 \right]$$

$$i_1 + i_2 \Big|_{180^\circ} = \frac{1}{2} \left[ (\text{Re } \sigma_{180})^2 + (\text{Im } \sigma_{180})^2 \right]$$

Because a relatively large fraction of the angles are concentrated in the forward peak, it is computationally advantageous to use the diffraction approximation in the forward peak if possible. Papers of Dave<sup>(B5)</sup> and Liou and Hansen<sup>(B5)</sup> have explored this possibility. Based on their work, we have approximated  $i_1 + i_2$  for  $\alpha \geq 100$  and for  $\theta \in [0^\circ, 1.5^\circ]$  by

$$i_1(\theta) + i_2(\theta) = 4(i_1 + i_2) \Big|_{\theta=0^\circ} \left[ \frac{J_1(\alpha \sin \theta)}{\alpha \sin \theta} \right]^2$$

This forces agreement at  $\theta = 0^\circ$ , which, since the error involved in using the diffraction approximation tends to be systematic, should force better agreement than Dave shows for all  $\theta \in [0^\circ, 1.5^\circ]$ . The Bessel function  $J_1$  is evaluated from approximations in Reference B4.

## B.2 TABLES

There are usually broad spectral regions across which the index of refraction (i.o.r.) of a substance changes little, if at all. For example, for liquid water in the spectral region  $0.3 - 0.9\mu$ , the real part  $n_1$  of the i.o.r. varies only from 1.33 to 1.36, while the imaginary part  $n_2$  is less than  $5 \times 10^{-7}$ . For reasons unrelated to Mie scattering, however, namely in order to resolve the  $\lambda^{-4}$  variation of Rayleigh scattering, ATRAD takes approximately 45 spectral intervals between  $0.3\mu$  and  $0.9\mu$ . Since  $i_1$  and  $i_2$  (see Equations (B.3) and (B.4)) depend only on  $n_1$ ,  $n_2$ ,  $\alpha$ , and  $\theta$ , and not on  $\lambda$ , it is clear that in each ATRAD spectral interval for which  $n_1$ ,  $n_2$ , and  $\{\theta_i\}$  are the same, we are recalculating many of the same  $i_1$ 's and  $i_2$ 's (provided that the size integration uses the same basic set  $\{\alpha_i\}$  of  $\alpha$ 's; of course, each size integration draws on a different range of  $\{\alpha_i\}$  because  $\lambda$  and therefore

$$\alpha_{\max} = \frac{2\pi a_{\max}}{\lambda} \quad , \quad \alpha_{\min} = \frac{2\pi a_{\min}}{\lambda}$$

are varying). Therefore, it is clear that a large amount of computation can be saved by making tables of  $\sigma_{\text{sca}}$ ,  $\sigma_{\text{ext}}$ , and  $i_1+i_2$  for fixed  $n_1$  and  $n_2$ , for a fixed set  $\{\theta_i\}$  of angles, and for a fixed set

$$\{\alpha_i\} \in \left(0, \frac{2\pi a_{\max}}{\lambda_{\min}}\right)$$

of  $\alpha$ 's. In fact, making these tables is not only desirable, but absolutely necessary for running ATRAD with water clouds; otherwise the Mie tables code of Appendix C would use more than 20 hours of computer time just to do 45 spectral intervals between  $0.3\mu$  and  $0.9\mu$ !

To illustrate the input for a typical set of tables, we quote here the parameter values actually used in creating  $i_1 - i_2$  tables for the Arctic stratus problem discussed in Volume I, Chapter 3 of this report:

$$n_1 = 1.335 \qquad n_2 = 0$$

$$\{\theta_i\} = 0(.1^\circ) \ 2^\circ(.2^\circ) \ 6^\circ(.5^\circ) \ 11^\circ(1^\circ) \ 20^\circ(2.5^\circ) \ 45^\circ(5^\circ) \ 90^\circ$$

+ the supplementary angles

$$\{\alpha_i\} = .1(.1) \ 450$$

This particular table involves 706,500 numbers. Obviously, such large tables cannot reside in core, and so they must be kept on peripheral devices (drum, disk, etc.) and read piece by piece as needed.

This code module (called I1I2-TABLES) receives input through the Namelist I1TABL, which is documented below.

Namelist I1TABL

<u>Variable</u>	<u>Type</u>	<u>Description</u>
N1	Real	Real part of index of refraction (1.335).
N2	Real	Imaginary part of index of refraction (0.).
NCH	Integer	Number ( $\leq 6$ ) of values of NSTEP to be used (6).
NSTEP(I)	Integer	Number of angular steps of size DANG(I) to take, starting at $\theta = 0^\circ$ with NSTEP(1) steps of size DANG(1) and finishing at $\theta = 90^\circ$ after NSTEP(NCH) steps of size DANG(NCH). (20, 20, 10, 9, 10, 9).

<u>Variable</u>	<u>Type</u>	<u>Description</u>
DANG(I)	Real	Angular increments, in degrees. (0.1, 0.2, 0.5, 1.0, 2.5, 5.0).
DELALP	Real	Increment $\Delta\alpha$ in the size parameter $\alpha$ used in generating tables and/or edits of $\sigma_{sca}$ , $\sigma_{ext}$ , and $i_1+i_2$ . (0.1)
ALPMIN	Real	Starting value $\alpha_{min}$ of the size parameter (see IPL). (0.1)
IPL	Integer	Number of steps of $\Delta\alpha$ to take beginning at ALPMIN. The $\alpha$ -mesh $\{\alpha_i\}$ is $\alpha_{min}$ , $\alpha_{min} + \Delta\alpha$ , ..., $\alpha_{min} + (IPL-1)\Delta\alpha$ . (1)
NOPT4	Integer	Number of values of $\alpha$ to skip when restarting, in order to continue writing into a partially completed table. For example, if a previous run wrote the tables up through and including $\alpha_{min} + N\Delta\alpha$ , we would set $NOPT4 = N+1$ . $NOPT4 = 0$ indicates tables are to be generated ab initio. (0)
NOPT5	Integer	Logical unit number on which tables are to be written. If = 0, table generation is suppressed.
MIEPRT(1)	Logical	If TRUE, causes edits of the coefficients $a_n$ and $b_n$ and of the functions $A_n$ for each $\alpha$ . This edit can be used for debugging and for selective studies of the Mie series, but must be turned off for a full table-making run. (FALSE)

<u>Variable</u>	<u>Type</u>	<u>Description</u>
MIEPRT(2)	Logical	If TRUE, causes edits of $i_1+i_2$ . Same comments apply as for MIEPRT(1). (FALSE)

REFERENCES

- B1 "The Effects of Meso-scale and Small-scale Interactions on Global Climate," semi-annual Technical Report SSS-R-72-1255, Systems, Science and Software, La Jolla, CA (September 1972).
- B2 Gautschi, W., "Computational Aspects of Three-Term Recurrence Relations," SIAM Rev. 9, 24 (1967).
- B3 Kattawar, G. and G. Plass, "Electromagnetic Scattering from Absorbing Spheres," Appl. Opt. 6, 1377 (1967).
- B4 Abramowitz, M. and I. Stegun, eds., Handbook of Mathematical Functions, Dover, New York (1965).
- B5 Dave, J., "Scattering of Visible Light by Large Water Spheres," Appl. Opt. 8, 155 (1969).
- B6 Liou, K. and J. Hansen, "Intensity and Polarization for Single Scattering by Polydisperse Spheres: A Comparison of Ray Optics and Mie Theory," J. Atm. Sci., 28, 995 (1971).

APPENDIX C  
TABULATION OF MIE SCATTERING  
FUNCTIONS FOR A SPHERICAL POLYDISPERSION

ATRAD has been divided into several modules in order to effect computational economies. The one to be described here (MIE-TABLES) creates tables of Mie scattering functions (cross sections and phase function) which may be read by ATRAD. This permits parameter studies which do not involve Mie scattering - such as varying the surface albedo, sun angle, etc. - to be performed without incurring the excessive computational burden of Mie scattering each time. (Actually the aerosol number density may also be varied in such parameter studies, since the Mie tables are created for size distributions normalized to unity). Also, although the Mie tables are usually made for the entire spectrum, ATRAD has the capability of running any subset of the spectrum by cycling past the unwanted spectral intervals.

Some notable features of MIE-TABLES are:

- (a) for spectral intervals  $\leq 0.3\mu$ , table generation is suppressed below the tropopause on the grounds that no radiation of these wavelengths reaches the troposphere;
- (b) aerosol size distributions may be specified analytically, using parameters C1, C2, C3 (see Namelist MIETAB) or in tabular form, using Namelist AEROS;

- (c) if several levels use the same size distribution (and the materials are the same) only one Mie calculation is stored - ATRAD then uses the results at any other levels where they are needed;
- (d) the code may either generate its own values of  $\sigma_{\text{sca}}$ ,  $\sigma_{\text{ext}}$ , and  $i_1 + i_2$  or it may read them from tables (see Appendix B);
- (e) the code may be easily restarted to continue writing into a partially completed table.

Input to MIE-TABLES is through the sequence of Name-lists indicated in Figure C.1. The variables in each Name-list are defined below.

	{	MIETAB Namelist
		Input Control Parameters
	}	END
Only if PRSETZ = TRUE	{	LEVELS Namelist
		Z, NZ, IBD, NBD
	}	END
Only if PRSETF = TRUE	{	FREQS Namelist
		WAVNUM, NNU
	}	END
Only if NOPT = 0	{	STRUCT Namelist
		P, T, H2ODEN, O3DEN, AERDEN, NAER, NMAT
	}	END
Only if NAER(I) = 0 for at least one I	{	AEROS Namelist
		RAD, AERNUM, NDAT, HIST
	}	END

Figure C.1 - Input deck set-up for a normal run of MIE-TABLES.

Namelist MIETAB

<u>Variable</u>	<u>Type</u>	<u>Description</u>
PRSETZ	Logical	If TRUE, the user intends to input the zone structure through the "LEVELS" Namelist. If FALSE, user intends to set OZONE, TROPO, CLDBAS, CLDTOP, NZONES, and EXPAN (see below) with which the code will calculate the zone structure. (FALSE)
OZONE	Logical	If TRUE, place the uppermost level at 50 km altitude. If FALSE, take the uppermost level at TROPO km (the tropopause or some level just below the ozone layer). In the latter case, the incident solar flux will be truncated at O3CUT. (TRUE)
TROPO	Real	If OZONE = FALSE, the height in km of the uppermost level in the problem is set to TROPO. This level should be reasonably close to the bottom of the ozone layer. (15.0)
NCLOUD	Integer	The number of cloud layers (only 0, 1, or 2 are allowed). This must always be input, however, the zone structure is to be set up.
CLDBAS (1,2)	Real	Heights in km of bases of lower (1) and upper (2) cloud. (2*0)
CLDTOP (1,2)	Real	Heights in km of tops of lower (1) and upper (2) cloud. (2*0)

<u>Variable</u>	<u>Type</u>	<u>Description</u>
NZONES(1-5)	Real	Number of zones in each of the sub-regions into which the clouds partition the atmosphere. E.g., NZONES(1) is the number of zones from the surface to the first cloud base, or if N CLOUD = 0, is the total number of zones. (20,4*0.)
EXPAN(1-5)	Real	Expansion factors for each sub-region. E.g., in sub-region 1, each zone has a geometrical width EXPAN(1) times the width of the zone below it. This enables one to generate zones of more or less constant mass, increasing mass, etc. (1.1,4*0.)
PRSETF	Logical	If TRUE, user intends to input spectral intervals through FREQS Namelist (see Figure C.1). If FALSE, user intends to set N W A V, W A V, and D W A V or else N G R P S, I W V to determine the spectral interval structure. (FALSE)
N W A V	Integer	Number of spectral "regions" defined by W A V's. (10)
W A V(1-15)	Integer	Wavenumber boundaries in $\text{cm}^{-1}$ in increasing order for each spectral "region." E.g., $W A V(1) < W A V(2)$ are the wavenumbers bounding spectral region 1. Must be integer multiples of $20 \text{ cm}^{-1}$ in order to agree with the McClatchey transmission data. (60, 600, 800, 1200, 1600, 2400, 4800, 8000, 32000, 35000, 48500)

<u>Variable</u>	<u>Type</u>	<u>Description</u>
DWAV(1-14)	Integer	Width in $\text{cm}^{-1}$ for each of the spectral intervals within a spectral "region." Must be integer multiples of $20 \text{ cm}^{-1}$ . E.g., between WAV(1) and WAV(2) all spectral intervals are of size DWAV(1). (60, 20, 40, 80, 160, 240, 320, 500, 1000, 1500)
NGRPS	Integer	If $15 \geq \text{NGRPS} > 0$ , it overrides the WAV, DWAV option. The NGRPS option allows one to do NGRPS possibly disjoint spectral intervals with boundaries IWV (see below); it can be used to sample the spectrum. (o)
IWV(1-30)	Integer	Used when NGRPS $> 0$ . Successive pairs of IWV values define the wave-number boundaries ( $\text{cm}^{-1}$ ) of the spectral intervals being sampled. E.g., if BGRPS = 2, the first interval is [IWV(1),IWV(2)] and the second is [IWV(3),IWV(4)]. (30*0)

<u>Variable</u>	<u>Type</u>	<u>Description</u>
PR1	Logical	If TRUE, causes edit of the atmospheric structure, including altitude, pressure, temperature, water vapor and ozone densities, aerosol number density, and aerosol material and size distribution flags at each level. (TRUE)
PR2	Logical	If TRUE, edits the contents of all input Namelists: MIETAB, LEVELS, FREQS, STRUCT, and AEROS. (MIETAB will always be edited, however, the others will only be edited if they are used to give the program input). (TRUE)
MIEPR(2)	Logical	If TRUE, edits information about the integration over size distribution every time the integration increment $\Delta\alpha$ is doubled (NOPT1 = 0 only). (TRUE)
MIEPR(3)	Logical	If TRUE, edits the Mie phase function and cross-sections resulting from integration over size distribution, as well as wavelength, index of refraction, integration limits, and renormalization factor. If the Henyey-Greenstein option is used, the actual phase function in the forward peak ( $0^\circ$ to ANGCUT $^\circ$ ), the area under this forward peak, and the equivalent 'g' are also edited. (TRUE)
NOTHG(I)	Logical	A set of logical flags, one for each level I starting at the top of the atmosphere, which if TRUE causes the Mie calculation to be done normally and if FALSE causes the Henyey-Greenstein

<u>Variable</u>	<u>Type</u>	<u>Description</u>
		phase function which has the same area under the forward peak to be substituted. (all TRUE)
ANGCUT	Real	Angle, in degrees, defining the size of the forward peak for the purposes of the Henyey-Greenstein option. (4.).
DELO	Real	Increment-doubling parameter for integration over size distribution. When the maximum relative change in any quantity being integrated, due to the previous integration step, is less than DELO, the size of the integration increment is doubled. This process is not begun until a fraction V1 of the size distribution has been integrated over. The integration is terminated after MAXDBL interval-doublings, if it does not first terminate normally (by proceeding all the way to the estimated $\alpha_{\max}$ ). (.001)
MAXDBL	Integer	Maximum number of doublings of integration increment permitted (see DELO). (6)
V1	Real	The size distribution integration increment is kept at a constant value (determined by V2) until the fraction V1 of the size distribution has been integrated over, at which point the interval-doubling feature is allowed to operate (see DELO and MAXDBL). (.99)
V2	Real	The initial size distribution integration increment $\Delta\alpha$ is determined by

<u>Variable</u>	<u>Type</u>	<u>Description</u>
		$\Delta\alpha = \min\left(\sqrt{2}, \frac{\alpha_{\max} - \alpha_{\min}}{200}\right)$ <p>where <math>\alpha_{\max}</math> and <math>\alpha_{\min}</math> are the upper and lower limits on the integration. (0.1)</p>
NOPT	Integer	<p>Atmospheric structure flag.</p> <p>= 0 Input atmospheric structure through "STRUCT" Namelist.</p> <p>= 6 Calculate structure from user-supplied analytic forms contained in subroutines TEMPER, SPFHUM, O3D, AERO, NMATL, NAERO (default forms of these subroutines are used if user does not intervene).</p> <p>Otherwise, use one of the following standard atmospheres:</p> <p>= 1 Tropical</p> <p>= 2 Mid-latitude summer</p> <p>= 3 Mid-latitude winter</p> <p>= 4 Sub-arctic summer</p> <p>= 5 Sub-arctic winter</p>
P0	Real	<p>Surface pressure in mb for case NOPT = 6. (1013.)</p>
NOPT1	Integer	<p><math>i_1</math>-<math>i_2</math> tables flag. If &gt; 0, use <math>i_1</math>-<math>i_2</math> tables on logical unit NOPT3. If = 0, calculate <math>i_1</math>, <math>i_2</math>, etc. in-line. (0)</p>

<u>Variable</u>	<u>Type</u>	<u>Description</u>
NOPT2	Integer	If > 0, stop calculation just before entering frequency loop. This allows user to check that his problem set-up is correct before doing a full run of the code. (1)
NOPT3	Integer	Logical unit number of $i_1$ - $i_2$ tables, if they are to be used (see NOPT1).
NOPT4	Integer	The number of "blocks" of Mie scattering data which are to be skipped in order to continue writing into a partially completed Mie table. (A block consists of the phase function and the angles at which it is specified, the cross-sections, the wavelength, and the wavenumber interval). If = 0, tables are to be generated ab initio. (0)
NOPT5	Integer	Logical unit number on which Mie tables are to be written. If $\leq 0$ , table generation is suppressed.
NSTEP (1-6)	Integer	Used in the determination of the angular mesh on which Mie phase function is calculated. $\Delta\theta$ is calculated in MIE, based on $\alpha_{\max}$ , and from it the angular mesh is calculated as follows: NSTEP(1) steps of $\Delta\theta$ starting at $\theta = 0^\circ$ , NSTEP(2) steps of $2\Delta\theta, \dots$ , NSTEP(K) steps of $2^{K-1}\Delta\theta, \dots$ . The angular step is, however, bounded by DANGMX. (16,3*10, 2*0)

<u>Variable</u>	<u>Type</u>	<u>Description</u>
NDOUB	Integer	Number of non-zero entries in NSTEP (i.e., number of doublings of the angular step). (4)
DANGLO	Real	Minimum permitted value of the initial angular step $\Delta\theta$ , in degrees (see NSTEP). (0.1)
DANGHI	Real	Maximum permitted value of the initial angular step $\Delta\theta$ , in degrees. (1.0)
DANGMX	Real	If at any point in the NSTEP procedure described above, $2^{K-1}\Delta\theta > \text{DANGMX}$ , then the NSTEP procedure is terminated and the rest of the steps to $90^\circ$ are taken with an increment $\Delta\theta_m$ which is as close as possible to DANGMX. (2.5)

C1(I),C2(I), Real  
C3(I)

Input parameters for one of the following commonly-used analytic aerosol size distributions:

Modified Gamma  

$$n(a) = ca^{C1} e^{-C2a} C3$$

Gaussian  

$$n(a) = ce^{-\frac{1}{2}(a-C1)^2/C2^2}$$

Log-Normal  

$$n(a) = \frac{c}{a-C1} \exp[-\{C2 \ln \frac{a-C1}{C3-C1}\}^2]$$

The constant  $c$  is a normalization factor such that

$$\int_0^{\infty} n(a) da = 1$$

In order to flag these distributions for level I, use NAER(I) (see Namelist STRUCT).

Namelist LEVELS

<u>Variable</u>	<u>Type</u>	<u>Description</u>
Z(I)	Real	The heights above the surface of the various levels in the vertical mesh, starting from the surface [Z(1)], in km.
NZ	Integer	The number of levels.
IBD(1-5)	Integer	The indices of the levels which divide the mesh into sub-regions. E.g., Z(IBD(1)) is the height of the lower cloud base, and Z(IBD(2)) is the height of the lower cloud top. If there are no clouds, IBD(1) = NZ.
NBD	Integer	The number of sub-regions required by the presence of clouds (NBD = 2 × # clouds + 1).

Namelist FREQS

WAVNUM (NU)	Integer	The frequencies in $\text{cm}^{-1}$ bounding the spectral intervals, in increasing order (WAVNUM(1) is the smallest).
NNU	Integer	The number of non-zero WAVNUM's (or one plus the number of spectral intervals).

Namelist STRUCT

P(I)	Real	Pressures in mb corresponding to Z(I). (P(1) is the surface pressure).
------	------	--

Namelist STRUCT (contd)

<u>Variable</u>	<u>Type</u>	<u>Description</u>
T(I)	Real	Temperatures in degrees Kelvin. T(1) is the temperature of the air immediately above the ground, and may be different from TG, the ground temperature.
H2ODEN(I)	Real	Water vapor density in g/m <sup>3</sup> .
O3DEN(I)	Real	Ozone density in atm-cm/km.
AERDEN(I)	Real	Aerosol number density in particles/cm <sup>3</sup> .
NAER(I)	Integer	Flag specifying aerosol size distribution: = -J Use size distribution from level J = 0 Tabular data from Namelist AEROS = 1 Deirmendjian Haze M = 2 Deirmendjian Haze L = 3 Deirmendjian Haze H = 4 Deirmendjian Cloud C.1 = 5 Deirmendjian Cloud C.2 = 6 Deirmendjian Cloud C.3 = 7 Modified gamma distribution with parameters C1(I),C2(I),C3(I) = 8 Gaussian distribution with parameters C1(I),C2(I) = 9 Log-normal distribution with parameters C1(I),C2(I),C3(I)
NMAT(I)	Integer	Flag specifying aerosol material: = 1 Water = 2 Sahara dust (Volz) = 3 Dust, $\gamma$ (Volz) = 4 Sea-salt (Volz) = 5 Water solubles, B1 (Volz)

<u>Variable</u>	<u>Type</u>	<u>Description</u>
NMAT(I) (contd)	Integer	= 6 Water solubles, M (Volz)
		= 7 Water solubles, T2 (Volz)
		= 8 Soot
		= 9 Ice

Namelist AEROS

RAD(K,I)	Real	Finite mesh of aerosol radii, in microns, K = 1 to NDAT(I), on which aerosol size distribution AERNUM is specified (level I).
NDAT(I)	Integer	Number of values of RAD for level I.
AERNUM(K,I)	Real	Aerosol number density distribution in particles/cm <sup>3</sup> /micron (level I). HIST = FALSE: Pointwise data, (RAD(K,I), AERNUM(K,I)), I = 1 to NDAT(I). HIST = TRUE: Histogram data, value of distribution = AERNUM(K,I) between RAD(K,I) and RAD(K+1,I).
HIST	Logical	If TRUE, data in AERNUM is of histogram type. If FALSE, it is of pointwise type.

## APPENDIX D

### ATRAD STRUCTURE AND INPUT

Appendices A and B of our previous semi-annual report described the input-output features of ATRAD, but since then ATRAD has been split into four separate code modules in order to obtain maximum computational efficiency. Only the central code module, ATRAD, actually calculates fluxes and heating rates. The others create tables which are used by ATRAD. EVANS-TABLES (Appendix A) makes tables of the exponential fits of transmission functions. I1I2-TABLES (Appendix B) makes tables of the Mie scattering functions for single homogeneous spheres of varying sizes, but fixed index of refraction. MIE-TABLES (Appendix C) makes tables of Mie scattering functions for spherical polydispersions. The relationship among the various code modules is illustrated in Figure D.1, which flow-charts ATRAD. The dotted line connecting I1I2-TABLES and MIE-TABLES is meant to indicate that MIE-TABLES has the option of either generating its own values of  $\sigma_{sca}$ ,  $\sigma_{ext}$ , and  $i_1+i_2$  or reading them from tables generated by I1I2-TABLES.

Figure D.2 illustrates schematically the arrangement of the input data required for starting or restarting an ATRAD calculation. Note that the only required Namelist is WISCOM; all the others may or may not be necessary, depending on the setting of certain parameters in WISCOM. The definitions of the variables in each Namelist in Figure D.2 are given below. Note that there is a parameter IFLCUT in WISCOM which controls

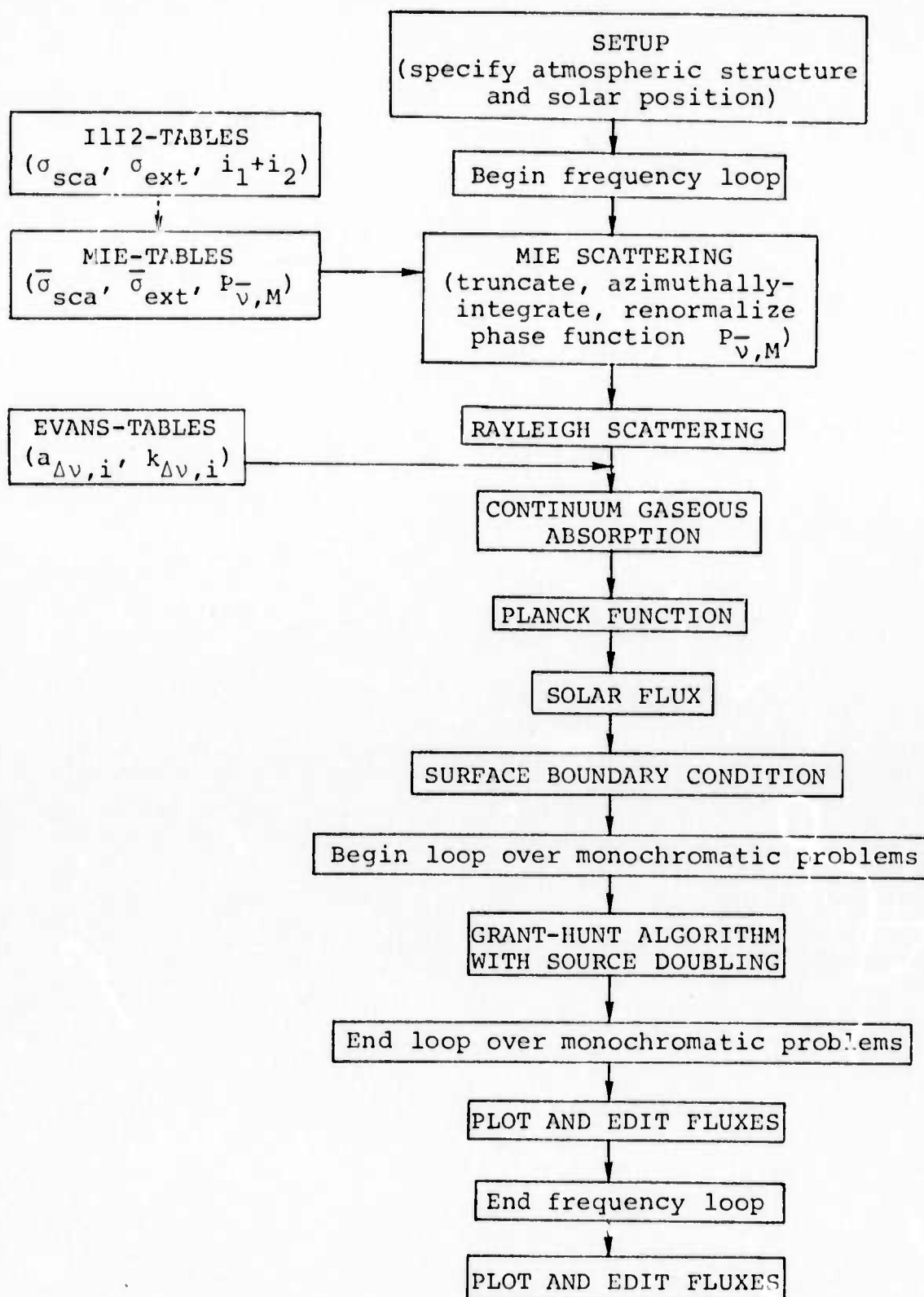


Figure D.1 - ATRAD code organization, showing the role of the three auxiliary table-making codes.

```
                                { WISCOM Namelist
                                {   Input Control Parameters
                                { END

only if
PRSETZ = TRUE                  { LEVELS Namelist
                                {   Z, NZ, IBD, NBD
                                { END

only if
PRSETF = TRUE                  { FREQS Namelist
                                {   WAVNUM, NNU
                                { END

only if
NOPT = 0                       { STRUCT Namelist
                                {   P, T, H2ODEN, O3DEN,
                                {   AERDEN, NMAT, NAER
                                { END
```

Figure D.2 - Normal input sequence for ATRAD.

the summing of 'partial' fluxes, which are simply sums of the spectral fluxes over contiguous subsets of the totality of spectral intervals. Thus, for example, the solar and IR sums may be done separately, as 'partial' fluxes. Note also that some of the parameters in WISCOM, and all of the Namelists LEVELS, FREQS, and STRUCT are the same in MIE-TABLES (Appendix C) and ATRAD.

Namelist WISCOM

<u>Variable</u>	<u>Type</u>	<u>Description</u>
PR1	Logical	If TRUE, causes edit of atmospheric structure (altitude, pressure, temperature, water vapor and ozone densities, aerosol number density, and aerosol flags). (TRUE)
PR2	Logical	If TRUE, edits and plots upward, downward, and net fluxes at every level ( $w/m^2$ ), and edits heating rates of every zone ( $^{\circ}C/day$ ) at the completion of the frequency loop; also edits the net flux spectrum at the top and bottom of the mesh. (TRUE)
PR3	Logical	If TRUE, edits upward, downward, and net fluxes and the current contents of the total and 'partial' flux arrays (also upward, downward, and net) at the end of each pass through the frequency loop. Also heating rates, incident solar flux at the top of the atmosphere, and earth + atmosphere albedo for each spectral interval. (FALSE)

<u>Variable</u>	<u>Type</u>	<u>Description</u>
PR4	Logical	If TRUE, edits solar flux, Planck function, scattering coefficient, and continuum absorption coefficient for both the current and previous frequency group, and the percent change of each quantity from the previous frequency group. Also edits the continuum part of the optical depth of each zone, and various surface quantities such as the directional emissivity $\epsilon(\mu)$ and reflection matrix $r_G(\mu, \mu')$ . (FALSE)
PR5	Logical	If TRUE, edits the intensities for each spectral interval. (FALSE)
SCTPRT	Logical	If TRUE, edits truncation information, Mie scattering and absorption coefficients, azimuthally-averaged Mie phase function both before and after renormalization, Rayleigh and total scattering coefficients, and total phase function. (FALSE)
TPR1	Logical	If TRUE, performs a "short" edit of each call to the Grant-Hunt algorithm, including the single-scattering albedo, line absorption coefficient, optical depth, doubling parameters, source vectors, and resultant (diffuse) intensities for each level. (FALSE)
TPR2	Logical	If TRUE, performs all of the edits of TPR1 plus the Planck and solar source vectors, the reflection and

<u>Variable</u>	<u>Type</u>	<u>Description</u>
		transmission matrices for each zone, and the various vectors and matrices (E, V <sub>1</sub> , etc.) used in the Grant-Hunt algorithm. (FALSE)
PRSETF	Logical	If TRUE, user intends to input spectral intervals through FREQS Namelist (see Figure D.2). If FALSE, user intends to set N WAV, WAV, and DWAV or else NGRPS, IWV to determine the spectral interval structure. (FALSE)
N WAV	Integer	Number of spectral "regions" defined by WAV's. (10)
WAV(1-15)	Integer	Wavenumber boundaries in cm <sup>-1</sup> in increasing order for each spectral "region." E.g., WAV(1) < WAV(2) are the wavenumbers bounding spectral region 1. Must be integer multiples of 20 cm <sup>-1</sup> in order to agree with the McClatchey transmission data. (60, 600, 800, 1200, 1600, 2400, 4800, 8000, 32000, 35000, 48500)
D WAV(1-14)	Integer	Width in cm <sup>-1</sup> for each of the spectral intervals within a spectral "region." Must be integer multiples of 20 cm <sup>-1</sup> . E.g., between WAV(1) and WAV(2) all spectral intervals are of size DWAV(1). (60, 20, 40, 80, 160, 240, 320, 500, 1000, 1500)

<u>Variable</u>	<u>Type</u>	<u>Description</u>
NGRPS	Integer	If $15 \geq \text{NGRPS} > 0$ , it overrides the WAV, DWAV option. The NGRPS option allows one to do NGRPS possibly disjoint spectral intervals with boundaries IWV (see below); it can be used to sample the spectrum. (0)
IWV(1-30)	Integer	Used when NGRPS > 0. Successive pairs of IWV values define the wave-number boundaries ( $\text{cm}^{-1}$ ) of the spectral intervals being sampled. E.g., if NGRPS = 2, the first interval is [IWV(1),IWV(2)] and the second is [IWV(3),IWV(4)]. (30*0)
PRSETZ	Logical	If TRUE, the user intends to input the zone structure through the "LEVELS" Namelist. If FALSE, user intends to set TROPO, CLDBAS, CLDTOP, NZONES, and EXPAN (see below) from which the code will calculate the zone structure. (FALSE)
OZONE	Logical	If TRUE, place the uppermost level at 50 km altitude. If FALSE, take the uppermost level at TROPO km (the tropopause or some level just below the ozone layer). In the latter case, the incident solar flux will be truncated at 03CUT. (TRUE)

<u>Variable</u>	<u>Type</u>	<u>Description</u>
TROPO	Real	If OZONE = FALSE, the height in km of the uppermost level in the problem is set to TROPO. This level should be reasonably close to the bottom of the ozone layer. (15.0)
NCLOUD	Integer	The number of cloud layers (only 0, 1, or 2 are allowed). This must always be set, however the levels are determined.
CLDBAS (1,2)	Real	Heights in km of bases of lower (1) and upper (2) cloud. (2*0)
CLDTOP (1,2)	Real	Heights in km of tops of lower (1) and upper (2) cloud. (2*0)
NZONES (1-5)	Real	Number of zones in each of the sub-regions into which the clouds partition the atmosphere. E.g., NZONES (1) is the number of zones from the surface to the first cloud base, or if NCLOUD = 0, is the total number of zones. (20,4*0.)
EXPAN (1-5)	Real	Expansion factors for each sub-region E.g., in sub-region 1, each zone has a geometrical width EXPAN(1) times the width of the zone below it. This enables one to generate zones of more or less constant mass, increasing mass, etc. (1.1,4*0.)

<u>Variable</u>	<u>Type</u>	<u>Description</u>
IWVANG(1-15)	Integer	Wavenumber boundaries in $\text{cm}^{-1}$ delineating regions in which the number of quadrature angles is constant. This allows one to use fewer angles in frequency regions where the intensity is more nearly isotropic (in each hemisphere separately). (50, 50000, 13*0)
NUMANG(1-14)	Integer	Number of quadrature angles used in each hemisphere in the corresponding frequency region delineated by IWVANG. E.g., the number of quadrature angles between IWVANG(1) and IWVANG(2) is NUMANG(1). (6, 13*0)
NUMANG(15)	Integer	Number of wavenumber regions delineated by IWVANG. (1)
RADOW(1-14)	Logical	If RADOW(K) = TRUE, then use Radau quadrature in wavenumber interval [IWVANG(K), IWVANG(K+1)]. Otherwise, Gaussian quadrature. (14*FALSE)
NOPT	Integer	Atmospheric structure flag. = 0 Input atmospheric structure through "STRUCT" Namelist. = 6 Calculate structure from user-supplied analytic forms contained in subroutines TEMPER, SPFHUM, O3D, AERD, NMATL, NAERO (default forms of these subroutines are used if user does not intervene).

<u>Variable</u>	<u>Type</u>	<u>Description</u>
		= 7 Restart. Read in structure from dump file (see NOPT3).  Otherwise, use one of the following standard atmospheres: = 1 Tropical = 2 Mid-latitude summer = 3 Mid-latitude winter = 4 Sub-arctic summer = 5 Sub-arctic winter
NOPT1	Integer	Phase function renormalization flag. = 1 Use Grant method. = 2 Use Wiscombe method. (2)
NOPT2	Integer	If > 0, stop calculation just before entering frequency loop. This allows user to check that his problem set-up is correct before doing a full run of the code. (1)
NOPT3	Integer	Logical unit number for picking up restart information in NOPT = 7 case.
NOPT4	Integer	Logical unit number for dumping restart information at the end of each pass through the frequency loop. If $\leq 0$ , suppress dumps.
NOPT5	Integer	Logical unit number of Mie tables which are to be used.
P0	Real	Surface pressure in mb for case NOPT = 6. (1013.)
DAY	Real	Day of the year, January 1 being day 1. (1.)

<u>Variable</u>	<u>Type</u>	<u>Description</u>
TIME	Real	Greenwich time, in hours. (0)
LONG	Real	Longitude, in degrees, counted positive west of Greenwich. (117.)
LAT	Real	Latitude, in degrees. (33.)
CUTPLK	Real	Wavenumber in $\text{cm}^{-1}$ above which Planck function is set to zero. (3333.)
CUTSOL	Real	Wavenumber in $\text{cm}^{-1}$ below which incident solar flux is set to zero. (1666.)
CUTRAY	Real	Wavelength in microns above which Rayleigh scattering is neglected. (3.)
O3CUT	Real	Wavenumber in $\text{cm}^{-1}$ above which incident solar flux is set to zero in case OZONE = FALSE. (33333.)
NMATG	Integer	Surface material flag. (1)
TG	Real	Surface temperature in °K. (300.)
WNSURF(1-11)	Real	Frequency boundaries in $\text{cm}^{-1}$ specifying regions within which the surface boundary condition is calculated according to the corresponding value of NSURF. (50.,50000.,9*0.)
NSURF(1-10)	Integer	Between WNSURF(K) and WNSURF(K+1), the surface boundary condition is flagged by NSURF(K). The options are:  NSURF = 1 Hemispherical reflectivity or hemispherical emissivity supplied by user as function of wavelength, in subroutine SURF1.

<u>Variable</u>	<u>Type</u>	<u>Description</u>
NSURF(1-10) (contd)	Integer	Diffuse emission and reflection assumed.  = 2 Directional emissivity or directional-hemispherical reflectivity supplied by user as a function of angle and wavelength, in subroutine SURF2. Diffuse reflection assumed.  = 3 Azimuthally-averaged bidirectional reflectivity supplied by user as a function of angle of incidence, angle of reflection, and wavelength, in subroutine SURF3. (1,9*0)
NSURF(11)	Integer	Number of non-zero WNSURF entries. (2)
NOTHG(I)	Logical	If NOTHG(I) = TRUE, use the normal procedure to calculate the Mie phase function for zone I. If NOTHG(I) = FALSE, calculate the Mie phase function only in the forward peak and use a Henyey-Greenstein phase function which has the same area under its forward peak to replace the actual phase function. (all TRUE)
ANGMAX	Real	The maximum allowed angle, in degrees, at which the Mie phase function may be truncated (a search is made through progressively larger angles in attempting to perform a satisfactory truncation). (20.)

<u>Variable</u>	<u>Type</u>	<u>Description</u>
CUTMIN	Real	The maximum allowed value at 0° of the truncated Mie phase function (actually, if the truncation search reaches ANGMAX without satisfying the CUTMIN criterion, the default truncation at ANGMAX may produce a truncated phase function whose value at 0° is larger than CUTMIN). (30.)
CHGMAX	Real	If $\geq 10^{-30}$ , overrides the normal surface boundary condition flags NSURF and WNSURF and sets the albedo = CHGMAX in the solar spectrum (0.2 - 3.0 $\mu$ ) and = 0 in the IR (for zero albedo, input CHGMAX = $10^{-30}$ ). (0.)
FACT	Real	The fraction of the maximum primary layer optical depth, $\Delta\tau_{\max}$ , which is to be used as a doubling interval in the Grant-Hunt algorithm. (0.5)
SCTMIN	Real	If the single-scattering albedo $\omega < \text{SCTMIN}$ , then the no-scattering path through the Grant-Hunt algorithm (involving considerably less calculation) is used. (1.E-5)
IFLCUT(1-10)	Integer	Wavenumber values, in $\text{cm}^{-1}$ , defining the points at which the 'partial' flux arrays (down, up, and net) are to be plotted and then zeroed out. The partial flux arrays may in this fashion accumulate spectral fluxes over only a portion of the full spectrum. (2500, 11000, 50000, 7*0)

<u>Variable</u>	<u>Type</u>	<u>Description</u>
SOLZEN	Integer	If it is desired to input the solar zenith angle directly rather than using DAY, TIME, LONG, LAT, then use SOLZEN. (The parameter DAY is still required in order to calculate the earth-sun distance). (0.)

Namelist LEVELS

Z(I)	Real	The heights above the surface of the various levels in the vertical mesh, starting from the surface [Z(1)], in km.
NZ	Integer	The indices of the levels which divide the mesh into sub-regions. E.g., Z(IBM(1)) is the height of the lower cloud base, and Z(IBM(2)) is the height of the lower cloud top. If there are no clouds, IBM(1) = NZ.
NBD	Integer	The number of sub-regions required by the presence of clouds (NBD = 2 × # clouds + 1).

Namelist FREQS

WAVNUM(NU)	Integer	The frequencies in $\text{cm}^{-1}$ bounding the spectral intervals, in increasing order (WAVNUM(1) is the smallest).
------------	---------	---

<u>Variable</u>	<u>Type</u>	<u>Description</u>
NNU	Integer	The number of non-zero WAVNUM's (or one plus the number of spectral intervals).

Namelist STRUCT

P(I)	Real	Pressures in mb corresponding to Z(I). (P(1) is the surface pressure).
T(I)	Real	Temperatures in degrees Kelvin. T(1) is the temperature of the air immediately above the ground, and may be different from TG, the ground temperature.
H2ODEN(I)	Real	Water vapor density in $\text{g/m}^3$ .
O3DEN(I)	Real	Ozone density in atm-cm/km.
AERDEN(I)	Real	Aerosol number density in particles/ $\text{cm}^3$ .
NAER(I)	Integer	Flag specifying aerosol size distribution: = -J Use size distribution from level J = 0 Tabular data = 1 Deirmendjian Haze M = 2 Deirmendjian Haze L = 3 Deirmendjian Haze H = 4 Deirmendjian Cloud C.1 = 5 Deirmendjian Cloud C.2 = 6 Deirmendjian Cloud C.3 = 7 Modified gamma distribution

<u>Variable</u>	<u>Type</u>	<u>Description</u>
		= 8 Gaussian distribution
		= 9 Log-normal distribution
		This flag is only used to check the input from the Mie tables as regards consistency.
NMAT(I)	Integer	Flag specifying aerosol material:
		= 1 Water
		= 2 Sahara dust (Volz)
		= 3 Dust, $\gamma$ (Volz)
		= 4 Sea-salt (Volz)
		= 5 Water solubles, B1 (Volz)
		= 6 Water solubles, M (Volz)
		= 7 Water solubles, T2 (Volz)
		= 8 Soot
		= 9 Ice
		This flag is only used to check the input from the Mie tables as regards consistency.